Novel Converter Solutions with a Modular Multilevel Structure for High-Power Medium-Voltage Electrical Machine Drive Applications

Gontijo, Gustavo

DOI (link to publication from Publisher):
10.54337/aau504491302

Publication date:
2022

Document Version
Publisher's PDF, also known as Version of record

NOVEL CONVERTER SOLUTIONS WITH A MODULAR MULTILEVEL STRUCTURE FOR HIGH-POWER MEDIUM-VOLTAGE ELECTRICAL MACHINE DRIVE APPLICATIONS

BY
GUSTAVO FIGUEIREDO GONTIJO

DISSERTATION SUBMITTED 2022

AALBORG UNIVERSITY
DENMARK

Novel Converter Solutions with a Modular Multilevel Structure for High-Power Medium-Voltage Electrical Machine Drive Applications

Ph.D. Dissertation

Gustavo Figueiredo Gontijo

Aalborg University
AAU Energy
Pontoppidanstraede 111
DK-9220 Aalborg East

Dissertation submitted: July 30, 2022

PhD supervisors: Professor Remus Teodorescu
Aalborg University

Associate Professor Tamas Kerekes
Aalborg University

PhD committee: Szymon Beczkowski (chairman)
Aalborg University, Denmark

Associate Professor Massimo Bongiorno
Chalmers University of Technology, Sweden

Professor Mariusz Malinowski
Warsaw University of Technology, Poland

PhD Series: Faculty of Engineering and Science, Aalborg University

Department: AAU Energy

ISSN (online): 2446-1636
ISBN (online): 978-87-7573-854-0

Published by:
Aalborg University Press
Kroghstræde 3
DK – 9220 Aalborg Ø
Phone: +45 99407140
aauf@forlag.aau.dk
forlag.aau.dk

Printed in Denmark by Stibo Complete, 2022

Biography

Gustavo Figueiredo Gontijo

Gustavo F. Gontijo received the B.Sc. and M.Sc. degrees in electrical engineering from the Federal University of Rio de Janeiro (UFRJ), Rio de Janeiro, Brazil, in 2016 and 2018, respectively. He is currently pursuing the Ph.D. degree with AAU Energy, Aalborg University, Aalborg Øst, Denmark.

From 2014 to 2015, he was an Intern with the Leopoldo Americo Miguez de Mello Research and Development Center (Cenpes) of the Brazilian energy company Petrobras, where he was involved with research works related to solar photovoltaic systems and wind turbines. From 2015 to 2019, he was with the Laboratory of Power Electronics and Medium Voltage Applications, which is part of the Alberto Luiz Coimbra Institute for Graduate Studies and Research in Engineering (LEMT/COPPE/UFRJ). In LEMT, he was involved in research works related to power electronics applied to wind turbines, STATCOMs, active filters, virtual synchronous machines, and microgrids. From 2020 to 2021, he was a Research Assistant with AAU Energy, Aalborg University. From 2021 to 2022, he was a Guest Researcher with Ørsted Wind Power A/S, Gentofte, Denmark, working in a research collaboration with the title "Eigenvalue-Based Stability Assessment of an Offshore Wind Power Plant with an MMC-Based HVDC Connection". Recently, he joined Ørsted Wind Power A/S as a Power System Engineer. His current research interests include modular multilevel converter solutions with and without energy-storage integration for medium-voltage applications, stability of power-electronic-based power systems, and modern HVDC transmission systems based on the modular multilevel converter.

English Abstract

The fast development of the modern industry has been leading to a constant increase in the energy demand. At the same time, serious environmental issues are calling for a severe change in the world's energy consumption paradigm moving from a fossil-fuel-based energy matrix to a green one. The high penetration of renewable-energy generation leads to an increased complexity of the control and operation of power systems. Power electronics is the technology that allows for the high flexibility and controllability of these modern electrical grids. However, until recently, the power ratings of the most advanced semiconductor devices limited the usage of power-electronic converters, especially if high-voltage applications were considered. The usage of stacks of several series-connected semiconductor devices operating at high frequencies was the only solution to build flexible high-voltage converters, even though these converters presented poor reliability and high switching losses.

The invention of the modular multilevel converter (MMC) represented a breakthrough in the electrical engineering filed. The scalability and modularity of this converter topology allows obtaining high voltages by connecting in series several low-voltage sub blocks that can be built with semiconductor devices with voltage ratings currently available in the industry. Moreover, the MMC is a flexible converter solution that presents high reliability and that can synthesize high-power-quality multilevel voltages at its AC terminals. Due to its many important features, the MMC became the standard power-electronic solution for high-power applications, especially for the flexible voltage-source-converter high-voltage direct-current (VSC-HVDC) transmission systems. MMC solutions have also been adopted for applications such as static synchronous compensators (STATCOMs) and for high-power medium-voltage electrical-machine drives. Despite its many advantages, the MMC also presents some drawbacks such as its high structural and control complexity, its high number of components, which leads to high volume, weight and cost, and finally its poor performance at low frequencies because of the intolerably high submodule-capacitor voltage ripple in this operation condition. In high-power industrial motor drives for example, the high submodule-capacitor voltage ripple at low frequencies can be quite critical. Another potential machine-drive application of an MMC are the modern/future high-power wind turbines (WTs) with

a medium-voltage structure aiming at avoiding technical issues with excessively high currents, and aiming at obtaining more compact solutions with reduced conductor and transformer requirements. In this case, the increased dimensions of the MMC would play a negative role in the general solution. In this Ph.D. thesis, novel converter solutions with a modular multilevel structure are proposed aiming at overcoming some of the drawbacks and limitations of the traditional MMC, and of other converters with a modular multilevel structure, in high-power medium-voltage machine drives. Moreover, the modular features of the converters with a modular multilevel structure are explored in a way as to integrate energy storage devices into the proposed topologies, aiming at obtaining flexible solutions that are capable to provide ancillary services to the electrical grid.

Dansk Resumé

Den hurtige udvikling af den moderne industri har ført til en konstant stigning i energiefterspørgslen. Samtidig kalder alvorlige miljøproblemer på en alvorlig ændring i verdens energiforbrugsparadigme, der går fra en fossilt brændstofbaseret energimatrix til en grøn. Den høje udbredelse af vedvarende energiproduktion fører til en øget kompleksitet af styringen og driften af strømsystemer. Kraftelektronik er den teknologi, der muliggør den høje fleksibilitet og kontrollerbarhed af disse moderne elektriske net. Indtil for nylig begrænsede effektmærkningerne for de mest avancerede halvlederenheder imidlertid brugen af strømelektroniske omformere, især hvis højspændingsapplikationer blev overvejet. Brugen af stakke af flere serieforbundne halvlederenheder, der opererede ved høje frekvenser, var den eneste løsning til at bygge fleksible højspændingsomformere, selvom disse konvertere udviste ringe pålidelighed og store koblingstab.

Opfindelsen af den modulære multilevel-konverter (MMC) repræsenterede et gennembrud i den indleverede elektroteknik. Skalerbarheden og modulariteten af denne konvertertopologi gør det muligt at opnå høje spændinger ved at seriekoble adskillige lavspændingsunderblokke, der kan bygges med halvlederenheder med spændingsklassificeringer, der i øjeblikket er tilgængelige i industrien. Desuden er MMC en fleksibel konverterløsning, der præsenterer høj pålidelighed, og som kan syntetisere multilevelspændinger af høj effektkvalitet ved sine AC-terminaler. På grund af dets mange vigtige egenskaber blev MMC den standard strøm-elektroniske løsning til høj-effekt applikationer, især for de fleksible spænding-kilde-konverter højspænding jævnstrøm (VSC-HVDC) transmissionssystemer. MMC-løsninger er også blevet vedtaget til applikationer såsom statiske synkrone kompensatorer (STATCOM'er) og til højeffekts mellemspændingsdrev til elektriske maskiner. På trods af dens mange fordele, præsenterer MMC også nogle ulemper, såsom dens høje strukturelle og kontrolkompleksitet, dens høje antal komponenter, hvilket fører til høj volumen, vægt og omkostninger, og endelig dens dårlige ydeevne ved lave frekvenser på grund af det uacceptabelt høje submodul -kondensatorspændingsrippel i denne driftstilstand. I industrielle motordrev med høj effekt kan den høje submodul-kondensatorspændingsrippel ved lave frekvenser være ret kritisk. En anden potentiel maskindrevet anvendelse af en MMC er de moderne/fremtidige højeffektvindmøller med en mellemspændingsstruktur, der sigter mod

at undgå tekniske problemer med for høje strømme og sigter mod at opnå mere kompakte løsninger med reducerede leder- og transformerkrav. I dette tilfælde ville de øgede dimensioner af MMC spille en negativ rolle i den generelle løsning. I denne ph.d. afhandling foreslås nye konverterløsninger med en modulær flerniveaustruktur med det formål at overvinde nogle af ulemperne og begrænsningerne ved den traditionelle MMC og andre konvertere med en modulær flerniveaustruktur i højeffekts mellemspændingsmaskinedrev. Desuden udforskes de modulære funktioner i konverterne med en modulær flerniveaustruktur på en måde, så de integrerer energilagringsenheder i de foreslåede topologier, med det formål at opnå fleksible løsninger, der er i stand til at levere hjælpetjenester til det elektriske net.

Contents

Thesis Details

Thesis Title:	Novel Converter Solutions with a Modular Multilevel Structure for High-Power Medium-Voltage Electrical Machine Drive Applications
Ph.D. Student:	Gustavo Figueiredo Gontijo
Supervisors:	Prof. Remus Teodorescu, Aalborg University Assoc. Prof. Tamas Kerekes, Aalborg University

The main part of the dissertation is based on the following publications:

Journal Publications:

[**J1**] **G. F. Gontijo**, S. Wang, T. Kerekes, and R. Teodorescu, "New AC-AC Modular Multilevel Converter Solution for Medium-Voltage Machine-Drive Applications: Modular Multilevel Series Converter," in *Energies,* vol. 13, no. 14, pp. 3664, Jul. 2020.

[**J2**] **G. F. Gontijo**, S. Wang, T. Kerekes, and R. Teodorescu, "Novel Converter Topology with Reduced Cost, Size and Weight for High-Power Medium-Voltage Machine Drives: 3x3 Modular Multilevel Series Converter," in *IEEE Access,* vol. 9, pp. 49082 - 49097, Mar. 2021.

[**J3**] **G. F. Gontijo**, S. Wang, T. Kerekes, and R. Teodorescu, "Performance Analysis of Modular Multilevel Converter and Modular Multilevel Series Converter under Variable-Frequency Operation Regarding Submodule-Capacitor Voltage Ripple," in *Energies,* vol. 14, no. 3, pp. 776, Feb. 2021.

[**J4**] **G. F. Gontijo**, T. Kerekes, D. Sera, M. Ricco, L. Mathe and R. Teodorescu, "New Converter Solution with a Compact Modular Multilevel Structure Suitable for High-Power Medium-Voltage Wind Turbines," under review in *IEEE Transactions on Power Electronics,* 2022.

[**J5**] **G. F. Gontijo**, T. Kerekes, D. Sera, M. Ricco, L. Mathe, and R. Teodorescu, "Medium-Voltage Converter Solution with Modular Multilevel Structure and Decentralized Energy Storage Integration for High-Power Wind Turbines," in *IEEE Transactions on Power Electronics,* vol. 36, no. 11, pp. 12954 - 12967, May 2021.

[**J6**] **G. F. Gontijo**, D. Sera, M. Ricco, L. Mathe, T. Kerekes, and R. Teodorescu, "Dispatchable High-Power Wind Turbine Based on a Multilevel Converter with Modular Structure and Hybrid Energy Storage Integration," in *IEEE Access,* vol. 9, pp. 152878 - 152891, Nov. 2021.

Conference Publications:

[**C1**] **G. F. Gontijo**, T. Kerekes, and R. Teodorescu, "Operational Advantages and Challenges of New AC-AC Converter Solution with Modular Multilevel Structure Suitable for High-Power Medium-Voltage Electrical Machine Drives," in *Proc. OPTIM-ACEMP,* Brasov, Romania, 2021.

[**C2**] **G. F. Gontijo**, D. Sera, M. Ricco, L. Mathe, T. Kerekes, and R. Teodorescu, "High-Power Medium-Voltage Wind Turbine Driven by Converter Solution with Modular Multilevel Structure and Decentralized Battery Integration Operating in Both Grid-Following and Grid-Forming Modes," in *Proc. EPE'21 ECCE Europe,* Ghent, Belgium, 2021.

Journal Publication Related to Research Collaboration with Ørsted Wind Power A/S

As part of the Ph.D. requirements, Gustavo stayed for 6 months as a Guest Researcher at Ørsted Wind Power A/S. In this collaboration, the Ph.D. student's acquired experience on modular multilevel converters was combined with the strong company's know-how in stability analysis to perform a work with the title: "Eigenvalue-Based Stability Assessment of an Offshore Wind Power Plant with an MMC-Based HVDC Connection". This successful research collaboration resulted in the following extra journal publication.

[**E1**] **G. F. Gontijo**, M. K. Bakhshizadeh, L. H. Kocewiak, and R. Teodorescu, "State Space Modeling of an Offshore Wind Power Plant with an MMC-HVDC Connection for an Eigenvalue-based Stability Analysis," under review in *IEEE Access,* 2022.

Other Relevant Journal Publications About Modular Multilevel Converters as a Co-Author

[**E2**] S. Wang, T. Dragicevic, **G. F. Gontijo**, S. K. Chaudhary, and R. Teodorescu, "Machine Learning Emulation of Model Predictive Control for Modular Multilevel Converters," in *IEEE Transactions on Industrial Electronics,* vol. 68, no. 11, pp. 11628 - 11634, Nov. 2020.

[**E3**] S. Wang, D. Bao, **G. F. Gontijo**, S. K. Chaudhary, and R. Teodorescu, "Modeling and Mitigation Control of the Submodule-Capacitor Voltage Ripple of a Modular Multilevel Converter under Unbalanced Grid Conditions," in *Energies,* vol. 14, no. 3, pp. 651, Jan. 2021.

Other Relevant Journal Publications About Other Power-Electronic Topics as a Co-Author

[**E4**] B. W. Franca, M. Aredes, L. F. Silva, **G. F. Gontijo**, T. C. Tricarico, and J. Posada, "An Enhanced Shunt Active Filter Based on Synchronverter Concept," in *IEEE Journal of Emerging and Selected Topics in Power Electronics,* vol. 10, no. 1, pp. 494 - 505, Aug. 2021.

This dissertation has been submitted for assessment in partial fulfillment of the Ph.D. degree. Based on the publications shown above, the thesis serves as a summary of those, highlighting the primary outcome of the Ph.D. project. Parts of the results are used directly or indirectly in the extended summary of the thesis. The co-author statements have been made available to the assessment committee and are also available at the Faculty of Engineering and Science, Aalborg University.

Preface

The content of this Ph.D. dissertation is a summary of the results obtained from the Ph.D. project: Novel Converter Solutions with a Modular Multilevel Structure for High-Power Medium-Voltage Electrical Machine Drive Applications, which was carried out at AAU Energy, Aalborg University, Denmark. The Ph.D. candidate would like to express his deepest gratitude to Aalborg University for providing such an amazing research environment, where the Ph.D. student had access to state-of-the-art hardware and all the necessary software licenses to perform his work.

Acknowledgements

I would like to start by thanking my supervisor Professor Remus Teodorescu from Aalborg University for all his kindness in accepting me as his Ph.D. student and for welcoming me in Aalborg since the first time I walked into his office when I visited the university in 2018, one year before I officially started my Ph.D. I am extremely grateful for all the technical knowledge I learned with Professor Remus, but his kindness and humbleness also taught me very important lessons. I would also like to thank my co-supervisor Associate Professor Tamas Kerekes from Aalborg University for his excellent technical support and for his help with other relevant administrative tasks related to my Ph.D. Remus and Tamas were not only great supervisors, but also friends who helped me settle down and feel comfortable in Denmark.

I am also thankful for the technical support and for the successful collaboration with Associate Professor Mattia Ricco from the University of Bologna in Italy, with Associate Professor Dezso Sera from the Queensland University of Technology in Australia, and with Dr. Laszlo Mathe from Robert Bosch in Hungary. Mattia, Dezso and Laszlo helped me in the development of one of my converter topologies, which resulted in different publications, and supported me with insightful technical discussions.

I would also like to thank all the AAU professors for the many interesting Ph.D. courses that allowed a very diversified professional qualification throughout my doctorate. I think it is amazing the fact that AAU counts with so many specialists in various topics within the field of electrical engineering, which allows students to have a broad

learning experience at the university. I am also very grateful for all the AAU staff for the kind help with administrative matters, and for always making sure to create a pleasant and fun atmosphere at the university.

I am also extremely thankful for having my good friend Songda Wang as a former colleague in my research group at AAU. Songda introduced me to the equipment and devices of the Modular Multilevel Converter Laboratory, and helped me in carrying out some experimental tests. Songda was also a sweet friend during some of the stressful times that are common to any Ph.D. project.

I would like to give a very special thanks to Dr. Mohammadkazem Bakhshizadeh Dowlatabadi and to Dr. Łukasz Hubert Kocewiak from Ørsted Wind Power A/S, where I was a Guest Researcher for six months as part of my Ph.D. project. Mohammadkazem and Łukasz gave me exceptional technical support, with weekly meetings that contributed for the very successful research collaboration we had. My stay at Ørsted Wind Power A/S was certainly an incredible learning experience where I was able to acquire important knowledge on the trending topic related to stability issues of modular multilevel converters in HVDC applications for offshore wind power plants. This great experience has improved my professional qualification with regard to knowledge about modular multilevel converters not only at the component level, but also at the system level. I am also very grateful for my other Ørsted's colleagues who made me feel comfortable and part of the team at the company.

I am so happy to have had the encouragement of my beautiful and supportive family. I thank my father Rogerio, my mother Maria Aparecida, my sister Bruna and my aunt Maria Silvia for their love and support throughout this journey.

Finally, I have to especially thank my lovely wife and best friend Karen for agreeing to embark on this adventure with me and for being by my side through the most difficult times.

Gustavo Figueiredo Gontijo
Aalborg University, July 30, 2022

Part I

Report

1 Introduction

1.1 Background

The rapid development of modern industry has led to a steady increase in energy demand. At the same time, environmental issues have forced the world to reduce the use of energy sources based on fossil fuels. To keep up with the rapid growth of modern industry and meet the environmental measures imposed by governments, there is a growing penetration of generation sources based on renewable energy all over the world. The high penetration of renewable energy generation leads to an increase in the complexity of controlling and operating power systems. Power electronics is the technology that allows high flexibility and controllability of these modern electrical networks. However, until recently, the power ratings of the most advanced semiconductor devices limited the use of power-electronic converters, especially if high voltage applications were considered. The traditional solution available to reach increased voltage levels was to connect in series several semiconductor devices aiming at obtaining a stack capable to behave as a high voltage switch. However, small delays in the turn-on/turn-of time of the many devices in the stack could result in serious problems related to static and dynamic voltage sharing among these devices, which would then result in a solution with poor reliability [1–6]. This problem would be particularly critical in flexible voltage-source converters operating with high switching frequencies. For example, traditional two-level three-phase converters would present various problems if operating at high voltage levels [6]. Besides the mentioned poor reliability, this topology would operate with intolerably high switching losses because of its high power devices switching at high frequencies. Another drawback of a two-level three-phase converter if operating at high voltages would be the high $\frac{dV}{dt}$ that would occur when synthesizing an AC voltage based on a two-level DC voltage. The high $\frac{dV}{dt}$ could be harmful to the insulation of grid elements or to an eventual electrical-machine load. There are some alternative converter solutions such as the diode-clamped converters (the three-level neutral-point-clamped (NPC) converter, the four-level diode-clamped converter and etc.) that could be used to reach slightly increased voltages [6]. The higher number of levels in these topologies lead to an improved power quality of the synthesized voltages and to a reduced $\frac{dV}{dt}$. Thus, depending on the power level of the given application, the diode-clamped converters could be interesting options. However, for extremely high power levels, these converters might become unsuitable since further increasing their number of levels would result in extremely complex solutions. Besides, high switching losses could still be an issue in such topologies when dealing with extremely high power.

The invention of the MMC (see Fig. 1) represented a major breakthrough in the electrical engineering field since this converter was capable to reach high voltage levels in a reliable manner due to its modular and scalable structure that allowed obtaining high-voltage strings composed of several series-connected low-voltage sub blocks (sub-

modules). The semiconductor devices of these submodules must be capable to block only the voltages of their own capacitors, which means that commercially available semiconductor devices can be used to build such sub blocks. The MMC reliability is improved even further because of the adopted redundancy, which means to have spare submodules available to replace any given eventually damaged submodule within its strings. Moreover, MMCs can synthesize high-power-quality multilevel voltages leading to reduced filtering requirements. Commercial MMCs are currently available and important high-power applications are emerging and being connected to the electrical grid allowing for increased flexibility. Among the most common MMC-based applications are the HVDC transmission systems, operating as voltage sources, and medium-voltage STATCOMs. These applications operate synchronized with the grid, which means with a fixed frequency (50 or 60 Hz) at their AC terminals. Nonetheless, there are some other modern high-power variable-frequency applications for which MMCs have been proposed. These are high-power medium-voltage electrical machine drives as, for example, modern/future upscaled WTs, flexible pumped hydro storage systems [7–9], industrial motor drives, gearless Semi-Autogenous Grinding (SAG) mills [10], and full-electric marine propulsion systems [10]. The benefits of having increased voltage levels in some of the mentioned applications are presented below.

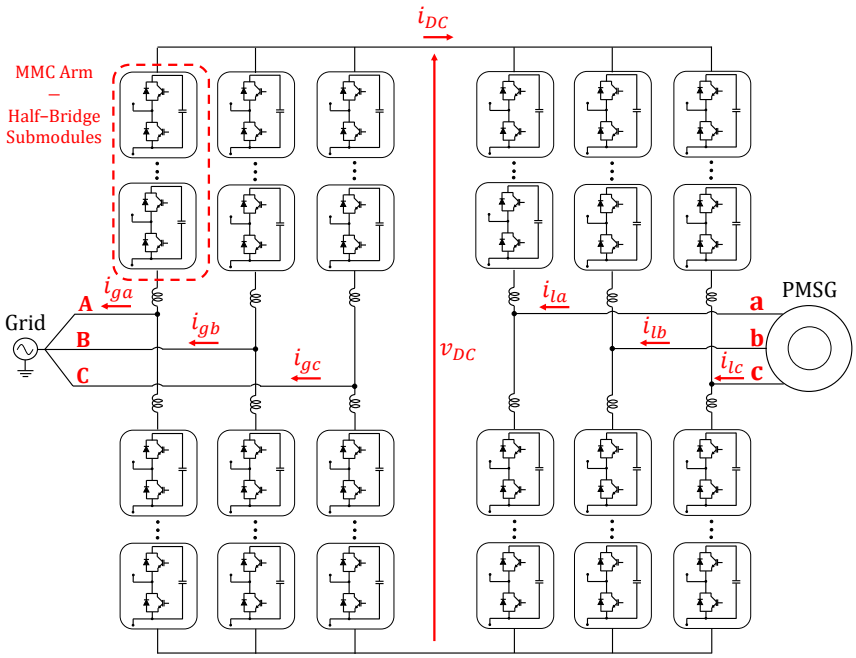

Fig. 1: MMC topology applied to a permanent-magnet-synchronous-generator (PMSG) drive.

Specifically, when it comes to the wind energy sector, upscaling is a trend that aims to achieve higher power levels of WTs while reducing structural costs, volume and weight [11–17]. For example, a 10-MW WT is lighter, cheaper and more compact than two 5-MW WTs. Besides, having a reduced number of WTs considerably reduces the cost of installation of these turbines at offshore wind power plants, and optimizes the usage of the available offshore area. As WT power levels increase, eventually higher voltages will be required. Indeed, at a given power level, a medium voltage structure (including generator, power-electronic converter and others) leads to reduced cost, size and weight [13,15,17]. The reduced currents resulting from the higher voltage levels lead to reduced losses and lead to the need for lighter and less expensive conductors [11]. Furthermore, a transformerless operation could eventually be achieved depending on the adopted voltage level [14, 16]. These are particularly important features that lead to an overall structure with reduced volume and weight, which is especially important for offshore WTs that require extremely complex and expensive foundations that must be capable to support the weight of the turbine.

Even though the battery technologies are in constant evolution, the most established energy-storage systems are the hydro turbines in the pumped-hydro-storage configuration [7–9]. The most common pumped-hydro-storage systems are based on doubly-fed induction generators since a reduced-power, reduced-cost converter can be used [7, 9]. However, this is not a flexible solution since it requires a blow down or dewatering procedure (to remove the water from the hydro turbine to reduce the friction force), in order to switch from pumping mode to generating mode, or vice versa, due to the low-torque characteristic of the doubly-fed induction generator at low speeds [7, 9]. To obtain a highly flexible pumped-hydro-storage system, a full-scale converter in combination with a synchronous machine (SM) is necessary [8, 9]. This system would require a considerably high voltage due to its high power levels.

The previously mentioned applications operate with variable frequency, some of them reaching extremely low frequency values or even crossing the 0-Hz operation point (as in the pumped-hydro-storage case). Besides, since these systems deal with high power values, then power-electronic devices with specific characteristics are required to drive them. Despite its many benefits, the adoption of the MMC for AC-AC medium-voltage variable-frequency applications could be undesirable. An especially critical drawback of the MMC is its poor performance at low frequencies, regarding the high amplitudes of its submodule-capacitor voltage ripple, which can lead to dangerous situations if the voltage ratings of the semiconductor devices are exceeded [18–22]. Moreover, in AC-AC applications, no DC stage is required and, thus, the problems of the MMC in dealing with DC-side faults [23,24] could be avoided. The MMC also presents some undesirable issues when operating under unbalanced grid conditions [25, 26]. Besides, the MMC's excessively high number of components (that leads to high costs, volume, and weight) could also be avoided by adopting alternative converter solutions. Finally, the MMC presents a complex operation and control, in which for example undesired circulating

currents must be continuously suppressed to keep the conduction losses within tolerable limits [27–29].

Various converter solutions with a modular multilevel structure have been proposed in the literature as alternatives for AC-AC applications [14, 30–48], and some of them specifically for high-power medium-voltage electrical-machine drives [7, 8, 14, 15, 30, 32, 35, 39–42, 48]. These topologies are proposed to overcome drawbacks of the MMC such as its high component count (which results in high costs, volume and weight) but especially to overcome the MMC poor performance at low frequencies regarding its excessive submodule-capacitor voltage ripple. Nonetheless, these alternative converter solutions present their own drawbacks. One interesting converter topology [35, 47] is often referred to as the series-connected H-bridge (SCHB) multilevel converter and it has attracted a lot of attention from industry, becoming a product regarded as the most proven medium-voltage drive in the market (SIEMENS SINAMICS PERFECT HARMONY GH180). This converter is composed of strings of full-bridge (FB) submodules connecting each phase of the machine to a common neutral point. In order to exchange power with the grid, rectifiers are connected to each of the submodule capacitors. These rectifiers maintain the capacitor voltages regulated as they do not experience voltage-ripple problems. Since this is a converter for medium-voltage applications, an extremely complex, heavy, and bulky transformer structure is required to adapt the grid voltage to the voltage at the terminals of each rectifier. Thus, this solution is not quite suitable for applications that require lightness and compactness such as WTs (especially offshore ones). The topology that probably stands out the most is the so called modular multilevel matrix converter (M^3C) [10, 14, 41] also referred to as direct MMC (DMMC) [7, 8, 45] or modular multilevel cascade converter based on triple-star bridge-cells (MMCC-TSBC) [30, 40, 42]. The M^3C topology is shown in Fig. 2. This is an AC-AC converter capable of operating as a controlled voltage source, from both grid and load perspectives, without a DC stage, which avoids problems with DC faults. Moreover, this converter presents a reduced submodule-capacitor voltage ripple at low frequencies, in comparison to the MMC, and an overall reduced number of components is required, which results in reduced costs, volume, and weight in relation to the MMC. Nonetheless, the M^3C presents some drawbacks such as its poor performance under unbalanced grid conditions [10, 49, 50], in which special control techniques are required to maintain its submodule-capacitor voltages stable and with a limited ripple. The M^3C also presents stability issues when operating with similar frequencies at its two AC terminals [10]. Besides, this converter topology presents extremely complex modulation and internal control where several control loops are necessary for its proper operation. Currently, only a few research groups in the world are capable to properly operate this converter topology [10]. Finally, similarly to the MMC, the M^3C also needs to deal with undesired circulating currents. In this Ph.D. thesis, a novel converter topology is proposed as an alternative for high-power medium-voltage electrical-machine drives. As will be explained in this thesis, this new topology presents structural and operational

advantages in comparison to the MMC, the M^{3}C, and other similar converter solutions.

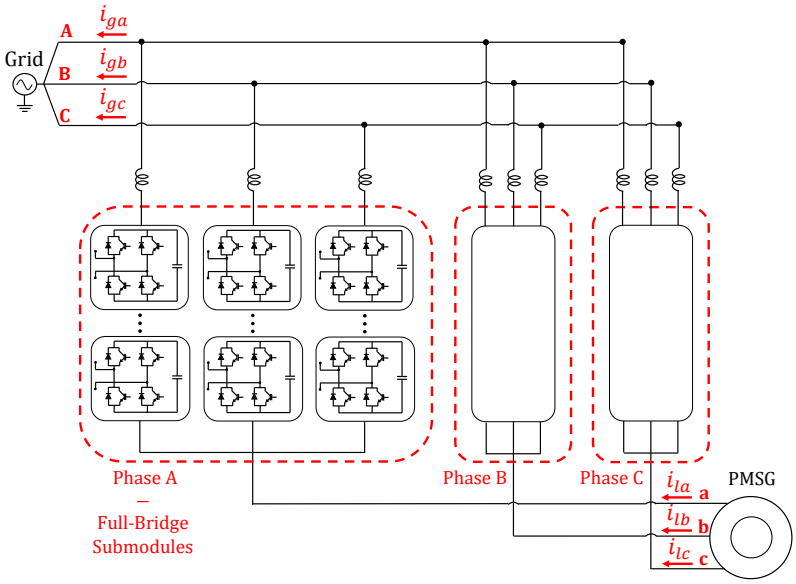

Fig. 2: M^{3}C topology applied to a PMSG drive.

Finally, another topic addressed in this thesis is related to the integration of energy storage systems (ESSs) into the converter solutions with a modular multilevel structure. The converter solutions with a modular multilevel structure allow for a straightforward integration of ESSs in both a centralized and a decentralized fashion [51–57]. In the decentralized one, the ESS devices are distributed among the various converter submodules. If batteries are adopted, then a system with a large storage capacity can be integrated into the converter without the need for high voltage values. The medium voltage level of the application is simply distributed among the various converter submodules in a way that the battery system integrated into each of these submodules only needs to handle a small fraction of the full system voltage. This way, battery packs with a reduced number of cells connected in series can be adopted, which should require a battery management system (BMS) with reduced complexity and therefore reduced cost. In this thesis, the integration of ESSs will be considered for the proposed converter topologies specifically for WTs. It is important to highlight that, with the increasing penetration of WTs and other sources of renewable generation in the electrical grid, ESSs become essential to maintain the control and stability of the power system. The variability and complex predictability of the wind resource makes WTs operate in a non-dispatchable way, imposing problems to the control of the electrical network that operates on demand, constantly balancing load and generation to maintain frequency

stability. In addition, WTs, decoupled from the grid through power-electronic converters, reduce the grid's spinning reserve, as they do not provide an inertial response in the event of faults. The integration of batteries into the WTs can be extremely beneficial for both power system operators and wind farm owners. A WT with an ESS could operate as a dispatchable generation, participating in grid frequency regulation and economic dispatch [58–60]. Furthermore, control strategies could be applied to the turbine so that it emulates a virtual inertia, in which the energy used would come from the batteries [59]. Moreover, the ESS allows wind generation to participate in the electricity market, improving the electricity price balance and providing greater profits to the turbine owners [61]. The wind farm with an integrated ESS can also improve the power quality at the point of connection to the main grid by damping the high variability of the wind power generation and, thus, reducing voltage fluctuations of the typical weak grid [60]. Finally, ESSs could keep a wind farm operational during a fault that would isolate the power plant from the grid, absorbing the generated energy and keeping the local grid active. When the fault was cleared, the WT with integrated battery could help to black start the grid if necessary [62]. So, in this Ph.D. thesis, a second novel converter topology is proposed mainly for modern/future high-power medium-voltage WTs. The integration of ESSs is also considered for this new topology.

1.2 Thesis Objectives - Research Questions and Hypothesis

As previously discussed, there are few power-electronic converter solutions suitable for high-power medium-voltage applications that operate with variable frequency. Despite their drawbacks and limitations previously presented, the converter topologies with a modular multilevel structure are among the most attractive options to deal with these considerably high voltage levels. Thus, the overall objective of this Ph.D. project can be summarized with the following general research question:

General Research Question

"Can the technology of converters with a modular multilevel structure be improved and further developed to make them more competitive for high-power medium-voltage electrical-machine drives?"

Based on this general research question, more specific objectives can be defined, which can be described through technical research questions that are presented below. As previously mentioned, the MMC presents poor performance at low frequencies since its submodule capacitors experience an extremely high voltage ripple at this frequency range. This could be seen as a limitation if such converter topology is used to drive electrical machines that operate with low speeds. As described in [63], if an MMC is supposed to synthesize an f_o-Hz voltage (where f_o is the desired load frequency), then each MMC arm must operate inserting submodules with an insertion-index pattern

($S(t)$) that is represented by a f_o-Hz signal that varies from 0 to N in a discrete fashion, corresponding to the instantaneous number of inserted submodules. This is a natural characteristic of the MMC topology and operation. An approximation can be made, which consists in considering $S(t)$ to be a continuous signal normalized by the total number of submodules in one arm (N). In this case, $S(t)$ becomes an f_o-Hz continuous signal that varies from 0 to 1. Let us suppose that the MMC should synthesize a low-frequency load voltage with frequency equal to $f_o = 1$ Hz. Then, the MMC arm insertion index and its fast Fourier transform (FFT) will be the ones shown in Fig. 3.

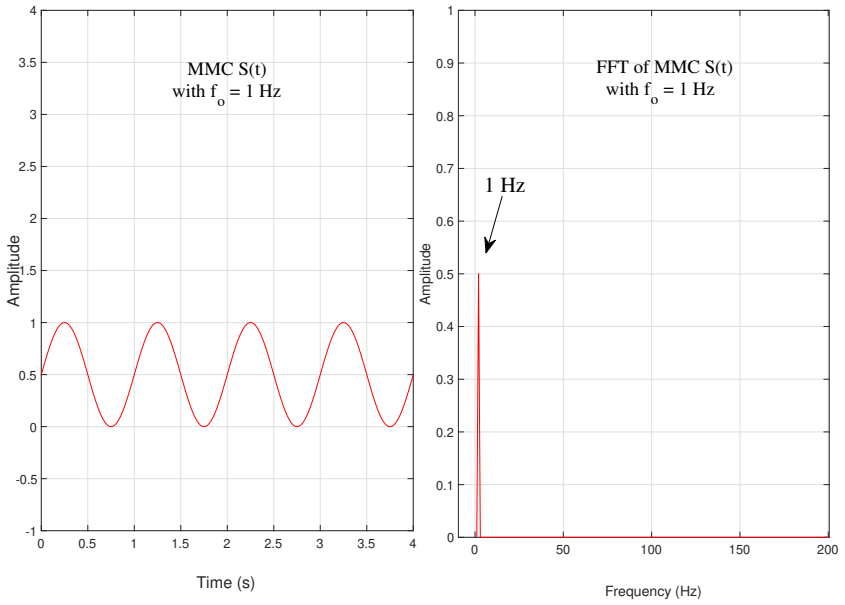

Fig. 3: MMC approximated insertion index and its FFT for $f_o = 1$ Hz.

The MMC insertion index can be mathematically described as follows:

$$S(t) = 0.5sin(\omega_o t) + 0.5 \tag{1}$$

In which $\omega_o = 2\pi f_o$. The current that flows through the MMC arms, considering that all the undesired AC circulating current components are suppressed, is equal to:

$$i_{arm}(t) = \frac{i_{AC}(t)}{2} + \frac{i_{DC}(t)}{3} \tag{2}$$

In which $i_{AC}(t)$ is the load current with frequency equal to $f_o = 1$ Hz and $i_{DC}(t)$ is the MMC DC current. The current that flows through the MMC submodule capacitors

(i_{cap}) producing the voltage ripple can be calculated as follows:

$$i_{cap}(t) = i_{arm}(t)S(t) \tag{3}$$

In other words, according to (3), by multiplying (1) and (2) the MMC capacitor current is obtained. Since both $S(t)$ and $i_{arm}(t)$ are signals with an f_o-Hz component and with a DC component, then the capacitor current will be composed of, not only a DC component, but also of an $f_o = 1$-Hz component and of a $2f_o = 2$-Hz component as illustrated in Fig. 4 that shows the FFT of the MMC capacitor current in this case. As an example, the product of the $f_o = 1$-Hz component, present in $S(t)$, by the $f_o = 1$-Hz component and the DC components, present in $i_{arm}(t)$, result in an $f_o = 1$-Hz component and in a $2f_o = 2$-Hz component.

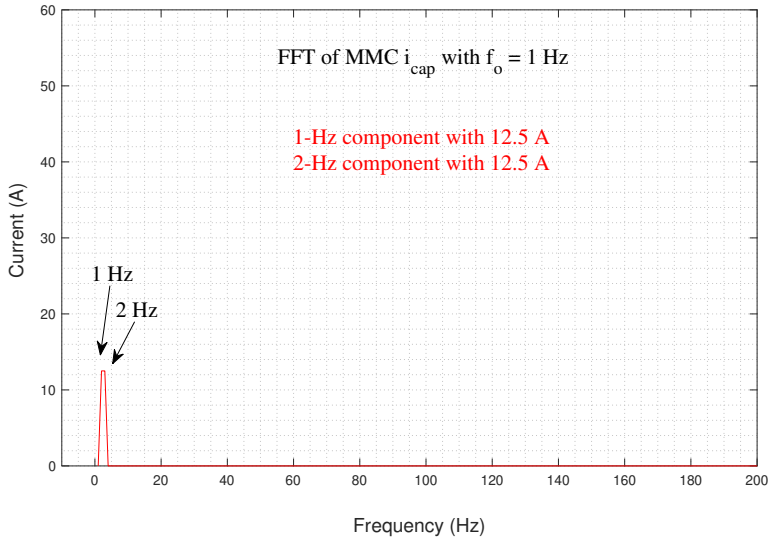

Fig. 4: FFT of MMC i_{cap} for $f_o = 1$ Hz.

These two low-frequency current components will produce an extremely high voltage ripple in the MMC submodule capacitors since the ripple is proportional to the capacitor reactance, which is inversely proportional to the frequency of the currents flowing through it, i.e., low frequency currents produce a higher voltage ripple. The waveform of the MMC insertion-index signal (as shown in Fig. 3 and as described in (1)) is a consequence of the MMC topology and of how it behaves inserting and by-passing submodules in order to synthesize a given AC voltage. In Fig. 5 an illustrative explanation of how the MMC behaves to synthesize an AC voltage is provided.

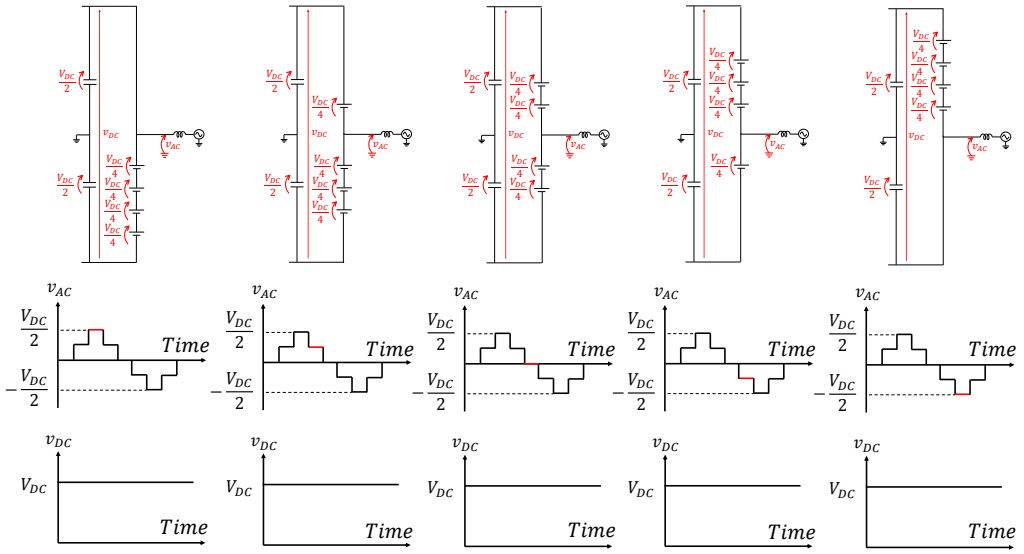

Fig. 5: MMC behavior when synthesizing the AC voltage v_{AC} at its AC terminals.

The frequency of the AC current that flows through the MMC arms ($\frac{i_{AC}(t)}{2}$) is equal to the frequency of the AC voltage synthesized by the converter (f_o). As a natural consequence of its topology, the MMC needs to insert and by-pass submodules with an insertion-index pattern ($S(t)$) with the same frequency of the synthesized AC voltage (f_o). As previously explained, if $f_o = 1$ Hz, then the product of the two f_o components, according to (3), will result in a $2f_o = 2$-Hz component. In other words, the current that flows through the submodule capacitors (i_{cap}) producing the voltage ripple, will contain a $2f_o = 2$-Hz component. What if, for example, a new hypothetical modular multilevel converter is proposed in which, in order to synthesize a 1-Hz AC voltage, it needs to operate inserting and by-passing submodules with a 50-Hz insertion index pattern ($S(t)$)? In this case, the product of the $f_o = 1$-Hz component, present in the AC current ($i_{AC}(t)$), by the 50-Hz component, present in $S(t)$, would result in a 49-Hz and in a 51-Hz components. These are high frequencies that would not result in a high voltage ripple in the submodule capacitors. Thus, the first technical research question of this Ph.D. project emerges, which is the following:

Technical Research Question 1

"Can a new modular multilevel converter topology with different submodule connections and, thus, different insertion-index pattern ($S(t)$), have a reduced submodule-capacitor voltage ripple?"

Research Hypothesis for Technical Research Question 1

- By proposing a new converter topology with modified submodule connections, it could be possible to obtain a different insertion-index pattern ($S(t)$), without a f_o component or with a f_o component with reduced amplitude, in such a way that the current that would flow through the submodule capacitors (i_{cap}) would present low-frequency components with reduced amplitudes, leading to a smaller voltage ripple.
- By proposing a new converter topology with modified submodule connections, it could be possible to obtain an AC-AC solution without a DC current component (i_{DC}) that flows through the submodule strings, contributing for the voltage ripple.

The MMC is the state-of-the-art solution for high-voltage AC-DC-AC applications such as the HVDC transmission systems or high-power AC-DC applications. However, for AC-AC applications, the MMC topology might present an unnecessarily high number of components, which translates into high costs, volume, and weight. The M^3C is an AC-AC converter solution with a modular multilevel structure and its direct AC-AC connection leads to a reduced overall component count, which is an important advantage in relation to the MMC. Nonetheless, in order for the M^3C to be able to operate as a controlled voltage source from both grid and load perspectives, it must have a large number of FB submodule strings (nine submodule strings in total or three submodule strings per phase), which still results in a relatively high component count. In addition, the M^3C presents some operational challenges due to its topology. After these observations, the second technical research question of this Ph.D. project emerges, as follows:

Technical Research Question 2

"Would it be possible to develop a new AC-AC converter solution with a modular multilevel structure and with a reduced component count?"

Research Hypothesis for Technical Research Question 2

- It could be possible to modify the M^3C topology, by changing the way it is connected to the grid, i.e., to behave as a current source instead of as a voltage source, in such a way as to obtain a converter solution with a reduced number of submodule strings and, thus, reduced component count, leading to reduced costs, volume and weight.

The MMC positive and negative DC terminals (see Fig. 1) act as neutral points for the converter arms in such a way that they form closed paths through which circulating currents flow. These undesired current components lead to an increase in the converter's

conduction losses and, thus, they need to be suppressed through control strategies. By suppressing the undesired AC circulating currents, other problems emerge as for example the increase of the submodule-capacitor voltage ripple. In the M^3C case (see Fig. 2), the neutral point that connects each set of three submodule strings to each load phase, as well as the simultaneous connection of multiple submodule strings to the same grid phase, also lead to closed paths through which undesired circulating currents flow. Thus, the third technical research question of this Ph.D. project emerges as follows:

Technical Research Question 3

"Would it be possible to develop a new AC-AC converter with a modular multilevel structure in which each of its phases are decoupled from each other in such a way that closed paths are never formed, thus, avoiding problems with undesired circulating currents?"

Research Hypothesis for Technical Research Question 3

- It could be possible to simplify the M^3C structure, by reducing its number of submodule strings, in such a way as to obtain an AC-AC converter solution with decoupled and independent phases, preventing the existence of closed paths for undesired circulating currents to flow through.

The MMC and the M^3C present problems when they are connected to an unbalanced grid. If the grid is unbalanced, negative-sequence and zero-sequence current components will flow through the MMC arms, increasing the submodule-capacitor voltage ripple and generating a DC-side pulsation that can be harmful to the converter [25, 26, 64]. These negative-sequence and zero-sequence components will flow through the submodule strings due to the existence of neutral points represented by the MMC positive and negative DC terminals. The zero-sequence components do not sum to zero in the neutral point, as they are transferred to the converter's DC link [25, 26, 64]. The M^3C is composed of three single-phase structures. Each single-phase structure is composed of three submodule strings connecting each grid phase to a common neutral point that is connected to one of the load phases, as illustrated in Fig. 2. Under unbalanced grid conditions, unbalanced currents will flow through the three submodule strings of one phase, leading to an uneven power distribution among these strings [10, 49, 50]. The uneven power distribution among the three strings in one phase make their submodule-capacitor voltages diverge, resulting in an unstable behavior. Complex control techniques are required to make sure that the M^3C submodule-capacitor voltages remain stable and with a low ripple under unbalanced grid conditions [10, 30, 40, 42]. Thus, the fourth technical research question of this Ph.D. project is the following:

Technical Research Question 4

"Would it be possible to develop a new AC-AC converter with a modular multilevel structure where each of its phases are independent from each other (without a neutral point), in such a way that the submodule-capacitor voltages remain stable and with a low ripple under unbalanced grid conditions?"

Research Hypothesis for Technical Research Question 4

- It could be possible to simplify the M^3C structure, by reducing its number of submodule strings, in such a way as to obtain an AC-AC converter solution with independent phases without a neutral point, avoiding problems under unbalanced grid conditions.
- It could be possible to build an AC-AC converter solution that would operate as a controlled voltage source from the load perspective but as a current source from the grid perspective, in such a way that grid power quality issues would not affect the currents flowing through the submodule strings.

Finally, as previously mentioned, another topic addressed in this Ph.D. project is related to the integration of ESSs into the converters with a modular multilevel structure for high-power WT applications. As previously explained, the integration of an ESS into a wind farm can be beneficial in multiple ways for both power system operators and wind farm developers. The integration of ESSs into wind power plants is typically done by having an extra converter, exclusively dedicated to the ESS, connected at the point of common coupling of the wind farm and the grid. Since medium-voltage levels are considered in this thesis, then an expensive extra converter (an MMC for example) would be required for the ESS integration. It would be interesting, however, if the ESS could be integrated into the same modular multilevel converter used to drive the medium-voltage WT, avoiding the need of an extra converter. It is important to highlight, however, that the way as converters with a modular multilevel structure exchange power between their terminals is through an intermediate stage inside the converter, i.e., the energy is first stored in their submodule capacitors, and then these capacitors are discharged supplying power to the output terminal. Thus, if the submodule capacitors were replaced by batteries, for example, then these batteries would have to be charged and discharged with the full WT power. This would result in the need of a large integrated ESS, and it would result in a solution with short lifespan because of the continuous charging/discharging cycles of the batteries. After these considerations, the final research question emerges as follows:

Technical Research Question 5

"Would it be possible to develop a converter solution with a modular multilevel structure and with an ESS integration suitable to drive a WT in a way that only the surplus power (not the full power) of the turbine would be stored in the ESS?"

Research Hypothesis for Technical Research Question 5

- It could be possible to develop a modular multilevel converter with a hybrid ESS integration, where part of its submodules would have integrated batteries, and part of its submodules would have integrated capacitors, for example. The conventional capacitors could be responsible for transferring the desired power to the grid, according to a pre-defined set point, and the batteries would only store the surplus power produced by the WT.

The objective of this Ph.D. thesis is to propose novel converter solutions, with a modular multilevel structure, capable to answer the previously presented research questions.

1.3 Thesis Outline

The Ph.D. thesis document is divided into two parts, i.e., the first is the ***Report***, where a summary of the main achievements of the Ph.D. project is presented, and the second is the presentation of the ***Ph.D. Project Publications***. The thesis structure is presented in an illustrative way in Fig. 6, where the thesis chapters and sub-chapters are connected to their corresponding publications.

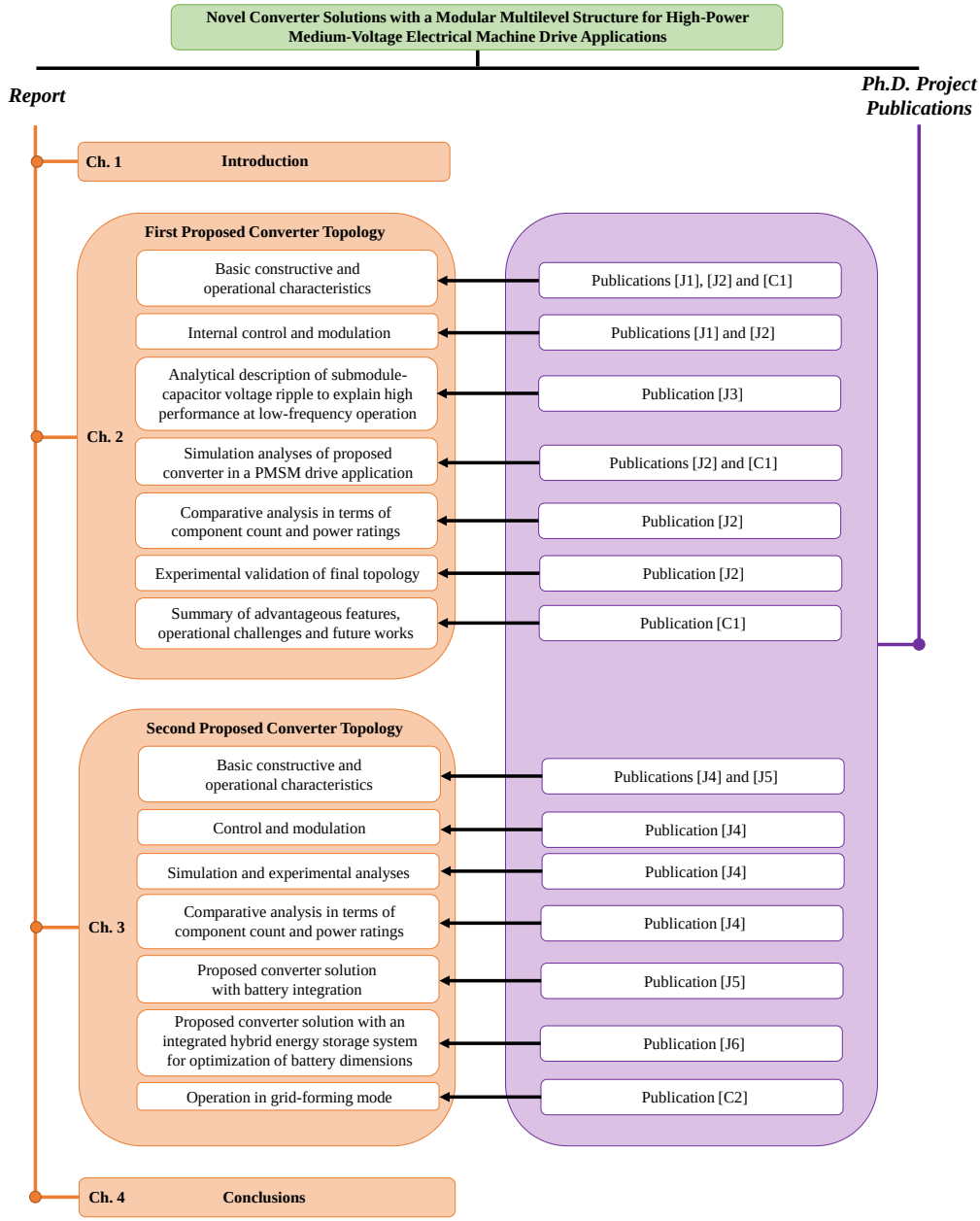

Fig. 6: Illustrative representation of thesis structure explaining connection of chapters/sub-chapters with Ph.D. project publications.

The Ph.D. thesis ***Report*** is essentially divided into two parts related to the two novel converter topologies proposed. In other words, in *Chapter 2*, the first converter topology is discussed, where its structural and operational features, internal control and modulation are presented. Various simulation and experimental results are also presented in *Chapter 2* to validate this novel converter solution. In addition, in *Chapter 2*, a mathematical analysis of the converter's submodule-capacitor voltage ripple is introduced, which explains the reason why this topology could eventually be suitable for high-power medium-voltage machine drives that operate with low frequencies. Moreover, in *Chapter 2*, a comparative analysis of the proposed converter solution in relation to the MMC and to the M^3C regarding component count, and overall semiconductor-device power ratings is presented. Finally, in *Chapter 2*, a summary of advantageous features, operational challenges and intended future works related to the first proposed converter topology are presented.

In *Chapter 3*, the second proposed converter solution is discussed. Its basic operational features, its internal control and modulation are presented in *Chapter 3*. Moreover, various simulation and experimental results are presented to validate the converter solution. A comparative analysis among the presented topology, the MMC and the M^3C in terms of number of components and in terms of the power ratings of these components is presented. Still in *Chapter 3*, the integration of ESSs into the second proposed converter topology is presented. The operation and control of the system with integrated ESS are explained in detail. Finally, the operation of the solution with integrated ESS in grid-forming mode is presented in *Chapter 3*. In *Chapter 4*, the conclusions of this Ph.D. project are presented.

1.4 List of Publications

The results and outcomes of this Ph.D. project have been disseminated as publications in the form of journal articles, and conference papers. The main content of this thesis is based on publications [J1], [J2], [J3], [J4], [J5], [J6], [C1], and [C2]. Nonetheless, the full list of publications performed during this Ph.D. study can be found below:

Journal Publications:

[**J1**] **G. F. Gontijo**, S. Wang, T. Kerekes, and R. Teodorescu, "New AC-AC Modular Multilevel Converter Solution for Medium-Voltage Machine-Drive Applications: Modular Multilevel Series Converter," in *Energies,* vol. 13, no. 14, pp. 3664, Jul. 2020.

[**J2**] **G. F. Gontijo**, S. Wang, T. Kerekes, and R. Teodorescu, "Novel Converter Topology with Reduced Cost, Size and Weight for High-Power Medium-Voltage Machine Drives: 3x3 Modular Multilevel Series Converter," in *IEEE Access,* vol. 9, pp. 49082 - 49097, Mar. 2021.

[**J3**] **G. F. Gontijo**, S. Wang, T. Kerekes, and R. Teodorescu, "Performance Analysis of Modular Multilevel Converter and Modular Multilevel Series Converter under Variable-Frequency Operation Regarding Submodule-Capacitor Voltage Ripple," in *Energies,* vol. 14, no. 3, pp. 776, Feb. 2021.

[**J4**] **G. F. Gontijo**, T. Kerekes, D. Sera, M. Ricco, L. Mathe and R. Teodorescu, "New Converter Solution with a Compact Modular Multilevel Structure Suitable for High-Power Medium-Voltage Wind Turbines," under review in *IEEE Transactions on Power Electronics,* 2022.

[**J5**] **G. F. Gontijo**, T. Kerekes, D. Sera, M. Ricco, L. Mathe, and R. Teodorescu, "Medium-Voltage Converter Solution with Modular Multilevel Structure and Decentralized Energy Storage Integration for High-Power Wind Turbines," in *IEEE Transactions on Power Electronics,* vol. 36, no. 11, pp. 12954 - 12967, May 2021.

[**J6**] **G. F. Gontijo**, D. Sera, M. Ricco, L. Mathe, T. Kerekes, and R. Teodorescu, "Dispatchable High-Power Wind Turbine Based on a Multilevel Converter with Modular Structure and Hybrid Energy Storage Integration," in *IEEE Access,* vol. 9, pp. 152878 - 152891, Nov. 2021.

Conference Publications:

[**C1**] **G. F. Gontijo**, T. Kerekes, and R. Teodorescu, "Operational Advantages and Challenges of New AC-AC Converter Solution with Modular Multilevel Structure Suitable for High-Power Medium-Voltage Electrical Machine Drives," in *Proc. OPTIM-ACEMP,* Brasov, Romania, 2021.

[**C2**] **G. F. Gontijo**, D. Sera, M. Ricco, L. Mathe, T. Kerekes, and R. Teodorescu, "High-Power Medium-Voltage Wind Turbine Driven by Converter Solution with Modular Multilevel Structure and Decentralized Battery Integration Operating in Both Grid-Following and Grid-Forming Modes," in *Proc. EPE'21 ECCE Europe,* Ghent, Belgium, 2021.

Journal Publication Related to Research Collaboration with Ørsted Wind Power A/S

As part of the Ph.D. requirements, Gustavo stayed for 6 months as a Guest Researcher at Ørsted Wind Power A/S. In this collaboration, the Ph.D. student's acquired experience on modular multilevel converters was combined with the strong company's

know-how in stability analysis to perform a work with the title: "Eigenvalue-Based Stability Assessment of an Offshore Wind Power Plant with an MMC-Based HVDC Connection". This successful research collaboration resulted in the following extra journal publication.

[**E1**] **G. F. Gontijo**, M. K. Bakhshizadeh, L. H. Kocewiak, and R. Teodorescu, "State Space Modeling of an Offshore Wind Power Plant with an MMC-HVDC Connection for an Eigenvalue-based Stability Analysis," under review in *IEEE Access,* 2022.

Other Relevant Journal Publications About Modular Multilevel Converters as a Co-Author

[**E2**] S. Wang, T. Dragicevic, **G. F. Gontijo**, S. K. Chaudhary, and R. Teodorescu, "Machine Learning Emulation of Model Predictive Control for Modular Multilevel Converters," in *IEEE Transactions on Industrial Electronics,* vol. 68, no. 11, pp. 11628 - 11634, Nov. 2020.

[**E3**] S. Wang, D. Bao, **G. F. Gontijo**, S. K. Chaudhary, and R. Teodorescu, "Modeling and Mitigation Control of the Submodule-Capacitor Voltage Ripple of a Modular Multilevel Converter under Unbalanced Grid Conditions," in *Energies,* vol. 14, no. 3, pp. 651, Jan. 2021.

Other Relevant Journal Publications About Other Power-Electronic Topics as a Co-Author

[**E4**] B. W. Franca, M. Aredes, L. F. Silva, **G. F. Gontijo**, T. C. Tricarico, and J. Posada, "An Enhanced Shunt Active Filter Based on Synchronverter Concept," in *IEEE Journal of Emerging and Selected Topics in Power Electronics,* vol. 10, no. 1, pp. 494 - 505, Aug. 2021.

1.5 Structural Features and Common Characteristics of Proposed Converter Solutions

As previously mentioned, in this Ph.D. thesis, two novel converter solutions with a modular multilevel structure suitable for high-power medium-voltage electrical machine drives are proposed. The two main topologies presented in this project are shown in Fig. 7 and in Fig. 8, and they were developed based on the same structural concepts, i.e., the combination of FB submdoule strings and of bidirectional-switch stacks. With this combination of devices, the proposed topologies can have interesting operational and structural features, as for example and overall reduced number of components in

relation to the MMC and the M^{3}C. The presence of the submodule strings allows for the traditional benefits of multilevel converters such as the possibility of synthesizing high-power-quality staircase-shape multilevel voltages. The bidirectional-switch stacks must be built with a few series-connected semiconductor devices due to the considerably high voltage levels considered. Nonetheless, only a few devices connected in series must be used since these are medium voltage levels and not high voltage ones. The feasibility of the proposed topologies relies in the fact that these bidirectional-switch stacks can operate with a very low switching frequency as will be shown in this thesis. Thus, problems related to static and dynamic voltage sharing among the series-connected devices could be avoided, or at least considerably reduced. Besides, there are some products currently available in the industry that correspond to stacks composed of several semiconductor devices connected in series that operate with high reliability due to modern drivers that ensure safe static and dynamic voltage sharing between the series-connected devices [6]. Another advantage of these devices switching with a low frequency is the reduced switching losses.

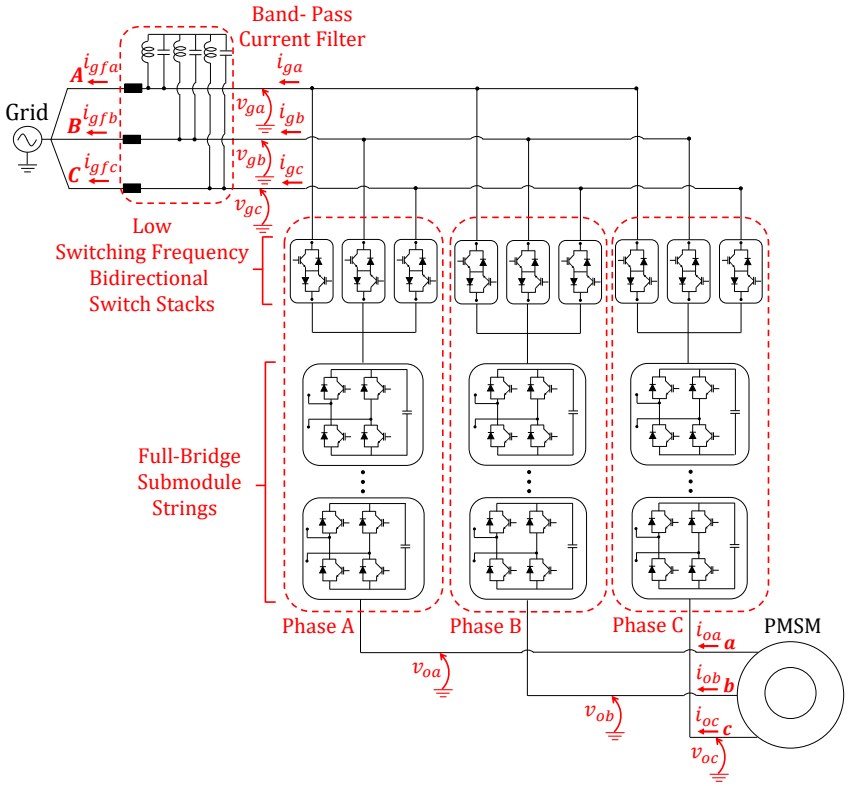

Fig. 7: Topology of first converter solution proposed in this Ph.D. project (the 3x3-MMSC).

In summary, the idea is that the proposed converter topologies can be classified between converters with a purely modular multilevel structure, and converters built with stacks of series-connected semiconductor devices operating with high switching frequencies in terms of both advantages and disadvantages. In comparison to converters with a purely modular multilevel structure, the proposed solutions have an overall reduced component count and some other relevant operational advantages, that will be presented in this thesis, even though they require the bidirectional-switch stacks that can be seen as sensitive parts of the converters that could eventually lead to a reduced reliability if not properly implemented. In comparison to converters built with stacks of series-connected semiconductor devices operating with high switching frequencies, such as the two-level converter, the proposed solutions can synthesize a staircase-shape multilevel voltage, resulting in reduced filtering requirements in terms of both harmonics and $\frac{dv}{dt}$, and they should present increased reliability since they are built with the reliable modular multilevel structure in combination with low-switching-frequency stacks of semiconductor devices. Nonetheless, the proposed converter solutions present increased structural and control complexity in relation to a two-level converter and to some other topologies such as the three-level NPC converter.

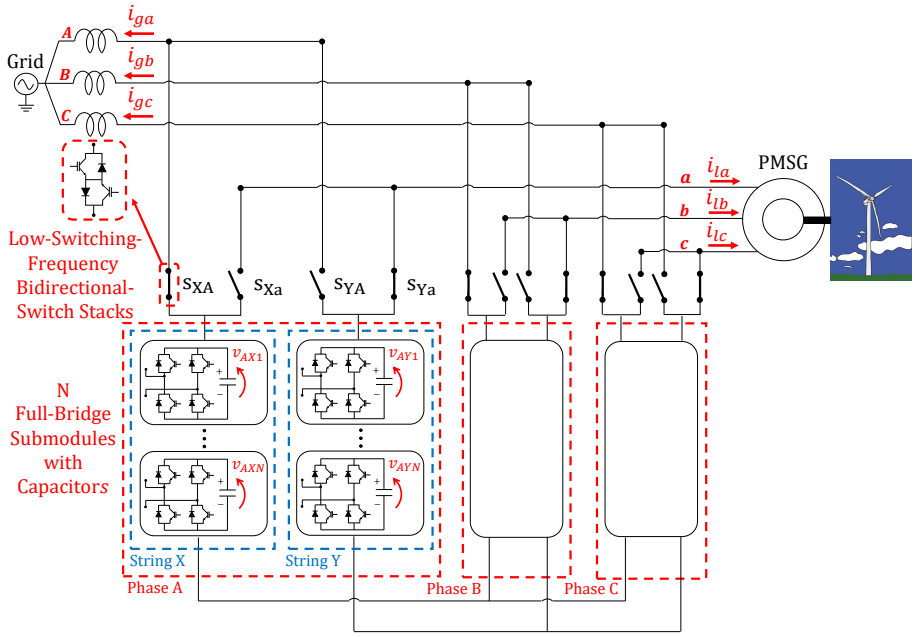

Fig. 8: Topology of second converter solution proposed in this Ph.D. project (the MMShC).

Obviously, the best converter topology to be adopted should be assessed depending on the specific application considered. The first topology shown in Fig. 7 is the one

with the least overall number of components and it presents interesting operational characteristics at low frequencies. However, this topology presents some operational challenges since it behaves as a current source from the grid perspective (similar to a Direct Matrix Converter (DMC) [65–67]). The topology shown in Fig. 8 has an increased overall number of components in comparison to the first one, but it presents a more controllable structure as it behaves as controlled voltage sources from both load and grid perspectives. The main difference between these two topologies is the way that the FB submodules and bidirectional-switch stacks are connected. In the first one, the FB submodules are connected in series between the grid and the load and, thus, it was named 3x3 Modular Multilevel Series Converter (3x3-MMSC). In opposition to the first topology, the second one was named Modular Multilevel Shunt Converter (MMShC) because of the way that the submodule strings and bidirectional-switch stacks are connected.

1.6 Description of Experimental Test Setups used in Ph.D. Project

In this Ph.D. project, experimental results were collected in three different test setups. The first setup was entirely built by the Ph.D. student during his Ph.D. project and it is shown in Fig. 9.

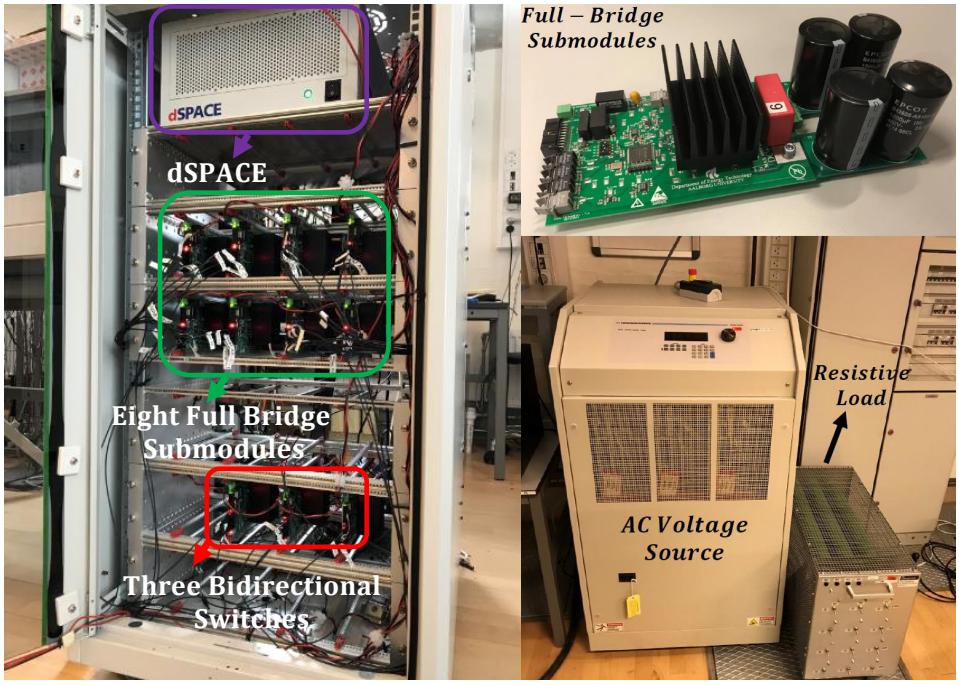

Fig. 9: Experimental test setup corresponding to the first proposed converter topology (3x3-MMSC), which was built at the Modular Multilevel Converters Laboratory at AAU Energy.

This experimental test bench corresponds to the first proposed topology (shown in Fig. 7) and it was built at the Modular Multilevel Converters Laboratory at Pontoppidanstraede 109, room 1.104, 9220, Aalborg East. The second test setup corresponds to the traditional MMC, and it was also located at the Modular Multilevel Converters Laboratory. The MMC test bench (see Fig. 10) was used to perform a comparative analysis between this well established topology and the proposed ones. Finally, the third experimental setup was located at the PV Systems Laboratory at Pontoppidanstraede 109, room 1.135, 9220, Aalborg East. The third test setup is illustrated in Fig. 11, and it corresponds to the second converter topology proposed in this thesis (shown in Fig. 8). The Ph.D. student had to make some modifications to the third test bench in order to implement the novel converter solution. More information about the three experimental test setups will be presented later in this thesis.

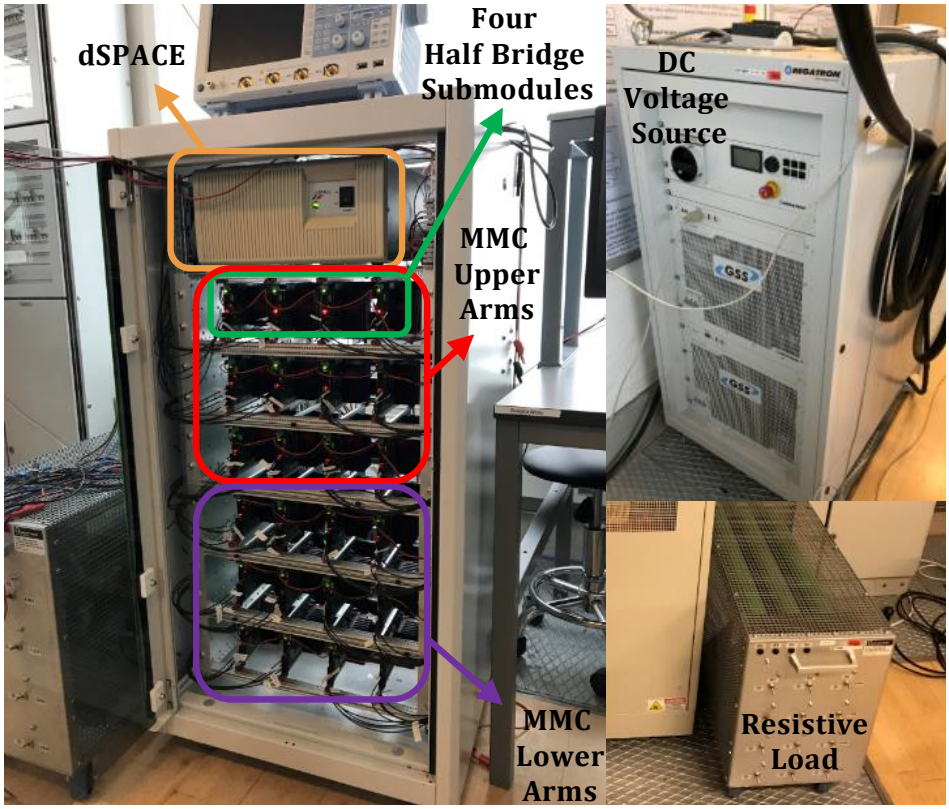

Fig. 10: Experimental test setup corresponding to the traditional MMC topology, which was located at the Modular Multilevel Converters Laboratory at AAU Energy.

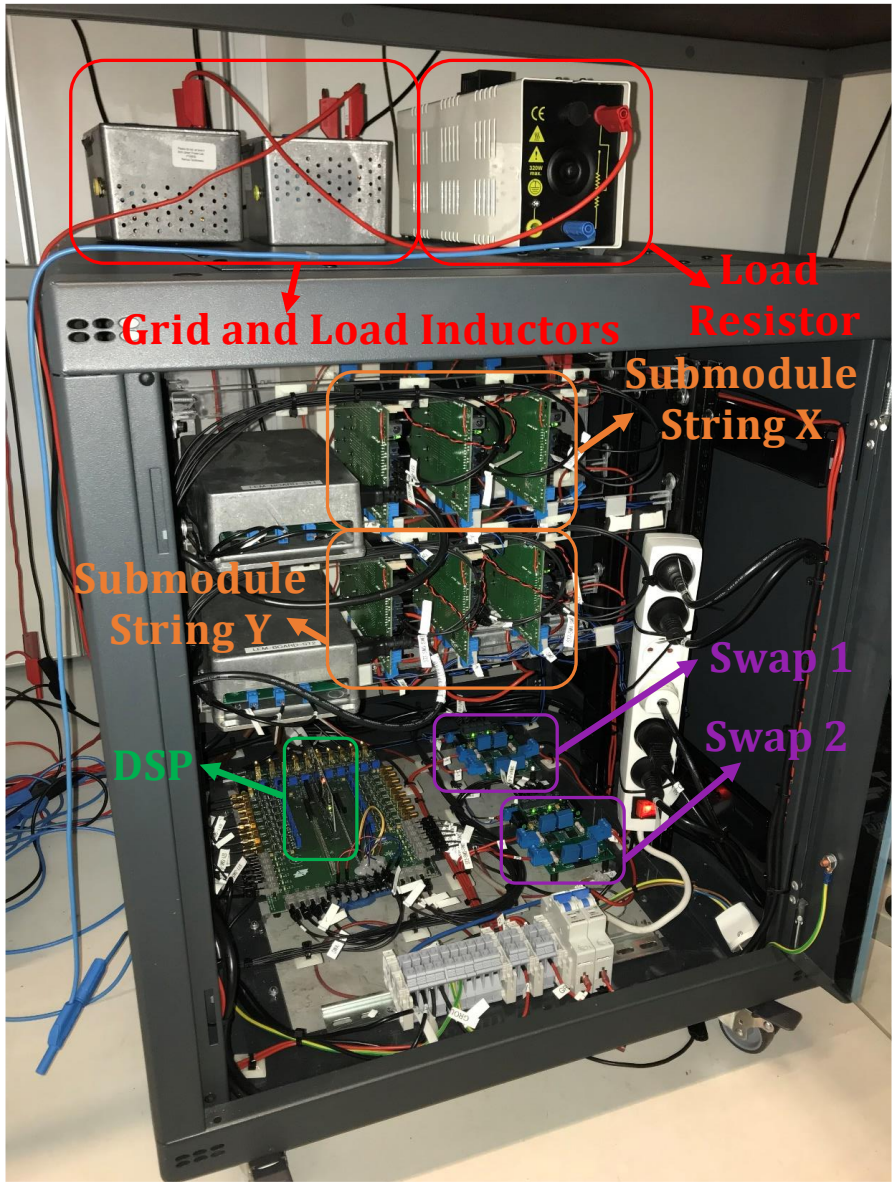

Fig. 11: Experimental test setup corresponding to the second proposed converter topology (MMShC), which was located at the PV Systems Laboratory at AAU Energy.

2 Novel Converter Topology with a Modular Multilevel Structure for Low-Frequency Machine Drive Applications

In this chapter, the first converter solution proposed in this thesis is presented in detail. This converter solution could be a suitable option for high-power medium-voltage machine drives that operate at low frequencies.

2.1 Basic Constructive and Operational Characteristics

The original version of the first proposed converter solution is shown in Fig. 12, and its topology was inspired in the M^3C. Similarly to the M^3C case, the idea was to try to develop an AC-AC converter solution with a modular multilevel structure but with an overall reduced number of components, i.e., instead of having nine strings of FB submodules (see Fig. 2), the proposed solution would only have three strings of FB submodules. As shown in Fig. 12, in the proposed solution, each of the three submodule strings is connected in series between a given phase of the grid and the corresponding load phase. Since FB submodules are used in the proposed topology, and since these blocks can synthesize voltages with both positive and negative polarities then, the string of FB submodules behaves as an AC controlled voltage source capable to synthesize the desired voltage in series between grid and load terminals aiming at controlling the voltage at the load terminals. For this reason, this converter topology was named Modular Multilevel Series Converter (MMSC). To be capable to operate as a controlled voltage source from the load perspective in every operation condition, each submodule string must be connected to different phases of the grid during its operation as will be explained later in this thesis. Thus, bidirectional-switch stacks are adopted to connect each submodule string to two different phases of the grid. With the bidirectional-switch stacks, the proposed converter is capable to operate as a controlled voltage source from the load perspective, synthesizing the desired voltage at the load terminals according to a given reference. In order to do that, the bidirectional-switch stacks do not have to operate with a high switching frequency, and the converter is capable to synthesize a high-power-quality multilevel load voltage because of the FB submodule strings. The voltages synthesized at the load terminals do not depend on the switching frequency of the bidirectional-switch stacks. On the contrary, the profile of the current that is injected into the grid is a function of the switching frequency of the bidirectional-switch stacks since the proposed converter behaves as a current source from the grid perspective. To have more flexibility and to facilitate the filtering of the currents injected into the grid, the addition of the third bidirectional-switch stack to each submodule string was required, resulting in the final topology named 3x3-MMSC as previously presented and as reproduced in Fig. 13 for convenience. At first glance,

it might look like the 3x3-MMSC would present an increased overall component count in comparison to the MMSC because of the addition of the three extra bidirectional-switch stacks. However, it is actually quite the opposite, i.e., as will be demonstrated in the comparative analysis of this thesis, having the three bidirectional-switch stacks, connecting each submodule string to the three phases of the grid, allows the 3x3-MMSC to synthesize the exact same load voltage as the MMSC but with a reduced voltage at its input terminals. This way, the converter can be built with a considerably reduced number of components.

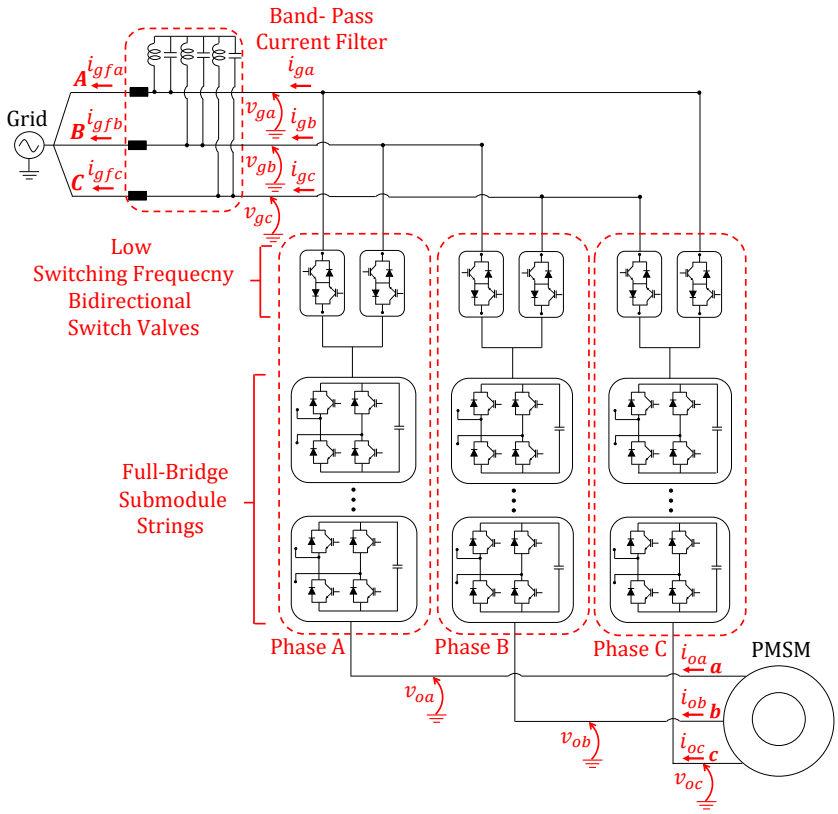

Fig. 12: Original version of proposed converter solution named Modular Multilevel Series Converter.

The bidirectional-switch stacks in the 3x3-MMSC can also operate with low switching frequencies while improving the profile of the current injected into the grid in a way as to reduce the filtering requirements. Nonetheless, an specific band-pass filter is still required to obtain high-power-quality currents injected into the grid. Finding a

proper topology for this filter is one of the challenges of this converter solution. The filter could potentially be complex, large and expensive. In this case, even though the proposed converter would present a reduced component count (including an expressively reduced number of the bulky submodule capacitors as will be explained later), it would also require a complex and potentially large input filter. Another option would be to increase the switching frequency of the bidirectional-switch stacks in such a way as to improve the profile of the current injected into the grid, consequently leading to reduced filtering requirements (a less complex and more compact filter). However, this trade-off should be carefully assessed since the increase of the bidirectional-switch-stack switching frequency, to reduce the size of the input filter, would also deteriorate the reliability of the solution.

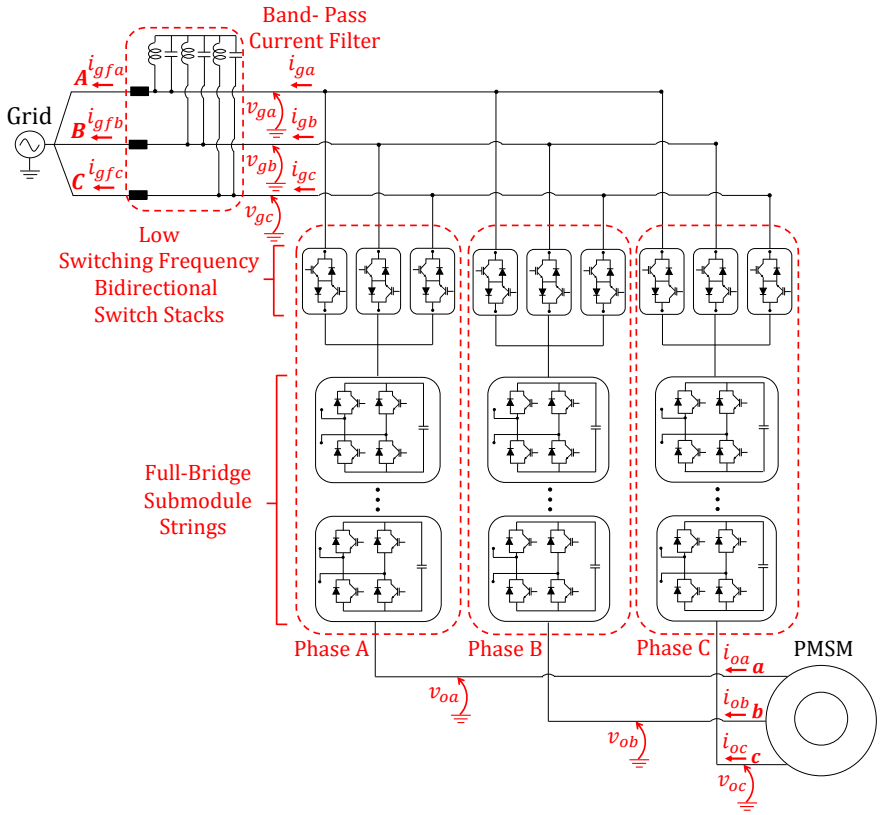

Fig. 13: Final version of the first proposed converter solution named 3x3-Modular Multilevel Series Converter.

The MMSC and the 3x3-MMSC have very similar operation, and the only difference is that the submodule strings of the 3x3-MMSC can be connected to all the three phases of the grid through the bidirectional-switch stacks. The 3x3-MMSC will be used to explain the basic operational characteristics of the two converters. This converter topology essentially operates synthesizing a given series voltage depending on the instantaneous value of the grid voltage in order to obtain the desired load voltage. Let us consider a situation in which the phase-A submodule string is connected to phase A of the grid, which means that the bidirectional-switch stack that connects the string to phase A of the grid is in *ON* mode while the bidirectional-switch stacks that connect the phase-A submodule string to phases B and C of the grid are in *OFF* mode. If it is desired to synthesize a given voltage at the phase-A load terminal equal to ($v_{oa} = v_a^*$), then a series voltage (v_{sa}) should be synthesized across the phase-A submodule string. The series voltage required to be synthesized across the phase-A submodule string can be calculated as follows:

$$v_{sa} = v_a^* - v_{ga} = V_o sin(\omega_o t) - V_g sin(\omega_i t) \tag{4}$$

Where v_a^* is the reference for the phase-A load voltage and v_{ga} is the instantaneous value of the phase-A grid voltage. V_o and V_g are the peak values of the voltage reference and of the grid voltage, respectively. Finally, in (4), $\omega_o = 2\pi f_o$, $\omega_i = 2\pi f_i$, and f_o and f_i are the load and grid frequency, respectively. A natural characteristic of the 3x3-MMSC due the series connection of its submodule strings between grid and load terminals is the fact that the grid voltage is distributed between the N capacitors of the N series-connected submodules of each string. This natural condition can be further understood by observing Fig. 14 where the submodule string is represented as a string of diode bridge rectifiers connected in series between the grid and the load. In other words, a closed voltage path can be defined from the grid voltage neutral point, passing through the submodule string until the load neutral point. Thus, after considering a small voltage drop across the load, the voltage in each capacitor will be approximately equal to $\frac{V_g}{N}$, where V_g is the peak value of the phase-to-neutral grid voltage and N is the number of submodules in the string, as previously explained. In this thesis, no control is adopted to regulate the submodule-capacitor voltages, i.e., these voltages are imposed by the grid, and they are kept regulated with a value equal to $\frac{V_g}{N}$. If a power variation occurs at the load side, the grid-side power varies accordingly in order to maintain the capacitor voltages regulated according to Kirchhoff's law and conservation of energy. The possibility of applying a control technique to regulate the submodule-capacitor voltages is an important topic to be considered in future works.

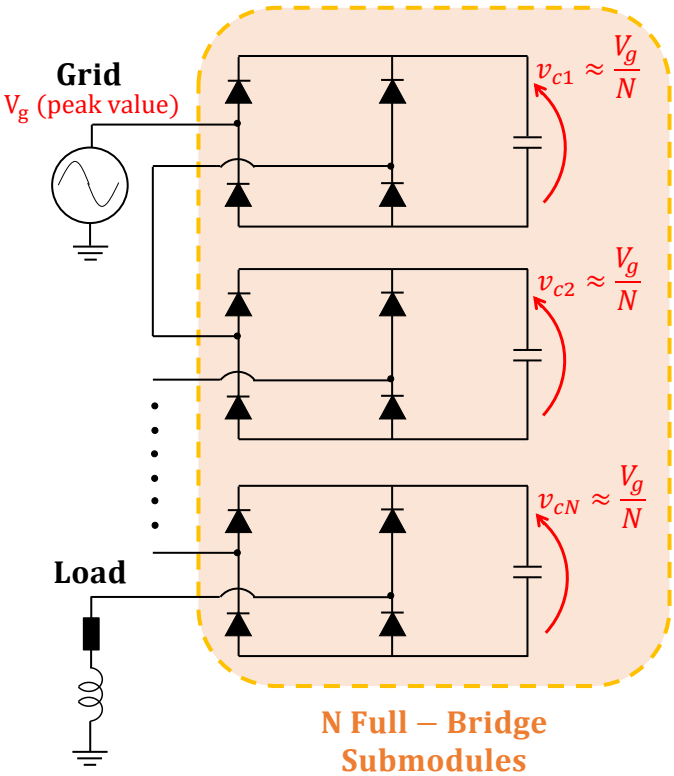

Fig. 14: Representation of submodule string as a string of diode rectifiers to explain the behavior of the capacitor voltages.

To explain the operational characteristics of the 3x3-MMSC in an illustrative way, a simulation was performed in the software PSCAD/EMTDC. In this simulation the 3x3-MMSC was modeled with $N = 20$ submodules per string, and it was connected to an AC grid with voltage amplitude equal to $V_g = 12$-kV and with frequency equal to $f_i = 50$ Hz. Besides, in this simulation, the proposed converter supplied power to a RL load (10 mH and 100 Ω). Initially, the amplitude of the voltages synthesized at the load terminals was set to $V_o = 10$ kV (peak value of phase-to-neutral voltage) and the frequency was set to $f_o = 10$ Hz. At $t = 3$ s, the amplitude of the voltages synthesized at the load terminals was set to $V_o = 7$ kV and the frequency was set to $f_o = 30$ Hz. In Fig. 15, the submodule-capacitor voltages of the converter's phase-A string are shown, which were obtained through the previously mentioned simulation. It is interesting to notice that the average value (DC value) of the submodule-capacitor voltages remains

constant (equal to approximately $\frac{V_g}{N} = \frac{12}{20} = 0.6$ kV) throughout the entire simulation. This average value is expected according to the explanation previously presented related to Fig. 14. When the voltage synthesized at the load terminals is modified, at $t = 3$ s, a power variation occurs, which leads to a different voltage drop across the load. Nonetheless, this voltage drop remains small enough so that the submodule-capacitor voltages are still equal to $\frac{V_g}{N} \approx \frac{12}{20} = 0.6$ kV, which is expected according to Kirchhoff's law and conservation of energy. Besides the DC value, the submodule-capacitor voltages also contain an AC ripple, which is a consequence of the continuous charging/discharging cycles of the capacitors that occur while the converter transfers power from the grid to the load. Finally, it is interesting to observe the zoom in Fig. 15, where the individual voltages of each capacitor within the submodule string can be observed. The N submodule capacitors within the string remain with similar voltage values as a consequence of the submodule-capacitor voltage-balancing algorithm that will be explained later in this thesis.

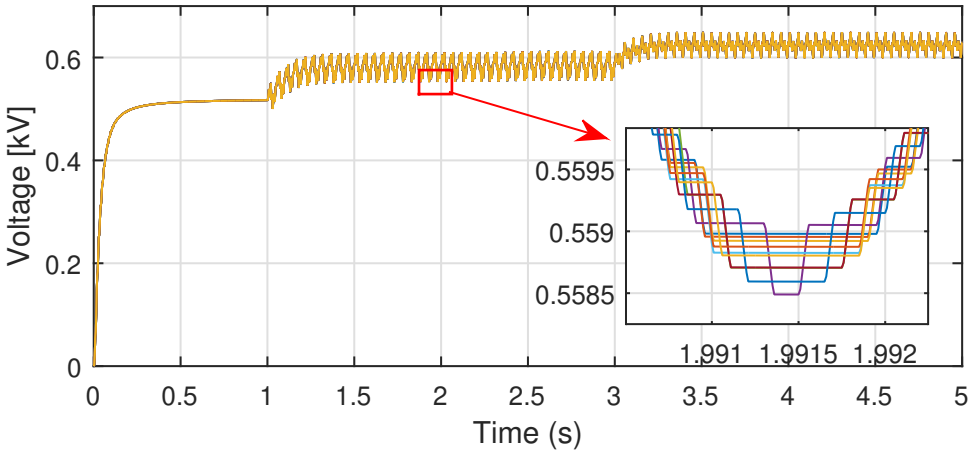

Fig. 15: Phase-A-string submodule-capacitor voltages of the 3x3-MMSC.

Since the 3x3-MMSC submodule-capacitor voltages are naturally regulated with a value equal to approximately $\frac{V_g}{N}$, and since there are obviously N submodules available to be inserted in series, then the maximum voltage possible to be synthesized across the submodule string terminals is equal to $N\frac{V_g}{N} = V_g$. Thus, according to (4), there will be moments where the amplitude of the voltage to be synthesized in series (v_{sa}) will be higher than V_g since AC-AC applications with different frequencies ($f_i \neq f_o$) are considered. In other words, in this example, $f_i = 50$ Hz $\neq f_o = 10$ Hz and, thus, there will be moments where the peak of the grid voltage will meet the valley of the load voltage reference for example. According to (4), in this case the instantaneous value

of the voltage to be synthesized in series if the phase-A submodule string remained connected to phase A of the grid would be equal to $|v_{sa}| = V_g + V_o = 12 + 10 = 22$ kV (if it happens before $t = 3$ s), which is a value obviously bigger than $V_g = 12$ kV, which is the maximum voltage possible to be synthesized in series. Thus, the converter would lose control over the load voltage, and this voltage would diverge from its reference. To always maintain control over the load voltage, the submodule strings must be continuously connected to different phases of the grid. For example, if the phase-A submodule string is connected to phase B or to phase C of the grid, then the voltage necessary to be synthesized in series is no longer the one described in (4), i.e., if the phase-A submodule string is connected to phase B or to phase C of the grid, then the voltage to be synthesized across this string should be calculated according to (5) and (6), respectively.

$$v_{sa} = v_a^* - v_{gb} = V_o sin(\omega_o t) - V_g sin(\omega_i t - \frac{2\pi}{3}) \tag{5}$$

$$v_{sa} = v_a^* - v_{gc} = V_o sin(\omega_o t) - V_g sin(\omega_i t + \frac{2\pi}{3}) \tag{6}$$

By being possible to connect the converter's submodule string to the three phases of the grid through the operation of the bidirectional-switch stacks, then it is possible to always maintain control over the load voltage as explained in Fig. 16, in which the three curves described by (4), (5), and (6) are illustrated along with two red lines representing the maximum voltage possible to be synthesized in series by the 3x3-MMSC, which is equal to $V_g = \pm 12$ kV in this example.

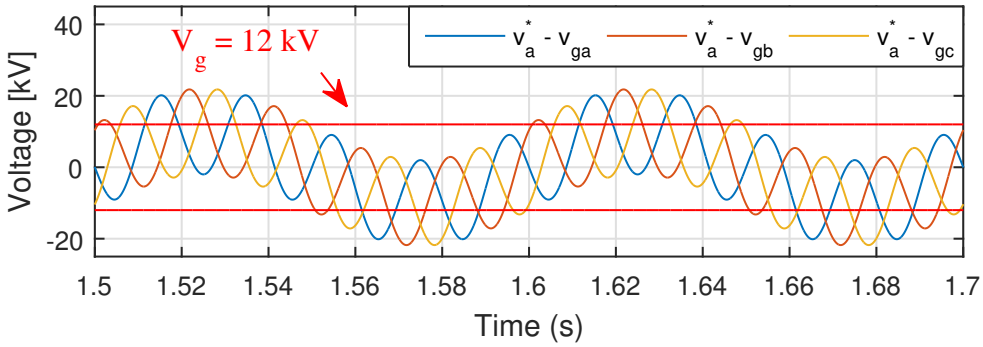

Fig. 16: Illustrative representation of (4), (5), and (6), which are the voltages that must be synthesized in series by the 3x3-MMSC in order to control the load voltage, depending to which grid phase the submodule string is connected.

It is interesting to notice that the oscillatory signals illustrated in Fig. 16 present two different frequency components, i.e., the $f_i = 50$-Hz component and the $f_o = 10$-

Hz component. The blue curve in Fig. 16 corresponds to the voltage that must be synthesized in series, across the phase-A submodule string, in order to synthesize the desired load voltage equal to $V_o sin(\omega_o t)$. It is interesting to observe that approximately every $t = \frac{1}{50\text{Hz}} = 0.02$ s, the blue curve exceeds the limits of the maximum voltage possible to be synthesized in series (red lines). It means, that the converter would lose control over the load voltage every 0.02 s if the submodule string remained connected to phase A of the grid. However, it is interesting to notice that every time that the blue curve is exceeding the red lines, either the orange or the yellow signals are within the limits represented by the two red lines. It means that if the phase-A submodule string is connected to either phase B or phase C of the grid (the one whose signal is instantaneously within the two red lines), then it would be possible to keep control over the load voltage. In Fig. 17(a), the three oscillatory signals shown in Fig. 16 are represented again along with the real multilevel voltage synthesized across the phase-A submodule string terminals (v_{sa}), which is represented by the purple signal.

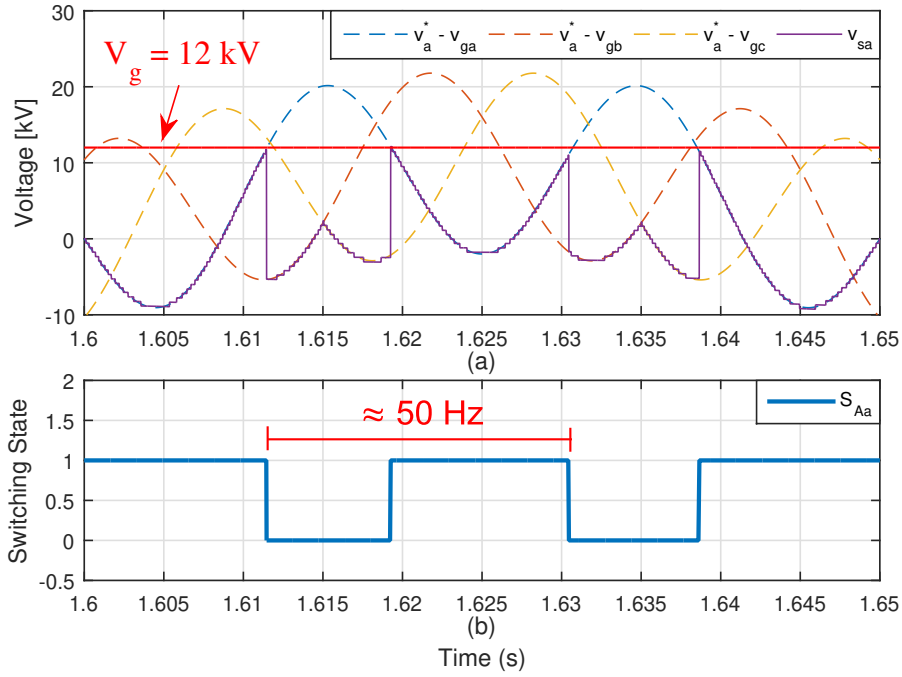

Fig. 17: (a) Simulation results illustrating signals represented by (4), (5), and (6), along with real voltage synthesized in series across the phase-A submodule string, and (b) simulation results showing the switching state of the phase-A submodule string.

One can observe that v_{sa} is equal to the blue curve while this curve is below the red line (equal to maximum voltage possible to be synthesized in series). As soon as

the blue signal exceeds the red line, then v_{sa} becomes equal to the orange signal, which means that the phase-A submodule string was connected to phase B of the grid. When the orange signal intersects with the yellow signal, then v_{sa} becomes equal to the yellow signal which means that the phase-A submodule string was connected to phase C of the grid. In Fig. 17(b), the switching state of the bidirectional-switch stack that connects the phase-A submodule string to phase A of the grid is shown. In this figure, one can notice that the bidirectional-switch stack only switches when the blue curve crosses the red lines. This situation happens with a frequency of approximately 50 Hz, which is the grid frequency, and the higher frequency present in the oscillatory signal represented by (4). This is the minimum switching frequency with which the bidirectional-switch stacks must operate in order to keep control of the load voltage. Even though the switching frequency could be increased, this low switching frequency is adopted in this thesis, aiming at preserving the reliability of the proposed converter solution.

By synthesizing the series voltages according to the approach previously presented, the proposed 3x3-MMSC is capable to synthesize the desired load voltage according to a given reference. The three phase voltages synthesized at the load terminals in this simulation example are shown in Fig. 18. As previously explained, the load voltage reference initially is set with an amplitude of $V_o = 10$ kV and with a frequency of $f_o = 10$ Hz. At $t = 3$ s, the amplitude of the load voltage reference is set to $V_o = 7$ kV and its frequency to $f_o = 30$ Hz. In Fig. 18, one can notice that the 3x3-MMSC is capable to properly synthesize the desired load voltage according to the received references. By observing the zoom in Fig. 18, one can observe the detail of the switched voltage synthesized at the load terminals, along with its reference.

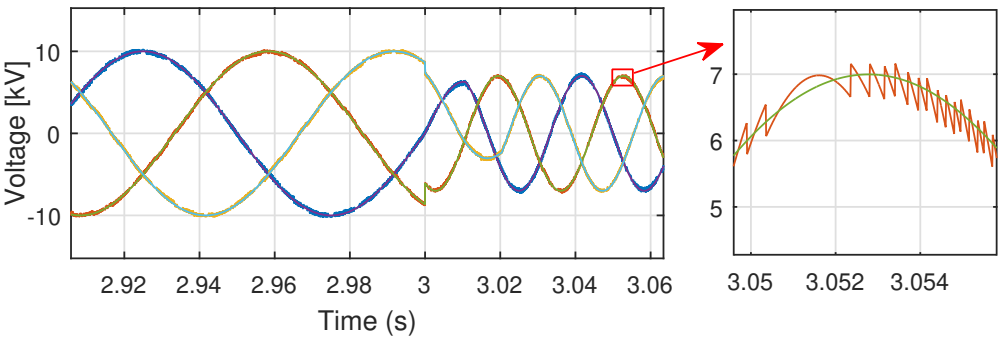

Fig. 18: Three-phase voltage synthesized by the 3x3-MMSC at the load terminals.

From Fig. 18, it is clear that the 3x3-MMSC behaves as a controlled voltage source from the load perspective, capable to synthesize the desired voltage with amplitude equal to V_o and frequency equal to f_o at the load terminals (see Fig. 19). From the grid perspective, however, the proposed converter solution behaves as a current source,

injecting into the grid currents with different frequency components. Because of the series connection of the submodule strings between the load and the grid, and because of the extremely low switching frequency adopted in this thesis for the bidirectional-switch stacks, then a current component with a considerable amplitude with the load frequency (i_o) flows to the grid, and it must be filtered out (see Fig. 19). Other frequency components higher than the fundamental frequency also flow to the grid, and that is why a complex (and potentially large) band-pass filter is required at the input terminals of the 3x3-MMSC. This filter must be capable to filter out all the undesired frequency components in such a way that only the fundamental component (i_{gf}) flows to the grid as shown in Fig. 19.

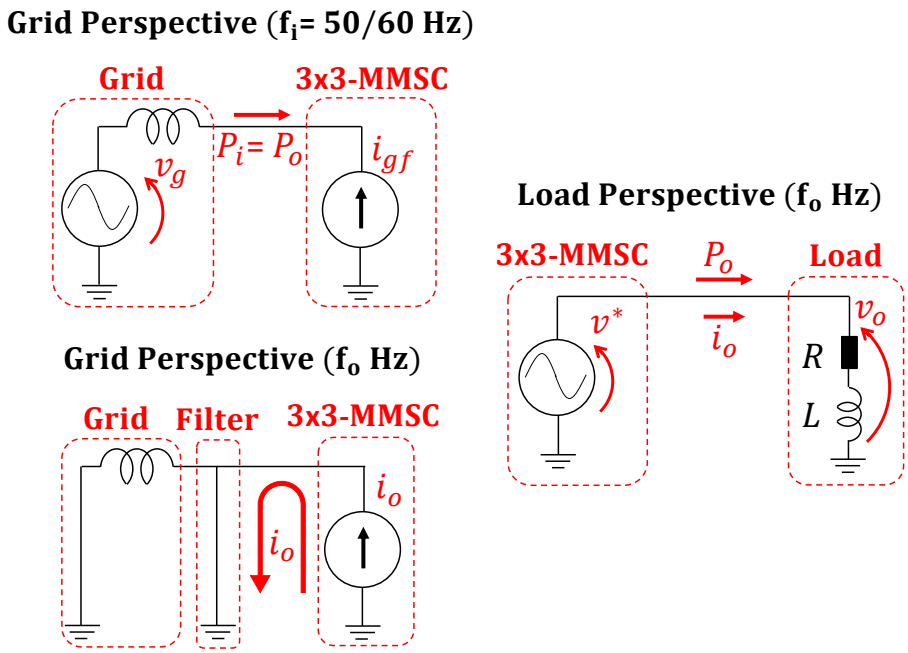

Fig. 19: Illustration of 3x3-MMSC electrical behavior from the grid and from the load perspectives.

In Fig. 20, the phase-A load current (i_{oa}), the switched current that is injected into phase A of the grid (i_{ga}), and the filtered current that is injected into the grid (i_{gfa}) are shown. These signals were obtained in the same simulation example of the previous figures. By observing the current i_{ga}, one can notice that this is indeed a switched current but without high frequency components due to the low switching frequency of the bidirectional-switch stacks. Moreover, one can also observe that the load frequency component ($f_o = 10$ Hz) is also present since the switched current is following the load

current waveform. The filtered grid current (i_{gfa}), however, is a sinusoidal signal with the fundamental frequency only ($f_i = 50$ Hz). This is a consequence of the RLC band-pass filter adopted as illustrated in Fig. 13. It is important to highlight, though, that the adopted filter is not an efficient one, and other filter topologies should be explored for the proper implementation of the proposed converter, aiming at obtaining a competitive solution. As previously discussed, the complexity of the filter could be reduced by increasing the switching frequency of the bidirectional-switch stacks in a way that the switched current injected into the grid (i_{ga}) would present high frequency components. This would be an operation similar to a DMC [65–67]. Nonetheless, once again, increased switching frequencies of the bidirectional-switch stacks would lead to a reduced reliability since these switches must be built with a few series-connected semiconductor devices. In the DMC case, a high switching frequency is required to properly synthesize the load-side voltage. In the 3x3-MMSC, however, the submodule strings are the ones responsible for the control of the load voltage, but the switching frequency of the bidirectional-switch stacks affect the power quality of the current injected into the grid. Thus, this switching frequency should be defined taking into consideration both the size and complexity of the input filter, and the reliability of the converter solution.

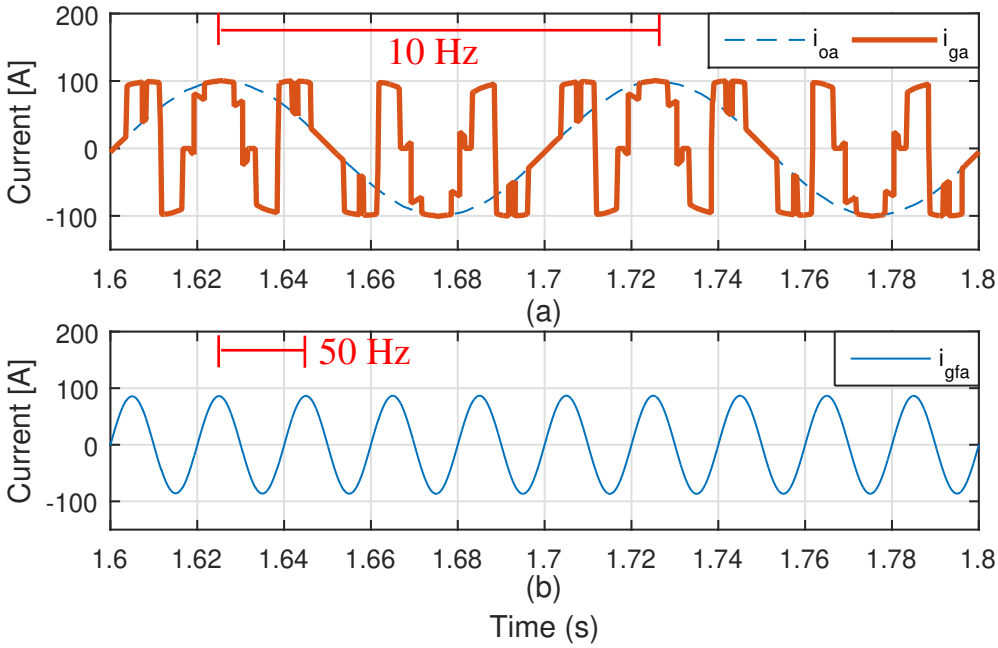

Fig. 20: (a) Simulation results of the phase-A load current (i_{oa}) and of the switched current that is injected into phase A of the grid (i_{ga}), and (b) simulation results of the filtered current that is injected into the grid (i_{gfa})

2.2 Internal Control and Modulation

In the previous section, the basic operation of the MMSC and of the 3x3-MMSC was presented. In this section, the internal control and modulation of the converter topologies are presented in detail through flowcharts since they were implemented in C programming codes. The algorithm of the internal control and modulation of the MMSC phase A is explained in the flowchart shown in Fig. 21. The same algorithm is also adopted for phases B and C. The MMSC phase-A internal control receives as inputs the measurements of the phase-A and phase-B grid voltages (v_{ga} and v_{gb}, respectively), the phase-A load current (i_{oa}), and the capacitor voltages of all the submodules in the phase-A string (v_{ca1}, v_{ca2}, ..., and v_{caN}). The MMSC phase-A internal control also receives as an input the reference of the voltage to be synthesized at the phase-A load terminal (v_a^*), which comes from outer control loops. The first stage of the control is the bidirectional-switch-stack logic that defines to which phase of the grid the submodule string should be connected. Thus, first, the difference between the instantaneous values of the grid voltage and of the voltage reference is calculated ($E = v_a^* - v_{ga}$). Then, the control tests if the calculated error (E) is within the limits of $-Nv_{ca1}$ and Nv_{ca1}, which corresponds to the maximum voltage possible that the converter can synthesize in series across its submodule string (with negative and positive polarities). In this case, the capacitor voltage of the first submodule in the string was used (v_{ca1}) since it is considered that all the capacitors within the submodule string have similar voltages because of the sorting algorithm responsible for the submodule-capacitor voltage balancing. In other words, the sorting algorithm, which will be explained later, makes sure that $v_{ca1} = v_{ca2} = ... = v_{caN} = \frac{Vg}{N}$ all the time. So, if $E > -Nv_{ca1}$ and $E < Nv_{ca1}$, then the phase-A submodule string can remain connected to phase A of the grid, which means that the bidirectional-switch stack that connects the phase-A submodule string to phase A of the grid remains in *ON* mode, and the bidirectional-switch stack that connects the phase-A submodule string to phase B of the grid remains in *OFF* mode ($S_{Aa} = 1$ and $S_{Ba} = 0$). On the contrary, if the instantaneous value of E is no longer within the limits of $-Nv_{ca1}$ and Nv_{ca1}, then $S_{Aa} = 0$ and $S_{Ba} = 1$, which means that the bidirectional-switch stack that connects the phase-A submodule string to phase A of the grid is turned off and the bidirectional-switch stack that connects the phase-A submodule string to phase B of the grid is turned on. In this case, a new value for the error E must be calculated as follows $E = v_a^* - v_{gb}$ since now the phase-A submodule string is connected to phase B of the grid. The second stage of the control algorithm is the modulation. The first step of the modulation is to check if the instantaneous value of E is positive or negative to define with which polarity the FB submodules must be inserted. If $E \geq 0$, then the FB submodules are inserted with positive polarity, and on the contrary they are inserted with negative polarity. After defining the polarity of the submodule to be inserted, then the next step is to decide the number of submodules (M) to be inserted to track the instantaneous value of the voltage reference (v_a^*). To do that, the control algorithm checks in which voltage range the calculated value of E is. For example, if

the absolute value of E is greater than zero ($|E| \geq 0$) and the absolute value of E is smaller than half the instantaneous value of the capacitor voltage ($|E| < \frac{v_{ca1}}{2}$), then no submodule should be inserted in the string, i.e., $M = 0$. As another example, if ($|E| \geq \frac{v_{ca1}}{2}$) and ($|E| < v_{ca1} + \frac{v_{ca1}}{2}$), then one submodule should be inserted, i.e., $M = 1$. In the simulation analyses performed in this thesis, the MMSC and 3x3-MMSC string were built with twenty submodules ($N = 20$). Thus, as shown in Fig. 21, there are $N + 1 = 21$ voltage ranges in which the instantaneous value of E can be, since there are twenty-one possibilities of submodule insertion in this case, i.e., the number of inserted submodules (M) can vary from 0 to 20. Finally, after defining the instantaneous number of submodules to be inserted, the last stage of the control algorithm is the voltage balance, which is responsible for keeping all the submodule capacitors within the same string with similar voltage values. Essentially, depending on the instantaneous current direction (if i_{oa} has a positive or negative value) and on the polarity of the submodules to be inserted, then the capacitors of the inserted submodules will be charged or discharged. Thus, if a charging current will flow through the capacitors of the inserted submodules, then the M submodules (out of the N available submodules) with lower instantaneous capacitor voltage values are selected to be inserted. On the contrary, if a discharging current will flow through the capacitors, then the M submodules with higher capacitor voltage values are selected to be inserted. With this simple sorting algorithm, all the capacitors within the same submodule string always remain with similar voltage values (see simulation results presented in Fig. 15). After running the entire algorithm, then the control acts so that the M selected submodules are inserted with the previously defined polarity.

The flowchart with the control algorithm of the 3x3-MMSC phase A is shown in Fig. 22 and it is essentially the same as the control of the MMSC phase A with an exception related to the control of the bidirectional-switch stacks. Since in the 3x3-MMSC case the submodule strings can be connected to the three phases of the grid, then the 3x3-MMSC phase-A control also receives as an input the measurement of the phase-C grid voltage (v_{gc}). As shown in Fig. 22, similarly to the MMSC control case, the 3x3-MMSC control algorithm checks if $E > -Nv_{ca1}$ and $E < Nv_{ca1}$, where $E = v_a^* - v_{ga}$. If this is the case, then the phase-A submodule string remains connected to phase A of the grid and the bidirectional-switch stacks that connect the phase-A submodule string to phases A, B and C of the grid receive triggering signals equal to $S_{Aa} = 1$, $S_{Ba} = 0$ and $S_{Ca} = 0$, respectively. If the instantaneous value of E is not within the limits of $-Nv_{ca1}$ and Nv_{ca1}, then the phase-A submodule string should be connected to either phase B or phase C of the grid.

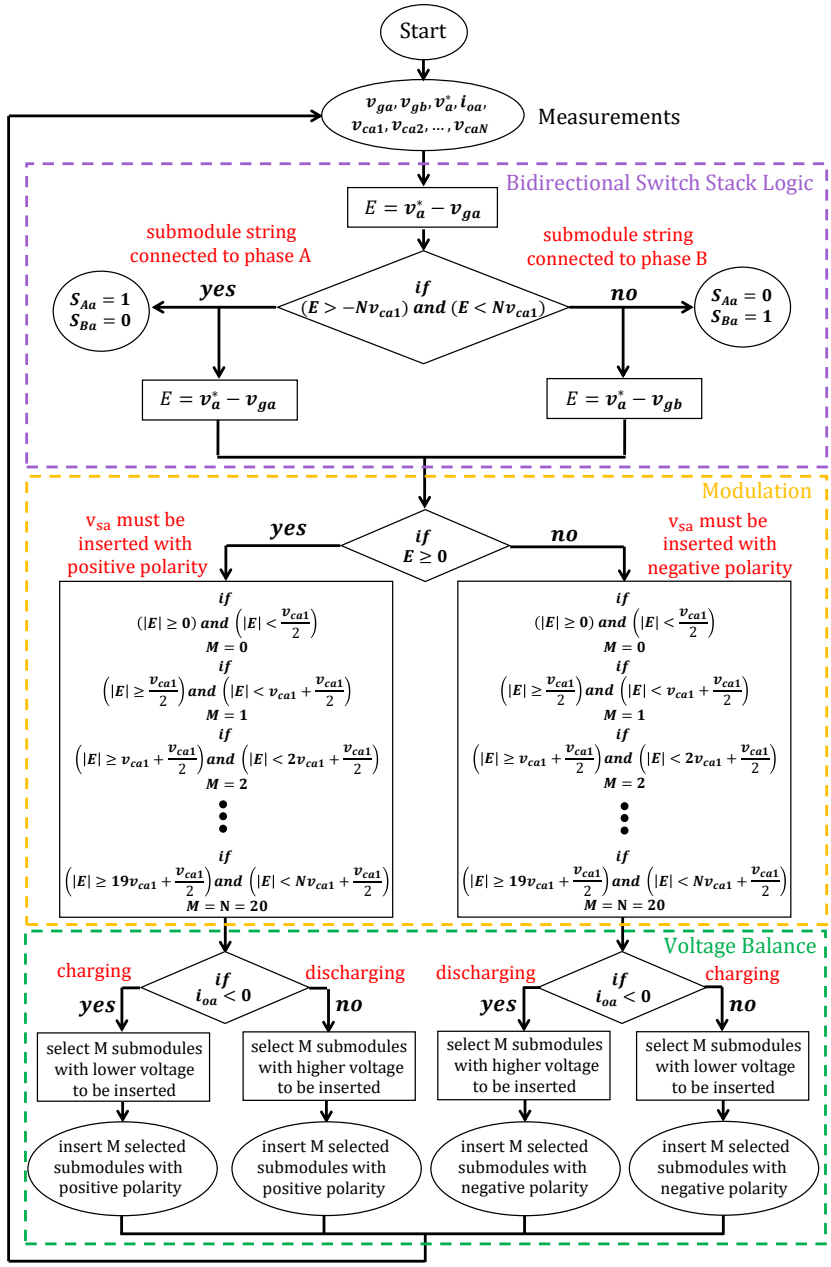

Fig. 21: Flowchart explaining algorithm related to the internal control and modulation of the MMSC phase A.

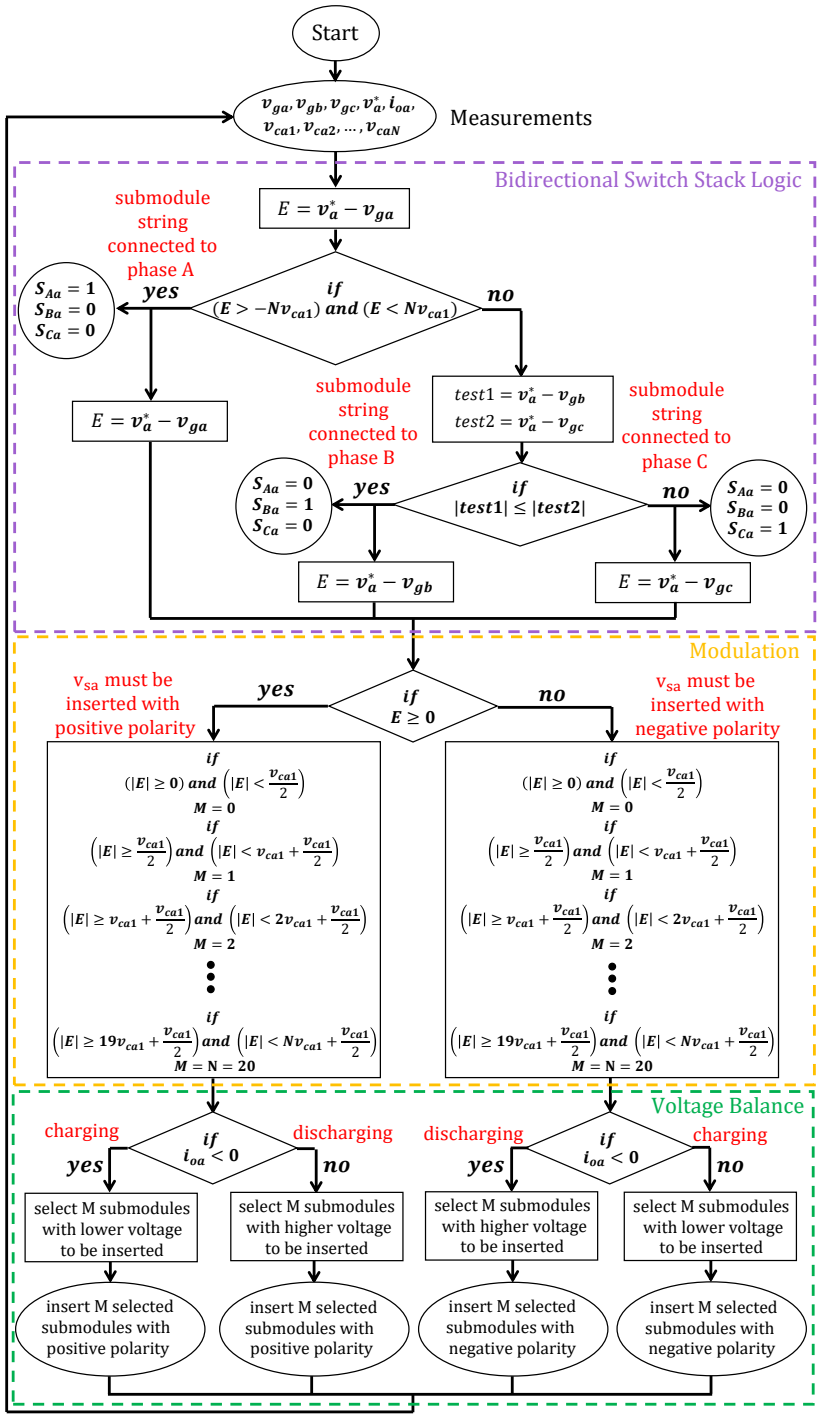

Fig. 22: Flowchart explaining algorithm related to the internal control and modulation of the 3x3-MMSC phase A.

In this thesis, the following procedure is adopted: if the absolute value of the test variable $test1 = v_a^* - v_{gb}$ is less or equal to the absolute value of the test variable $test2 = v_a^* - v_{gc}$, then the phase-A submodule string should be connected to phase B of the grid and the bidirectional-switch stacks that connect the phase-A submodule string to phases A, B and C of the grid receive triggering signals equal to $S_{Aa} = 0$, $S_{Ba} = 1$ and $S_{Ca} = 0$, respectively. On the contrary, if the absolute value of $test1$ is greater than the absolute value of $test2$, then the phase-A submodule string should be connected to phase C of the grid and the bidirectional-switch stacks that connect the phase-A submodule string to phases A, B and C of the grid receive triggering signals equal to $S_{Aa} = 0$, $S_{Ba} = 0$ and $S_{Ca} = 1$, respectively. As previously mentioned, the rest of the 3x3-MMSC internal control (modulation and voltage balancing algorithm) is equal to the MMSC control.

2.3 Analytical Description of Submodule-Capacitor Voltage Ripple to Explain High Performance at Low-Frequency Operation

In this section, a mathematical description of the MMC's and of the MMSC's submodule-capacitor voltages is presented to explain the low performance of the MMC at low-frequency operation (the extremely high voltage ripple in its submodule capacitors) and to explain why the proposed MMSC presents improved performance at low frequencies in comparison to the MMC. As will be demonstrated later in this thesis, the 3x3-MMSC also presents improved performance at low frequencies because of the similar structural and operational characteristics in relation to the MMSC.

2.3.1 Mathematical Analysis of Submodule-Capacitor Voltage Ripple

As previously presented, the MMC submodules should be inserted with an insertion index pattern that can be approximated by a continuous signal composed of a DC component and of an AC component with the frequency of the voltage to be synthesized at the load terminals ($\omega_o = 2\pi f_o$). This signal is reproduced in (7) for convenience.

$$S(t) = 0.5sin(\omega_o t) + 0.5 \tag{7}$$

Once again, considering that all the undesired AC circulating-current components are properly suppressed, then the currents flowing through the MMC arms can be described as follows:

$$i_{arm}(t) = \frac{i_{AC}(t)}{2} + \frac{i_{DC}(t)}{3} \tag{8}$$

The voltage synthesized by an MMC at its load terminals can be mathematically described as follows:

$$v_{AC}(t) = V_o sin(\omega_o t) \tag{9}$$

Where, once again, V_o and $\omega_o = 2\pi f_o$ are the amplitude and frequency of the load-voltage reference, respectively. Considering an RL load, the load current can be calculated as follows:

$$i_{AC}(t) = \frac{v_{AC}(t)}{|R + j\omega_o L|} = \frac{V_o sin(\omega_o t + \theta)}{|R + j\omega_o L|} \tag{10}$$

Where θ is the load angle that is neglected in this analysis since it is considered that $R >> L$, which means an operation with unit power factor. By considering the approximation that the MMC AC-side power is equal to its DC-side power ($P_{AC} = P_{DC}$), then the following is obtained:

$$\sqrt{3}(\frac{\sqrt{3}}{\sqrt{2}}V_o)I_{AC} = V_{DC}I_{DC} \tag{11}$$

By rearranging (11), the MMC DC current can be calculated as a function of the DC voltage (V_{DC}), of the amplitude of the load-voltage reference (V_o), and of the rms value of the load current (I_{AC}), as described in (12).

$$i_{DC}(t) = I_{DC} = \frac{3V_o I_{AC}}{\sqrt{2}V_{DC}} \tag{12}$$

The rms value of the load current can be calculated as follows:

$$I_{AC} = \frac{V_o}{\sqrt{2}|R + j\omega_o L|} \tag{13}$$

By substituting (13) into (12) the following is obtained:

$$i_{DC}(t) = I_{DC} = \frac{3V_o^2}{2V_{DC}|R + j\omega_o L|} \tag{14}$$

By substituting (10) and (14) into (8), the final equation for the MMC arm current is obtained as described in (15).

$$i_{arm}(t) = \Big(\frac{V_o}{2|R + j\omega_o L|}\Big)sin(\omega_o t) + \frac{V_o^2}{2V_{DC}|R + j\omega_o L|} \tag{15}$$

Finally, the MMC capacitor current can be calculated by substituting (7) and (15) into (16).

$$i_{cap}(t) = i_{arm}(t)S(t) \tag{16}$$

To perform a fair comparative analysis between the MMC and the MMSC in terms of the amplitude of the submodule-capacitor voltage ripple, equivalences between the two converters were made. The first equivalence was to consider that the two converters had to synthesize the exact same load voltage (described in (9)), supplying power to the same RL load, resulting in the same AC current flowing through the two converters with an rms value equal to I_{AC}. In the comparative analysis, the amplitude of the load voltage reference was set to $V_o = 10$ kV, and three different frequency values were considered for the load voltage, i.e., $f_o = 1, 10, 45$ Hz. The considered load resistance and inductance were equal to $R = 100\ \Omega$ and $L = 10$ mH, respectively. Ideally, the minimum DC voltage possible so that the MMC can synthesize the desired load voltage (with amplitude $V_o = 10$ kV) is equal to $V_{DC} = 2V_o = 20$ kV. This was the voltage value adopted for the MMC DC-link voltage in the comparative analysis. As will be explained later, the MMSC will also be designed with its minimum voltage ratings to allow for a fair comparative analysis. In Fig. 23(a), (c), and (e) the MMC insertion index signals ($S(t)$) calculated according to (7) for the cases where $f_o = 1, 10, 45$ Hz, respectively, are shown. In Fig. 23(b), (d), and (f), the FFTs of the insertion index signals shown in Fig. 23(a), (c), and (e), are presented, respectively. As expected, the oscillatory components of these signals present frequency equal to $f_o = 1, 10, 45$ Hz, respectively, which are the different values considered for the frequency of the synthesized load voltages. In Fig. 24(a), (c), and (e), the FFTs of the MMC capacitor current (i_{cap}(t)) for the cases where $f_o = 1, 10, 45$ Hz are shown, respectively. The capacitor currents were calculated through (16) considering $V_o = 10$ kV, $R = 100\ \Omega$, $L = 10$ mH, and $V_{DC} = 2V_o = 20$ kV. By observing the results of the FFTs, one can notice that the product of the DC and the ω_o components, present in both $S(t)$ and in i_{arm}(t), lead to ω_o and $2\omega_o$ components in i_{cap}(t). It is important to observe that for the case where $f_o = 1$ Hz, low frequency components with frequency of $\omega_o = 1$ Hz and $2\omega_o = 2$ Hz appear in the MMC capacitor current, which produce a high voltage ripple in the converter's submodule capacitors. This is because the submodule capacitor voltages are floating ones, and their ripple is related to the voltage drop across the capacitor reactance (X_c), which is inversely proportional to the frequency of the currents flowing through it as described in (17).

$$X_c = \frac{1}{2\pi f C} \tag{17}$$

To perform the comparative analysis, the mathematical description of the MMSC submodule-capacitor voltage ripple should also be presented. Considering that the MMSC phase-A submodule string is connected to phase A of the grid, then, according to Kirchhoff's law, the voltage that should be synthesized in series across the string terminals (v_{sa}) in order to obtain the desired voltage (v_{AC}) at the load terminals is equal to:

$$v_{sa}(t) = v_{AC}(t) - v_{ga}(t) = V_o sin(\omega_o t) - V_g sin(\omega_i t + \phi) \tag{18}$$

Where v_{ga} is the instantaneous value of the phase-A grid voltage, V_g is the amplitude of the grid voltage (phase-to-neutral peak value) and $\omega_i = 2\pi f_i$ is the grid frequency. As previously explained, the DC component of the MMSC submodule-capacitor voltages naturally converges to a value equal to approximately $\frac{V_g}{N}$. Thus, if the capacitor ripple is neglected, the voltage that the MMSC is capable to synthesize in series can be described as:

$$v_{sa}(t) = \frac{V_g}{N} S(t) \tag{19}$$

Where, in this case, $S(t)$ is a discrete signal that can vary between $-N$ and N representing the instantaneous number of inserted submodules in the string. The fact that $S(t)$ can assume both positive and negative values is a consequence of the use of FB submodules, which can be inserted with both positive and negative polarities. Similarly to the MMC case, an approximation can be made to consider the insertion index as a continuous signal normalized by the number of submodules in the string (N) in a way that the MMSC series voltage will be described as follows:

$$v_{sa}(t) = \frac{V_g}{N} S(t) N = V_g S(t) \tag{20}$$

In other words, according to (20), v_{sa} can be defined as the product of V_g, which is equal to the sum voltage of all the submodule capacitors within the string, times $S(t)$, which is a continuous signal varying from -1 to 1. By substituting (20) into (18), the MMSC insertion index can be described as follows:

$$S(t) = \frac{V_o}{V_g} sin(\omega_o t) - sin(\omega_i t + \phi) \tag{21}$$

The MMSC insertion index described by (21) corresponds to the situation where the phase-A submodule string is connected to phase A of the grid. However, during normal operation, the connection of this submodule string will be continuously switching between the phase-A and phase-B grid terminals, through the operation of the bidirectional-switch stacks. Thus, every time the signal described in (21) exceeds the limits of ± 1, then this signal becomes equal to (22).

$$S(t) = \frac{V_o}{V_g} sin(\omega_o t) - sin(\omega_i t + \phi - \frac{2\pi}{3}) \tag{22}$$

The signal described in (22) corresponds to the situation where the MMSC phase-A submodule string is connected to phase B of the grid, and it was obtained by substituting v_{ga} by v_{gb} in (18), i.e., the angle $\frac{2\pi}{3}$ corresponds to the phase shift between phases A and B of the grid. It is clear, then, that the MMSC insertion index signal is discontinuous since it can be equal to (21) and to (22) depending on to which phase of the grid the submodule string is connected. In Fig. 23(g), (i), and (k), the MMSC insertion index

signals ($S(t)$) are shown for the cases where $f_o = 1, 10, 45$ Hz, respectively. Similarly to the MMC case, $V_o = 10$ kV, $R = 100\ \Omega$, and $L = 10$ mH were considered for the MMSC calculations. Besides, as will be explained in detail later in this thesis, the peak value of the phase-to-neutral grid voltage was considered to be equal to $V_g = 2V_o = 20$ kV, which is the minimum voltage possible so that the MMSC is capable to synthesize the desired load voltage with amplitude V_o. Once again, both the MMC and the MMSC were designed with their minimum voltage ratings so that a fair comparative analysis could be performed. In Fig. 23(h), (j), and (l), the FFT of the signals presented in Fig. 23(g), (i), and (k) are shown, respectively. It is clear that the MMSC insertion index signal is composed of various frequency components. The main frequency components of the signal's frequency spectrum are the following:

$$f_{S(t)} = \sum nf_i + \sum mf_i \pm f_o \tag{23}$$

Where $n = 1, 3, 5, ...\infty$ and $m = 2, 4, 6, ...\infty$. Specifically for the $f_o = 1$-Hz case, it interesting to observe that there are no low frequency components with a relevant amplitude in the MMSC's insertion index signal. As shown in Fig. 23(h), only a 3-Hz component with relatively small amplitude is present in the MMSC's insertion index signal for the $f_o = 1$-Hz case. As will be explained later, this insertion index pattern contributes for the low submodule-capacitor voltage ripple of the MMSC at low frequencies. Similarly to the MMC case, the MMSC load current can be calculated as follows:

$$i_{AC}(t) = \frac{v_{AC}(t)}{|R + j\omega_o L|} = \frac{V_o sin(\omega_o t + \theta)}{|R + j\omega_o L|} \tag{24}$$

Due to the series connection of the MMSC's submodule strings between the load and the grid, the current that flows through these strings is equal to the load current as follows:

$$i_{string}(t) = i_{AC}(t) = \frac{V_o sin(\omega_o t + \theta)}{|R + j\omega_o L|} \tag{25}$$

Finally, the current that flows through the MMSC submodule capacitors, producing the voltage ripple, can be calculated as described in (26), which is the product of the string current presented in (25) by the converter's insertion index, which is equal to (21) if $S(t)$ is within ± 1 and equal to (22) if $S(t)$ exceeds these limits.

$$i_{cap}(t) = i_{string}(t)S(t) \tag{26}$$

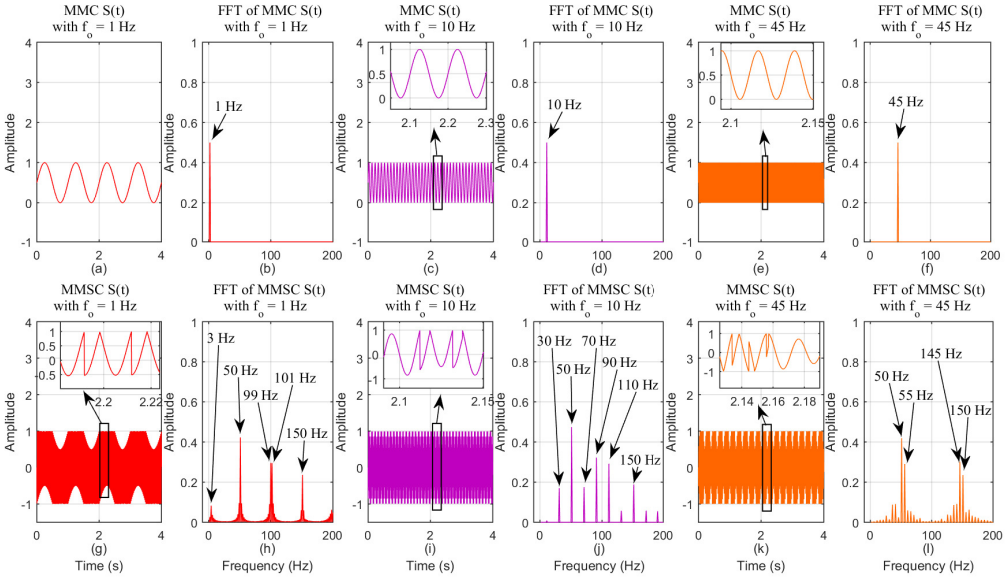

Fig. 23: (a), (c), and (e) MMC's insertion index signals ($S(t)$) for the cases where $f_o = 1, 10, 45$ Hz, respectively. (b), (d), and (f) FFT of MMC's insertion index signals for the cases where $f_o = 1, 10, 45$ Hz, respectively. (g), (i), and (k) MMSC's insertion index signals ($S(t)$) for the cases where $f_o = 1, 10, 45$ Hz, respectively. (h), (j), and (l) FFT of MMSC's insertion index signals for the cases where $f_o = 1, 10, 45$ Hz, respectively.

In Fig. 24(b), (d), and (f), the FFT of the MMSC's capacitor currents (i_{cap}) are presented for the cases where $f_o = 1, 10, 45$ Hz, respectively. These currents were calculated through (26), considering $V_o = 10$ kV, $R = 100\ \Omega$, $L = 10$ mH, and $V_g = 20$ kV. It is interesting to notice that i_{string} is a current with one frequency component only, which is the load frequency (f_o). In the case where $f_o = 1$ Hz, the product of this frequency component present in i_{string} by the 3-Hz component present in the modulation index signal ($S(t)$) will result in components with frequency equal to $3 \pm f_o = 2$ Hz and 4 Hz in the capacitor current (i_{cap}). Since the 3-Hz component of $S(t)$ presents a relatively low amplitude, then the 2-Hz and the 4-Hz present in i_{cap} also present a low amplitude as shown in Fig. 24(b). Another important fact to be observed for the $f_o = 1$-Hz operation is that, in the MMC case, a DC component exists in both the arm current (i_{arm}) and in the insertion index signal ($S(t)$), and the product of the DC component by the $f_o = 1$-Hz component, present both in i_{arm} and in $S(t)$, will lead to the $f_o = 1$-Hz component in the MMC capacitor current (i_{cap}). This component is the most critical one since the capacitor's reactance is inversely proportional to the current frequency. There are no DC components neither in the MMSC string current

(i_{string}) nor in its insertion index signal ($S(t)$), thus, there is no 1-Hz component in the MMSC capacitor current (i_{cap}). In fact, by comparing the 1-Hz and the 2-Hz components in the MMC's capacitor currents (see Fig. 24(a)) with the 2-Hz and the 4-Hz components in the MMC's capacitor currents (see Fig. 24(b)), one can notice that the MMC's components present considerably higher amplitudes in comparison to the MMSC's components. This is because of the considerably reduced amplitude of the 3-Hz component in the MMSC's insertion index signal (see Fig. 23(h)) in comparison to the 1-Hz component in the MMC's insertion index signal (see Fig. 23(b)). Besides the reduced amplitudes of the 2-Hz and the 4-Hz components, as previously mentioned, there is no 1-Hz component in the MMSC's capacitor current (see Fig. 24(b)).

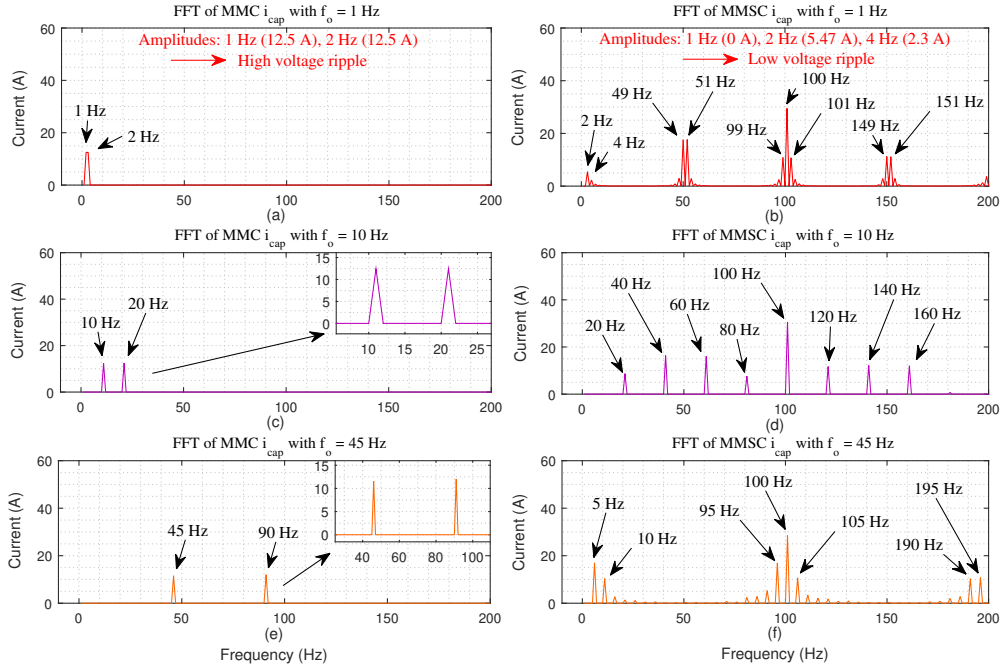

Fig. 24: (a), (c), and (e) FFT of MMC's capacitor current (i_{cap}) for the cases where $f_o = 1, 10, 45$ Hz, respectively. (b), (d), and (f) FFT of MMSC's capacitor current (i_{cap}) for the cases where $f_o = 1, 10, 45$ Hz, respectively.

Since the capacitor's reactance is inversely proportional to the current frequency, and since the voltage ripple is propotional to the voltage drop across this reactance, then the voltage ripple will be higher the lower the frequency components of the capacitor currents are, and the higher the amplitude of these current components are. Thus, it is clear that the submodule-capacitor voltage ripple will be considerably higher in the MMC than in the MMSC, for the $f_o = 1$-Hz case.

It is important to highlight that if the MMSC phase-A submodule string remained connected to the phase A of the grid only, then its insertion index signal would be the one presented in (21), which would be composed of the frequency components f_o and f_i only. In other words, for the case where $f_o = 1$ Hz, the MMSC insertion index signal would be composed of the $f_o = 1$-Hz and the $f_i = 50$-Hz components only. In this case, the frequency spectrum of the MMSC capacitor current, calculated according to (26), would be completely different. The fact that the MMSC operates connecting its submodule strings to different phases of the grid is what leads to the discontinuous insertion index pattern observed in Fig. 23. These discontinuous insertion indexes present various components in their frequency spectrum, and low frequency components are essentially attenuated as shown in Fig. 23(h). In the 3x3-MMSC case, the connection of the submodule strings is continuously varied between the three phases of the grid, which leads to an even more discontinuous insertion index signal, which also attenuates the low-frequency components present in this signal. Thus, it should be expected that the 3x3-MMSC would also present a low voltage ripple at low frequencies, which is something that will be confirmed later in this thesis.

2.3.2 Simulation Results

In this subsection, simulation results based on the software PSCAD/EMTDC are presented to analyze the submodule-capacitor voltage ripple of the MMC and of the MMSC. In these simulations, the same MMC and MMSC parameters adopted for the comparative analysis of the previous subsection are considered. In other words, in the MMC case the following parameters are adopted: $V_o = 10$ kV, $R = 100\ \Omega$, $L = 10$ mH, and $V_{DC} = 20$ kV, and for the MMSC case the following parameters are adopted: $V_o = 10$ kV, $R = 100\ \Omega$, $L = 10$ mH, $V_g = 20$ kV, and $f_i = 50$ Hz. Moreover, the exact same submodule-capacitor capacitance (equal to $C = 5$ mF) is adopted for both converters so that a fair comparative analysis can be performed. Finally, the MMC arms are built with $N = 10$ half-bridge (HB) submodules and the MMSC strings are built with $N = 10$ FB submodules. The first simulation analysis was performed by varying the load-side frequency (f_o) of both converters by 1 Hz until the whole frequency range was covered. The results of the simulations are shown in Fig. 25, where the submodule-capacitor voltage ripple of both topologies can be observed for the entire frequency range of operation. In Fig. 25, it is interesting to observe that, indeed, the MMSC presents a considerably reduced voltage ripple at very low frequencies in comparison to the MMC. This could be an important feature if the MMSC is adopted to drive electrical machines that need to operate at this low frequency range. Nonetheless, it is visually clear that the MMSC presents a considerably higher submodule-capacitor voltage ripple for higher frequencies. In fact, the MMSC submodule-capacitor voltage ripple increases the closer to the grid-side frequency ($f_i = 50$ Hz) the load-side frequency (f_o) gets. Since the MMSC insertion index signal is composed of various frequency components including the grid fundamental frequency (f_i), as described in (23), and since the MMSC string

current in composed of the load-side frequency (f_o), then the MMSC capacitor current will have components with frequencies $f_i \pm f_o$, according to (26). This fact can be confirmed by observing Fig. 24(b), where the MMSC capacitor current presents 50 ± 1-Hz components equal to 49 Hz and 51 Hz, for the case where $f_o = 1$ Hz, by observing Fig. 24(d), where the MMSC capacitor current presents 50 ± 10-Hz components equal to 40 Hz and 60 Hz, for the case where $f_o = 10$ Hz, and by observing Fig. 24(f), where the MMSC capacitor current presents 50 ± 45-Hz components equal to 5 Hz and 95 Hz, for the case where $f_o = 45$ Hz. If $f_o = 49$ Hz, then a current component with frequency equal to $50 - 49 = 1$ Hz will appear in the MMSC capacitor current, which will lead to a high voltage ripple in the converter's submodule capacitors. The conclusion is that the MMSC is a converter topology suitable for machine drives that operate with low frequencies, as its performance is deteriorated for operation with higher frequency values.

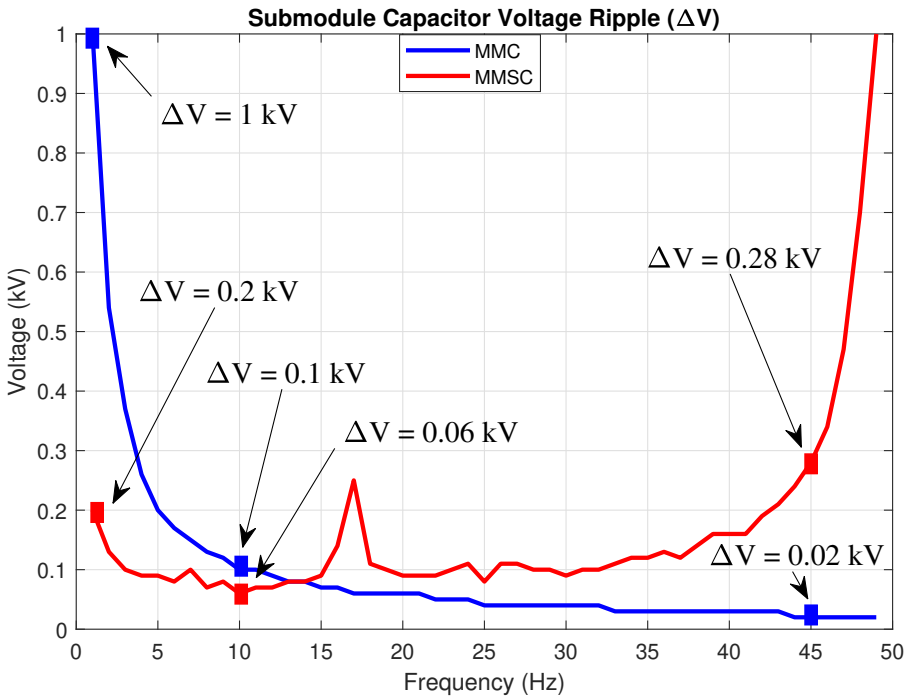

Fig. 25: Simulation results with submodule-capacitor voltage ripple of MMC and MMSC for different load frequency values.

The following simulation results are presented to validate the mathematical description of the submodule-capacitor voltages of the MMC and of the MMSC. By substituting

$V_o = 10$ kV, $R = 100\ \Omega$ and $L = 10$ mH into equation (10), the following numerical value is obtained for the load current:

$$i_{AC}(t) = 100sin(\omega_o t + \theta)\ A \tag{27}$$

The load current rms value calculated through (13) is equal to $I_{AC} = 70.72$ A. By substituting $I_{AC} = 70.72$ A, $V_{DC} = 20$ kV and $V_o = 10$ kV into equation (12), the MMC DC current can be calculated resulting in:

$$i_{DC}(t) = 75\ A \tag{28}$$

Finally, by substituting (27) and (28) into (8), the following arm current with numerical values is obtained

$$i_{arm}(t) = [50sin(\omega_o t + \theta) + 25]\ A \tag{29}$$

In the mathematical analysis presented in the previous subsection, the MMC insertion index was approximated by a continuous signal normalized by the number of submodules in the converter's arms (N). In reality, the MMC insertion index is a discrete signal that varies from 0 to N representing the instantaneous number of inserted submodules in the converter's arm. In Fig. 26(a), (b) and (c), the MMC's insertion index signal is shown for the cases where $f_o = 1, 10, 45$ Hz, respectively, and it is interesting to notice its staircase shape, representing the insertion of a different number of submodules, with a maximum value equal to $N = 10$. In Fig. 26(d), (e) and (f), the MMC's arm current is shown for the cases where $f_o = 1, 10, 45$ Hz, respectively, and it is interesting to observe that these signals, obtained through PSCAD simulations, are accurately described by (29), which means that the the mathematical model presented in the previous subsection is properly matching with the simulation model analyzed in this subsection. In Fig. 26(g), (h) and (i), the MMC's submodule-capacitor voltage (v_{cap}) is presented for the cases where $f_o = 1, 10, 45$ Hz, respectively. Since the same MMC that was analyzed through the mathematical description of the previous subsection was also modelled in the PSCAD simulation, then it should be expected that the same submodule-capacitor voltage ripple observed in the simulation could be calculated through the mathematical model presented in the previous subsection. By measuring the submodule-capacitor voltage ripple in Fig. 26(g), (h) and (i), the peak-to-peak voltage values (ΔV) can be obtained for the cases where $f_o = 1, 10, 45$ Hz, respectively, and these results are reproduced in Table 1.

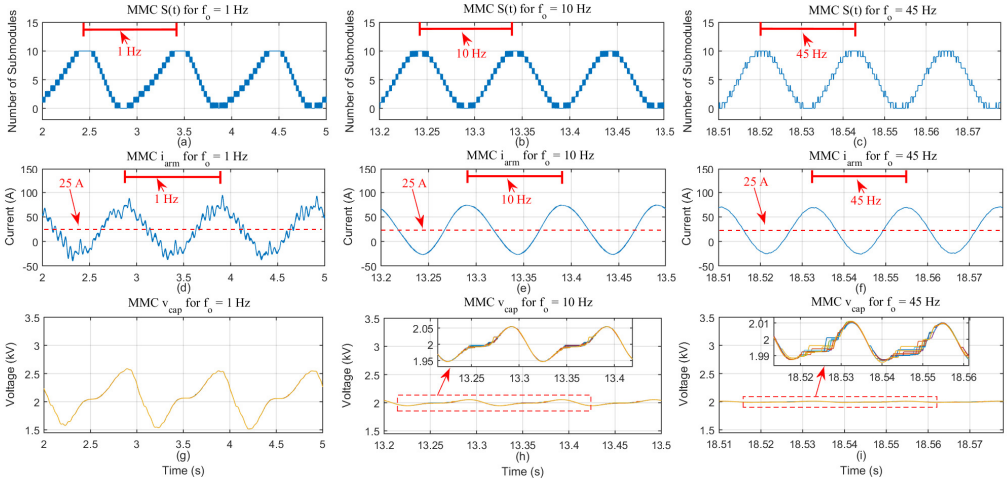

Fig. 26: (a), (b) and (c), simulation results with MMC's insertion index signals ($S(t)$) for the cases where $f_o = 1, 10, 45$ Hz, respectively. (d), (e) and (f), simulation results with MMC's arm currents ($i_{arm}(t)$) for the cases where $f_o = 1, 10, 45$ Hz, respectively. (g), (h) and (i), simulation results with MMC's submodule-capacitor voltages ($v_{cap}(t)$) for the cases where $f_o = 1, 10, 45$ Hz, respectively.

Table 1: MMC's Submodule-Capacitor Voltage ripple.

f_o	Peak-to-Peak Voltage (ΔV)
1 Hz	1 kV
10 Hz	0.1 kV
45 Hz	0.02 kV

By observing the FFT results presented in Fig. 24, it is possible to notice that the MMC's capacitor current, which charges the submodule capacitor producing the voltage ripple, is composed of a f_o-Hz component and of a $2f_o$-Hz component. When flowing through the submodule capacitors, these two current components will produce voltage ripple components with their frequencies according to the value of the capacitor's reactance (calculated through (17)). If for example the f_o = 1-Hz case is considered, then a voltage ripple with an f_o = 1-Hz component and with a $2f_o$ = 2-Hz component will appear in the submodule capacitors. As previously explained, in Fig. 26(g), (h), and (i), the MMC's submodule-capacitor voltages are presented, and by applying an FFT to these signals, it is possible to extract the amplitude of each frequency component present in the voltage signals. The results of the FFT applied to the submodule-capacitor voltage corresponding to the f_o = 1-Hz case (shown in Fig. 26(g)) are the following: the peak value of the 1-Hz component is equal to 392 V while the peak value of the 2-Hz component is equal to 184.5 V. By having these two voltage components, and by

calculating the capacitor's reactance (according to (17)) for each of these components, then the corresponding currents, responsible for producing the ripple, can be calculated. By calculating the current components, the following results were obtained: the peak value of the 1-Hz current component was equal to 12.32 A while the peak value of the 2-Hz current component was equal to 11.6 A. It is quite interesting to observe that the amplitudes of the two current components calculated from the PSCAD simulation results match very accurately with the amplitudes of the current components obtained through the mathematical analysis presented in previous subsection, whose results are shown in Fig. 24(a). By applying the same method, the amplitudes of the current components for the cases where $f_o = 10, 45$ Hz are obtained, and these results are summarized in Table 2. By observing the amplitudes of the two current components for the cases where $f_o = 10, 45$ Hz, it is possible to notice that these results are also precisely matching with the results obtained through the analytical model, whose results are presented in Fig. 24(c) and (e).

Table 2: Two Most Influential Harmonic Components of MMC's Submodule-Capacitor Quantities.

$f_o = 1$ Hz		
Harmonic Component	$f_{h1} = 1$ Hz	$f_{h2} = 2$ Hz
Voltage Peak Value	392 V	184.5 V
Current Peak Value	12.32 A	11.6 A
$f_o = 10$ Hz		
Harmonic Component	$f_{h1} = 10$ Hz	$f_{h2} = 20$ Hz
Voltage Peak Value	38 V	17.8 V
Current Peak Value	11.94 A	11.18 A
$f_o = 45$ Hz		
Harmonic Component	$f_{h1} = 45$ Hz	$f_{h2} = 90$ Hz
Voltage Peak Value	9.6 V	4.2 V
Current Peak Value	13.57 A	11.88 A

Now the exact same procedure that was previously presented for the MMC case, will be presented for the MMSC case. For the proper comparative analysis, the voltage profile synthesized by the MMSC at the load terminals, and the load itself were considered to be equal to the MMC case, in such a way as to obtain the exact same load current flowing through the converters. This current is reproduced in (30) for convenience, and it was obtained by substituting $V_o = 10$ kV, $R = 100\ \Omega$ and $L = 10$ mH into (24).

$$i_{AC}(t) = 100sin(\omega_o t + \theta)\ A \tag{30}$$

Then, according to (25), the MMSC string current is obtained, and it is described with numerical values as follows:

$$i_{string}(t) = i_{AC}(t) = 100sin(\omega_o t + \theta)\ A \tag{31}$$

In the mathematical analysis presented in the previous subsection, the MMSC insertion index was approximated by a continuous signal normalized by the number of submodules in the converter's arms (N). In reality, the MMSC insertion index is a discrete signal that varies from $-N$ to N representing the instantaneous number of inserted FB submodules, and their polarity, in the converter's string. In Fig. 27(a), (b) and (c), the MMSC's insertion index signal is shown for the cases where $f_o = 1, 10, 45$ Hz, respectively. In Fig. 27(d), (e) and (f), the MMSC's string current is shown for the cases where $f_o = 1, 10, 45$ Hz, respectively, and it is interesting to observe that these signals, obtained through PSCAD simulations, are accurately described by (31), which means that the the mathematical model presented in the previous subsection is properly matching with the simulation model analyzed in this subsection. In Fig. 27(g), (h) and (i), the MMSC's submodule-capacitor voltage (v_{cap}) is presented for the cases where $f_o = 1, 10, 45$ Hz, respectively. Since the same MMSC that was analyzed through the mathematical description of the previous subsection was also modelled in the PSCAD simulation, then it should be expected that the same submodule-capacitor voltage ripple observed in the simulation could be calculated through the mathematical model presented in the previous subsection. By measuring the submodule-capacitor voltage ripple in Fig. 27(g), (h) and (i), the peak-to-peak voltage values (ΔV) can be obtained for the cases where $f_o = 1, 10, 45$ Hz, respectively, and these results are reproduced in Table 3.

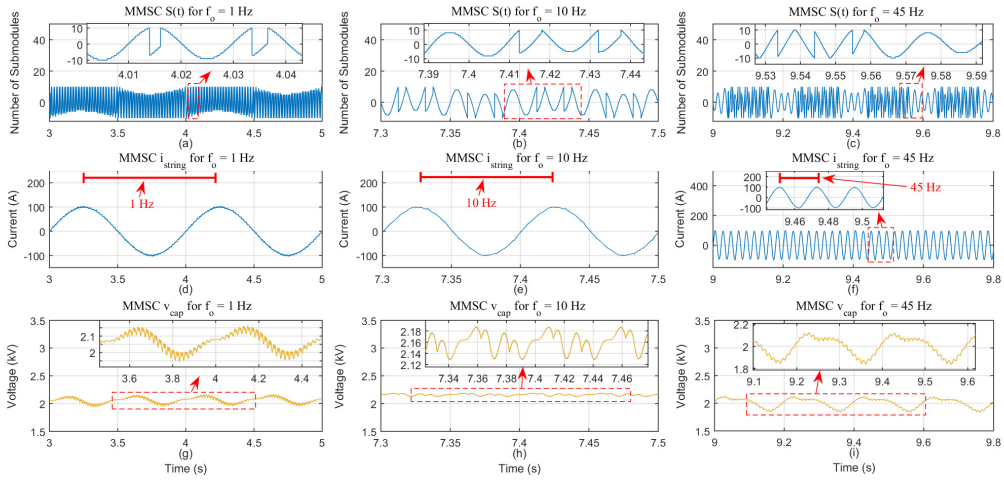

Fig. 27: (a), (b) and (c), simulation results with MMSC's insertion index signals ($S(t)$) for the cases where $f_o = 1, 10, 45$ Hz, respectively. (d), (e) and (f), simulation results with MMSC's string currents ($i_{string}(t)$) for the cases where $f_o = 1, 10, 45$ Hz, respectively. (g), (h) and (i), simulation results with MMSC's submodule-capacitor voltages ($v_{cap}(t)$) for the cases where $f_o = 1, 10, 45$ Hz, respectively.

Table 3: MMSC's Submodule-Capacitor Voltage ripple.

f_o	Peak-to-Peak Voltage (ΔV)
1 Hz	0.2 kV
10 Hz	0.06 kV
45 Hz	0.28 kV

By observing the submodule-capacitor voltage ripple of the MMC and of the MMSC presented in Table 1 and in Table 3, respectively, it can be noticed that the ratio between the highest ripple, in the worst-case scenario considered, for the MMC and for the MMSC is equal to $ratio = \frac{1\text{kV}}{0.28\text{kV}} = 3.57$. The worst-case scenario occurs when $f_o = 1$ Hz, in the MMC case, it occurs when $f_o = 45$ Hz, in the MMSC case. As illustrated in Fig. 24(b), the two most relevant harmonic components present in the MMSC's capacitor current when $f_o = 1$-Hz are the 2-Hz component and the 4-Hz component. As previously explained, in Fig. 27(g), (h), and (i), the MMSC's submodule-capacitor voltages are presented, and by applying an FFT to these signals, it is possible to extract the amplitude of each frequency component present in the voltage signals. The results of the FFT applied to the submodule-capacitor voltage corresponding to the $f_o = 1$-Hz case (shown in Fig. 27(g)) are the following: the peak value of the 2-Hz voltage component was equal to 69.7 V while the peak value of the 4-Hz voltage component was equal to 18.4 V. By having these two voltage components, and by calculating the capacitor's reactance (according to (17)) for each of these components, then the corresponding currents, responsible for producing the ripple, can be calculated. By calculating the current components, the following results were obtained: the peak value of the 2-Hz current component was equal to 4.38 A while the peak value of the 4-Hz current component was equal to 2.31 A. It is quite interesting to observe that the amplitudes of the two current components calculated from the PSCAD simulation results match very accurately with the amplitudes of the current components obtained through the mathematical analysis presented in previous subsection, whose results are shown in Fig. 24(b). By applying the same method, the amplitudes of the current components for the cases where $f_o = 10, 45$ Hz are obtained, and these results are summarized in Table 4. Similarly to the MMC case, by observing the amplitudes of the two current components for the situations where $f_o = 10, 45$ Hz, it is possible to notice that these results are also precisely matching with the results obtained through the analytical model, whose results are presented in Fig. 24(d) and (f).

Table 4: Two Most Influential Harmonic Components of MMSC's Submodule-Capacitor Quantities.

$f_o = 1$ Hz		
Harmonic Component	$f_{h1} = 2$ Hz	$f_{h2} = 4$ Hz
Voltage Peak Value	69.7 V	18.4 V
Current Peak Value	4.38 A	2.31 A
$f_o = 10$ Hz		
Harmonic Component	$f_{h1} = 20$ Hz	$f_{h2} = 40$ Hz
Voltage Peak Value	13 V	13 V
Current Peak Value	8.17 A	16.34 A
$f_o = 45$ Hz		
Harmonic Component	$f_{h1} = 5$ Hz	$f_{h2} = 10$ Hz
Voltage Peak Value	105.5 V	42 V
Current Peak Value	16.57 A	13.19 A

Each component of the submodule-capacitor voltage ripple (V_{cap}^n) can be calculated as follows:

$$V_{cap}^n = I_{cap}^n X_c \tag{32}$$

By substituting (17) into (32), and by rearranging the resulting equation, the following is obtained:

$$C = \frac{I_{cap}^n}{2\pi f V_{cap}^n} \tag{33}$$

The submodule-capacitor voltage ripple with the highest amplitude occurs when $f_o = 1$ Hz in the MMC case. The highest component of the MMC's submodule-capacitor voltage ripple ($V_{MaxMMC} = 392$ V) is caused by the 1-Hz current component as shown in Table 2. The submodule-capacitor voltage ripple with highest amplitude occurs when $f_o = 45$ Hz in the MMSC case. The highest component of the MMSC's submodule-capacitor voltage ripple ($V_{MaxMMSC} = 105.5$ V) is caused by the $f_{MaxMMSC} = 5$-Hz current component with amplitude equal to $I_{MaxMMSC} = 16.57$ A as shown in Table 4. By substituting I_{cap}^n, V_{cap}^n and f, in (33), by $I_{MaxMMSC}$, V_{MaxMMC} and $f_{MaxMMSC}$, respectively, the following capacitance value is obtained:

$$C = 1.35\ mF \tag{34}$$

This result means that if the MMSC were designed with submodule capacitors with a capacitance value equal to 1.35 mF instead of equal to 5 mF, then the highest amplitude of the MMSC's submodule-capacitor voltage ripple (which would occur when $f_o = 45$

Hz) would be equal to the highest amplitude of the MMC's submodule-capacitor voltage ripple (which would occur when $f_o = 1$ Hz), i.e., $V_{MaxMMSC} = V_{MaxMMC} = 392$ V. Another way to explain this is the following: if the capacitance value of the MMSC's submodule capacitors was equal to 1.35 mF, then when the converter operated with $f_o = 45$ Hz, a $f_{MaxMMSC} = 5$-Hz current would flow through its submodule capacitors producing a corresponding 5-Hz voltage ripple with amplitude equal to 392 V. This important conclusion states that if the MMSC and the MMC were used in an application that operated within a low-frequency range (from 1 Hz to 45 Hz in this case), then the MMSC could be designed with submodule capacitors approximately 73% smaller than the MMC's submodule capacitors (reduced from 5 mF to 1.35 mF), and still experience the same voltage ripple in the worst-case scenario. These results further emphasize that the MMSC could be an interesting converter solution to be adopted to drive electrical machines that operate with low frequencies.

2.3.3 Experimental Results

In this subsection, experimental results are presented, which were collected in two different test setups: one representing the MMC (shown in Fig. 28) and the other representing the MMSC (shown in Fig. 29). The MMC test setup is composed of a DC power supply, whose voltage was set to $V_{DC} = 220$ V, that represents the stiff DC link of the converter. The MMC test bench is also composed of six arms, each composed of $N = 4$ HB submodules, and of one arm inductor with inductance equal to $L = 5$ mH. Each HB submodule was built with two insulated-gate bipolar transistor (IGBTs) and with one $C = 2$-mF capacitor. A $R = 100$-Ω three-phase resistive load was connected to the output terminals of the MMC test setup. Since the MMSC is a three-phase converter composed of three independent single-phase structures, then a single-phase test setup was built to perform this experimental analysis. The MMSC prototype was built with one string composed of $N = 8$ FB submodules. Two bidirectional switches were implemented connecting the submodule string to two different phases of the grid. The grid was emulated by an AC power supply with a phase-to-neutral peak voltage value equal to $V_g = 220$ V and with frequency equal to $f_i = 50$ Hz. Each FB submodule was built with four IGBTs and with one $C = 2$-mF capacitor, which is the same value adopted in the MMC prototype. Once again, similarly to the MMC test bench, a $R = 100$-Ω three-phase resistive load was connected to the output terminals of the MMSC test setup. To obtain a three-phase result, three different experimental tests were carried out related to each phase (A, B and C). The exact same voltage profile was synthesized by the two converters at their load terminals, i.e., a voltage with phase-to-neutral peak value equal to $V_o = 100$ V, and with frequency values equal to $f_o = 1, 10, 45$ Hz. The resulting load current presented peak value equal to 1 A, in both test setups, which allowed for a fair comparative analysis between the two topologies.

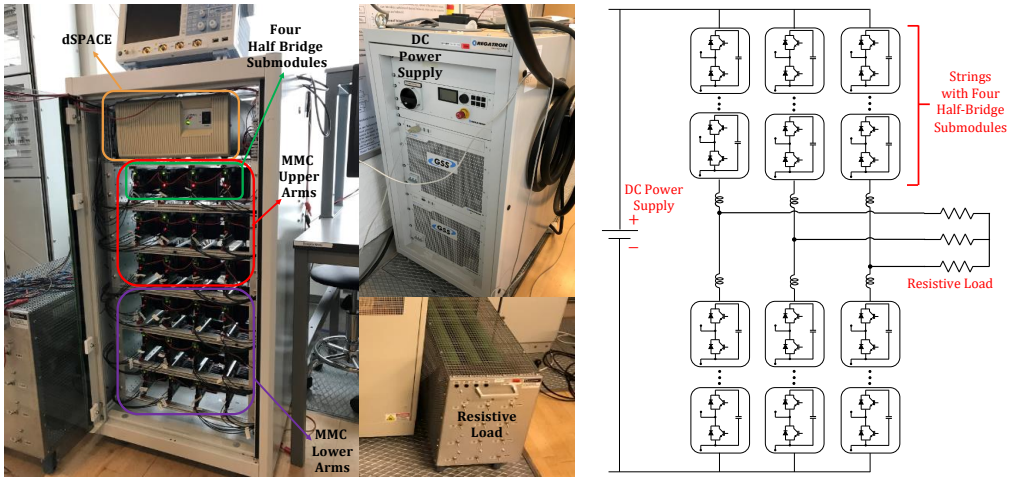

Fig. 28: The left-hand-side image shows a picture of the MMC test setup, and the right-hand-side image shows a diagram with the main components of the test setup.

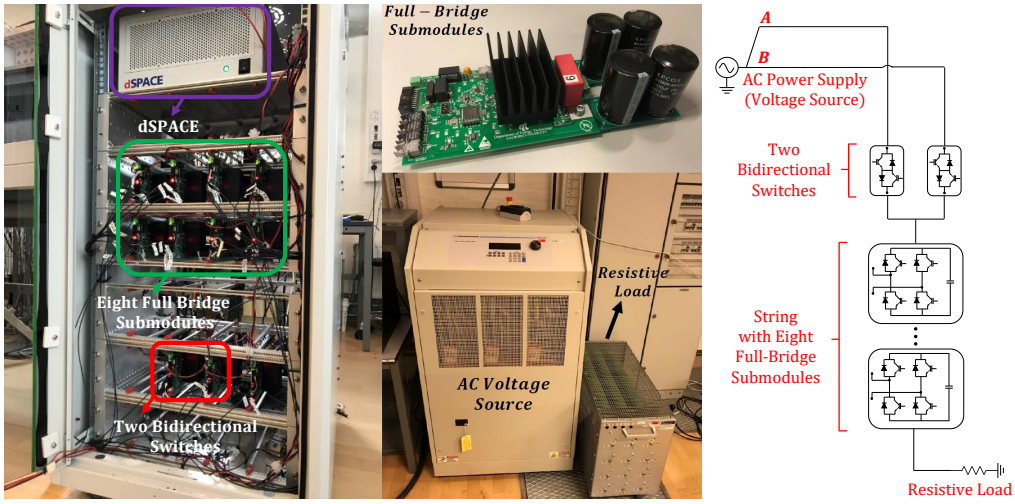

Fig. 29: The left-hand-side image shows a picture of the MMSC test setup, and the right-hand-side image shows a diagram with the main components of the test setup.

In Fig. 30(a), (c) and (e), the MMC load currents (i_{oabc}) are shown for the cases where $f_o = 1, 10$ and 45 Hz, respectively. In Fig. 30(b), (d) and (f), the MMSC load currents are shown for the cases where $f_o = 1, 10$ and 45 Hz, respectively. By observing Fig. 30, it is possible to notice that the load currents of both converters present the same amplitude, which is something that was intentionally imposed to allow for a fair

comparative analysis regarding the submodule-capacitor voltage ripple. Even though purely resistive loads were considered in both test setups, the MMC arm inductors, which are essential for its proper operation, serve as filters and, thus, the MMC's load currents present a higher power quality in comparison to the MMSC's load currents, as demonstrated in Fig. 30. Nonetheless, it is important to highlight that the MMSC's load currents present a quite high power quality even though no filtering was adopted. The power quality of these currents would be further improved if an MMSC with an increased number of submodules (N) was adopted. In Fig. 31(a), (c) and (e), the MMC submodule-capacitor voltages are shown for the cases where $f_o = 1, 10$ and 45 Hz, respectively. In Fig. 31(b), (d) and (f), the MMSC submodule-capacitor voltages are shown for the cases where $f_o = 1, 10$ and 45 Hz, respectively. In Table 5, the peak-to-peak values of the MMC's and of the MMSC's submodule-capacitor-voltage ripple are summarized.

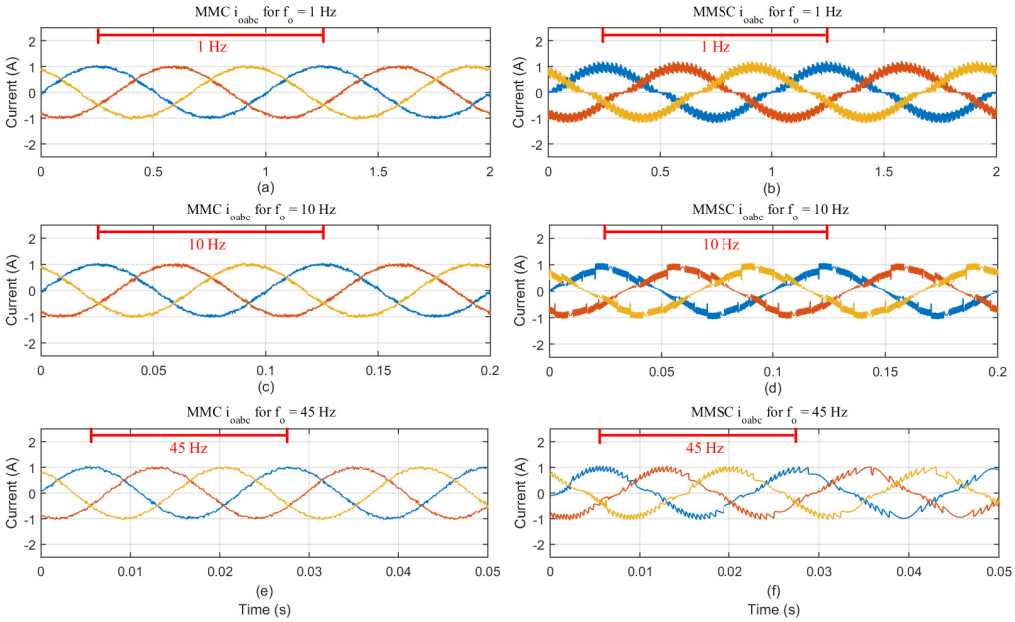

Fig. 30: Experimental results. In (a), (c) and (e) the MMC load currents (i_{oabc}) are presented for the cases where where $f_o = 1, 10$ and 45 Hz, respectively. In (b), (d) and (f) the MMSC load currents (i_{oabc}) are presented for the cases where $f_o = 1, 10$ and 45 Hz, respectively.

Similarly to the simulation subsection, in the experimental analysis it is also considered that the MMC and the MMSC operate within the frequency range of $f_o = 1$ Hz to $f_o = 45$ Hz. Thus, considering the highest submodule-capacitor voltage ripple in the MMC case (that occurs when $f_o = 1$ Hz) and the highest submodule-capacitor voltage

ripple in the MMSC case (that occurs when $f_o = 45$ Hz), then the following ratio is obtained: $ratio = \frac{24\text{V}}{6.2\text{V}} = 3.87$. This ratio is quite similar to the ratio obtained in the simulation subsection that was equal to 3.57. The conclusion is that the experimental results agree with the simulation results, validating the analysis presented in this thesis related to the submodule-capacitor voltage ripple of the MMC and of the MMSC. Similarly to the simulation results, the experimental results also conclude that the MMSC could be designed with capacitors approximately 73% smaller than the MMC capacitors since $(1 - \frac{1}{3.87})100 = 74.16 \approx 73\%$.

Table 5: MMC's and MMSC's Submodule Capacitor Voltage ripple.

f_o	MMC Peak-to-Peak Voltage (ΔV)	MMSC Peak-to-Peak Voltage (ΔV)
1 Hz	24 V	4.6 V
10 Hz	2.6 V	1.3 V
45 Hz	0.8 V	6.2 V

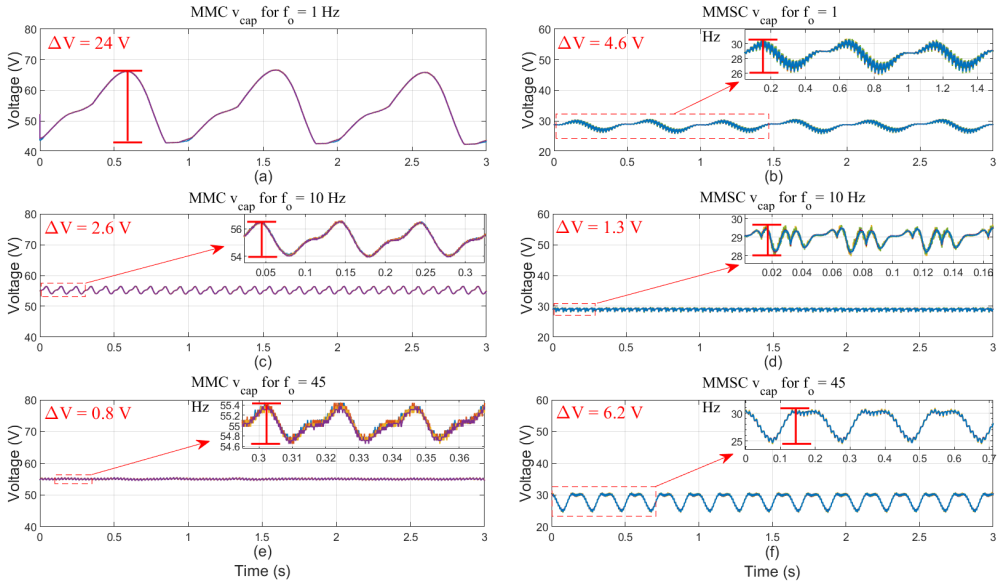

Fig. 31: Experimental results. In (a), (c) and (e) the MMC submodule-capacitor voltage (v_{cap}) is presented for the cases where where $f_o = 1, 10$ and 45 Hz, respectively. In (b), (d) and (f) the MMSC submodule-capacitor voltage (v_{cap}) is presented for the cases where $f_o = 1, 10$ and 45 Hz, respectively.

2.4 Simulation Analyses of Proposed Converter in a PMSM Drive Application

As will be further explained later in this thesis, the 3x3-MMSC can be considered as an improved version of the MMSC since the availability of the third bidirectional-switch stack in each phase allows for an increased operational flexibility and for improved structural features. Thus, from this section on, studies focused on the 3x3-MMSC will be presented.

2.4.1 Operation at Low Frequencies

In this subsection, a simulation analysis based on the software PSCAD/EMTDC is performed to demonstrate that the 3x3-MMSC also presents high performance at low frequencies. To do that, a comparison with the MMC is performed since, as previously explained, the MMC presents a high submodule-capacitor voltage ripple when it operates at low frequencies. To perform a fair comparative analysis, equivalent parameters and operational quantities were adopted for the two converters, i.e., both converters were controlled to synthesize the same load voltage, with phase-to-neutral peak value equal to $V_o = 10$ kV, while supplying power to the same RL load with resistance equal to 100 Ω and inductance equal to 10 mH, resulting in an equal load current. Furthermore, both converters were designed with minimum voltage ratings, i.e., the MMC DC-link voltage was set to $V_{DC} = 1.25(2V_o) = 25$ kV while the 3x3-MMSC input-terminal voltage was set to $V_g = 1.25V_o = 12.5$ kV. As will be explained in this thesis, these are the minimum voltages necessary for the MMC and for the 3x3-MMSC to be capable to synthesize the desired load voltage (V_o), after considering a 25% margin to avoid overmodulation because of the submodule-capacitor voltage ripple. The MMC and the 3x3-MMSC were connected to a $f_i = 60$-Hz grid and the frequency of the synthesized load voltage (f_o) was varied from 0 Hz to 60 Hz in discrete steps of 1 Hz. Finally, both converters were built with the same 5-mF submodule capacitors.

The obtained simulation results are shown in Fig. 32. Similarly to the MMSC (see Fig. 25), the 3x3-MMSC also presents a low submodule-capacitor voltage ripple at low frequencies, and the ripple is increased as the load-side frequency approximates from the grid-side frequency. By observing Fig. 32, one can notice that the 3x3-MMSC's submodule-capacitor voltage ripple is lower than the MMC one for frequency values lower than $f_o = 19$ Hz. Indeed, for extremely low frequency values the 3x3-MMSC's capacitor voltage ripple is expressively lower that the MMC one. The extremely high submodule-capacitor voltage ripple of the MMC close to the 0-Hz operation point could be dangerous, and it could exceed the voltage ratings of the converter's IGBTs. It is also important to notice that, even though the 3x3-MMSC's submodule-capacitor voltage ripple becomes higher than the MMC one after $f_o = 19$ Hz, this ripple remains quite low until approximately $f_o = 50$ Hz. From $f_o = 19$ Hz to $f_o = 50$ Hz the submodule-capacitor voltage ripple of both converter topologies remain low and quite similar to

each other. It means that, in this specific case, the 3x3-MMSC could be built with considerably smaller submodule capacitors in relation to the MMC, if these converters were used to drive a 50-Hz electrical machine operating within a frequency range of $f_o = 0$ Hz to $f_o = 50$. If the 3x3-MMSC is used to drive a 50-Hz electrical machine while connected to a 60-Hz grid, it could be built with small submodule capacitors and still operate safely.

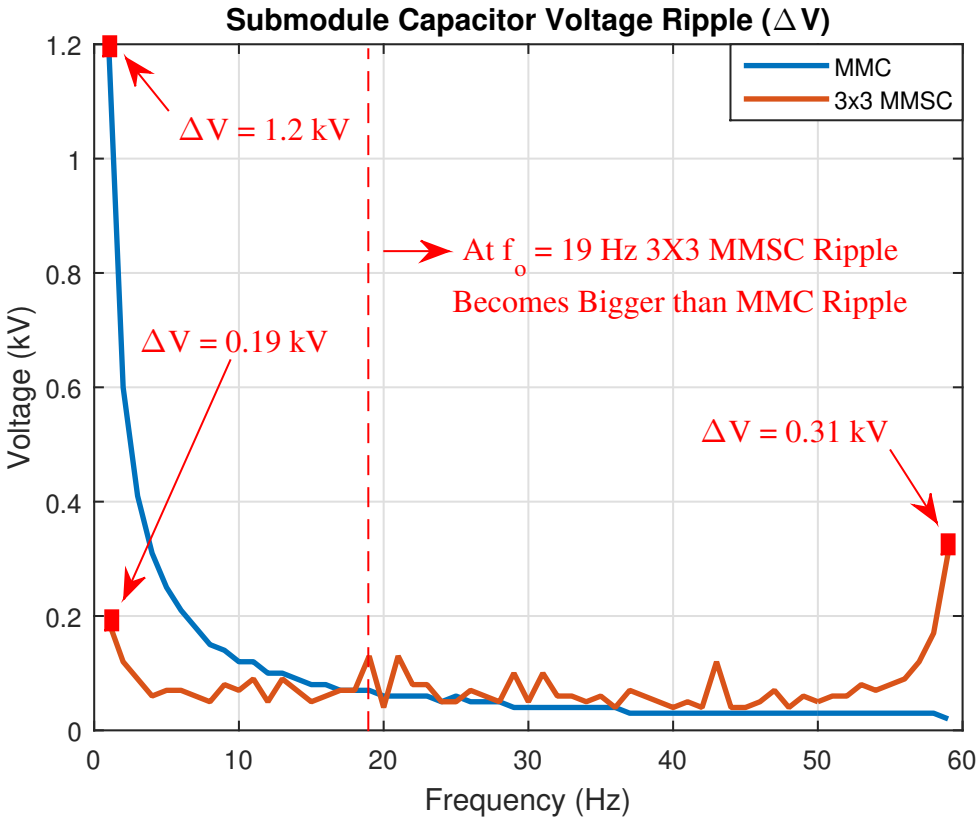

Fig. 32: Simulation results with submodule-capacitor voltage ripple of MMC and 3x3-MMSC for different load frequency values.

2.4.2 Operation in Generator and Motor Modes

From this subsection on, the 3x3-MMSC is used to drive a permanent-magnet synchronous machine (PMSM), which is the application for which this converter topology was proposed. The 3x3-MMSC was designed as follows: it was modeled with $N = 20$ FB submodules per string, plus nine bidirectional-switch stacks and a band-pass filter.

The band-pass filter was designed with the following parameters: $R = 25\ \Omega$, $L = 10.13$ mH and 1 mF. The 3x3-MMSC was modeled with 5-mF submodule capacitors. The converter was connected to a grid with phase-to-neutral peak value equal to $V_g = 20$-kV and with frequency equal to $f_i = 50$ Hz. The PMSM rated power was equal to 3 MVA, its rated voltage equal to 10 kV and its rated frequency equal to 50 Hz. The simulation results related to this subsection are presented in Fig. 33.

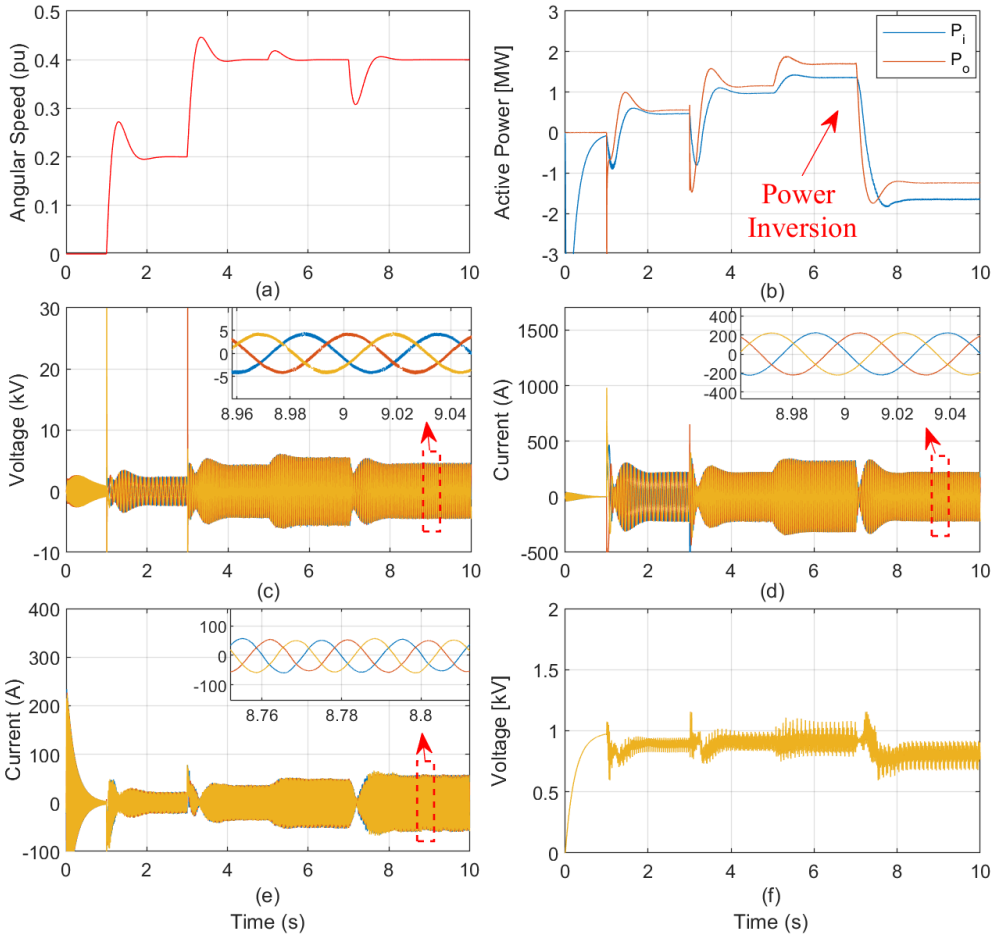

Fig. 33: Simulation results related to 3x3-MMSC driving PMSM. (a) PMSM speed (ω_R), (b) 3x3-MMSC grid-side and load-side active power (P_i and P_o, respectively), (c) load voltage (v_{oabc}), (d) load current (i_{oabc}), (e) 50-Hz current injected into the grid (i_{gfabc}) and (f) phase-A submodule-string capacitor voltages (v_{ca1}, v_{ca2} ... v_{ca20}).

In this simulation, a field-oriented-control (FOC) technique [68] is adopted to control the electrical machine speed, in which the q-axis current component (i_{oq}) is the one used to achieve this goal. The FOC algorithm generates the stator voltage references (v^*_{abc}) that serve as inputs to the 3x3-MMSC internal control illustrated in Fig. 22. the PMSM speed reference is initially adjusted to $\omega^* = 0.2$ pu and the machine torque is adjusted to 1 pu (operating in generator mode). At $t = 3$ s, the PMSM's speed reference changes to $\omega^* = 0.4$ pu. At $t = 5$ s, the machine's torque is changed to 1.2 pu and finally, at $t = 7$ s, the PMSM torque is changed to -1 pu (operating in motor mode) and, thus, an inversion occurs in the active power direction. In Fig. 33(a), the PMSM angular speed is shown, and it is possible to notice that the 3x3-MMSC is capable to properly regulate the machine's speed according to the received reference. In Fig. 33(b), the 3x3-MMSC's grid-side power (P_i) and load-side power (P_o) are presented, where it is possible to observe the operation of the system in both generator mode (injecting power into the grid) and motor mode (absorbing power from the grid). It is important to highlight that an effective but inefficient input filter was adopted in this simulation as considerably high losses can be observed in Fig. 33(b). As previously mentioned, it is essential to explore in future works different filter topologies so that the 3x3-MMSC can become a competitive solution. In Fig. 33(c), the three-phase voltage synthesized by the 3x3-MMSC at the PMSM terminals are shown. It is imoprtant to notice that these are high-power-quality voltages even though no filtering stage was applied to these signals, i.e., these are the switched voltages synthesized at the load terminals. These results demonstrate that the 3x3-MMSC designed with $N = 20$ submodules per string is capable to synthesize such high-power-quality voltages. In Fig. 33(d), the three-phase currents supplied to the PMSM are shown. As a consequence of the high-power-quality synthesized voltage, the resulting currents also present a high power quality. In Fig. 33(e), the currents injected into the grid by the 3x3-MMSC after the filtering stage (i_{gfabc}) are shown. It is important to observe that these are also high-power-quality signals, essentially only composed of the 50-Hz component, since the other components were properly filtered out by the band-pass filter. Once again, the adopted filter is effective in performing its filtering functionality, even though it is inefficient. Finally, in Fig. 33(f), the phase-A submodule-capacitor voltages are presented. As previously explained, in this thesis, no regulation was applied to the submodule-capacitor voltages since they are self regulated, according to Kirchhoff's law and conservation of energy, due to the series connection of the submodule string between the grid and the load. It is interesting to notice that when the power variations are applied to the PMSM, then the grid-side power (P_i) naturally tracks these variations so that the submodule capacitors are not charged/discharged, to preserve Kirchhoff's law. Thus, as shown in Fig. 33(f), the submodule-capacitor voltages are kept regulated with a value equal to approximately $\frac{V_g}{N} = \frac{20\text{kV}}{20} = 1$ kV.

2.4.3 Reactive Power Control

In this subsection, a discussion is carried on how to control the grid-side reactive power of the proposed 3x3-MMSC. As illustrated in Fig. 20(a), the current injected into the grid by the 3x3-MMSC (i_{gabc}) is a switched current whose instantaneous value can be equal to the phase-A load current (i_{oa}), to the phase-B load current (i_{ob}), to the phase-C load current (i_{oc}), equal to a combination of these currents or equal to zero. In other words, i_{gabc} is a function of the load current (i_{oabc}) and of the switching pattern of the bidirectional-switch stacks. The grid-side reactive power of the 3x3-MMSC is a function of the phase shift between the grid voltage (v_{gabc}) and the filtered 50-Hz current injected into the grid by the converter (i_{gfabc}). As will be shown, one way to control the 3x3-MMSC grid-side reactive power is by controlling the d-axis component of the PMSM current (i_{od}). By controlling this current component, it is possible to modify the relation between the load current profile and the switching of the bidirectional-switch stacks in such a way as to modify the phase shift of the 50-Hz current injected into the grid by the 3x3-MMSC (i_{gfabc}). By varying the phase of the 50-Hz current, the grid-side reactive power would vary as well. In Fig. 34, simulation results are presented to demonstrate the control of the grid-side reactive power of the 3x3-MMSC, using the approach above explained. Nonetheless, another way to regulate the grid-side reactive power would be to control the switching pattern of the bidirectional-switch stacks similarly to how it is done in the well-established DMC. This method should be investigated in future works, even though it is important to highlight that an increase in the switching frequency of the bidirectional-switch stacks might be required, which would reduce the reliability of the converter solution that is built with stacks of a few series-connected semiconductor devices. In the simulation presented in this subsection, the reference of the PMSM angular speed (ω^*) remains fixed with a value equal to 0.4 pu throughout the entire simulation. Once again, this quantity is regulated through the control of the q-axis current component (i_{oq}). The reference of the d-axis current component (i_d^*), however, is continuously modified so that variations in the grid-side reactive power can be observed.

In Fig. 34(a), the angular speed of the PMSM is shown, and it is possible to notice that this quantity remains constant and regulated, in steady state, according to its reference. In Fig. 34(b), the PMSM d-axis current is shown along with its reference. As previously mentioned, this component was varied to observe the variation in the grid-side reactive power of the 3x3-MMSC. In Fig. 34(c), the 3x3-MMSC active power is shown, and it is important to notice that it remains constant, in steady state, despite the various variation of i_{od}. This is because both the PMSM torque and speed were kept constant throughout this simulation. In Fig. 34(d), the 3x3-MMSC grid-side reactive power is shown and it can be observed that it varies according to the variation of i_{od} (see Fig. 34(b)). In Fig. 34(e), the 3x3-MMSC phase-A submodule-capacitor voltages are shown. It is interesting to notice that neither the average value nor the ripple of the capacitor voltages are affected by the variations of i_{od}, and consequently the

variation of the grid-side reactive power. Finally, Fig. 34(f), the phase-A grid voltage is shown along with the upscaled filtered current injected into phase A of the grid by the 3x3-MMSC. These quantities are shown during the period where the grid-side reactive power is controlled to be null, which means that an unit power factor is obtained at the converter's terminals.

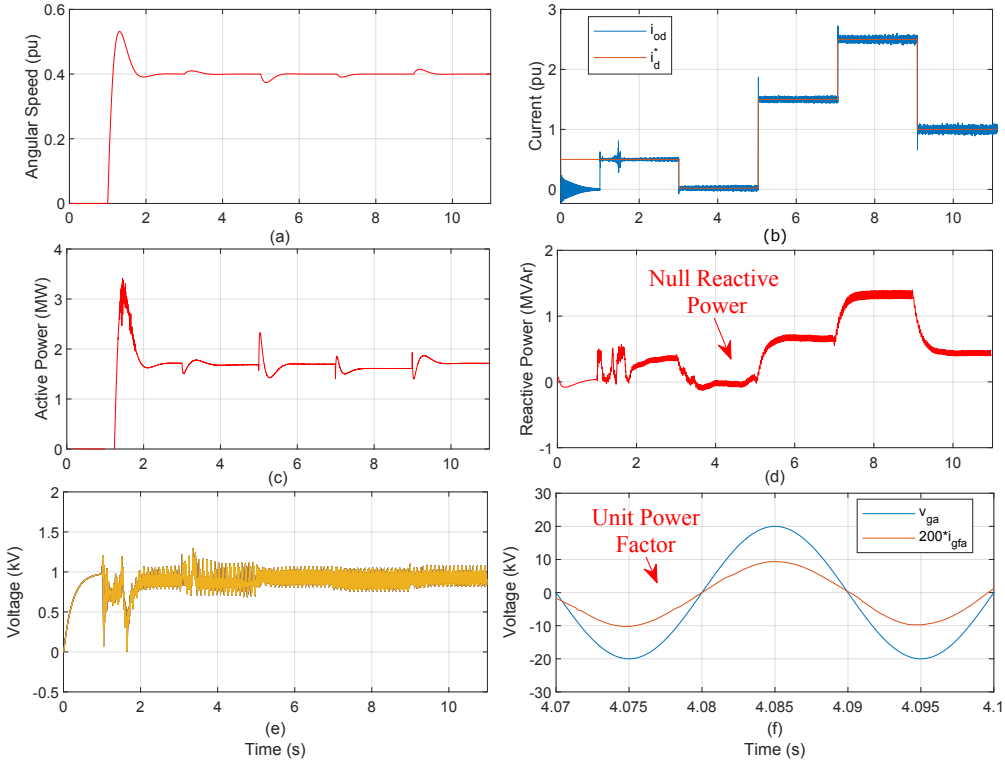

Fig. 34: Simulation results related to reactive power control. (a) PMSM speed (ω_R), (b) PMSM d-axis current (i_{od}) and its reference (i_d^*), (c) PMSM active power (P_o), (d) 3x3-MMSC grid-side reactive power (Q_i), (e) phase-A submodule-capacitor voltages (v_{ca1}, v_{ca2} ... v_{ca20}), and (f) phase-A grid voltage (v_{ga}) along with upscaled filtered current ($200i_{gfa}$).

2.4.4 Operation Under Unbalanced Grid Conditions

This subsection discusses the 3x3-MMSC behavior when operating connected to an unbalanced grid. In the simulation of this section, at $t = 3$ s, a 50% voltage sag is imposed to phase A of the grid and it is cleared at $t = 5$ s. In Fig. 35(a), the three-phase grid voltages are shown and the 50% voltage sag can be observed in phase A of the grid. In Fig. 35(b), (d) and (f), the phase-A-string, phase-B-string and phase-C-string

submodule-capacitor voltages of the 3x3-MMSC are shown, respectively.

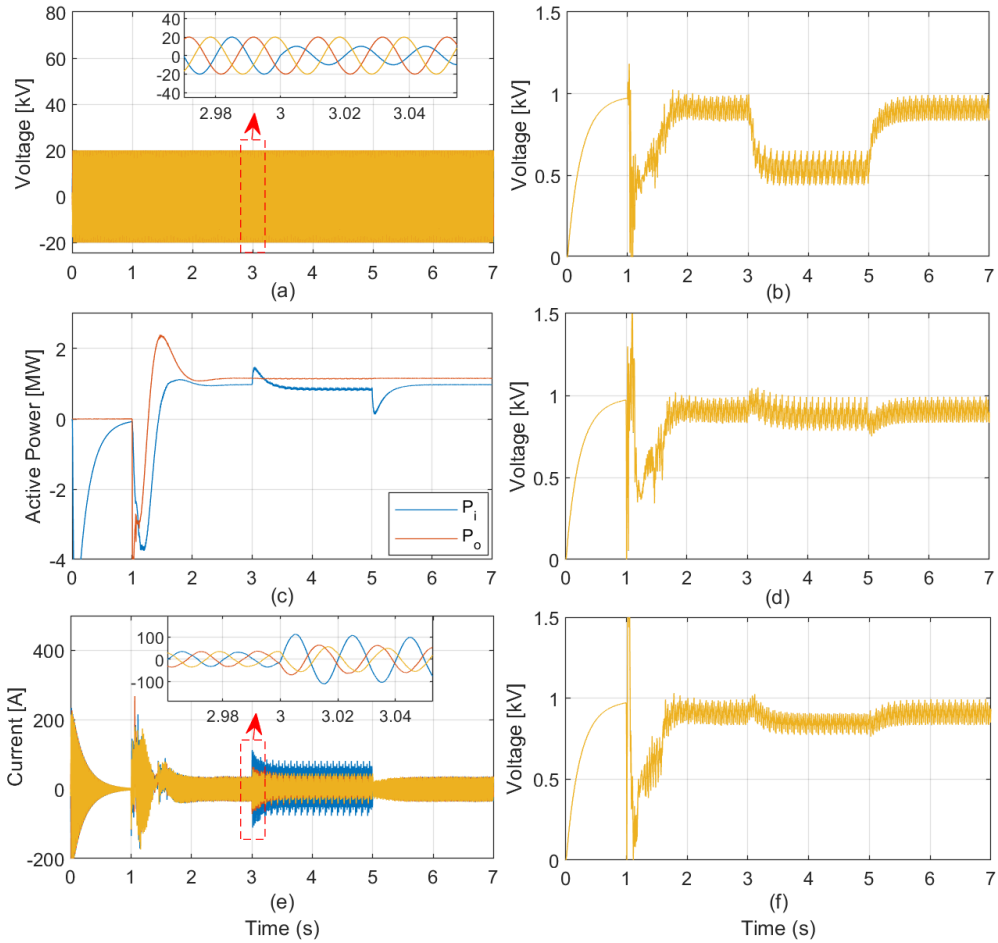

Fig. 35: Simulation results related to unbalanced grid conditions. (a) Grid voltages (v_{gabc}), (b) phase-A submodule-string capacitor voltages (v_{ca1}, v_{ca2} ... v_{ca20}), (c) 3x3-MMSC grid-side and load-side active power (P_i and P_o, respectively), (d) phase-B submodule-string capacitor voltages (v_{cb1}, v_{cb2} ... v_{cb20}), (e) 3x3-MMSC grid-side current (i_{gfabc}) and (f) phase-C submodule-string capacitor voltages (v_{cc1}, v_{cc2} ... v_{cc20}).

It is interesting to observe that the voltage sag in the phase A of the grid produces a corresponding sag in the average value of the phase-A-string submodule-capacitor voltages. It is important to notice, however, that the voltages of the phase-B-string and phase-C-string are barely affected by the voltage sag in phase A of the grid. Essentially, the phase-A submodule-capacitor voltages are naturally regulated with a value equal to

approximately $\frac{V_{ga}}{N}$, the phase-B submodule-capacitor voltages are naturally regulated with a value equal to approximately $\frac{V_{gb}}{N}$, and the phase-C submodule-capacitor voltages are naturally regulated with a value equal to approximately $\frac{V_{gc}}{N}$. More importantly, it is very important to notice that the submodule-capacitor voltages of the three phases remain stable and with a low ripple even under such extreme unbalanced conditions. This is an important advantage in comparison to the MMC but, especially, in comparison to the M^3C that presents unstable behavior under unbalanced grid conditions. Since the 3x3-MMSC behaves as a current source from the grid perspective, then the currents that flow through its submodule strings are not affected by the power quality of the grid voltage. In Fig. 35(c), the grid-side and machine-side power of the 3x3-MMSC are shown, and it is interesting to observe that the converter is capable to continue to operate normally, supplying power to the grid, even during the severe unbalanced conditions. In Fig. 35(e), the filtered currents injected into the grid by the 3x3-MMSC (i_{fgabc}) are shown. These currents become unbalanced when the grid voltage is unbalanced, which is an inherent characteristic of direct converters such as the well known DMC. It is important to highlight that unbalanced currents is not an issue considered in grid codes.

2.5 Comparative Analysis in Terms of Component Count and Power Ratings

In this section, a comparative analysis between the MMC, the M^3C, the MMSC and the 3x3-MMSC in terms of component count and component power ratings is performed. Before starting the comparative analysis, an explanation will be provided regarding the advantages of having the third bidirectional-switch stack in each phase of the 3x3-MMSC in comparison to the MMSC in terms of the total component count of the two solutions. In other words, as well be explained, the addition of the third bidirectional-switch stack to each phase of the 3x3-MMSC allows it to synthesize the same voltage at the load side as the MMSC while having an input voltage with half the amplitude of the MMSC's input voltage. This way, the 3x3-MMSC can be built with a considerably reduced number of components in comparison to the MMSC. As previously explained, considering the phase-A of the MMSC, and considering that the phase-A submodule string is connected to phase A of the grid (bidirectional-switch stack that connects phase-A string to phase A of the grid is in *ON* state and bidirectional-switch stack that connects phase-A string to phase B of the grid is in *OFF* state), then the MMSC operates synthesizing a series voltage equal to v_{sa}, depending on the instantaneous value of the grid voltage (v_{ga}) in order to obtain the desired voltage at the load's terminal according to a given reference v_a^*. In other words, because of the series connection of the submodule string between the grid and the load, according to Kirchhoff's law, the following equation can be used to calculate the instantaneous voltage to be synthesized in series by the converter.

$$v_{sa} = v_a^* - v_{ga} = V_o sin(\omega_o t) - V_g sin(\omega_i t) \tag{35}$$

As previously explained, the average value of the MMSC submodule-capacitor voltages is naturally regulated to $\frac{V_g}{N}$, in steady state, where V_g is the peak value of the phase-to-neutral grid voltage. So, if all the N available submodules in the string are simultaneously inserted, then a voltage equal to V_g is obtained across the submodule-string terminals if the capacitor voltage ripple is neglected. Since the grid frequency (ω_i) is fixed and the load voltage frequency (ω_o) is continuously varying then, according to (35), there will be moments where the instantaneous value of the voltage that must be synthesized in series will be higher than V_g, which is the maximum voltage possible to be synthesized by the string, i.e., ($|v_{sa}| > V_g$). In these situations, the MMSC would lose control over the load voltage. To always keep control over the load voltage, the MMSC phase-A submodule string must be connected to phase B of the grid every time $|v_{sa}| > V_g$. By connecting the phase-A submodule string to phase B of the grid, the voltage to be synthesized in series becomes equal to the one described in (36), which is lower than V_g ($|v_{sa}| < V_g$) if a proper amplitude is designed for the voltage at the input terminals of the converter (V_g).

$$v_{sa} = v_a^* - v_{gb} = V_o sin(\omega_o t) - V_g sin(\omega_i t - \frac{2\pi}{3}) \tag{36}$$

After presenting the above equations, an explanation of how to design the amplitude of the voltage connected at the input terminals of the MMSC can be presented through an illustrative example. In this example, a grid voltage with amplitude equal to $V_g = 20$ kV and frequency equal to $f_i = 50$ Hz is imposed to the MMSC input terminals, and a load-voltage reference (v_a^*) with amplitude equal to $V_o = 10$ kV and frequency equal to $f_o = 10$ Hz is provided to the converter. In Fig. 36(a), the phases A and B of the grid voltage (v_{ga} and v_{gb}, respectively) are shown along with the voltage reference to be synthesized at the phase-A terminal of the MMSC load (v_a^*). The situation shown in Fig. 36(a) illustrates the worst-case scenario of the MMSC operation, which defines the minimum amplitude possible of the voltage at its input terminals so that it can always properly track the desired voltage reference. The situation shown in Fig. 36(a) corresponds to a moment where the voltage reference is at its peak value and the phase-A and phase-B grid voltages have the same amplitude and opposite polarity in relation to the voltage reference. According to this example, at the mentioned moment, the instantaneous value of the voltage reference is equal to $V_o = 10$ kV and the instantaneous value of the phase-A and phase-B grid voltages is equal to $v_{ga} = v_{gb} = -\frac{V_g}{2} = -\frac{20}{2} = -10$ kV. In this situation, the voltage that must be synthesized in series across the submodule string is equal to $|v_{sa}| = |V_o - (-\frac{V_g}{2})| = 20$ kV, no matter if the submodule string is connected to phase A or phase B of the grid. Since in this example the MMSC input-terminal voltage was designed with an amplitude of $V_g = 20$ kV, then the converter is ideally capable to keep control over the load voltage even in the worst-case scenario

since the instantaneous value of v_{sa} in the worst-case scenario is equal to the maximum value that the converter can synthesize in series ($V_{smax} = V_g = 20$ kV).

Let us now consider another illustrative example as demonstrated in Fig. 36(b). In this example, the same load voltage reference as in the previous example is considered (with amplitude equal to $V_o = 10$ kV and frequency equal to $f_o = 10$ Hz), but a grid voltage with amplitude equal to $V_g = 10$ kV and frequency equal to $f_i = 50$ Hz is now imposed to the MMSC input terminals. The same situation considered in the previous example is also considered in this example. In this case, at the considered moment, the instantaneous value of the voltage reference is equal to $V_o = 10$ kV and the instantaneous value of the phase-A and phase-B grid voltages is equal to $v_{ga} = v_{gb} = -\frac{V_g}{2} = -\frac{10}{2} = -5$ kV. Thus, voltage that must be synthesized in series across the submodule string is equal to $|v_{sa}| = |V_o - (-\frac{V_g}{2})| = 15$ kV, no matter if the submodule string is connected to phase A or phase B of the grid. This voltage is higher than the maximum voltage that the converter is capable to synthesize across its submodule string ($V_{smax} = V_g = 10$ kV), which means that the MMSC cannot keep control over the load voltage. These two illustrative examples explain the criteria for defining the amplitude of the voltage connected to the input terminals of the MMSC, which can be described as follows:

$$V_{smax} = V_g \geq V_o + \frac{V_g}{2} \tag{37}$$

And thus:

$$V_g \geq 2V_o \tag{38}$$

The criteria for designing the MMSC input-terminal voltage is presented in (38), which states that the voltage imposed to the MMSC input terminals should be equal or greater than two times the amplitude of the load-voltage reference. Let us now consider the situation where the third phase of the grid (phase C) is also available in the second illustrative example in a way that the illustrative example shown in Fig. 36(c) is obtained. By analyzing Fig. 36(c), it is possible to notice that if the phase-A submodule string can only be connected to phases A and B of the grid, then the MMSC would lose control over the load voltage. However, if the connection to phase C of the grid is also possible, then the converter is able to keep tracking the load-voltage reference since, at the moment considered in Fig. 36(c), the voltage to be synthesized in series if the phase-A submodule string is connected to phase C of the grid is equal to $|v_{sa}| = |v_a^* - v_{gc}| = |V_o - V_g| = 10 - 10 = 0$ kV, which is obviously less than $V_{smax} = V_g = 10$ kV. The availability of the phase C of the grid, as illustrated in Fig. 36(c), can easily be achieved by connecting a third bidirectional-switch stack between the phase-A submodule string and phase C of the grid, in such a way that the MMSC turns into the 3x3-MMSC. According to the explanation provided about Fig. 36(c), the criteria for designing the 3x3-MMSC's input-terminal voltage is the one described in (39).

$$V_g \geq V_o \tag{39}$$

For the 3x3-MMSC to be capable to properly synthesize a load voltage with amplitude equal to V_o, the amplitude of the voltage imposed to its input terminals must be equal or greater than V_o. By comparing, (38) and (39), it is clear that the 3x3-MMSC is capable to synthesize a load voltage with the same amplitude of the load voltage synthesized by the MMSC (amplitude equal to V_o) while having a voltage imposed to its input terminals with half the amplitude of the voltage required to be imposed to the MMSC's input terminals. This characteristic is extremely important since the 3x3-MMSC can be built with a considerably reduced number of components in relation to the MMSC, as will be presented in the comparative analysis of this section.

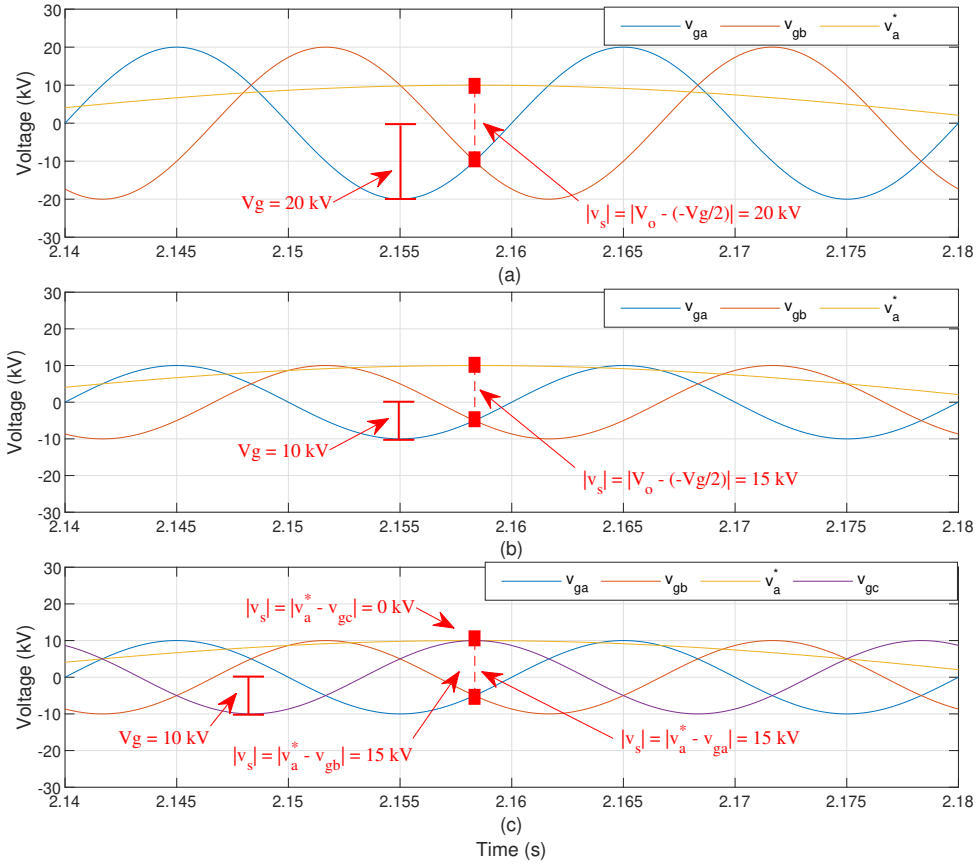

Fig. 36: Illustrative examples explaining the design criteria for the MMSC and the 3x3-MMSC input-terminal voltages. (a), (b) show the phase-A voltage reference (v_a^*), along with phases A and B of the grid voltage (v_{ga} and v_{gb}). (c) show the phase-A voltage reference (v_a^*), along with phases A, B and C of the grid voltage (v_{ga}, v_{gb}, and v_{gc}).

To perform a fair comparative analysis between the MMC, the M^{3}C, the MMSC and the 3x3-MMSC, some assumptions were made. First, it was considered that all the converter topologies had to synthesize a voltage at both their terminals with peak phase-to-neutral value equal to V_{peak}. It was also considered that the four converters had to supply power to the same load, resulting in a load current with the same rms value equal to I_{RMS}. The last assumption was to consider that all the converters had to operate with the same power profile at their grid-side and load-side terminals (purely active power or unit power factor) in a way that the currents injected into the grid by the converters had the same rms value as the load current, i.e., $I_g = I_l = I_{RMS}$. Finally, to perform the comparative analysis regarding submodule and capacitor component count, a fixed rated voltage equal to V_{IGBT} was considered for the IGBTs of the four converter topologies under analysis.

2.5.1 MMC

According to [6], the MMC's DC-link voltage (V_{DC}) should ideally be designed as described in (40) so that the converter is capable to synthesize an AC voltage with amplitude equal to V_{peak}.

$$V_{DC} \geq 2V_{peak} \tag{40}$$

As a consequence of the MMC operation, the full DC-link voltage (V_{DC}) is naturally distributed between the N submodule capacitors that compose one converter arm. Since a sorting algorithm is always adopted to maintain all the submodule capacitors within one arm with similar voltage values, then it is a fair assumption to consider that the nominal operational voltage of each submodule capacitor is equal to $V_{cap} = \frac{V_{DC}}{N}$. The string submodules (and their IGBTs) must be capable to withstand ideally at least the nominal operational voltage of their capacitors. In other words:

$$V_{sub} \geq V_{cap} = \frac{V_{DC}}{N} \tag{41}$$

Where V_{sub} is the maximum voltage tolerated by the submodule's IGBTs. The current that flows through an MMC arm can be described as follows:

$$I_{arm} = \frac{I_{RMS}}{2} + \frac{I_{DC}}{3} + I_{circ} \tag{42}$$

Where I_{DC} is the current flowing through the MMC's DC terminal and I_{circ} corresponds to the AC components of the MMC circulating currents. By considering the approximation that the MMC AC-terminal power is equal to its DC-terminal power, then the following is obtained:

$$V_{DC}I_{DC} = \sqrt{3}(\frac{\sqrt{3}V_{peak}}{\sqrt{2}})I_{RMS} \tag{43}$$

By rearranging (43), the MMC DC current can be calculated as a function of V_{peak}, V_{DC} and I_{RMS} as follows:

$$I_{DC} = \frac{3}{\sqrt{2}}\frac{V_{peak}I_{RMS}}{V_{DC}} \tag{44}$$

For this comparative analysis, the minimum DC-link voltage value that is ideally possible is adopted according to (40), i.e., $V_{DC} = 2V_{peak}$. Thus, (44) can be rewritten as follows:

$$I_{DC} = 1.06I_{RMS} \tag{45}$$

By substituting (45) into (42), and by disregarding the component I_{circ} (considering that the undesired AC components of the circulating currents were properly suppressed), then the MMC arm current can be described as a function of the AC current only, as presented in (46).

$$I_{arm} = 0.85I_{RMS} \tag{46}$$

As previously mentioned, the MMC is built with HB submodules, which are composed of two IGBTs and of one capacitor. The submodule IGBTs must be capable to block the voltage V_{sub}, defined according to (41), and must be capable to conduct the arm current (I_{arm}), defined according to (46). Considering the ideal case where $V_{sub} = V_{cap} = \frac{V_{DC}}{N} = \frac{2V_{peak}}{N}$ (which means to consider that the maximum voltage tolerated by the IGBT is equal to its nominal operational voltage), then the power ratings of the MMC's IGBTs can be described as follows:

$$P_{IGBT} = V_{sub}I_{arm} = 1.7\frac{V_{peak}I_{RMS}}{N} \tag{47}$$

The back-to-back MMC is composed of twelve arms (see Fig. 1), each arm is composed of N HB submodules and each HB submodule is composed of two IGBTs. Thus, the total number of IGBTs in the MMC is equal to $N_{IGBT} = 12 \times N \times 2 = 24N$. The total MMC semiconductor-device power ratings can be calculated as follows:

$$P_{SD} = P_{IGBT}N_{IGBT} = 40.8V_{peak}I_{RMS} \tag{48}$$

Now keeping the IGBT's rated voltage fixed with the previously defined value of V_{IGBT}, and remembering that the sum of the voltages of all the capacitors within one MMC arm is equal to $V_{DC} = 2V_{peak}$, then the number of HB submodules composing each arm of the converter is equal to:

$$N = \frac{V_{DC}}{V_{IGBT}} = \frac{2V_{peak}}{V_{IGBT}} \tag{49}$$

Once again, the back-to-back MMC is composed of twelve arms, each arm is composed of N HB submodules and each HB submodule is composed of one capacitor. Thus, the total number of submodules and of capacitors in the MMC is equal to $N_{sub} = N_{cap} = 12 \times \frac{2V_{peak}}{V_{IGBT}} \times 1 = \frac{24V_{peak}}{V_{IGBT}}$. It is also important to emphasize that the back-to-back MMC requires twelve arm inductors for its proper operation.

2.5.2 M^{3}C

According to [10], the M^{3}C's string voltage (V_{string}) should ideally be designed as described in (50) so that the converter is capable to synthesize an AC voltage with amplitude equal to V_{peak}.

$$V_{string} \geq V_g + V_l + V_{com} \tag{50}$$

Where $V_g = V_l = V_{peak}$ in this case, and where V_{com} is a common-mode voltage component that might be necessary in some situations for the proper operation of the converter. Neglecting this component, the equation with the design criteria of the M^{3}C's string voltage is obtained as follows:

$$V_{string} \geq V_g + V_l = 2V_{peak} \tag{51}$$

The string voltage is divided between the N submodule capacitors that compose one converter string. Similarly to the MMC case, a sorting algorithm is used to maintain all the submodule capacitors within one string with similar voltage values. Thus, it is a fair assumption to consider that the nominal operational voltage of each submodule capacitor is equal to $V_{cap} = \frac{V_{string}}{N}$. The string submodules (and their IGBTs) must be capable to withstand at least the nominal operational voltage of their capacitors. In other words:

$$V_{sub} \geq V_{cap} = \frac{V_{string}}{N} \tag{52}$$

Where V_{sub} is the maximum voltage tolerated by the submodule's IGBTs. Similarly to the MMC case, the ideal situation is also considered for the M^{3}C, i.e., $V_{string} = 2V_{peak}$, and $V_{sub} = V_{cap} = \frac{V_{string}}{N} = \frac{2V_{peak}}{N}$. The current that flows through an M^{3}C string can be described as follows:

$$I_{string} = \frac{I_g}{3} + \frac{I_l}{3} + I_{circ} \tag{53}$$

Where I_g and I_l are the grid-side and load-side currents of the M^{3}C, respectively,

and I_{circ} represents the circulating currents that might be necessary for the proper and stable operation of the converter in some specific situations. By disregarding I_{circ} and by considering $I_g = I_l = I_{RMS}$, then the M^{3}C string current can be described as a function of the AC current only, as presented in (54).

$$I_{string} = \frac{I_{RMS}}{3} + \frac{I_{RMS}}{3} = 0.67 I_{RMS} \tag{54}$$

The M^{3}C is built with FB submodules, which are composed of four IGBTs and of one capacitor. The submodule IGBTs must be capable to block the voltage V_{sub}, defined according to (52), and must be capable to conduct the string current (I_{string}), defined according to (54). Once again, considering the ideal case where $V_{sub} = V_{cap} = \frac{V_{string}}{N} = \frac{2V_{peak}}{N}$, then the power ratings of the M^{3}C's IGBTs can be described as follows:

$$P_{IGBT} = V_{sub} I_{string} = 1.34 \frac{V_{peak} I_{RMS}}{N} \tag{55}$$

The M^{3}C is composed of nine strings (see Fig. 2), each string is composed of N FB submodules and each FB submodule is composed of four IGBTs. Thus, the total number of IGBTs in the M^{3}C is equal to $N_{IGBT} = 9 \times N \times 4 = 36N$. The total M^{3}C semiconductor-device power ratings can be calculated as follows:

$$P_{SD} = P_{IGBT} N_{IGBT} = 48.24 V_{peak} I_{RMS} \tag{56}$$

Now keeping the IGBT's rated voltage fixed with the previously defined value of V_{IGBT}, and remembering that M^{3}C string voltage is equal to $V_{string} = 2V_{peak}$, then the number of FB submodules composing each string of the converter is equal to:

$$N = \frac{V_{string}}{V_{IGBT}} = \frac{2V_{peak}}{V_{IGBT}} \tag{57}$$

Once again, the M^{3}C is composed of nine strings, each string is composed of N FB submodules and each FB submodule is composed of one capacitor. Thus, the total number of submodules and of capacitors in the M^{3}C is equal to $N_{sub} = N_{cap} = 9 \times \frac{2V_{peak}}{V_{IGBT}} \times 1 = \frac{18V_{peak}}{V_{IGBT}}$. It is also important to emphasize that the M^{3}C requires nine string inductors for its proper operation.

2.5.3 MMSC

As previously explained in (38), the MMSC's input-terminal voltage should be designed with a value equal to the one described in (58), so that the converter is capable to synthesize an AC voltage with amplitude equal to V_{peak} at its load terminals.

$$V_g \geq 2V_{peak} \tag{58}$$

As a natural consequence of the MMSC topology and operation, the grid voltage (V_g) is distributed between the N capacitors of the MMSC submodule string. Similarly to the previous two topologies, a sorting algorithm is always adopted to maintain all the submodule capacitors within one string with similar voltage values, then it is a fair assumption to consider that the nominal operational voltage of each submodule capacitor is equal to $V_{cap} = \frac{V_g}{N}$. The string submodules (and their IGBTs) must be capable to withstand at least the nominal operational voltage of their capacitors. In other words:

$$V_{sub} \geq V_{cap} = \frac{V_g}{N} \tag{59}$$

Where V_{sub} is the maximum voltage tolerated by the submodule's IGBTs. Similarly to the MMC and the M^{3}C cases, the ideal situation is also considered for the MMSC, i.e., $V_g = 2V_{peak}$, and $V_{sub} = V_{cap} = \frac{V_g}{N} = \frac{2V_{peak}}{N}$.

Not only the MMSC submodule strings, but its bidirectional-switch stacks must also be considered in the analysis. These bidirectional-switch stacks are connected between two phases of the grid, which means that they must be capable to tolerate the peak value of the line-to-line grid voltage, when operating in blocking mode, i.e.:

$$V_{BS} \geq \sqrt{3}V_g \tag{60}$$

Where V_{BS} is the maximum voltage tolerated by the bidirectional-switch stack. Since the ideal case where $V_g = 2V_{peak}$ is considered, then (60) can be rewritten as:

$$V_{BS} \geq 2\sqrt{3}V_{peak} \tag{61}$$

The ideal case is also considered for these stacks, i.e., $V_{BS} = 2\sqrt{3}V_{peak}$, which means that the maximum voltage tolerated by the stack is designed to be equal to its nominal operational voltage when in blocking mode. The current that flows through each submodule string and through each bidirectional-switch stack of the MMSC is equal to:

$$I_{string} = I_{BS} = I_l = I_{RMS} \tag{62}$$

The MMSC submodule string is built with FB submodules, which are composed of four IGBTs and of one capacitor. The submodule IGBTs must be capable to block the voltage V_{sub}, defined according to (59), and must be capable to conduct the string current (I_{string}), defined according to (62). Once again, considering the ideal case where $V_{sub} = \frac{2V_{peak}}{N}$, then the power ratings of the IGBTs of the MMSC's FB submodules can be described as follows:

$$P_{IGBT_{FB}} = V_{sub}I_{string} = \frac{2V_{peak}I_{RMS}}{N} \tag{63}$$

By observing the topology of a bidirectional switch, it is possible to notice that this switch is composed of two IGBTs. Since medium-voltage levels are considered in this thesis, then the bidirectional-switch stacks must be built with two stacks of series-connected IGBTs. As a consequence of the natural operation and current commutation behavior of a bidirectional switch, each IGBT stack must be capable to block the full bidirectional-switch-stack voltage ($V_{BS} = 2\sqrt{3}V_{peak}$), and each IGBT stack must be capable to conduct the string current ($I_{BS} = I_{string} = I_{RMS}$). Then, the power ratings of each IGBT stack of the MMSC bidirectional-switch stacks can be calculated as follows:

$$P_{IGBT_{BS}} = V_{BS}I_{BS} = 2\sqrt{3}V_{peak}I_{RMS} = 3.46V_{peak}I_{RMS} \tag{64}$$

The MMSC is composed of three strings (see Fig. 12), each string is composed of N FB submodules and each FB submodule is composed of four IGBTs. Thus, the total number of IGBTs in the MMSC FB submodules is equal to $N_{IGBT_{FB}} = 3\times N\times 4 = 12N$. The MMSC is also composed of six bidirectional-switch stacks, each of them is composed of two IGBT stacks. Thus, the total number of IGBT stacks in the MMSC is equal to $N_{IGBT_{BS}} = 6 \times 2 = 12$. The total MMSC semiconductor-device power ratings can be calculated as follows:

$$\begin{aligned} P_{SD} &= P_{IGBT_{FB}}N_{IGBT_{FB}} + P_{IGBT_{BS}}N_{IGBT_{BS}} \\ &= 24V_{peak}I_{RMS} + 41.57V_{peak}I_{RMS} = 65.57V_{peak}I_{RMS} \end{aligned} \tag{65}$$

Now keeping the IGBT's rated voltage fixed with the previously defined value of V_{IGBT}, and remembering that MMSC string voltage is equal to $V_{string} = 2V_{peak}$, then the number of FB submodules composing each string of the converter is equal to:

$$N = \frac{V_{string}}{V_{IGBT}} = \frac{2V_{peak}}{V_{IGBT}} \tag{66}$$

Once again, the MMSC is composed of three strings, each string is composed of N FB submodules and each FB submodule is composed of one capacitor. Thus, the total number of submodules and of capacitors in the MMSC is equal to $N_{sub} = N_{cap} = 3\times\frac{2V_{peak}}{V_{IGBT}}\times 1 = \frac{6V_{peak}}{V_{IGBT}}$. The MMSC does not require any string inductor for its operation, which is an advantage in comparison to the previously analyzed topologies. Nonetheless, the MMSC requires the input current filer, which can potentially be bulky and heavy. Since a final and optimal filter topology is not defined in this thesis (this is an open topic for future works), then concrete conclusions about the MMSC's input filter in comparison to the arm/string inductors of the other topologies cannot be achieved.

2.5.4 3x3-MMSC

As previously explained in (39), the 3x3-MMSC's input-terminal voltage should be designed with a value equal to the one described in (67), so that the converter is capable to synthesize an AC voltage with amplitude equal to V_{peak} at its load terminals.

$$V_g \geq V_{peak} \tag{67}$$

As a natural consequence of the 3x3-MMSC topology and operation, the grid voltage (V_g) is distributed between the N capacitors of the 3x3-MMSC submodule string. Similarly to the previous three topologies, a sorting algorithm is always adopted to maintain all the submodule capacitors within one string with similar voltage values, then it is a fair assumption to consider that the nominal operational voltage of each submodule capacitor is equal to $V_{cap} = \frac{V_g}{N}$. The string submodules (and their IGBTs) must be capable to withstand at least the nominal operational voltage of their capacitors. In other words:

$$V_{sub} \geq V_{cap} = \frac{V_g}{N} \tag{68}$$

Where V_{sub} is the maximum voltage tolerated by the submodule's IGBTs. Similarly to the MMC, the M^3C, and the MMSC cases, the ideal situation is also considered for the 3x3-MMSC, i.e., $V_g = V_{peak}$, and $V_{sub} = V_{cap} = \frac{V_g}{N} = \frac{V_{peak}}{N}$.

Not only the 3x3-MMSC submodule strings, but its bidirectional-switch stacks must also be considered in the analysis. These bidirectional-switch stacks are connected between two phases of the grid, which means that they must be capable to tolerate the peak value of the line-to-line grid voltage, when operating in blocking mode, i.e.:

$$V_{BS} \geq \sqrt{3} V_g \tag{69}$$

Where V_{BS} is the maximum voltage tolerated by the bidirectional-switch stack. Since the ideal case where $V_g = V_{peak}$ is considered, then (69) can be rewritten as:

$$V_{BS} \geq \sqrt{3} V_{peak} \tag{70}$$

The ideal case is also considered for these stacks, i.e., $V_{BS} = \sqrt{3} V_{peak}$, which means that the maximum voltage tolerated by the stack is designed to be equal to its nominal operational voltage when in blocking mode. The current that flows through each submodule string and through each bidirectional-switch stack of the 3x3-MMSC is equal to:

$$I_{string} = I_{BS} = I_l = I_{RMS} \tag{71}$$

The 3x3-MMSC submodule string is built with FB submodules, which are composed of four IGBTs and of one capacitor. The submodule IGBTs must be capable to block

the voltage V_{sub}, defined according to (68), and must be capable to conduct the string current (I_{string}), defined according to (71). Once again, considering the ideal case where $V_{sub} = \frac{V_{peak}}{N}$, then the power ratings of the IGBTs of the 3x3-MMSC's FB submodules can be described as follows:

$$P_{IGBT_{FB}} = V_{sub} I_{string} = \frac{V_{peak} I_{RMS}}{N} \tag{72}$$

Similarly to the MMSC case, each IGBT stack of the 3x3-MMSC bidirectional-switch stacks must be capable to block the full bidirectional-switch-stack voltage (which is equal to $V_{BS} = \sqrt{3} V_{peak}$ in this case), and each IGBT stack must be capable to conduct the string current ($I_{BS} = I_{string} = I_{RMS}$). Then, the power ratings of each IGBT stack of the 3x3-MMSC bidirectional-switch stacks can be calculated as follows:

$$P_{IGBT_{BS}} = V_{BS} I_{BS} = \sqrt{3} V_{peak} I_{RMS} = 1.73 V_{peak} I_{RMS} \tag{73}$$

The 3x3-MMSC is composed of three strings (see Fig. 13), each string is composed of N FB submodules and each FB submodule is composed of four IGBTs. Thus, the total number of IGBTs in the 3x3-MMSC FB submodules is equal to $N_{IGBT_{FB}} = 3 \times N \times 4 = 12N$. The 3x3-MMSC is also composed of nine bidirectional-switch stacks, each of them is composed of two IGBT stacks. Thus, the total number of IGBT stacks in the 3x3-MMSC is equal to $N_{IGBT_{BS}} = 9 \times 2 = 18$. The total 3x3-MMSC semiconductor-device power ratings can be calculated as follows:

$$\begin{aligned} P_{SD} &= P_{IGBT_{FB}} N_{IGBT_{FB}} + P_{IGBT_{BS}} N_{IGBT_{BS}} \\ &= 12 V_{peak} I_{RMS} + 31.14 V_{peak} I_{RMS} = 43.14 V_{peak} I_{RMS} \end{aligned} \tag{74}$$

Now keeping the IGBT's rated voltage fixed with the previously defined value of V_{IGBT}, and remembering that 3x3-MMSC string voltage is equal to $V_{string} = V_{peak}$, then the number of FB submodules composing each string of the converter is equal to:

$$N = \frac{V_{string}}{V_{IGBT}} = \frac{V_{peak}}{V_{IGBT}} \tag{75}$$

Once again, the 3x3-MMSC is composed of three strings, each string is composed of N FB submodules and each FB submodule is composed of one capacitor. Thus, the total number of submodules and of capacitors in the 3x3-MMSC is equal to $N_{sub} = N_{cap} = 3 \times \frac{V_{peak}}{V_{IGBT}} \times 1 = \frac{3V_{peak}}{V_{IGBT}}$. Similarly to the MMSC case, the 3x3-MMSC does not require any string inductor for its operation, which is an advantage in comparison to the MMC and to the M^{3}C. Similarly to the MMSC, the 3x3-MMSC also requires the input current filer, which can potentially be bulky and heavy. Once again, since a final and optimal filter topology is not defined in this thesis, then concrete conclusions about the 3x3-MMSC's input filter in comparison to the arm/string inductors of the other topologies cannot be achieved.

2.5.5 Summary

In Table 6 and in Table 7, a summary of the results obtained through the comparative analysis is presented. One of the conclusions of this analysis is that the 3x3-MMSC presents considerably improved structural features in comparison to the MMSC, i.e., the addition of the third bidirectional-switch stack connecting each submodule string to the third phase of the grid, allows the 3x3-MMSC to be connected to a grid with a reduced voltage amplitude, which results in a considerably reduced component count and semiconductor-device power requirements in relation to the MMSC. The 3x3-MMSC semiconductor-device power-rating requirements is 34.2 % less than the MMSC semiconductor-device power-rating requirements. The 3x3-MMSC also can be built with half the number of submodules and capacitors in comparison to the MMSC. Another interesting conclusion of the comparative analysis is that, in fact, the combination of submodule strings along with bidirectional-switch stacks makes the MMSC and the 3x3-MMSC to have a reduced number of submodules and, thus, a reduced number of the potentially bulky and heavy submodule capacitors in comparison to the MMC and the M^3C. For this reason, specially the 3x3-MMSC can potentially be a more compact and lighter solution in relation to the MMC and the M^3C. Obviously, the size of these capacitors must be considered for more concrete conclusions. However, the size of the capacitors of each topology will have to be analyzed depending on the specific application and on the specific frequency of operation since, as previously explained, each of these topologies present different performances at different frequency ranges regarding the amplitude of their submodule-capacitor voltage ripple. In any case, having a reduced number of submodules and of capacitors should contribute in general for a reduced volume and weight. First, because even though the capacitor is the bulkiest and heaviest element of a submodule, the heatsink, the mechanical by-pass switch, and the submodule metallic structure itself also play an important role in the total volume and weight of a submodule. Second, because a larger number of submodules will always require more space since there should be some distance between each submodule for insulation purposes. By observing Table 6, it is possible to notice that the 3x3-MMSC semiconductor-device power-rating requirements is similar to the ones of the MMC and the M^3C, which means that expenditures with semiconductor devices should be similar in these three topologies. Finally, it is also important to highlight the fact that the MMC and the M^3C must be built with twelve and nine string inductors, respectively, which are essential for the proper operation of these converters. The MMSC and the 3x3-MMSC, however, do not need these string inductors, even though they require the input filter that should potentially be large and bulky. Since a specific filter topology was not defined in this thesis, then a comparative analysis among these passive elements cannot be performed. It is important to analyze in future works the feasibility of designing input filters with tolerable size for the MMSC and for the 3x3-MMSC.

Table 6: Semiconductor-Device Power Requirements (P_{SD}).

MMC	M^{3}C	MMSC	3x3-MMSC
$40.8V_{peak}I_{RMS}$	$48.24V_{peak}I_{RMS}$	$65.57V_{peak}I_{RMS}$	$43.14V_{peak}I_{RMS}$

Table 7: Submodule and Capacitor Count.

MMC	M^{3}C	MMSC	3x3-MMSC
$\frac{24V_{peak}}{V_{IGBT}}$	$\frac{18V_{peak}}{V_{IGBT}}$	$\frac{6V_{peak}}{V_{IGBT}}$	$\frac{3V_{peak}}{V_{IGBT}}$

2.6 Experimental Validation of Final Topology

In this section, an experimental validation of the 3x3-MMSC is presented, where experimental tests of the converter operating with different frequency values at its load-side terminal are performed. The 3x3-MMSC can be regarded as a three-phase converter built based on three independent single-phase structures. For this reason, only one phase of the 3x3-MMSC was implemented in the experimental prototype as illustrated in Fig. 37, in which the test-setup hardware and its electrical diagram are presented. The built prototype is composed of a string of eight FB submodules. Three bidirectional switches are used to connect the submodule string to each phase of the grid. The prototype FB submodules and bidirectional switches are based on IGBTs. An AC power supply is used to represent a three phase grid with voltage amplitude equal to $V_g = 200$ V and frequency equal to $f_i = 50$ Hz. The single-phase 3x3-MMSC operated supplying power to a $100-\Omega$ resistive load. Since the 3x3-MMSC behaves as a controlled voltage source, from the load perspective, which is capable to track a provided voltage reference then, in these experimental tests, the converter was controlled in an open-loop fashion, receiving as a reference a voltage with amplitude equal to $V_o = 150$ V. Three different tests were performed, where the frequency of the voltage reference was set with three different values equal to $f_o = 1, 10$ and 45 Hz. To control the converter, the algorithm described in the flowchart of Fig. 22 was implemented in a dSPACE through a MATLAB code. To obtain a three-phase result, one experimental test was performed for each phase using the single-phase prototype, resulting in the three-phase voltage waveform shown in Fig. 38(b), (d) and (f). In Fig. 38(b), (d) and (f), the experimental load voltages are depicted for the cases where $f_o = 1, 10$ and 45 Hz, respectively. In Fig. 38(a), (c) and (e), the experimental submodule-capacitor voltages are presented for the cases where $f_o = 1, 10$ and 45 Hz, respectively.

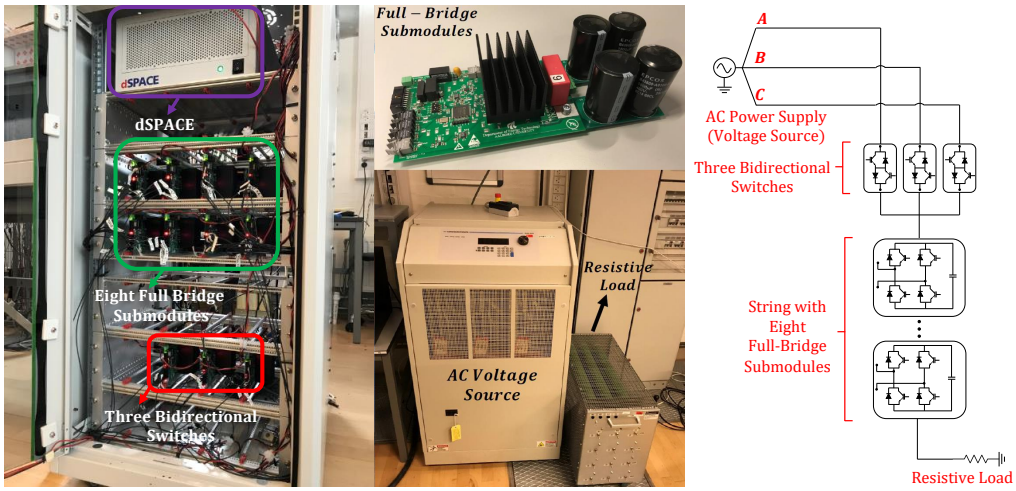

Fig. 37: 3x3-MMSC experimental test setup along with its corresponding electrical diagram.

The 3x3-MMSC submodule-capacitor voltages presented in Fig. 38(a), (c) and (e), validate some important aspects of the proposed converter solution. For example, these results demonstrate that, in fact, the 3x3-MMSC presents a high performance at low frequencies and a deteriorated performance as the load frequency (f_o) approaches the grid frequency (f_i), i.e., the converter's submodule-capacitor voltage ripple is small for the $f_o = 1$-Hz operation illustrated in Fig. 38(a) but it is considerably increased for the $f_o = 45$-Hz operation illustrated in Fig. 38(c). By observing the zoom in the submodule-capacitor voltages, the eight individual voltages of the eight submodule capacitors can be seen, and it is interesting to notice that these voltages remain with very similar values because of the implemented sorting algorithm responsible for the submodule-capacitor voltage balancing. It is also interesting to observe the waveform of the voltages synthesized by the 3x3-MMSC at the load terminal as depicted in Fig. 38(b), (d) and (f). These are the switched voltages synthesized by the converter without any filtering stage. It is noticeable that these are voltages with a quite high power quality even in this case where only $N = 8$ submodules were composing the converter's submodule string. By increasing the number of submodules, the voltages synthesized by the 3x3-MMSC would become extremely close to perfectly sinusoidal signals as, for example, the simulation results presented in Fig. 18.

In Fig. 39(a), the experimental results obtained for the voltage across the 3x3-MMSC submodule string is shown, for the case where $f_o = 10$ Hz. As expected, this is a staircase-shape multilevel voltage that can have both positive and negative polarities since FB submodules are used. Disregarding the discontinuities, the staircase-shape voltage is close to an oscillatory signal composed of two frequency components, i.e.,

f_o = 10 Hz and f_i = 50 Hz. In fact, while the submodule string is kept connected to phase A of the grid, the voltage across this string is close to an oscillatory signal composed of these two frequency components. When the voltage across the string terminals reaches the limits of ±200 V, then the submodule string must be connected to either phase B or phase C of the grid in order to keep tracking the voltage reference. In other words, 200 V is the maximum voltage possible to be synthesized in series, across the submodule string, since the average value of the submodule-capacitor voltage is equal to approximately 25 V, as illustrated in Fig. 38, and since there are $N = 8$ submodules available to be inserted. Thus, the discontinuities observed in the voltage signal shown in Fig. 39(a) correspond to moments where the submodule string is either connected to phase B or phase C of the grid.

Finally, in Fig. 39(b), experimental results of the voltage across the bidirectional switch that connects the submodule string to phase A of the grid are shown, along with two line-to-line grid voltages, i.e., v_{gab} and v_{gac}. By comparing Fig. 39(a) and (b), it is possible to notice that the moments where the voltage synthesized across the submodule string is close to a continuous sinusoidal signal correspond to the moments where the voltage across the bidirectional switch is null since this switch is in conducting mode (submodule string connected to phase A of the grid). When the discontinuities occur in the signal of the voltage across the submodule-string terminals, then the voltage across the bidirectional switch that connects the string to phase A of the grid is no longer null since the switch is in blocking mode in this case. It is important to notice that the voltage across the bidirectional switch that connects the string to phase A of the grid can be either equal to v_{gab} or to v_{gac} depending to each phase of the grid the submodule string is connected. If the submodule string is connected to phase B of the grid, then the phase-B grid voltage will be connected to the mid point that connects the submodule string to the three bidirectional switches (see Fig. 37) and, thus, the voltage across the bidirectional switch that connects the string to phase A of the grid will be equal to v_{gab}. On the contrary, if the submodule string is connected to phase C of the grid, then the phase-C grid voltage will be the one connected to the mid point that connects the submodule string to the three bidirectional switches (see Fig. 37) and, thus, the voltage across the bidirectional switch that connects the string to phase A of the grid will be equal to v_{gac}. These results prove that the bidirectional switches of the 3x3-MMSC in fact must be capable to block the line-to-line grid voltage as discussed in the comparative analysis section.

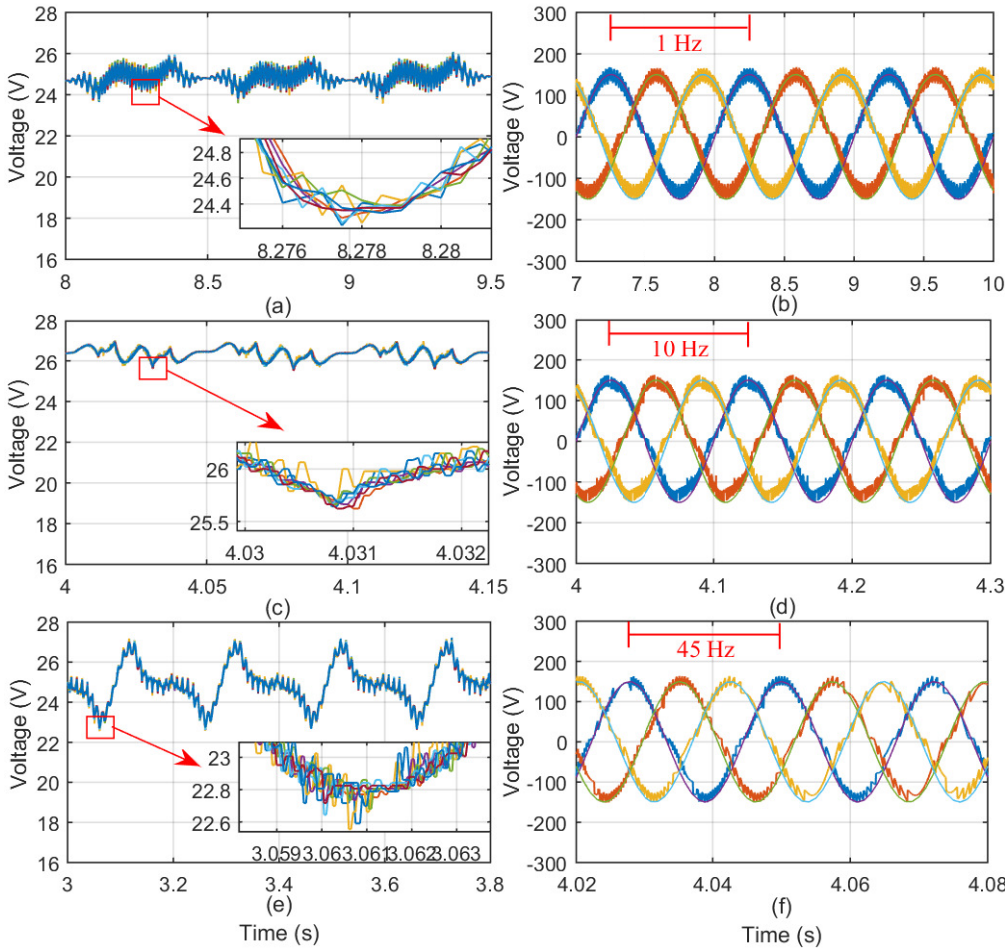

Fig. 38: Experimental results. (a), (c) and (e) show the 3x3-MMSC submodule-capacitor voltages for the cases where $f_o = 1, 10$ and 45 Hz, respectively. (b), (d) and (f) show the synthesized load voltages for the cases where $f_o = 1, 10$ and 45 Hz, respectively.

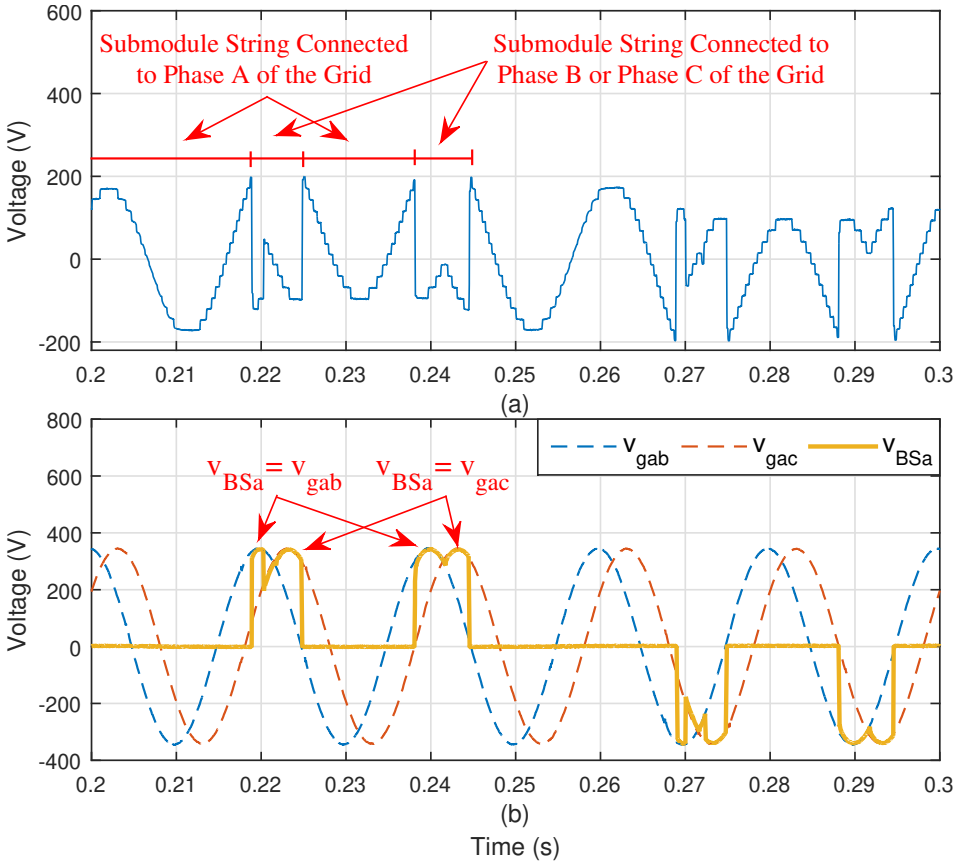

Fig. 39: Experimental results. (a) Voltage synthesized across submodule-string terminals, and (b) voltage across the bidirectional switch that connects the submodule string to phase A of the grid (v_{BSa}), along with two line-to-line grid voltages (v_{gab} and v_{gac}).

2.7 Summary of Advantageous Features, Operational Challenges and Future Works

In this section, a summary of the 3x3-MMSC's advantageous features and operational challenges that deserve special attention in future works are presented. The MMSC is not considered in this section because the 3x3-MMSC can be seen as an enhanced version of the MMSC as previously discussed.

2.7.1 Advantageous Operational and Structural Features

- The 3x3-MMSC presents an improved performance at low-frequency operation in comparison to the MMC, since it experiences a considerably reduced submodule-capacitor voltage ripple, in relation to the MMC, when it operates at the low-frequency range, specially close to the 0-Hz operation point. This operational feature indicates that the 3x3-MMSC could potentially be a competitive solution to drive industrial motors and pumped-hydro-storage systems.

- The 3x3-MMSC presents a high performance when it is connected to an unbalanced grid since its submodule-capacitor voltages remain stable and with a low ripple under such circumstances. This is an advantage in relation to the MMC but, specially, in relation to the M^3C that faces instability when operating under an unbalanced grid condition.

- The 3x3-MMSC presents straightforward control and modulation, for a converter with a modular multilevel structure, as explained in this thesis. This is an advantageous feature in comparison to the MMC but, specially, in comparison to the M^3C that requires many internal control loops so that it can operate in a stable and safe fashion. Once again, it is important to highlight that there are only a few research groups in the world that are currently capable to operate this converter topology.

- As explained in the comparative analysis, the 3x3-MMSC presents an overall reduced component count in comparison to the MMC and the M^3C, specially a significantly reduced number of submodules and of capacitors, which should potentially result in a solution with reduced cost, volume and weight.

2.7.2 Operational Challenges that Deserve Further Investigation

- One of the biggest challenges of the 3x3-MMSC is to find an adequate input filter, to filter out the undesired current components injected into the grid by the converter. This filter must be effective, efficient and must present a tolerable volume and size. As previously explained, the filter adopted in this thesis was effective in filtering out the undesired currents but it was inefficient. If finding an appropriate filter is not possible, then the increase of the switching frequency of the converter's bidirectional-switch stacks might be required to increase the order of the harmonic currents injected into the grid so that it is easier to filter out these currents. However, this would reduce the reliability of the topology since these bidirectional-switch stacks must be built with a few series-connected semiconductor devices in order to tolerate medium-voltage levels.

- In this thesis, the 3x3-MMSC grid-side reactive power was regulated by controlling the d-axis current component of the electrical machine (i_{od}) since the current

injected into the grid by the converter is a function of its load current (machine current in this case) and the switching pattern of the bidirectional-switch stacks. It should be possible to control the reactive power injected into the grid by the 3x3-MMSC by adjusting the switching pattern of the bidirectional-switch stacks instead of controlling the load current. This would be similar to how the grid-side reactive power of well-established matrix converters [65] is controlled. The grid-side reactive-power control of the 3x3-MMSC is an important topic that requires further investigation in future works.

- The regulation of the 3x3-MMSC's submodule-capacitor voltages is another important issue to be investigated in future works. A potential approach to achieve this objective is to synthesize common-mode voltages at the load terminals aiming at regulating the submodule-capacitor voltages without affecting the control of the electrical machine.

- In this thesis, the operation of the 3x3-MMSC under severe unbalanced grid conditions caused by single-phase-to-ground faults was analyzed, and it was demonstrated that the proposed converter presents high performance under such conditions. In future works, it is important to investigate the behavior of the 3x3-MMSC under three-phase grid faults, and to analyze the fault-ride-through performance of the converter.

In summary, the 3x3-MMSC is a new converter topology that could potentially become a competitive solution for high-power machine-drive applications because of its advantageous operational and structural features in relation to other well-established industrial solutions. Nonetheless, some challenges related to this converter topology must still be assessed and further investigated in future works.

3 Novel Converter Topology with a Modular Multilevel Structure for Modern/Future High-Power Medium-Voltage Wind Turbines

In this chapter, the second converter solution proposed in this paper is presented in detail. Differently from the first proposed topology, which is suitable for high-power medium-voltage machine drives that operate at low frequencies, the second solution is specifically suitable for modern/future high-power WTs adopting a medium-voltage structure.

3.1 Basic Constructive and Operational Characteristics

As previously mentioned, the second proposed topology was named Modular Multilevel Shunt Converter (MMShC) in opposition to the first topology that was named Modular Multilevel Series Converter (MMSC) because of the series connection of its submodule strings between the grid and the load. However, both converters are essentially built with the same power-electronic-component structure, i.e., they are both built with strings of FB submodules along with low-switching-frequency bidirectional-switch stacks. The MMShC topology is shown in Fig. 40, where it is possible to notice that each phase of the converter is composed of two submodule strings (String X and String Y), along with four bidirectional-switch stacks.

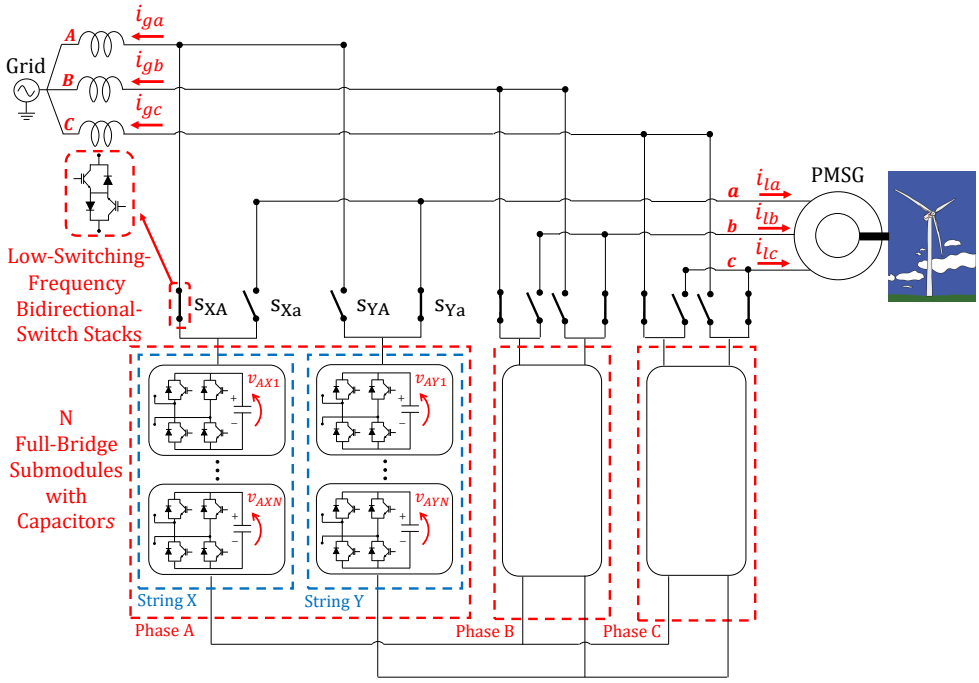

Fig. 40: Second proposed converter solution named Modular Multilevel Shunt Converter.

The converter's bidirectional-switch stacks are responsible for connecting the submodule strings (String X and String Y) to the grid and to the generator terminals, alternately and in a complementary fashion, in such a way that a continuous power flow is established between the generator and the grid. In other words, while one submodule string is connected to the generator terminals and its capacitors are being charged (absorbing power from the generator), the other submodule string is connected to the grid terminals and its capacitors are being discharged (supplying power to the grid). The

basic operation of the MMShC is explained through Fig. 41 that shows an illustrative representation of the converter's phase A. The MMShC essentially operates switching between State 1 and State 2 as shown in Fig. 41. In State 1, String X is connected to the grid and it is responsible for synthesizing a given voltage at the grid terminal in order to control the submodule-capacitor voltages while injecting power (P_{ga}) to the grid. In the meantime, String Y is connected to the generator and it is responsible for synthesizing a given voltage at the generator's terminal in order to regulate the machine speed while absorbing the power produced by the WT (P_{la}). In State 2, on the other hand, String Y is the one connected to the grid and it is responsible for synthesizing a given voltage at the grid terminal in order to control the submodule-capacitor voltages while injecting power (P_{ga}) to the grid. In this case, String X is connected to the generator and it is responsible for synthesizing a given voltage at the generator's terminal in order to regulate the machine speed while absorbing the power produced by the WT (P_{la}).

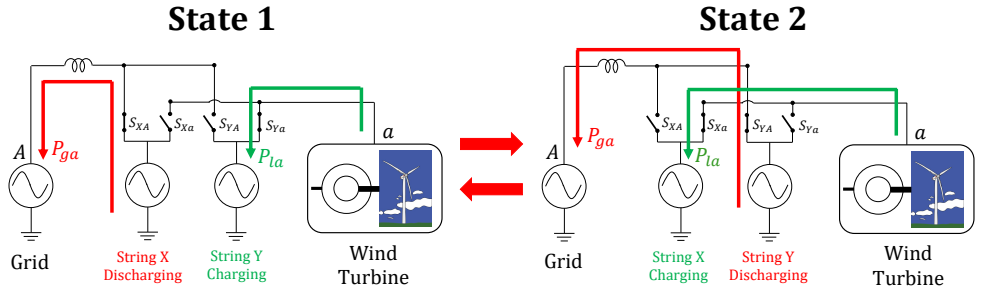

Fig. 41: Illustration of basic operation of the MMShC, where its two complementary strings are connected to the grid and to the generator's terminals alternately.

As will be explained later in this thesis, the MMShC topology, and the way that its submodule strings and bidirectional-switch stacks are connected, lead to the need of an increased number of components in comparison to the 3x3-MMSC. However, differently from the 3x3-MMSC, the MMShC behaves as a controlled voltage source from both load and grid perspectives, which allows it to be a more flexible solution. The MMShC's submodule strings can be modeled as AC voltage sources, as shown in Fig. 41, since they are built with FB submodules that can synthesize voltages with positive and with negative polarities. If these strings are built with a relatively high number of submodules, then a staircase-shape signal close to a sinusoidal can be synthesized across the converter's strings. By observing Fig. 40, it is possible to notice that the Strings X of each phase of the converter are connected to a common neutral point, and the Strings Y of each phase of the converter are connected to a different neutral point. If the converter's bidirectional-switch stacks are controlled in a way that the three Strings X are simultaneously connected to one of the terminals while the three Strings Y are simultaneously connected to the opposite terminal, then the MMShC can essentially be considered as a three-phase converter built with two independent structures, as the one shown in Fig. 42,

that are connected alternately and in a complementary manner to the grid and to the generator terminals. The structure shown in Fig. 42 can be regarded as a three-phase voltage source since its submodule strings can synthesize staircase-shape voltages with both positive and negative polarities, as previously mentioned. Since there is always one structure as the one shown in Fig. 42 connected to the grid and to the generator's terminals (either the one composed of the three Strings X or the one composed of the three Strings Y), then it is possible to state that the MMShC behaves as a controlled voltage source from both grid and load perspectives. It is also important to notice that the structure shown in Fig. 42 is equal to the Single-Star Bridge-Cells (SSBC) converter [69–71] widely adopted for static synchronous compensator (STATCOM) applications. As will be explained later in this thesis, the control technique to regulate the submodule-capacitor voltages of the MMShC can be similar to the one traditionally adopted for the SSBC converter.

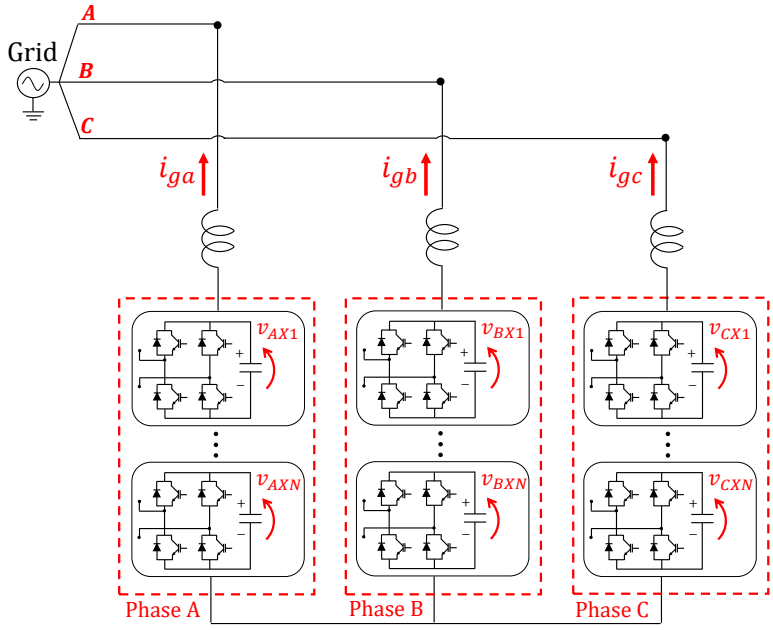

Fig. 42: SSBC converter topology.

One of the challenges to the implementation of the MMShC is related to the operation and current commutation of its bidirectional-switch stacks. As demonstrated in the illustrative representation of the MMShC shown in Fig. 43, the voltage across the bidirectional-switch stacks when operating in blocking mode is equal to the difference between the instantaneous values of the voltages synthesized by Strings X and Y, which are represented by voltage sources in Fig. 43. Since voltages with different frequencies

can be synthesized by each string, then the bidirectional-switch stacks must be capable to withstand the sum of the peak values of the voltages synthesized by the two strings. Since the converter is proposed for medium-voltage applications, then a few series-connected semiconductor devices should be required to build these bidirectional-switch stacks. Nonetheless, as will be shown later in this thesis, these switches can work with a considerably low switching frequency, which contributes for a reliable and efficient operation. Besides, there are some products currently available in the industry, which correspond to stacks of a few series-connected semiconductor devices that behave as a single switch with increased voltage ratings, and that operate with high reliability due to the use of modern drivers that ensure proper static and dynamic voltage sharing among the various devices connected in series [6]. These modern devices could be adopted to build the bidirectional-switch stacks of the MMShC. Another approach to guarantee a safe and reliable operation of the bidirectional-switch stacks would be to use snubber circuits, in which low losses would potentially be obtained because of the low switching frequency of the bidirectional-switch stacks.

Regarding the current commutation, some constraints must be respected when switching the bidirectional-switch stacks as illustrated in Fig. 43. First, switches S_{XA} and S_{YA}, and switches S_{Xa} and S_{Ya} cannot be simultaneously in ON state because then a short circuit would occur between Strings X and Y that behave as voltage sources. In other words, switches S_{XA} and S_{YA}, and switches S_{Xa} and S_{Ya} must operate in a complementary fashion. At the same time, there must always be a path for the inductive load current to flow through, which means that either switch S_{Xa} or switch S_{Ya} must always be in ON state. Since different turn-on and turn-off times naturally exist between each semiconductor device, then special strategies are required to allow for a proper current commutation without producing short circuits and without producing over voltages because of the lack of a path for the inductive current to flow through. One of the strategies that could be used to allow for a current commutation while respecting the previously mentioned constraints is the dead-time in combination with a circuit to divert the inductive current during the commutation. In other words, when a swapping action was required, then the first step of the commutation strategy would be to send turn-off signals to the switches conducting current. As a second step, a dead-time period would be waited to guarantee that all the switches were turned off before turning their complementary switches on. This way, a short circuit would not occur. The inductive currents would flow through the diverting circuit during the dead-time period. Finally, as a last step, the turn-on signals would be sent to the switches required to turn on. Some of the circuits that could be used to divert the inductive currents would be snubber circuits [2], as shown in Fig. 44, or diode clamping circuits [66]. Nonetheless, it is important to highlight that the mentioned commutation constraints are similar to the ones of the well-established DMC [66, 67]. Thus, techniques such as the four-step method [66, 67] could be adopted to obtain an efficient current commutation, similarly to how it is done in DMCs. The four-step method is explained through Fig. 45.

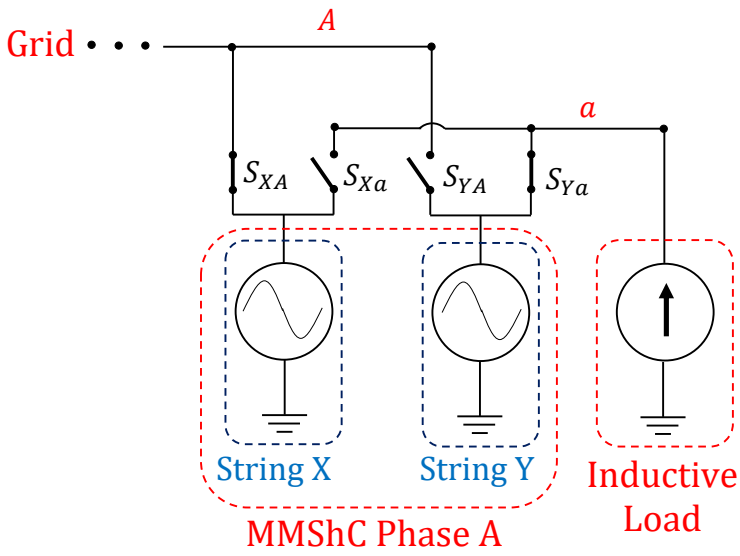

Fig. 43: Illustrative representation of constraints for current commutation in the MMShC.

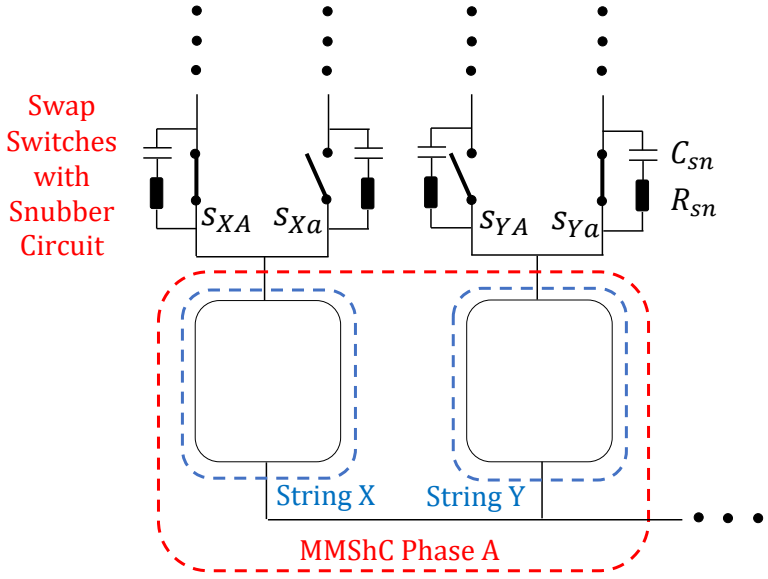

Fig. 44: Illustration of snubber circuits that can be used to guarantee a reliable operation of the MMShC's bidirectional-switch stacks.

In Fig. 45, String X and String Y are represented by the two voltage sources. The bidirectional switches S_{Xa} and S_{Ya} (that connect String X and String Y, respectively, to the phase-A load terminal) are illustrated in detail in Fig. 45. In this figure, the green color is used to represent the switches in ON state and conducting current along with the current path. The red color is used to represent the semiconductor devices in ON state but not conducting current. Finally, the black color is used to represent the semiconductor devices in OFF state. Let us consider that the system is operating in the initial state depicted in Fig. 45 when a swapping signal is sent to the bidirectional switches. In the initial state, String X is connected to the load, synthesizing the voltage v_{sX} at its terminal, and the load current has the instantaneous direction illustrated in Fig. 45. The two bidirectional-switch IGBTs (S_{Xa1} and S_{Xa2}) are in ON state but S_{Xa1} is the one conducting the load current because of the instantaneous direction of this current. The four-step method requires an accurate measurement of the load current because the steps to be followed for the commutation process rely on the information of the instantaneous current direction. The first step is to turn off S_{Xa2}, which is the device that is not conducting current in the active bidirectional switch. The second step is to turn on S_{Ya1}, which is the IGBT of the non-active bidirectional switch that could conduct the load current according to its instantaneous direction. It is important to notice that, in Step 2, the diodes of the two bidirectional switches guarantee that a short circuit between the two voltage sources does not occur, i.e., supposing that the voltages synthesized by the two strings have an instantaneous positive polarity, then the anti-parallel diodes of S_{Xa2} and of S_{Ya2} would make sure that only the voltage with higher instantaneous amplitude would be connected to terminal a, avoiding a short circuit. Thus, in Step 2, a short circuit is avoided by the diodes and, at the same time, a path for the load current is guaranteed. The third step is to turn off S_{Xa1}, which makes the load current to naturally start flowing through S_{Ya1} that was turned on in Step 2. Finally, the fourth step in to turn on S_{Ya2} to create a path for the load current to flow through when it changes direction. Once again, the four-step method could be adopted to allow for a safe and efficient current commutation in the bidirectional-switch stacks of the proposed MMShC.

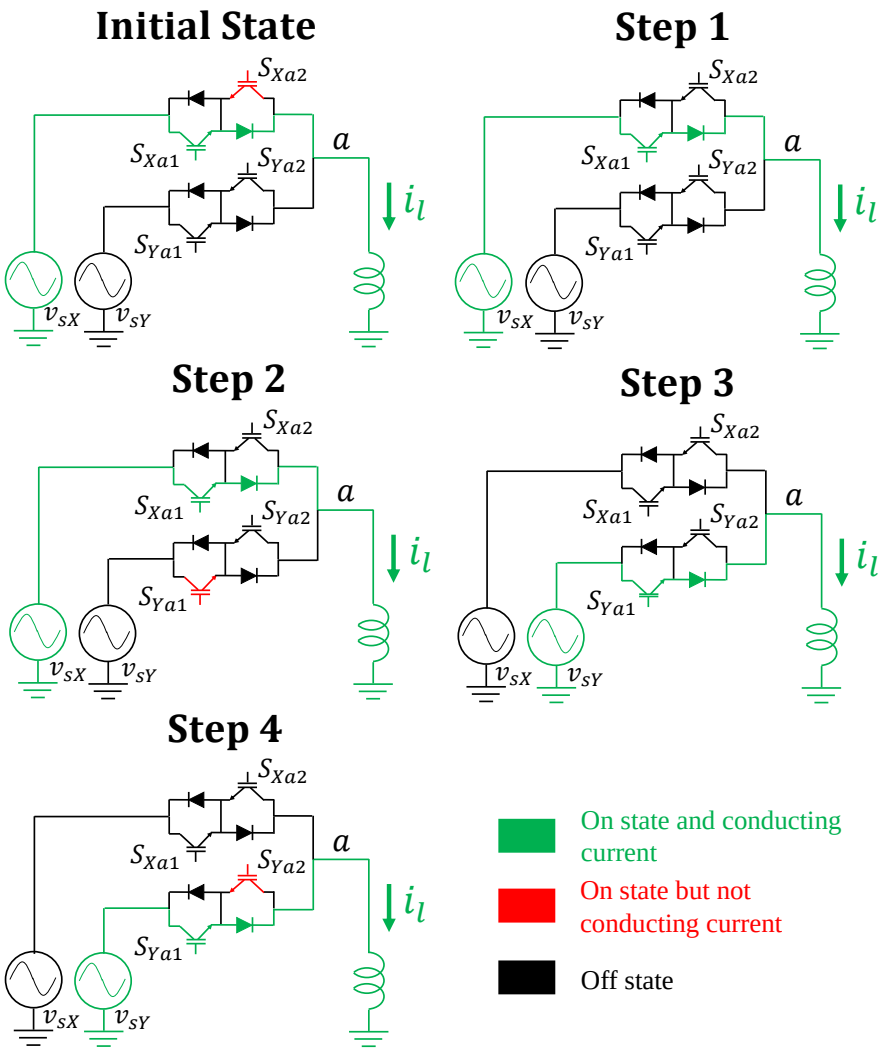

Fig. 45: Illustration of the four-step method that could be adopted for the current commutation of the MMShC.

3.2 Control and Modulation

In this section, the control and modulation of the MMShC are presented and explained. The MMShC's control is divided into external and internal control as shown in Fig. 46. The MMShC's external control is based on traditional cascade loops utiliz-

ing proportional-integral (PI) and proportional-resonant (PR) controllers. The external control is further divided into grid-side and load-side control. The grid-side control is responsible for regulating the converter's submodule-capacitor voltages while injecting power into the grid. This is a single-phase control applied to each phase of the converter (see Fig. 46). The three grid-side control loops generate the references of the voltages to be synthesized at the grid-side terminals of the converter (v^*_{ga}, v^*_{gb} and v^*_{gc}) that serve as inputs to the MMShC's internal control blocks. The converter's load-side control is based on a FOC technique [68], which is responsible for regulating the generator's speed. This is a three-phase control performed in a *dq* rotating reference frame and it generates the references of the voltages to be synthesized at the generator terminals (v^*_{la}, v^*_{lb} and v^*_{lc}), which serve as inputs to the MMShC's internal control blocks. The MMShC's internal control is a single-phase algorithm that was implemented in a programming code for each phase of the converter. The MMShC's phase-A internal control is used as an explanatory example and it is illustrated in Fig. 47. The same algorithm is also applied to the other two phases of the converter.

Before explaining the details of the converter's external control loops, the MMShC's phase-A internal control will be explained. As illustrated in both Fig. 46 and Fig. 47, the MMShC's phase-A internal control receives as inputs the voltage references v^*_{ga} and v^*_{la}, coming from the external control, the phase-A currents measured at the grid and at the load terminals (i_{ga} and i_{la}, respectively), and the voltages from the N submodule capacitors within String X and from the N submodule capacitors within String Y (v_{AX1}, v_{AX2}, ..., v_{AXN}, and v_{AY1}, v_{AY2}, ..., v_{AYN}, respectively). Finally, the control algorithm also receives as an input a triangular signal (named *tri* in this thesis), which varies between 0 and 1, and that is used for the control logic of the converter's bidirectional-switch stacks. The first stage of the control algorithm is the bidirectional-switch stack control logic. Essentially, when the triangular signal is greater than 0.5 ($tri > 0.5$), then String X is connected to the generator as it operates in charging mode, and String Y is connected to the grid terminal as it operates in discharging mode. On the contrary, when the triangular signal is less than 0.5 ($tri < 0.5$), then String Y is connected to the generator as it operates in charging mode, and String X is connected to the grid terminal as it operates in discharging mode. In other words, these two operation modes correspond to State 1 and State 2 illustrated in Fig. 41. Since the signal *tri* is the one used to decide the time of the swapping action, then it is clear that the switching frequency of the bidirectional-switch stacks is equal to the frequency of this triangular signal. Since when $tri > 0.5$ String X is connected to the machine terminal and String Y is connected to the grid terminal then, in this case, the following gate signals are sent to the bidirectional-switch stacks $S_{XA} = 0$, $S_{Xa} = 1$, $S_{YA} = 1$, and $S_{Ya} = 0$, where 0 means OFF state and 1 means ON state. Besides, in this case, the voltage to be synthesized across String X becomes equal to the load-side voltage reference ($v^*_{sX} = v^*_{la}$), the voltage to be synthesized across String Y becomes equal to the grid-side voltage reference ($v^*_{sY} = v^*_{ga}$), the String-X current becomes equal to the current measured at

the load terminal ($i_X = i_{la}$), and the String-Y current becomes equal to the current measured at the grid terminal ($i_Y = i_{ga}$). On the contrary, since when $tri < 0.5$ String Y is connected to the machine terminal and String X is connected to the grid terminal then, in this case, the following gate signals are sent to the bidirectional-switch stacks $S_{XA} = 1$, $S_{Xa} = 0$, $S_{YA} = 0$, and $S_{Ya} = 1$. Besides, in this case, the voltage to be synthesized across String Y becomes equal to the load-side voltage reference ($v^*_{sY} = v^*_{la}$), the voltage to be synthesized across String X becomes equal to the grid-side voltage reference ($v^*_{sX} = v^*_{ga}$), the String-Y current becomes equal to the current measured at the load terminal ($i_Y = i_{la}$), and the String-X current becomes equal to the current measured at the grid terminal ($i_X = i_{ga}$).

The next stage of the algorithm is the String-X and String-Y control. The first step is the modulation, which is based on the well-established level-shifted-carrier pulse-width- modulation (LSC-PWM) technique [6]. Considering the String-X control as an example, the LSC-PWM block receives as an input the instantaneous value of v^*_{sX} and it provides as an output the instantaneous number of submodules to be inserted (M), and with which polarity these submodules must be inserted, in order to track the voltage reference received as an input (v^*_{sX}). After the modulation, a sorting algorithm is performed for the submodule-capacitor voltage balancing. This algorithm basically measures the instantaneous polarity of the voltage to be synthesized across the string (v^*_{sX} in the considered example) and the instantaneous direction of the string current (i_X in the considered example). Depending on the instantaneous combination of voltage polarity and current direction, then the capacitors of the M submodules to be inserted will be charged or discharged. If the instantaneous current is a charging one, then the M submodules with lower instantaneous voltage values are selected to be inserted. On the contrary, if the instantaneous current is a discharging one, then the M submodules with higher instantaneous voltage values are selected to be inserted. Finally, a signal is sent to insert the M selected submodules, with the previously defined polarity, and to by-pass the remaining $N - M$ submodules of the string. The exact same control algorithm is applied to String Y and, thus, the output of the control algorithm are the gate signals to be sent to the bidirectional-switch stacks (S_{XA}, S_{Xa}, S_{YA}, and S_{Ya}), and the gate-signal vectors to be sent to the N FB submodules within String X ($\vec{S}_{FB1AX}, \vec{S}_{FB2AX}, ..., \vec{S}_{FBNAX}$) and to the N FB submodules within String Y ($\vec{S}_{FB1AY}, \vec{S}_{FB2AY}, ..., \vec{S}_{FBNAY}$). As an example, the vector $\vec{S}_{FB1AX}$ is equal to $\vec{S}_{FB1AX} = [S_{FB1AX1}, S_{FB1AX2}, S_{FB1AX3}, S_{FB1AX4}]$, where these four terms correspond to the gate signals sent to the four IGBTs of the FB submodule number one of the converter's phase-A String X.

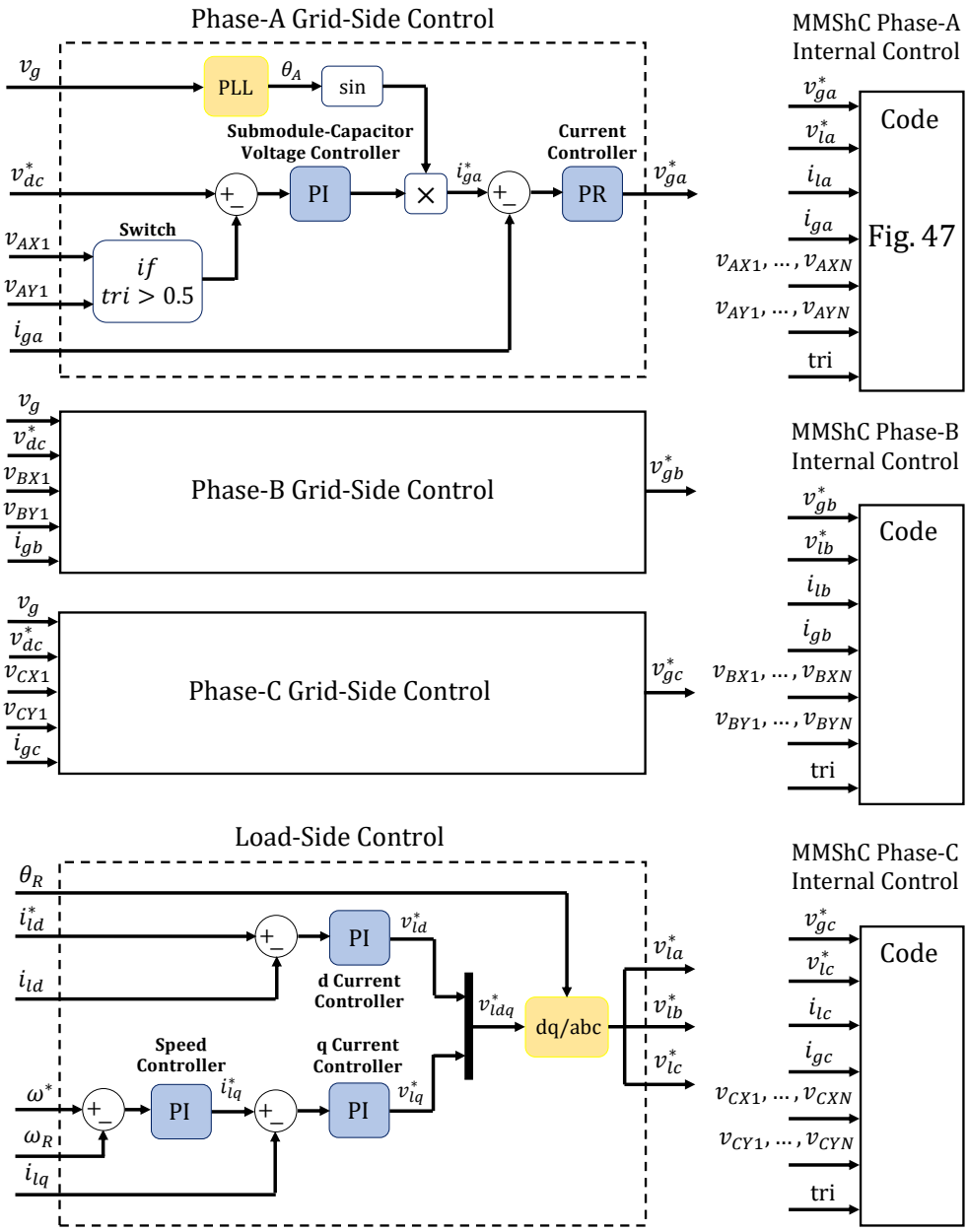

Fig. 46: Block diagram explaining MMShC's external and internal control.

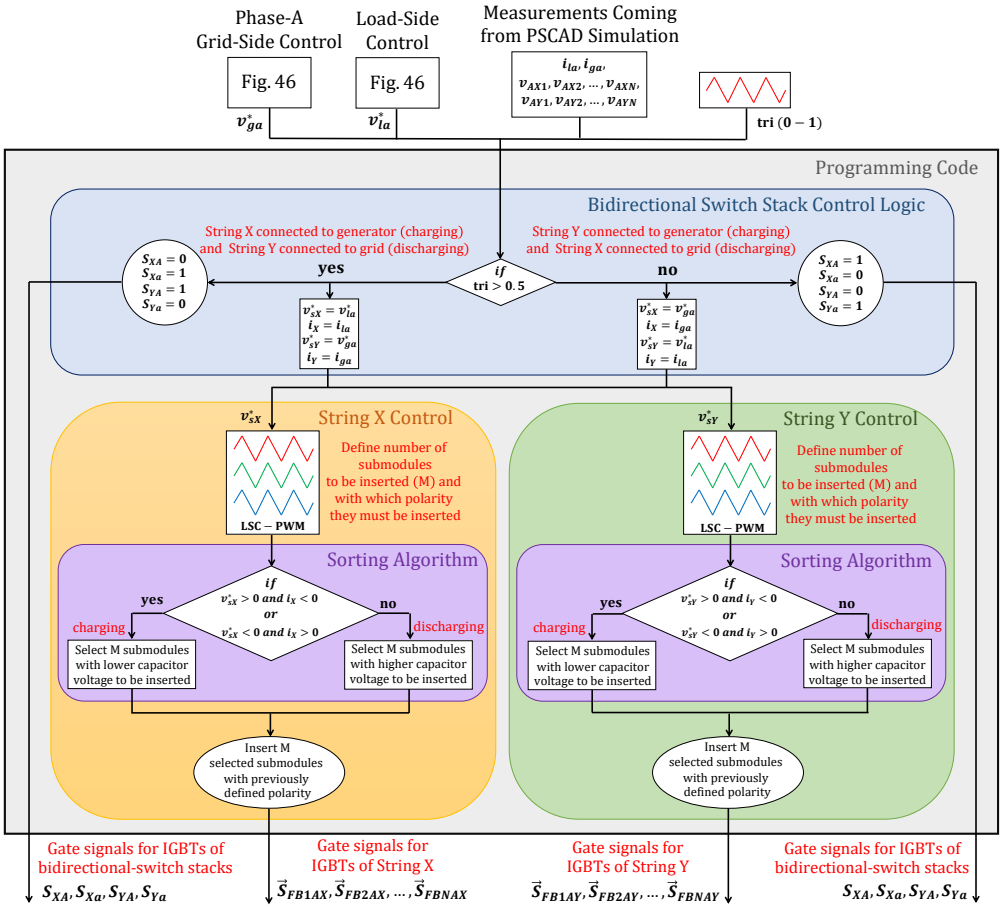

Fig. 47: Flowchart explaining the algorithm of the MMShC's phase-A internal control, which was implemented through a programming code.

After explaining the MMShC's internal-control algorithm, now the converter's external control can be explained as depicted in Fig. 46. As previously mentioned, the MMShC's grid-side control is a single-phase control applied individually to each phase of the converter. The phase-A grid-side control is highlighted in Fig. 46 and it is used as an example to explain how the submodule-capacitor voltages of the converter are regulated. The control is composed of an inner current loop based on a PR controller, acting on the sinusoidal phase-A grid current (i_{ga}), and on an outer submodule-capacitor voltage loop based on a PI controller. The submodule-capacitor voltage controller must be capable to regulate the voltages of all the submodule capacitors within String X and within String Y, according to the voltage reference v_{dc}^{*}. As previously explained, String X and

String Y are connected to the grid terminal, alternately and in a complementary fashion, depending on the instantaneous value of the triangular signal tri, which is used for the bidirectional-switch stack control. Thus, the regulation of the submodule-capacitor voltages is performed as follows: when String X is connected to the grid terminal, then its submodule-capacitors are the ones to be regulated. On the contrary, when String Y is connected to the grid terminal, then its submodule capacitors are the ones to be regulated. To achieve this objective, a "Switch" block is used to select which measured voltage should be instantaneously compared to the voltage reference (v_{dc}^{*}), producing the error that serves as an input to the submodule-capacitor voltage controller. If $tri > 0.5$, then String Y is connected to the grid terminal and, thus, its submodule-capacitor voltage (v_{AY1}) is the one compared to the voltage reference producing the error for the PI controller. On the contrary, if $tri < 0.5$, then String X is connected to the grid terminal and, thus, its submodule-capacitor voltage (v_{AX1}) is the one compared to the voltage reference producing the error for the PI controller. It is important to highlight that even though the capacitor voltages of submodule number one of Strings X and Y (v_{AX1} and v_{AY1}, respectively) were used, the capacitor voltages of any other submodule within the strings could be used since the sorting algorithm makes sure that all the submodule capacitors within the string remain with very similar voltage values. In other words, if one submodule-capacitor voltage is regulated by the PI controller, then the voltages of all the other capacitors within the string will be automatically regulated through the sorting algorithm responsible for the submodule-capacitor voltage balancing. The output of the submodule-capacitor voltage controller is the amplitude of the current reference i_{ga}^{*}. This amplitude value is multiplied by a sinusoidal signal aligned with the phase A of the grid voltage, i.e., the sinusoidal signal receives as an input the angle of the phase-A grid voltage (θ_A) obtained through a phase-locked loop (PLL). In other words, since the grid-side control is responsible for regulating the submodule-capacitor voltages by injecting active power into the grid, then the grid-current reference (i_{ga}^{*}) must be in phase with the grid voltage (v_{ga}). Finally. the error between i_{ga}^{*} and i_{ga} serves an an input to the PR current controller that produces the reference for the voltage to be synthesized at the grid-side terminal of the converter (v_{ga}^{*}). The same grid-side control is applied to phases B and C. The MMShC's load-side control is a three-phase one and it is based on two inner current control loops, to regulate the d-axis and q-axis load current components, and of an outer speed controller, responsible for regulating the generator's speed, which is connected in a cascade fashion with the q-axis current control. This is a well-established FOC technique and, thus, its details will not be explained in this thesis.

3.3 Simulation and Experimental Analyses

In this section, simulation and experimental analyses are presented to validate the control and operation of the proposed MMShC.

3.3.1 Converter Supplying Power to an RL Load

The first simulation analysis corresponds to the operation of the MMShC supplying power to an RL load. The grid side of the converter is controlled in a way as to regulate its submodule-capacitor voltages, while absorbing power from the grid. This control is performed according to the strategy presented in Fig. 46. The load side of the MMShC, however, is controlled in an open-loop fashion since the main goal of the simulation is to simply demonstrate that the converter is capable to operate as a controlled voltage source capable of tracking a voltage reference with different amplitudes and with different frequency values. Nonetheless, this simulation is also capable to explain the internal control and operation of the proposed topology by demonstrating the behavior of its submodule-capacitor voltages, the operation of its bidirectional-switch stacks, and the operation of the converter's sorting algorithm responsible for the submodule-capacitor voltage balancing. In this simulation, the MMShC is connected to a 50-Hz, 5-kV grid, and it supplies power to a 10-mH, 25-Ω load. The converter is built with $N = 5$ FB submodules per string and a 5-mH inductor is connected between each converter phase and each phase of the grid. Initially, the amplitude of the voltage reference to be synthesized at the load terminals is set to 5 kV and the frequency to 50 Hz. Moreover, initially, the average value of the submodule-capacitor voltages is regulated to 1 kV. At $t = 2.5$ s, the reference for the submodule-capacitor voltages is set to $v_{dc}^{*} = 1.2$ kV and, at $t = 4$ s, the reference for the submodule-capacitor voltages is set back to its initial value equal to $v_{dc}^{*} = 1$ kV. At $t = 6$ s, a new RL load is connected with the following parameters: $L = 5$ mH and $R = 25\ \Omega$. At the beginning of the simulation, the switching frequency of the bidirectional-switch stacks is set to 50 Hz. At $t = 8$ s, the switching frequency of the bidirectional-switch stacks is increased to 150 Hz. At $t = 10$ s, the amplitude of the voltage reference to be synthesized at the load terminals is set to 3.5 kV and the frequency to 20 Hz.

The simulation results obtained through the software PSCAD/EMTDC are shown in Fig. 48, Fig. 49, and in Fig. 50. In Fig. 48(a), the three-phase voltages synthesized at the converter's grid-side terminal, without any intermediate filtering stage, are shown. These are 50-Hz signals with a relatively high power quality due to the multilevel characteristic of the converter. In Fig. 48(b), the three-phase voltages synthesized by the MMShC at its load-side terminals, without any intermediate filtering stage, are shown. It is important to notice that the converter is capable to synthesize the desired load voltage, with different amplitude and frequency values, since it behaves as a controlled voltage source as previously explained. In Fig. 48(c), the MMShC's grid-side and load-side power (P_g and P_l, respectively) are shown. As expected, the grid-side power is always following the load-side power, in steady state, which is a consequence of the converter's grid-side control aiming at maintaining the submodule-capacitor voltages constant and regulated. In Fig. 48(c), it is interesting to observe the power transients caused by the variation of the DC-voltage-reference value (v_{dc}^{*}) that happens at $t = 2.5$ s and at $t = 4$ s. The power variations corresponding to the connection of the new

load, which happens at $t = 6$ s, and corresponding to the variation of the amplitude and frequency of the load voltage, which happens at $t = 10$ s, can also be observed in Fig. 48(c).

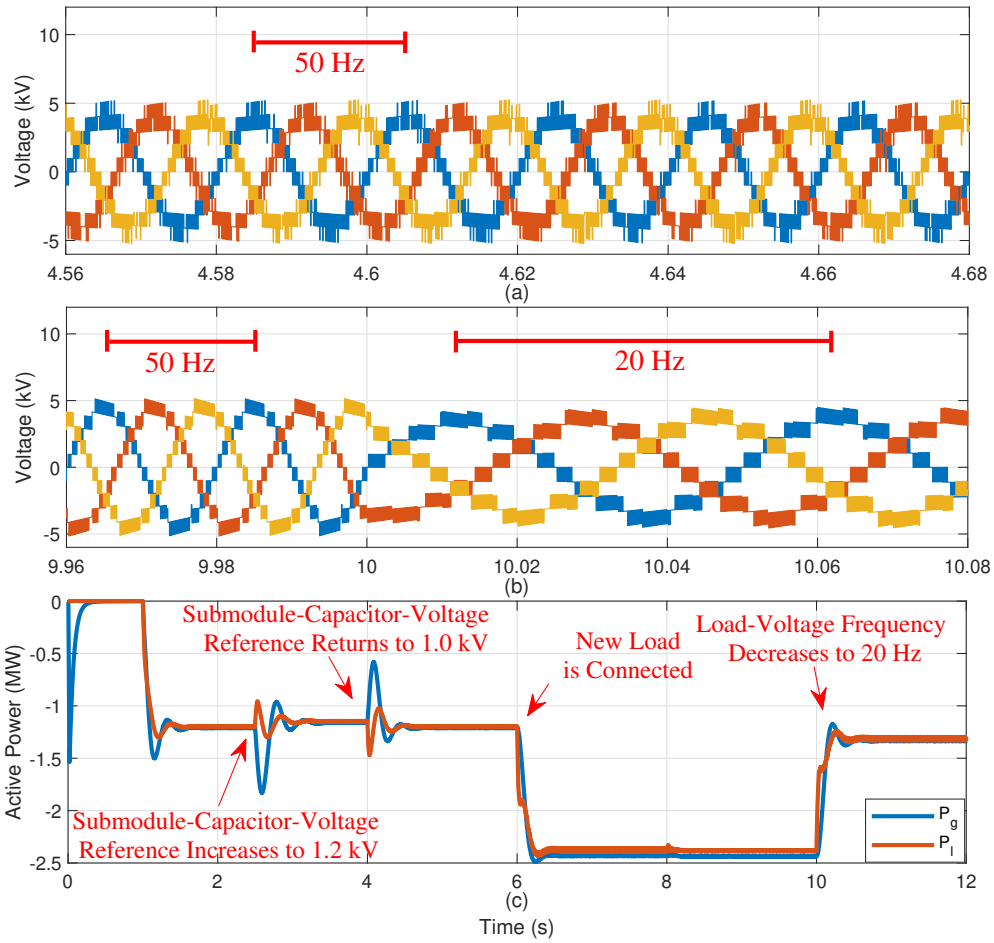

Fig. 48: Simulation results corresponding to the MMShC's operation supplying power to RL load. (a) Three-phase voltages synthesized at the grid-side terminals, (b) three-phase voltages synthesized at the load-side terminals, and (c) grid-side and load-side power.

In Fig. 49(a) and (b), the converter's grid-side and load-side currents are shown, respectively. These currents present a relatively high power quality, below 5% of total harmonic distortion (THD), even though the converter's strings were built with only $N = 5$ submodules. As in any converter with a modular multilevel structure, a higher

power quality of voltages and currents will be obtained the higher the number of levels in the converter. The power quality of the voltages and currents can also be improved by increasing the frequency of the LSC-PWM carriers.

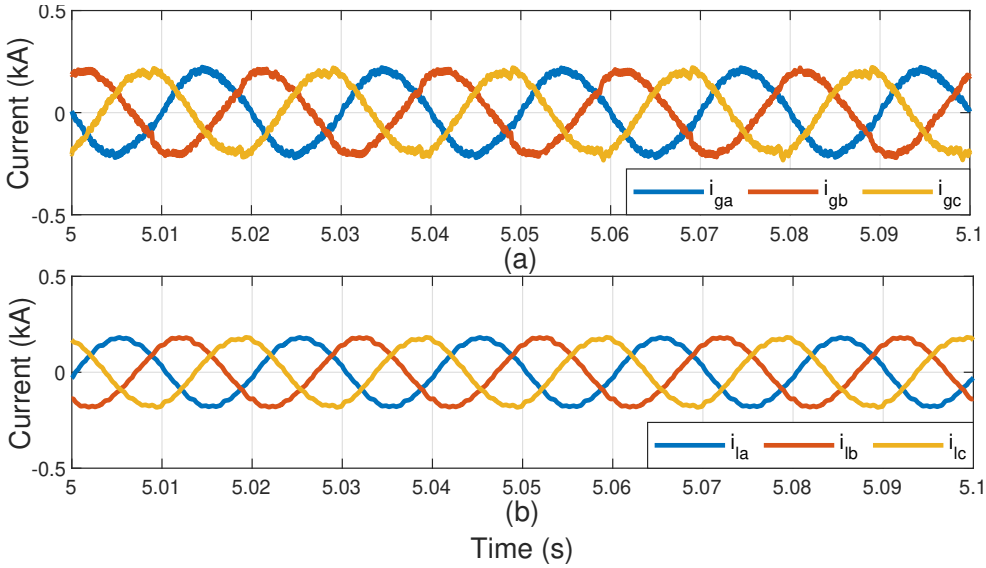

Fig. 49: (a) MMShC's grid-side currents, and (b) MMShC's load-side currents.

In Fig. 50(a) and (b), the MMShC's phase-A String-X and phase-A String-Y submodule-capacitor voltages are shown, respectively. It is interesting to observe in this figure that the proposed MMShC's grid-side control is capable to properly regulate the converter's submodule-capacitor voltages of both strings, according to the provided voltage reference (v_{dc}^{*}). As will be explained in the experimental result subsection, the MMShC's submodule-capacitor voltages are composed of two ripple components, i.e., the swapping ripple and the AC ripple. The swapping ripple is caused by the operation of the swap switches (bidirectional-switch stacks) that connect the submodule strings to the grid and to the load terminals in an alternate fashion. In other words, in this simulation case, when a given submodule string is connected to the load terminal, it supplies power to the RL load and, thus, its submodule capacitors are discharged, which means that the capacitor's voltage is reduced. On the contrary, when a given submodule string is connected to the grid terminal, it absorbs power from the grid and, thus, its submodule capacitors are charged, which means that the capacitor's voltage is increased.

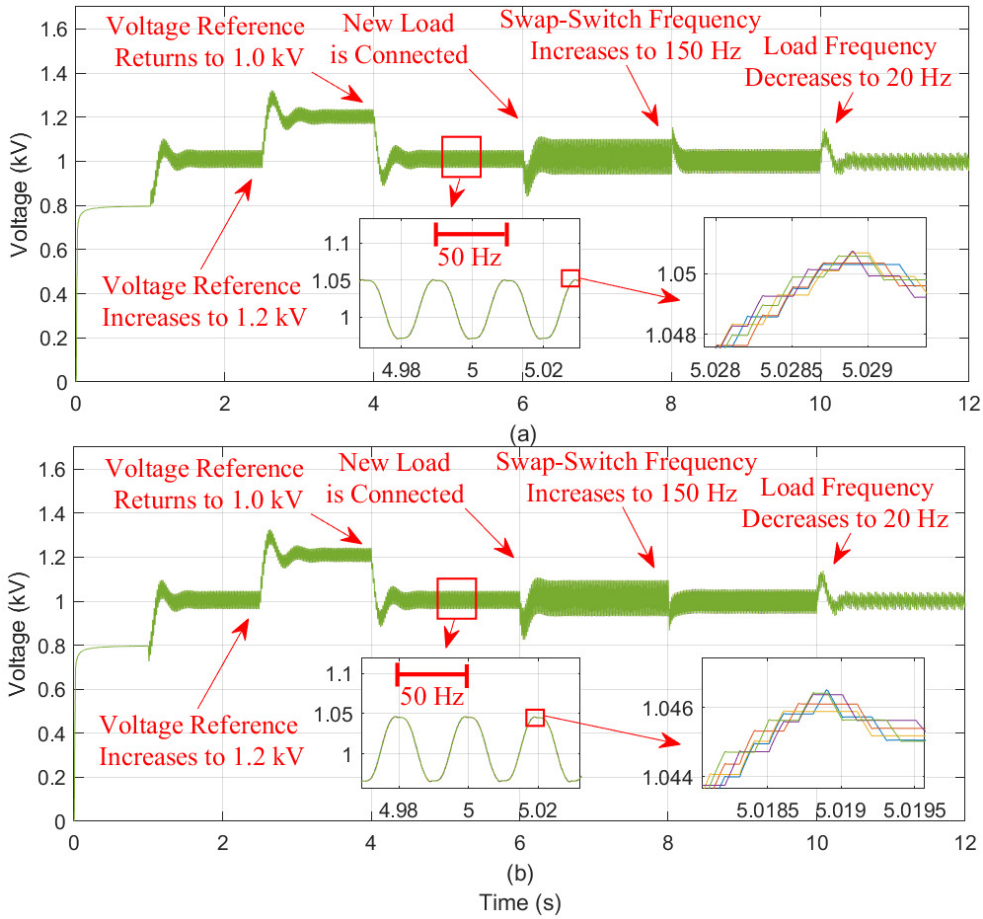

Fig. 50: Simulation results corresponding to the MMShC's operation supplying power to RL load. (a) Phase-A String-X submodule-capacitor voltages, and (b) Phase-A String-Y submodule-capacitor voltages.

By observing the zoom in the submodule-capacitor voltages illustrated in Fig. 50(a) and (b), it is possible to notice that a 50-Hz swapping ripple occurs. This is a consequence of the 50-Hz switching frequency applied to the bidirectional-switch stacks. The swapping ripple amplitude depends on the amount of power charging/discharging the capacitors (essentially the power ratings of the application), on the capacitance of these capacitors, and on the switching frequency of the bidirectional-switch stacks. The swapping ripple will be smaller for higher values of switching frequency of the swap switches, i.e., for the same power being handled by the converter, the capacitors of the string connected to the charging terminal will be less charged before they are connected to the

discharging terminal. The faster the switching between the charging and discharging terminals, the smaller the swapping ripple of the capacitor voltages. At $t = 6$ s, the new load is connected, which means that a higher amount of power starts to flow through the converter. Thus, the amplitude of the swapping voltage ripple increases as the switching frequency of the bidirectional-switch stacks remains fixed. At $t = 8$ s, however, the swap-switch switching frequency is increased to 150 Hz and, thus, the amplitude of the swapping voltage ripple is reduced as shown in Fig. 50(a) and (b). The swapping ripple component is further reduced at $t = 10$ s since a reduced power starts to flow through the converter, at this moment, as illustrated in Fig. 48. Even though the swapping component of the submodule-capacitor voltage ripple is reduced at $t = 10$ s, a different voltage waveform can be observed from this time of the simulation. This is caused by the AC ripple component that is modified because of the change in the frequency value of the voltage synthesized at the load terminals. This ripple component will be further explained later in this thesis. By observing the deeper zoom in the voltage signals of Fig. 50(a) and (b), the $N = 5$ individual voltages of each submodule capacitor within Strings X and Y can be seen. The voltages of all the capacitors within the same string remain with similar values throughout the entire simulation due to the sorting algorithm responsible for the submodule-capacitor voltage balancing (see Fig. 47). Another thing that is interesting to notice in Fig. 50(a) and (b) is how the proposed control is capable to maintain the MMShC's submodule-capacitor voltages regulated, in steady state, according to the received reference, after the transients that occur because of the power variations at the load terminals (at $t = 6$ s and at $t = 10$ s). In other words, the power variations represent disturbances to the submodule-capacitor voltage control, but the average value of the capacitor voltages remain regulated in steady state, proving the effectiveness of the proposed control. Finally, it is important to notice that the MMShC is capable to operate in a stable fashion when its grid-side and load-side terminals operate with equal frequency values ($f_g = f_l = 50$ Hz in this case), which is an advantage in relation to the M^3C that presents unstable behavior in such operation condition, which can easily happen in a WT application.

3.3.2 Converter Driving PMSG-based Wind Turbine

In this subsection, a simulation analysis is performed where the MMShC operates driving a PMSG representing a WT generator. The same converter parameters adopted in the previous subsection are also used in this subsection. The RL load, however, is replaced by the PMSG with rated power, rated voltage, and rated frequency equal to 3 MVA, 5 kV and 60 Hz, respectively. In this case, both the grid side and the load side of the MMShC are controlled in a closed-loop fashion according to the techniques shown in Fig. 46. The simulation results obtained through the software PSCAD/EMTDC are shown in Fig. 51 and in Fig. 52. In this simulation, at $t = 1$ s, the system is initialized and the generator's speed reference is set to $\omega^* = 022$ pu. At $t = 3$ s, the speed reference is increased to $\omega^* = 025$ pu. Finally, at $t = 6$ s, a step up in the machine's

mechanical torque is applied representing a step in the wind speed. In Fig. 51(a), the three-phase voltages synthesized by the converter at its grid-side terminals are shown, which are obviously 50-Hz signals. In Fig. 51(b), the three-phase voltages synthesized by the MMShC at its load-side terminals are shown, which are 15-Hz signals, at the depicted instant, since, at this moment, the generator speed is regulated with a 0.25 pu value, and since the generator's rated frequency is equal to 60 Hz. The generator speed can be seen in Fig. 51(c), where it is clear that the MMShC is capable to properly drive the machine, controlling its speed according to the received speed reference. In Fig. 51(d), the MMShC's grid-side and load-side power (P_g and P_l, respectively) are shown. Similarly to the previous simulation, the converter's grid-side power also follows the load-side power because of the converter's grid-side control, which regulates the submodule-capacitor voltages. In this case, the MMShC's grid-side control injects power into the grid, according to the instantaneous power produced by the WT, in order to always maintain the converter's capacitor voltages regulated. In Fig. 51(d), the power variations caused by the change in the generator's speed reference, and caused by the step up in the wind speed, can be observed.

The MMShC's phase-A String-X and phase-A String-Y submodule-capacitor voltages are shown in Fig. 52(a) and in Fig. 52(b), respectively. Once again, the proposed control is capable to maintain the submodule-capacitor voltages of both strings regulated, and with a relatively low ripple, throughout the entire simulation period. The swapping ripple component could be further reduced by increasing the switching frequency of the bidirectional-switch stacks, as previously explained. By taking a closer look into the submodule-capacitor voltage waveforms (zoom in voltage signals), one can observe the individual voltages of the N capacitors within each submodule string. Once again, these voltages remain with similar values because of the sorting algorithm responsible for the submodule-capacitor voltage balancing.

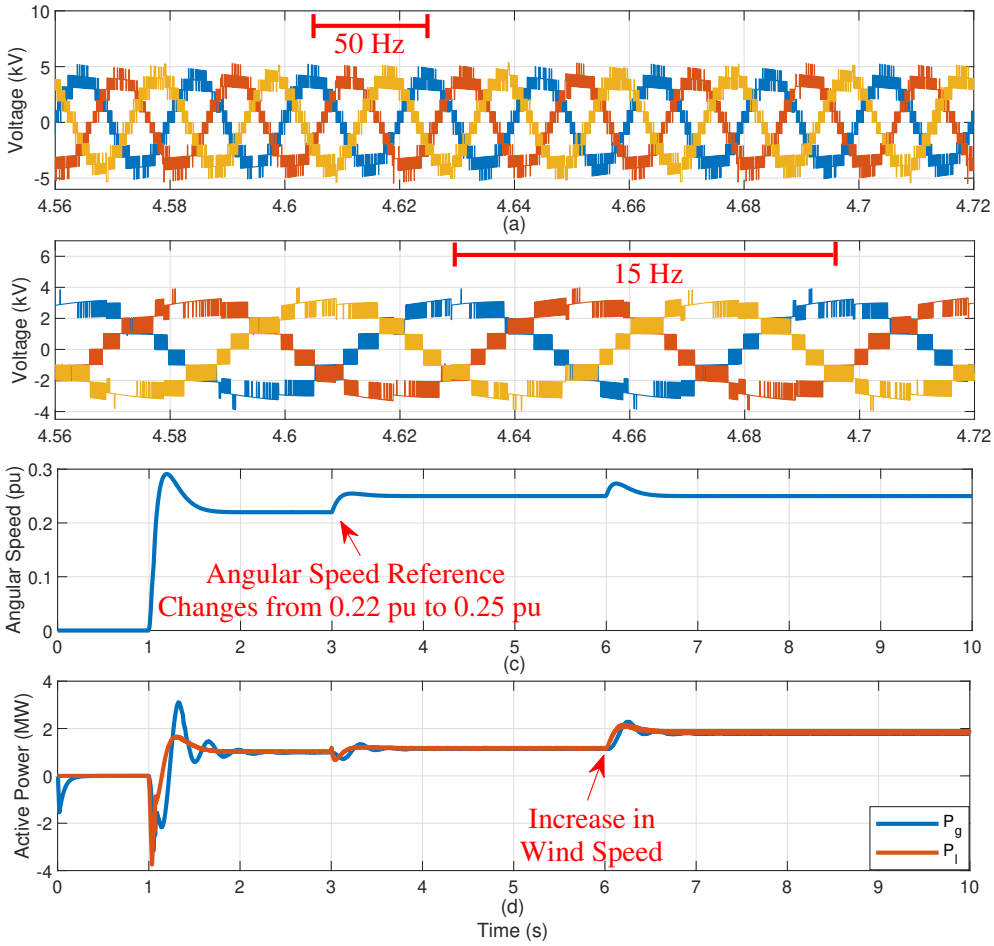

Fig. 51: Simulation results corresponding to the MMShC's operation driving a PMSG. (a) Three-phase voltages synthesized at the grid-side terminals, (b) three-phase voltages synthesized at the load-side terminals, (c) generator's speed, and (d) grid-side and load-side power.

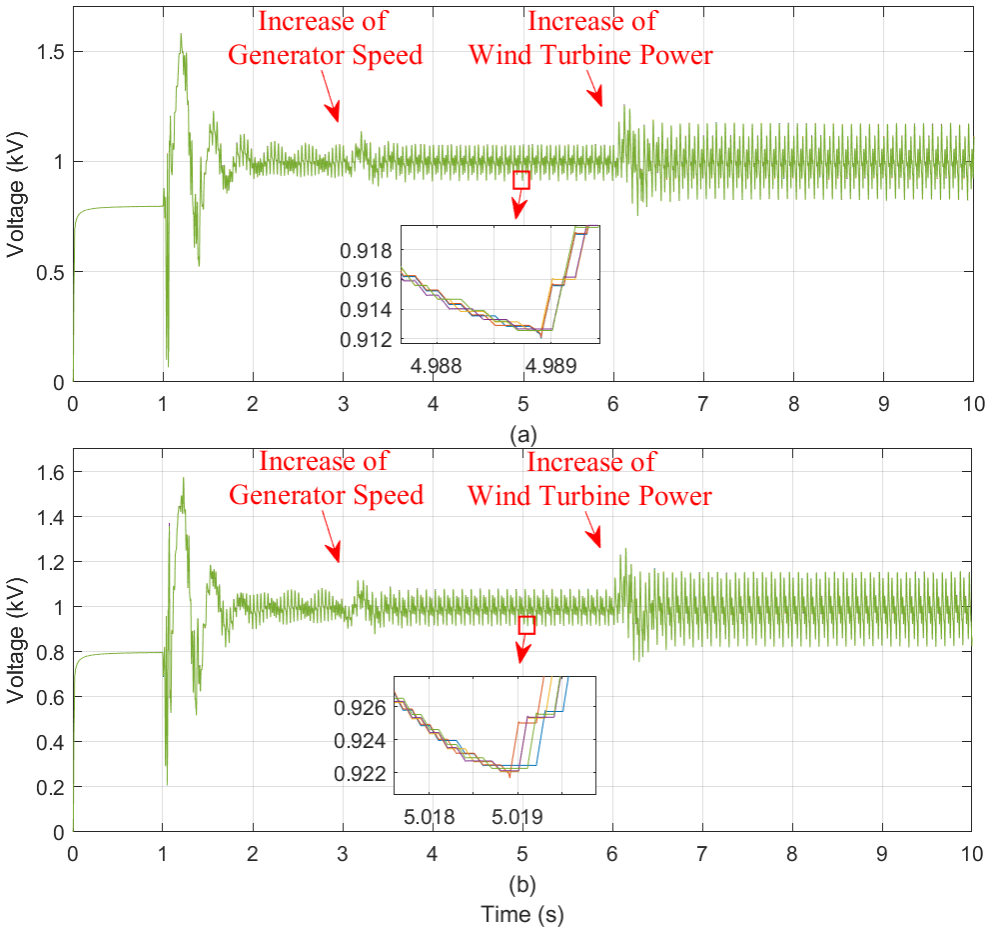

Fig. 52: Simulation results corresponding to the MMShC's operation driving a PMSG. (a) Phase-A String-X submodule-capacitor voltages, and (b) Phase-A String-Y submodule-capacitor voltages.

3.3.3 Experimental Validation

In this section, experimental results are presented, which were obtained through a low-scale prototype of the MMShC. In Fig. 53, a picture of the MMShC's experimental test setup is shown, along with an electrical diagram explaining the prototype hardware. The test setup hardware corresponds to a single-phase version of the MMShC that is composed of two strings (String X and String Y) with $N = 3$ FB submodules each. These submodules are built with four IGBTs and with one $C = 16$-mF capacitor. The test setup hardware is also composed of four bidirectional switches in a way that two

of these switches form one swap circuit, resulting in the two swap circuits, i.e., Swap 1 and Swap 2. A Texas Instruments TMS320F28379D digital-signal processor (DSP) was used to control the converter. A 5-mH inductor was connected to both the grid-side terminal and to the load-side terminal of the converter (inductors L_g and L_L). An AC power supply was used to emulate a $V_g = 50$-V, $f_g = 50$-Hz grid. The converter supplied power to a resistive load with a resistance of $R_l = 16$ mΩ. The grid-side control technique proposed in this thesis, and explained in Fig. 46, was used to regulate the converter's submodule-capacitor voltages. These voltages were regulated with a value equal to 23 V. The load-side control was performed in an open-loop fashion receiving a voltage reference with amplitude equal to 50 V and with frequency equal to 20 Hz. The MMShC's internal control presented in Fig. 47 was implemented through a programming code into the DSP. The switching frequency of the swap switches (bidirectional switches) was kept fixed with a value equal to 20 Hz.

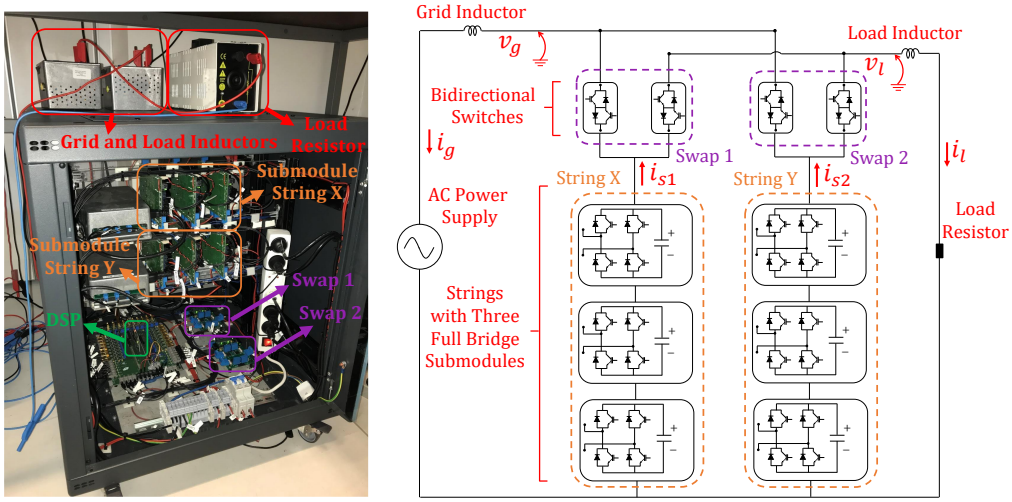

Fig. 53: MMShC experimental test setup along with the electrical diagram explaining the test setup hardware.

In Fig. 54, the experimental results of the MMShC's grid-side and load-side voltages and currents are shown. In the first sub figure of Fig. 54 (the uppermost one), the voltage synthesized by the converter at its load-side terminal, without any filtering stage, is shown. In the second sub figure of Fig. 54, the load current is shown. In the third sub figure of Fig. 54, the voltage synthesized by the converter at its grid-side terminal, without any filtering stage, is shown. Finally, in the fourth sub figure of Fig. 54 (the lowest one), the grid current is shown. It is very interesting to observe in this figure how the MMShC is in fact capable to operate as a controlled voltage source synthesizing voltages with different frequencies at its two terminals. Besides, it is also interesting to

notice that the converter is capable to synthesize voltages with a relatively high power quality (multilevel voltages) even though its submodule strings were built with three FB submodules only. Once again, it is important to highlight that the voltage signals shown in Fig. 54 are the switched voltages synthesized at the converter terminals without any intermediate filtering stage. A small filter would be enough to filter out the harmonics of these voltages, specially if a higher number of levels was adopted for the converter submodule strings.

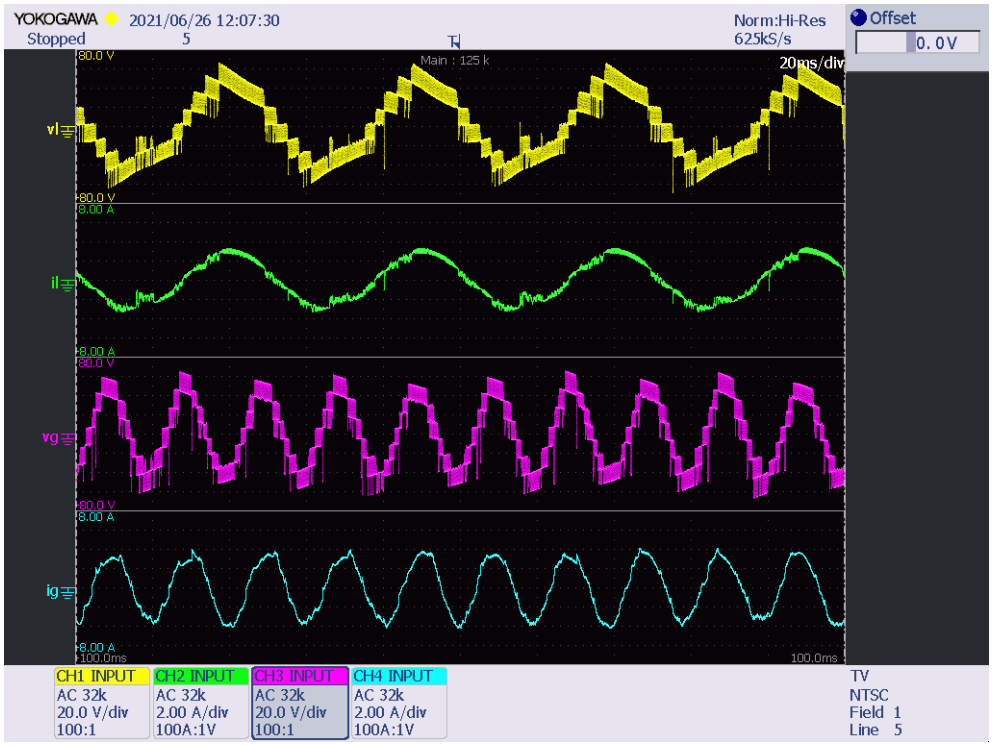

Fig. 54: Experimental results. The voltage synthesized by the MMShC at its load-side terminal is shown in the first and uppermost sub figure. The load current is shown in the second sub figure. The voltage synthesized by the MMShC at its grid-side terminal is shown in the third sub figure. The grid current is shown in the fourth and lowest sub figure.

In Fig. 55, the experimental results corresponding to the MMShC's String-X submodule-capacitor voltages are shown. In this figure, it is possible to notice that the proposed control is capable to regulate the converter's submodule capacitor voltages with the desired value equal to $v_{dc}^{*} = 23$ V. In this figure, the previously explained swapping ripple component can be observed. In this experimental test, the swapping voltage ripple

presents a 20-Hz frequency, which is a consequence of the switching frequency defined for the bidirectional switches (swap switches).

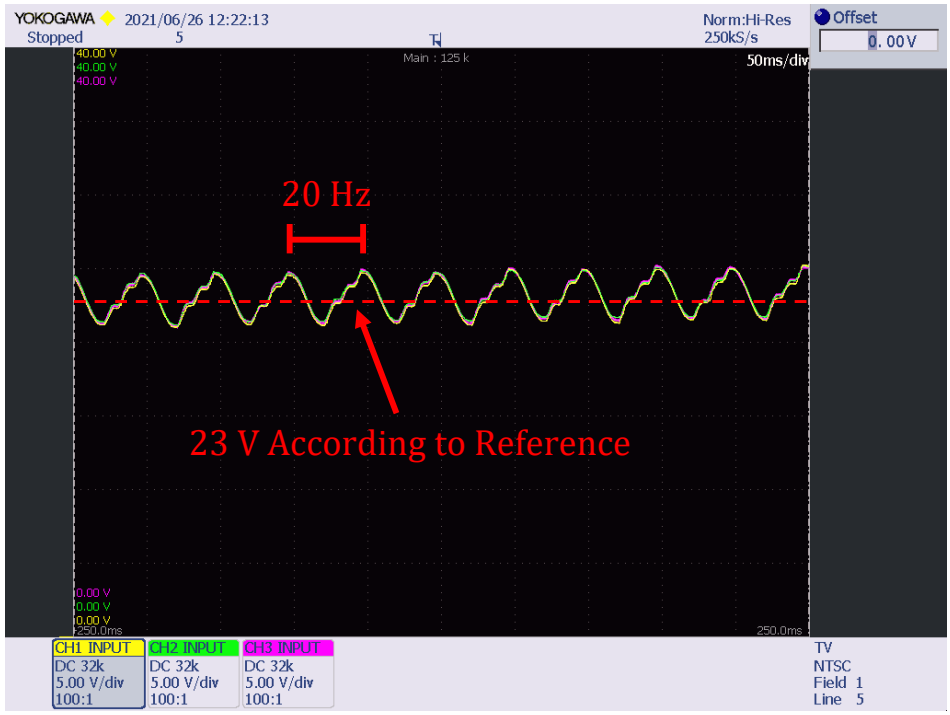

Fig. 55: Experimental results of MMShC's String-X submodule-capacitor voltages.

In Fig. 56, a zoom of the MMShC's String-X and String-Y submoule-capacitor voltage signals are shown. In this closer view, the individual voltages of each submodule capacitor within the strings can be observed. These voltages are balanced and they present similar values because of the sorting algorithm responsible for the submodule-capacitor voltage balancing, which was previously presented. The voltage signals illustrated in Fig. 56 are capable to demonstrate in a clear way the second ripple component of the MMShC's submodule-capacitor voltages, i.e., the AC ripple component. The AC ripple occurs in between the swapping ripple, and it is caused by the AC currents flowing through the converter's submodule strings. As previously explained, the MMShC can essentially be seen as two SSBC converters that are connected in an alternate and complementary fashion to the grid and to the load terminals through the action of the swap switches. Similarly to the SSBC converter, the MMShC operates inserting and bypassing submodules with an insertion pattern that can be approximated by a sinusoidal

signal with a frequency equal to w_t, which is the frequency of the voltage to be synthesized at the given terminal. The w_t voltage will produce a w_t current, which will flow through the submodule string. The product of the w_t current by the w_t insertion index pattern results in a $2w_t$ current component flowing through the submodule capacitor producing the $2w_t$ AC voltage ripple. However, since the MMShC's submodule strings are connected to the grid and to the load terminals in an alternate and complementary fashion, then the AC ripple component of the submodule-capacitor voltages will have a frequency of w_g, while the corresponding string is connected to the grid terminal, and it will have a frequency of w_l, while the corresponding string is connected to the load terminal.

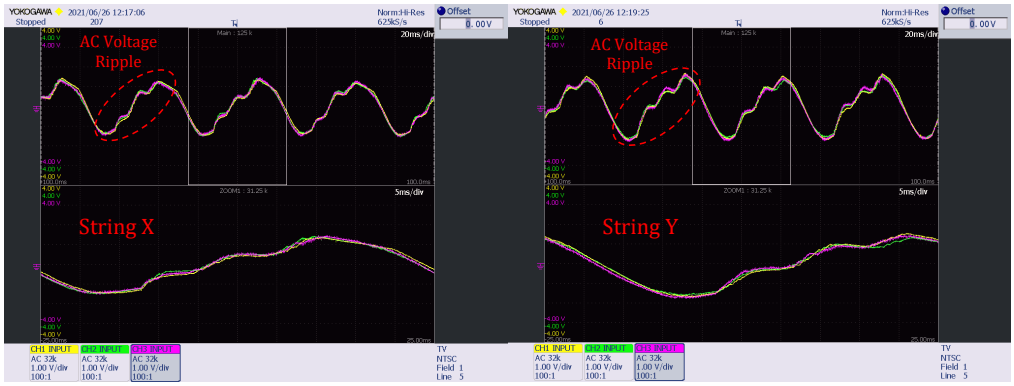

Fig. 56: The left-hand-side sub figure shows the MMShC's String-X submodule-capacitor voltages while the right-hand-side sub figure shows the MMShC's String-Y submodule-capacitor voltages.

In summary, the experimental results presented in this section proved that the MMShC is capable to operate synthesizing high-power-quality voltages with different frequencies at its two terminals, while maintaining its submodule-capacitor voltages regulated and stable because of the proposed grid-side closed-loop control. The MMShC's internal control was also validated through the experimental results presented in this section. The converter's internal control is composed of the swap-switch control logic, of the voltage modulation, and of the submodule-capacitor voltage-balancing algorithm.

3.4 Comparative Analysis in Terms of Component Count and Power Ratings

In this section, the same comparative analysis that was performed in Section 2.5 for the MMC, the M^{3}C, the MMSC, and the 3x3-MMSC, will be performed now considering also the MMShC. The MMShC's string voltage (V_{string}) should ideally be designed as described in (76) so that the converter is capable to synthesize an AC voltage with

amplitude equal to V_{peak} at its two terminals.

$$V_{string} \geq V_g = V_l = V_{peak} \tag{76}$$

The string voltage is divided between the N submodule capacitors that compose one converter string. Similarly to other topologies analyzed in this thesis, a sorting algorithm is adopted to maintain all the MMShC's submodule capacitors within one string with similar voltage values, then it is a fair assumption to consider that the nominal operational voltage of each submodule capacitor is equal to $V_{cap} = \frac{V_{string}}{N}$. The string submodules (and their IGBTs) must be capable to withstand at least the nominal operational voltage of their capacitors. In other words:

$$V_{sub} \geq V_{cap} = \frac{V_{string}}{N} \tag{77}$$

Where V_{sub} is the maximum voltage tolerated by the submodule's IGBTs. Similarly to the other topologies analyzed in this thesis, the ideal situation is also considered for the MMShC, i.e., $V_{string} = V_{peak}$, and $V_{sub} = V_{cap} = \frac{V_{peak}}{N}$.

Not only the converter's submodule strings, but its bidirectional-switch stacks must also be considered in the analysis. These bidirectional-switch stacks must be capable to block a voltage equal to the sum of the peak values of the voltages synthesized at the grid and at the load terminals by String X and by String Y. In other words:

$$V_{BS} \geq V_g + V_l \tag{78}$$

Where V_{BS} is the maximum voltage tolerated by the bidirectional-switch stack. Since $V_g = V_l = V_{peak}$ is considered, then (78) can be rewritten as:

$$V_{BS} \geq V_g + V_l = 2V_{peak} \tag{79}$$

The current that flows through each submodule string and through each bidirectional-switch stack of the MMShC is equal to:

$$I_{string} = I_{BS} = I_g = I_l = I_{RMS} \tag{80}$$

The MMShC submodule string is built with FB submodules, which are composed of four IGBTs and of one capacitor. The submodule IGBTs must be capable to block the voltage V_{sub}, defined according to (77), and must be capable to conduct the string current (I_{string}), defined according to (80). Once again, considering the ideal case where $V_{sub} = \frac{V_{peak}}{N}$, then the power ratings of the IGBTs of the MMSC's FB submodules can be described as follows:

$$P_{IGBT_{FB}} = V_{sub} I_{string} = \frac{V_{peak} I_{RMS}}{N} \tag{81}$$

Each IGBT stack of the MMShC's bidirectional-switch stacks must be capable to block the full bidirectional-switch-stack voltage (which is equal to $V_{BS} = 2V_{string}$ in the ideal case), and each IGBT stack must be capable to conduct the string current ($I_{BS} = I_{string} = I_{RMS}$). Then, the power ratings of each IGBT stack of the MMShC bidirectional-switch stacks can be calculated as follows:

$$P_{IGBT_{BS}} = V_{BS} I_{BS} = 2V_{peak} I_{RMS} \tag{82}$$

The MMShC is composed of six strings (see Fig. 40), each string is composed of N FB submodules and each FB submodule is composed of four IGBTs. Thus, the total number of IGBTs in the MMShC FB submodules is equal to $N_{IGBT_{FB}} = 6 \times N \times 4 = 24N$. The MMShC is also composed of twelve bidirectional-switch stacks, each of them is composed of two IGBT stacks. Thus, the total number of IGBT stacks in the MMShC is equal to $N_{IGBT_{BS}} = 12 \times 2 = 24$. The total MMShC semiconductor-device power ratings can be calculated as follows:

$$\begin{aligned} P_{SD} &= P_{IGBT_{FB}} N_{IGBT_{FB}} + P_{IGBT_{BS}} N_{IGBT_{BS}} \\ &= 24V_{peak} I_{RMS} + 48V_{peak} I_{RMS} = 72V_{peak} I_{RMS} \end{aligned} \tag{83}$$

Now keeping the IGBT's rated voltage fixed with the previously defined value of V_{IGBT}, and remembering that the MMShC's string voltage is equal to $V_{string} = V_{peak}$, then the number of FB submodules composing each string of the converter is equal to:

$$N = \frac{V_{string}}{V_{IGBT}} = \frac{V_{peak}}{V_{IGBT}} \tag{84}$$

Once again, the MMShC is composed of six strings, each string is composed of N FB submodules and each FB submodule is composed of one capacitor. Thus, the total number of submodules and of capacitors in the MMShC is equal to $N_{sub} = N_{cap} = 6 \times \frac{V_{peak}}{V_{IGBT}} \times 1 = \frac{6V_{peak}}{V_{IGBT}}$. It is also important to emphasize that the MMShC only requires three inductors connected between each phase of the converter and each phase of the grid.

The results of the comparative analysis between the MMC, the M^{3}C, the MMSC, the 3x3-MMSC, and the MMShC are summarized in Table 8 and in Table 9. To eliminate the literal expressions, and to obtain fully numerical values, the results presented in Table 8 are divided by $V_{peak} I_{RMS}$, and the results presented in Table 9 are multiplied by $\frac{V_{IGBT}}{V_{peak}}$. Since the results presented in in Table 8 and in Table 9 aim at only providing a comparative view between the converter topologies, then having units for the quantities is not necessary. As previously explained in Section 2.5, the 3x3-MMSC seems to be the converter solution with the best structural characteristics, i.e., it is the one with the least number of submodules and of capacitors and with semiconductor-device power ratings only slightly higher than the MMC, which is the solution with the least semiconductor-device power ratings. Obviously, as previously explained, the 3x3-MMSC's input current

filter is an issue that requires further investigation in the future. In other words, even though the 3x3-MMSC does not require arm/string inductors, as in the MMC and in the M^{3}C case, the converter requires the potentially bulky current filter. Deeper investigations to find efficient and relatively compact filters are required as future works, so that concrete comparative conclusions can be made on the cost, volume and weight of this filter in comparison to the MMC's and the M^{3}C's arm/string inductors. The MMShC is the topology with the highest semiconductor-power requirements, which contributes for an increased cost. Nonetheless, the MMShC presents a considerably reduced submodule and capacitor count in comparison with the MMC and with the M^{3}C. This fact certainly contributes to an overall reduced cost, volume, and weight, specially because these capacitors can be quite bulky and heavy depending on the power levels of the considered application. Besides, the MMShC only requires three inductors, which is an advantage in relation to the MMC (that requires twelve arm inductors) and in relation to the M^{3}C (that requires nine string inductors). Furthermore, the MMShC does not require the potentially bulky and heavy input current filter required in the 3x3-MMSC. Thus, even though the 3x3-MMSC requires half the number of submodules and of capacitors in comparison to the MMShC, the MMShC could potentially be the topology with the least overall volume and weight between all the considered converter topologies, at least if a compact filter cannot be found for the 3x3-MMSC. Besides the structural features, the MMShC also presents important operational characteristics (which are advantageous over the 3x3-MMSC) such as its behavior as a controlled voltage source from both the grid and the load perspectives, which certainly contributes for its commercial feasibility and competitiveness. However, it is important to highlight that the 3x3-MMSC and the MMShC are not proposed for the same applications, as the 3x3-MMSC presents high performance at low frequencies (which should be suitable for machine drives that operate with low speeds), whereas the MMShC should be more suitable for WT applications where similar frequencies can occur at the two terminals of the converter.

Table 8: Semiconductor-Device Power Requirements (P_{SD}).

MMC	**M^{3}C**	**MMSC**	**3x3-MMSC**	**MMShC**
40.8	48.24	65.57	43.14	72

Table 9: Submodule and Capacitor Count.

MMC	**M^{3}C**	**MMSC**	**3x3-MMSC**	**MMShC**
24	18	6	3	6

The comparative analysis in terms of submodule and capacitor count (whose results are summarized in Table 9) is based on the concept illustrated in Fig. 57, where an example comparing the MMC and the proposed MMShC is presented. In other words, let

us suppose a situation in which a 5-level voltage with peak value equal to 2 kV (see the lower-right sub figure of Fig. 57) is desired. The MMC and the MMShC must be capable to synthesize the desired voltage at their AC terminals, while being built with submodules with nominal voltage equal to 1 kV (considering the ideal case where the IGBT rated voltage is equal to the nominal submodule-capacitor voltage, which are both equal to 1 kV). In order to synthesize the desired voltage, the MMC would have to be designed with a DC-side voltage equal to 4 kV, which means that the sum of the voltages of all the submodule capacitors in the converter's arm would also have to be equal to 4 kV. Based on the previously explained conditions, then one leg of the MMC would have to be built with eight 1-kV HB submodules as illustrated in the left-hand-side sub figure of Fig. 57. The MMShC, on the other hand, could be built with only two FB submodules (as illustrated in the upper-right sub figure of Fig. 57) to be capable to synthesize the exact same 5-level voltage, with peak value equal to 2 kV, at its AC terminals. Since the back-to-back MMC is composed of six legs, and the MMShC is composed of six strings, then the MMC would have to be built with four times more submodules and capacitors than the MMShC to be capable to synthesize the same voltage profile at its AC terminals. Obviously, only the information of the number of capacitors does not give us very concrete conclusions since the size (capacitance) of these capacitors must also be considered. Nonetheless, having a reduced number of submodules/capacitors should naturally contribute for a reduced volume and weight of the solution since, for example, two 1-kV 5-mF capacitors should be heavier and should occupy more space than one 1-kV 10-mF capacitor because the volume and weight of high-power capacitors are not completely linear with their capacitances. Besides, even though the high-power capacitor is the heaviest and bulkiest element of a submodule, some other elements such as the heatsink, the mechanical by-pass switch, and the submodule metallic structure itself also play an important role in the total volume and weight of a submodule. For this reason, heaving a reduced number of submodules also contributes for an overall reduced volume and weight of the converter solution. Finally, there should be some space between the submodules for insulation purposes and, thus, the overall space occupied by two submodules with 1-kV 5-mF capacitors should be considerably bigger than the space occupied by one single submodule with a 1-kV 10-mF capacitor.

As previously explained, the 3x3-MMSC is proposed for machine-drive applications that operate with low frequencies due to its considerably reduced submodule-capacitor voltage ripple at low-frequency operation in relation to the MMC. The high performance of the 3x3-MMSC at low frequencies (related to its low submodule-capacitor voltage ripple at this frequency range) was explained and demonstrated in this thesis. Thus, besides having the advantages related to being built with a reduced number of submodules and of capacitors, this topology should also require submodule capacitors with a reduced capacitance, which further contributes for its lightness and compactness. The MMShC, on the other hand, is not proposed for low-frequency operation, and the size of its capacitors should be analyzed to obtain more concrete conclusions in terms

of volume and weight of the solution. An analysis of the MMShC submodule-capacitor voltage ripple in comparison to the MMC one is presented below.

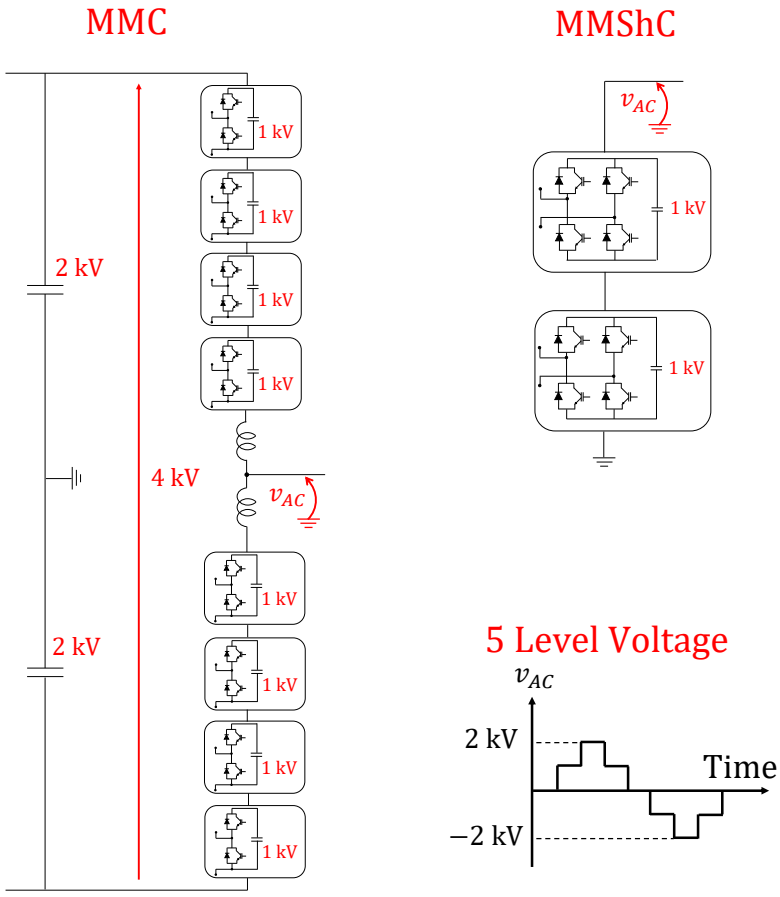

Fig. 57: Illustrative example explaining basic concept adopted for the comparative analysis in terms of submodule and capacitor count.

As previously explained in this thesis, if the MMC is supposed to synthesize a ω voltage at its AC terminals, then its arm submodules will have to be inserted and by-passed with the following pattern:

$$S_{MMC}(t) = 0.5sin(\omega t) + 0.5 \tag{85}$$

The signal presented in (85) is a continuous approximation of the real submodule insertion pattern of the MMC. $S_{MMC}(t)$ is a sinusoidal signal that varies between 0

and 1, in which 0 means that all the arm submodules are by-passed, and 1 means that all the arm submodules are inserted. If the AC circulating currents are neglected, the MMC's arm current can be described as follows:

$$i_{arm}(t) = \frac{i_{AC}(t)}{2} + \frac{i_{DC}(t)}{3} \tag{86}$$

Let us suppose that the MMC's AC current for a given operation condition is the one described below:

$$i_{AC}(t) = I_{peak} sin(\omega t + \theta) \tag{87}$$

Supposing an operation with unit power factor, and supposing an approximation that the MMC's AC-side and DC-side power are equal, then the following expression can be obtained:

$$\sqrt{3}(\frac{\sqrt{3}}{\sqrt{2}} V_{peak}) \frac{I_{peak}}{\sqrt{2}} = V_{DC} I_{DC} \tag{88}$$

The following expression can be obtained for the MMC's DC current by rearranging (88):

$$i_{DC}(t) = I_{DC} = \frac{3 V_{peak} I_{peak}}{2 V_{DC}} \tag{89}$$

Then, by substituting (87) and (89) into (86), the following equation is obtained for the MMC's arm current:

$$i_{arm}(t) = \frac{I_{peak}}{2} sin(\omega t + \theta) + \frac{V_{peak} I_{peak}}{2 V_{DC}} \tag{90}$$

The MMC's submodule-capacitor current, which produces the voltage ripple, can be calculated as the product of (85) and (90), as described in the equation below:

$$i_{capMMC}(t) = S_{MMC}(t) i_{arm}(t) \tag{91}$$

If the MMShC is supposed to synthesize a ω voltage at its AC terminals, then its string submodules will have to be inserted and by-passed with the following pattern:

$$S_{MMShC}(t) = sin(\omega t) \tag{92}$$

Similarly to the MMC case, the signal presented in (92) is a continuous approximation of the real submodule insertion pattern of the MMShC. $S_{MMShC}(t)$ is a sinusoidal signal that varies between -1 and 1, in which -1 means that all the string's FB submodules are inserted with negative polarity, and 1 means that all the string's FB submodules are inserted with positive polarity. The MMShC's string current can be described as

follows:

$$i_{string}(t) = i_{AC}(t) = I_{peak} sin(\omega t + \theta) \tag{93}$$

The MMShC's submodule-capacitor current, which produces the voltage ripple, can be calculated as the product of (92) and (93), as described in the equation below:

$$i_{capMMShC}(t) = S_{MMShC}(t) i_{string}(t) \tag{94}$$

Let us consider an example where $I_{peak} = 1$ kA, and $V_{DC} = 2V_{peak}$ (which is the ideal case considered in the comparative analysis), then the following numerical expressions are obtained for the MMC's arm current and for the MMShC's string current:

$$i_{arm}(t) = 0.5 sin(\omega t + \theta) + 0.25 \quad \text{kA} \tag{95}$$

And

$$i_{string}(t) = sin(\omega t + \theta) \quad \text{kA} \tag{96}$$

By substituting (85) and (95) into (91), then a numerical expression can also be obtained for the MMC's submodule-capacitor current as described bellow:

$$i_{capMMC}(t) = [0.5 sin(\omega t) + 0.5] \times [0.5 sin(\omega t + \theta) + 0.25] \quad \text{kA} \tag{97}$$

By substituting (92) and (96) into (94), then a numerical expression can also be obtained for the MMShC's submodule-capacitor current as described bellow:

$$i_{capMMShC}(t) = sin(\omega t) \times sin(\omega t + \theta) \quad \text{kA} \tag{98}$$

By considering the trigonometric identity presented in (99), and by considering $\theta = 0$, then (97) can be rewritten as presented in (100). Similarly, by considering the trigonometric identity presented in (99), and by considering $\theta = 0$, then (98) can be rewritten as presented in (101).

$$sin^2(\omega t) = \frac{1 - cos(2\omega t)}{2} \tag{99}$$

$$i_{capMMC}(t) = -0.125 cos(2\omega t) + 0.375 sin(\omega t) + 0.25 \quad \text{kA} \tag{100}$$

$$i_{capMMShC}(t) = -0.5 cos(2\omega t) + 0.5 \quad \text{kA} \tag{101}$$

In (100) and (101), numerical expressions of the MMC's and of the MMShC's submodule-capacitor currents are presented, respectively, which were obtained through equal assumptions ($I_{peak} = 1$ kA), which means that a fair comparison can be es-

tablished. These are the currents flowing through the submodule capacitors of the converters producing the AC voltage ripple. By observing these two currents, one can conclude that the capacitor's AC voltage ripple will be higher in the MMC case than in the MMShC case. In order to understand the reason why, first it is important to emphasize that a capacitor's reactance is inversely proportional to the frequency of the current flowing through it ($X_C = \frac{1}{\omega C}$). Then, let us suppose an example in which $\omega = 314.16$ rad/s (corresponding to 50 Hz), and where $C = \frac{1}{314.16}$. In this specific case, the capacitor's reactance for the ω component is equal to 1 Ω, and it is equal to 0.5 Ω for the 2ω component. Thus, in this specific example, the voltage ripple (or voltage drop) for the MMC's ω component would be equal to $V_{\omega ripple} = 0.375 \times X_C = 0.375 \times 1 = 0.375$ kV. The voltage ripple for the MMShC's 2ω component would be equal to $V_{2\omega ripple} = 0.5 \times X_C = 0.5 \times 0.5 = 0.25$ kV. It is important to notice that the MMC's ω voltage ripple is considerably higher than the MMShC's 2ω voltage ripple. Besides, the MMC's submodule capacitor also experiences an extra voltage ripple component caused by the 2ω current component. The MMC's 2ω voltage ripple component would have an amplitude of $V_{2\omega ripple} = 0.125 \times X_C = 0.125 \times 0.5 = 0.0625$ kV. The 2ω ripple component could add up to the ω component, leading to an even higher submodule-capacitor voltage ripple.

To validate the previously presented analysis, simulations were carried out in the software PSCAD/EMTDC with the simple model shown in Fig. 58. In these simulations, the MMC's and the MMShC's submodule-capacitor currents (described in (100) and (101), respectively) were provided to a current source (in two independent simulations), and this current source was used to charge a 1-mF capacitor. A high-pass filter was used to eliminate the DC current components of (100) and (101) in such a way that only the capacitor's AC voltage ripple could be analyzed.

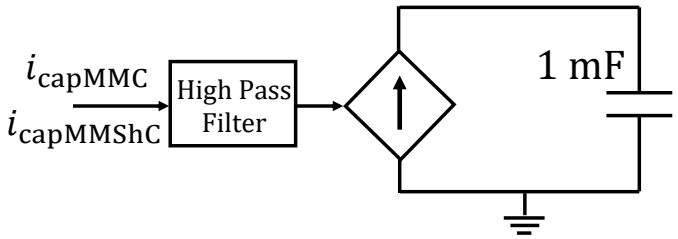

Fig. 58: Simulation model used to analyze and to compare the MMC's and the MMShC's AC submodule-capacitor voltage ripple.

In Fig. 59(a), the MMC's and the MMShC's submodule capacitor currents (applied to the current source, after eliminating the DC components) are presented. In Fig. 59(b), the corresponding submodule-capacitor voltage ripple is shown for the MMC and for the MMShC cases. As expected from the mathematical analysis previously explained, the MMC's submodule-capacitor voltage ripple is in fact considerably higher than the MMShC's one.

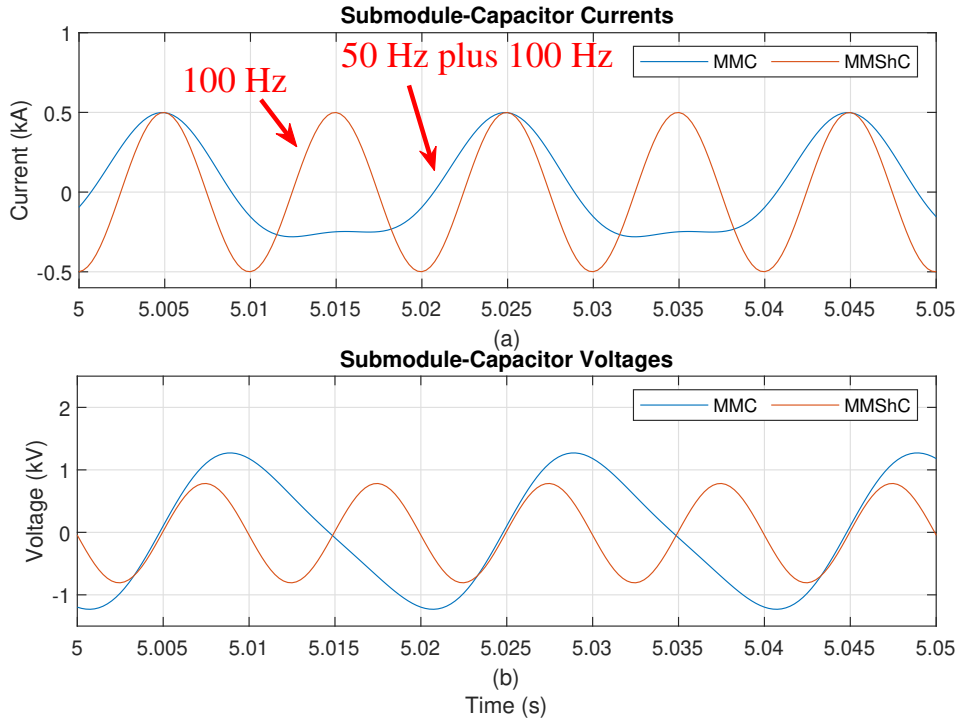

Fig. 59: Simulation results comparing the MMC's and the MMShC's capacitor voltage ripple. (a) MMC's and MMShC's capacitor currents, and (b) MMC's and MMShC's capacitor voltage ripple.

The analysis whose results are presented in Fig. 59 corresponds to the case where $\theta = 0$ was considered. However, it is widely known that the MMC's submodule-capacitor voltage-ripple amplitude can considerably vary depending on the converter's operational power factor [72]. To analyze the MMC's capacitor voltage ripple for different power factor values, then some different simulations were carried out considering different values for the angle θ. The simulation results are presented in Fig. 60(a) and (b). The MMShC's capacitor ripple does not change for different values of θ, and that is why there is only one curve representing the MMShC's capacitor voltage ripple in Fig. 60(a) and (b). In Fig. 60(a), the cases where the MMC's capacitor voltage ripple is bigger than the MMShC's one are shown, whereas in Fig. 60(b), the cases where the MMC's capacitor voltage ripple is smaller than the MMShC's one are shown. As demonstrated in Fig. 60(a), the MMC's capacitor voltage ripple is bigger than the MMShC's one for several values of θ, which means that for several different operation conditions (different power factor values), the MMC's capacitor voltage ripple is bigger and, thus the MMC's submodule capacitor capacitance would have to be bigger than the MMShC's one so that a voltage ripple with equal amplitude was obtained in the worst-case scenario.

According to Fig. 60(a), the MMC's capacitor voltage ripple is approximately 1.63 times bigger than the MMShC's one, in the worst-case scenario. This figure is comparing the capacitor voltage ripple of the MMC's arm in relation to the MMShC's string. Since the back-to-back MMC is composed of twelve arms, and the MMShC is composed of six strings, then it is possible to state that the total capacitance of the MMC would have to be approximately equal to $2 \times 1.63 = 3.26$ times bigger than the MMShC's total capacitance so that an AC submodule-capacitor voltage ripple with the same amplitude was obtained in the worst-case scenario.

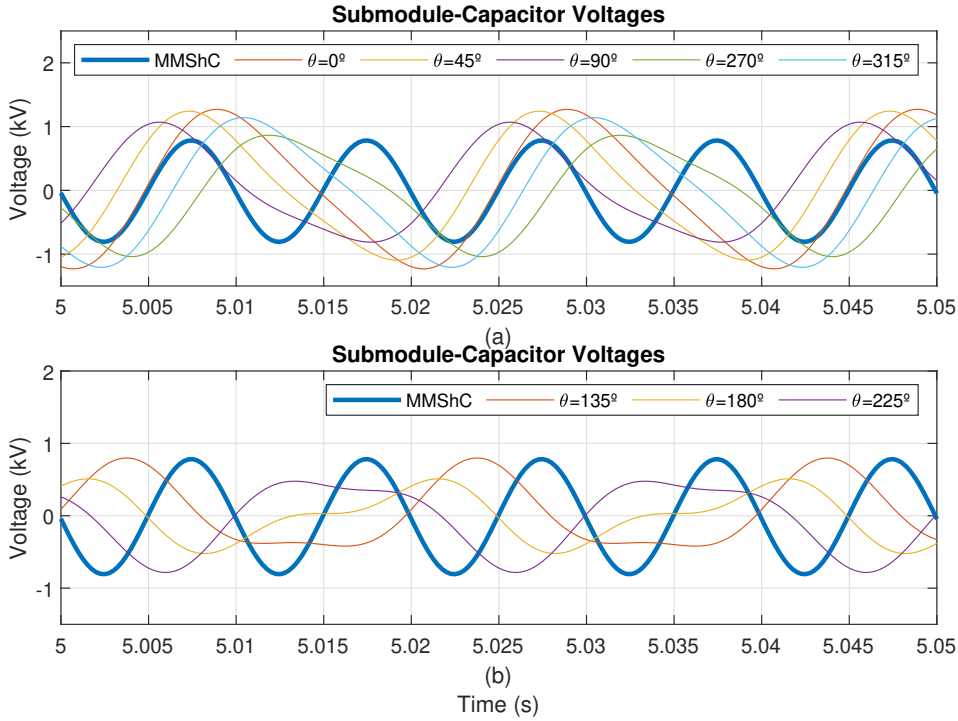

Fig. 60: Simulation results to compare MMC's and MMShC's capacitor voltage ripple. (a) Cases where MMC's capacitor voltage ripple is bigger than MMShC's one, and (b) cases where MMC's capacitor voltage ripple is smaller than MMShC's one.

The previously presented analysis was related to the MMShC's AC capacitor voltage ripple component. As previously explained in this thesis, there is a second voltage ripple component imposed to the MMShC's submodule capacitors, i.e., the swapping voltage ripple. The swapping ripple is a natural consequence of the MMShC's topology and operation. In other words, while the converter's strings remain connected to the generator terminals, its submodule capacitors are always charged by the DC component of the submodule-capacitor current (as described in (101)). On the contrary, while the

converter's strings remain connected to the grid terminals, its submodule capacitors are always discharged by the DC component of the submodule-capacitor current. The sbmodule-capacitor voltage variation during these charging/discharging cycles will be bigger or smaller depending on how fast the submodule strings are swapped between the charging and the discharging terminals, i.e., depending on the switching frequency of the bidirectional-switch stacks (swap switches). Obviously, the submodule-capacitor voltage variation (the swapping ripple) will be bigger or smaller depending on the amount of power handled by the converter, and depending on the energy stored in these submodule capacitors. Thus, it is clear that, if the same power is handled by the converter and if the same bidirectional-switch-stack switching frequency is adopted, then the swapping ripple will be bigger or smaller depending on how big the capacitance of the submodule capacitors is. However, its is also important to highlight that the capacitor's energy is equal to $E_c = \frac{1}{2}CV^2$, which means that it increases with the square of the capacitor's voltage. Thus, considering the same converter's power ratings, if higher voltage ratings (and thus lower current ratings) is adopted, then more energy will be stored in the converter's submodule capacitors contributing for a smaller capacitor voltage variation during the charging/discharging cycles, i.e., leading to a smaller swapping voltage ripple.

In any case, the switching frequency of the swap switches is a variable that can be continuously adjusted to limit the amplitude of the converter's submodule-capacitor swapping voltage ripple component. However, it is important to highlight that increased capacitance values should be required if it is desired to keep the switching frequency of the bidirectional-switch stacks (swap switches) low. It means that the trade-off between having reduced capacitance requirements (potentially resulting in a reduced cost, volume, and weight), and having an improved reliability (due to the low switching frequency of the bidirectional-switch stacks) must be assessed case by case, depending on the specific application of the MMShC.

3.5 Proposed Converter Solution with Battery Integration

In this section the MMShC with integrated ESS is considered. The MMShC is proposed for WT applications and, by integrating an ESS into the converter, the WTs driven by it could provide many benefits for the turbine owner and for the overall power system operation. The WT owner could increase his revenues in the electricity market and could provide various ancillary services to the electrical grid by having an integrated ESS. Wind power plants with integrated energy storage can support the grid frequency regulation, can improve the unit commitment and economic dispatch, and could even eventually assist in the black-start of the electrical grid. The traditional approach for integrating ESSs into a wind power plant is to have an extra converter exclusively dedicated to the centralized ESS. In the solution proposed in this thesis, the ESS is integrated into the same converter that drives the WTs, avoiding the need of the extra converter for the ESS. Besides, in order to reduce current levels, and to

avoid the expensive, bulky and heavy transformers, medium-voltage structures could be adopted in the wind power plant as proposed in this thesis. In this case, complex issues could emerge related to the ESS integration. If batteries are considered, then several series-connected battery cells would be required to build a stack with voltage levels compatible with the considered application. This kind of solution is probably not mature enough in the industry since complex and expensive BMSs would be required to operate the battery stacks in a safe and reliable fashion. Converters with a modular multilevel structure, which is the case of the MMShC, allow for the decentralized integration of batteries, i.e., the battery system can be distributed between the several submodules of the converter in such a way that each battery system, integrated into each submodule, only needs to handle the reduced voltage level of its submodule. This would certainly facilitate the operation of the series-connected battery cells, even though other challenges can emerge related to thermal issues caused by the heating of the semiconductor devices and their proximity to the battery system.

In this section, the MMShC with only batteries is presented as shown in Fig. 61. This was the first configuration analyzed to study the basic operation of the proposed converter with an integrated ESS. However, the topology with batteries only is not the most competitive solution due to some inherent and natural operational characteristics of converters with a modular multilevel structure. In other words, the power exchange between the two terminals of a converter with a modular multilevel structure occurs through an intermediate stage inside the converter, i.e., the converter's ESS elements (typically submodule capacitors) are first charged, absorbing power from one of the converter's terminals, and then they are discharged, supplying power to the other converter's terminal. If batteries only are implemented into the converter's submodules, then a solution with a potentially low commercial competitiveness would be obtained. In other words, the continuous charging/discharging cycles of the batteries with the full WT power (as in the proposed application) would lead to the need of a large ESS, and it would lead to a short lifetime of the battery system. A more competitive solution will be presented in Section 3.6, where the hybrid version of the MMShC with integrated ESS is considered. The hybrid solution is built with part of its submodules with integrated batteries and part of its submodules with conventional capacitors integrated. In this case, the batteries only have to handle the surplus power either absorbed from the WT or injected into the grid. The conventional capacitors are the ones responsible for handling most of the power exchanged between the two terminals of the converter. A detailed explanation of the hybrid solution will be given in Section 3.6.

3.5.1 Converter Topology

The MMShC with integrated batteries (see Fig. 61) is essentially equal to the MMShC with capacitors (see Fig. 40) if the submodule capacitors are replaced by battery packs. As explained for the original MMShC with capacitors, the frequency of operation of the swap switches (bidirectional-switch stacks) is defined based on how fast

the converter's ESS elements are charged/discharged. When capacitors only are considered, the switching frequency of the swap switches can be set to values in the range of 50 Hz to 200 Hz, which is already a low switching frequency for a semiconductor device. When batteries are integrated into the converter, the switching frequency of the swap switches can be much lower since the charging/discharging time of this high-energy-density ESS is considerably higher. The switching frequency of the swap switches of the MMShC with integrated batteries could occur in a scale of several minutes. For this reason, the swap switches could eventually be mechanical ones, avoiding the need of stacks of series-connected semiconductor devices to build these switches. Nonetheless, swap switches based on semiconductor-device stacks are considered in this thesis. The control and operation of the MMShC with integrated batteries will be explained in the next subsections.

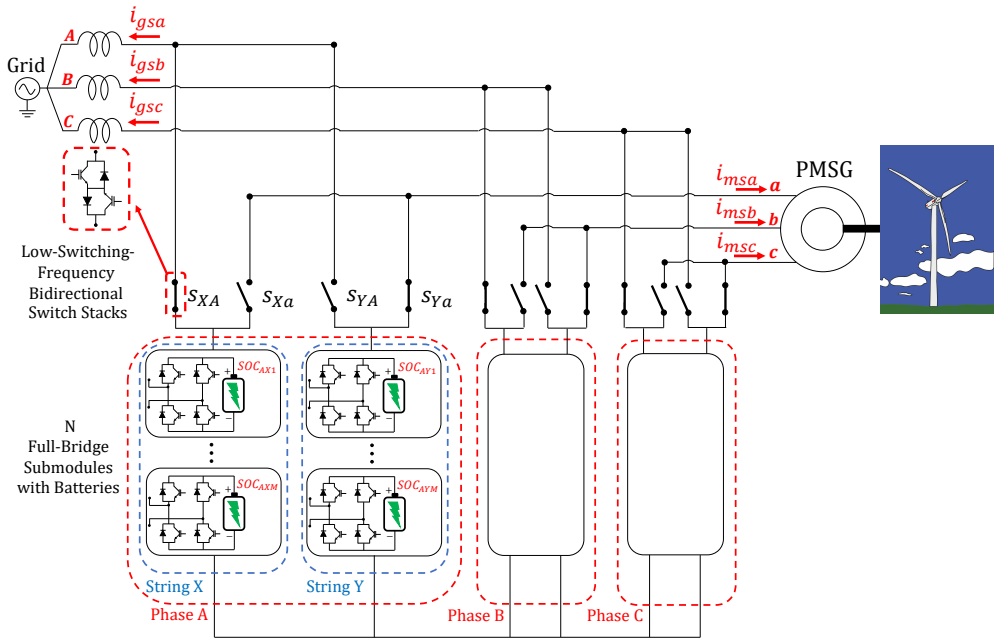

Fig. 61: Topology of the MMShC with integrated batteries only.

3.5.2 Internal Control and Modulation

The internal control and modulation of the MMShC with integrated batteries is very similar to the internal control and modulation of the original MMShC with capacitors only, as illustrated in Fig. 62. One of the main differences is that, in the case where the converter has integrated batteries, the internal control receives as input the

state-of-charge (SOC) values of all the submodule battery packs within Strings X and Y (SOC_{AX1}, SOC_{AX2}, ..., SOC_{AXN}, SOC_{AY1}, SOC_{AY2}, ..., SOC_{AYN}), instead of receiving the submodule-capacitor voltages. Besides, instead of operating with a constant switching frequency, the swap switches of the MMShC with integrated batteries operate with a variable switching frequency, which is defined based on upper and lower limits for the SOC values of the battery packs. In other words, the swapping action of the swap switches will occur every time that either the battery-SOC values of the string being charged reach a pre-defined upper limit, or every time that the battery-SOC values of the string being discharged reach a pre-defined lower limit. This way, the SOC values of the converter's battery packs will always remain within a pre-defined range. In this case, the frequency of operation of the swap switches will obviously depend on the power level handled by the converter at the given operational condition, i.e., depending on the amount of power being injected into the grid and being absorbed from the turbine, the swapping operations can happen more or less frequently. Considering that the WT is operating in a dispatchable fashion, if the power being injected into the grid is higher than the power being absorbed from the WT, then the discharging string will be the one to first reach its lower SOC limit, which will lead to a swapping operation. On the contrary, if the power being injected into the grid is less than the power being absorbed from the WT, then the charging string will be the one to first reach its upper SOC limit, which will lead to a swapping operation. The explanation of the swap-switch operation is given inside the blue box of Fig. 62 with the name "Limitation of SOC Range". For example, if at a given moment String X is connected to the grid, operating in discharging mode, and String Y is connected to the machine, operating in charging mode, then the control algorithm will continuously check if $SOC_{AY1} > UpperLimit$ and if $SOC_{AX1} < LowerLimit$. While these limits are not exceeded by neither of the strings, then no swapping action occurs. As soon as one of the limits is exceeded by one of the strings, then a swapping action occurs connecting each of the strings to their opposite terminals, i.e., String X will then be connected to the turbine terminal and, thus, a charging process will begin, and String Y will then be connected to the grid terminal and, thus, a discharging process will begin. It is important to highlight that even though the SOC values of the first submodules of Strings X and Y (SOC_{AX1} and SOC_{AY1}, respectively) were used for the swapping decision, any other SOC value of any submodule within the string could have been adopted since a sorting algorithm is used to maintain all the batteries within the same string with similar SOC values. It means that when, for example, SOC_{AX1} reaches a given limit, then the SOC values of the other batteries within String X will simultaneously also reach the same limit.

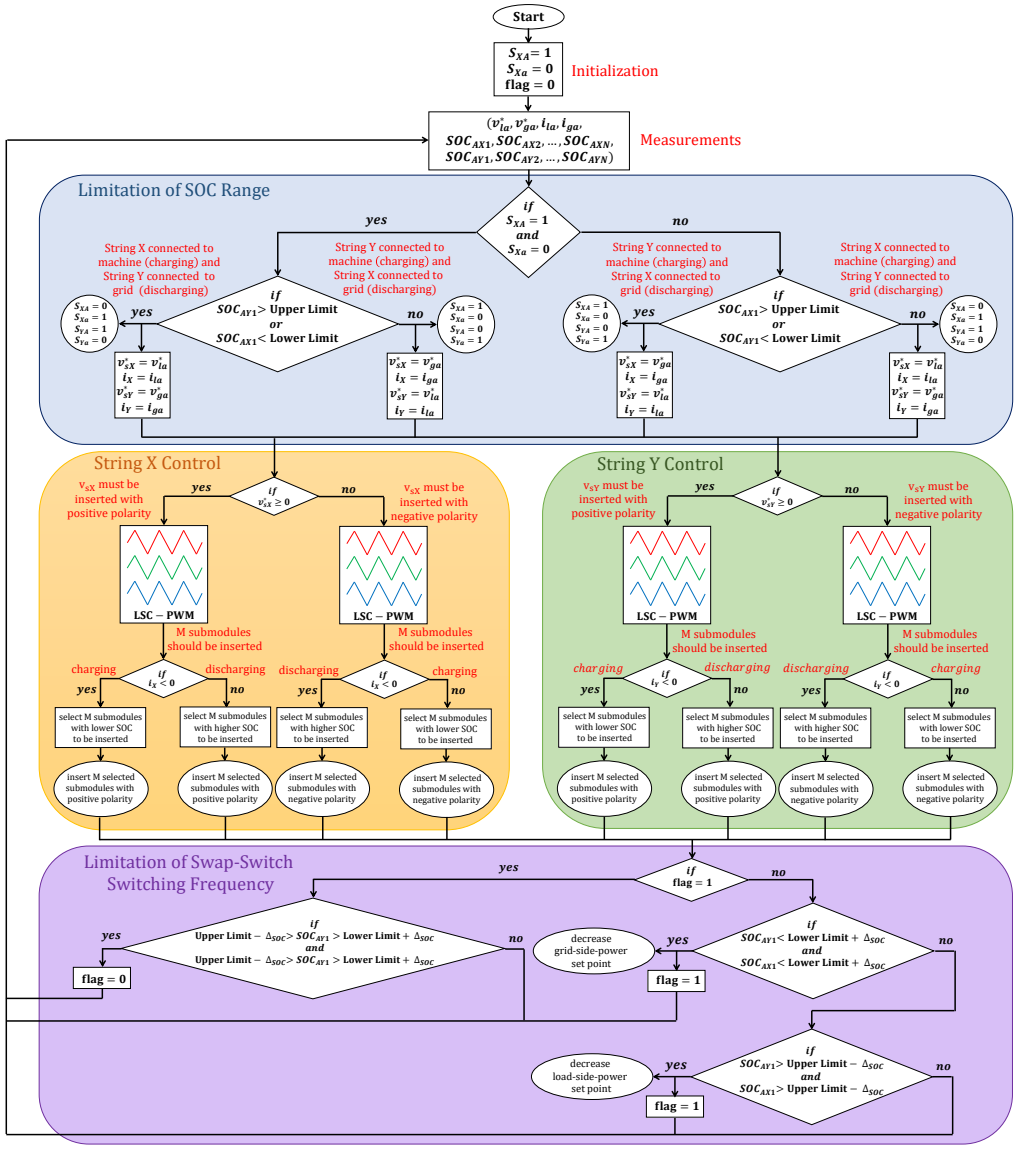

Fig. 62: Flowchart explaining internal control and modulation of the MMShC with integrated batteries.

The next step of the control algorithm is the String-X and String-Y control, which is exactly the same as the case where the MMShC is built with capacitors only. In this control stage, a LSC-PWM modulation technique is used to decide the instantaneous

number of submodules to be inserted (M), and the polarity of the submodules to be inserted so that the voltage reference can be tracked by the converter. After that, a sorting algorithm is performed to maintain all the batteries within the same submodule string with similar SOC values. Finally, the last stage of the control algorithm is called "Limitation of Swap-Switch Switching Frequency" and it will be explained later in the Simulation Results subsection.

3.5.3 Simulation Results

In this subsection, simulation results are presented to demonstrate and further explain the operation of the MMShC with integrated batteries. In the simulation, the MMShC with integrated batteries was used to drive a PMSG, which represented the WT generator. The generator was modeled with the following power, voltage, and frequency ratings: 3 MVA, 10 kV, and 60 Hz. The converter was connected to a 5-kV, 50-Hz grid. The MMShC was built with strings of $N = 4$ submodules, where each submodule had its own battery pack integrated. Each battery pack had the following voltage and energy ratings: 1 kV and 0.125 Ah. A low battery energy was adopted so that it was possible to analyze the converter behavior in a 15-second simulation. The initial SOC value of the battery packs was set to 60%. For the converter LSC-PWM, 5-kHz carriers were used. The generator control was performed through a FOC technique, aiming at regulating the generator speed. The grid side of the converter, however, was controlled in an open-loop fashion aiming at injecting a fixed and constant power into the grid, i.e., a voltage reference with equal amplitude and slightly different phase in relation to the grid voltage was provided for the converter's grid-side control. This small phase difference led to the injection of a constant power into the grid with a value of approximately 1.05 MW. In the simulation, at $t = 0.5$ s, the generator was started with a speed reference of $\omega^* = 0.2$ p.u., and with a mechanical torque of 1.4 p.u. imposed to its shaft. At $t = 4$ s, the generator speed reference was increased to $\omega^* = 0.3$ p.u. At $t = 8$ s, the mechanical torque imposed to the generator's shaft was increased to 1.8 p.u., representing a step in the wind speed. The results obtained in this simulation are shown in Fig. 63 and in Fig. 64. In Fig. 63(a) and (b), the three-phase voltages synthesized by the MMShC at the generator terminals and at the grid terminals are shown, respectively. As expected, these are staircase-shape multilevel voltages with a relatively high power quality that can easily be filtered out. In Fig. 63(c), the active power injected into the grid by the converter (P_g) and the active power absorbed from the WT (P_l) are shown. Due to the presence of the ESS, the WT was capable to operate in a dispatchable fashion, injecting into the grid a pre-defined power value according to a setpoint, independently of the instantaneous power generated by the WT. By observing Fig. 63(c), one can notice that throughout the simulation, the power extracted from the WT presented values both less and greater than the power injected into the grid, depending on the instantaneous values of the generator speed and of the mechanical torque imposed to the generator shaft. The mismatch between the power injected into the grid and the power produced

by the WT was either stored or supplied into/by the ESS. In Fig. 63(d), the generator speed is shown, and it is clear that the MMShC was capable to regulate the machine speed according to the received reference.

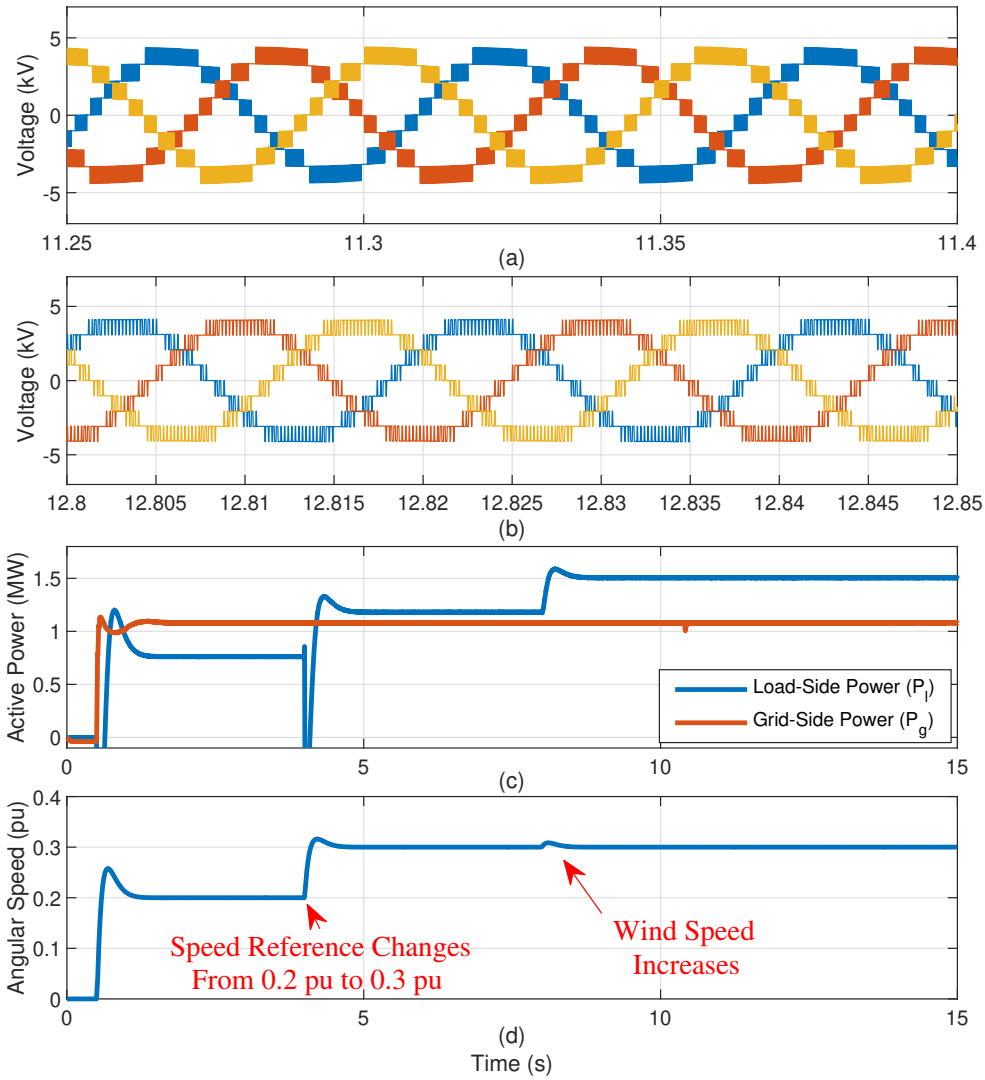

Fig. 63: Simulation results of MMShC with integrated batteries. (a) Voltage synthesized at generator terminals, (b) voltage synthesized at grid terminals, (c) grid-side and load-side power values, and (d) generator speed.

In Fig. 64(a), (c), and (e) the SOC values of the MMShC's phase-A String-X, phase-B String-X, and phase-C String-X submodule batteries are shown, respectively. In Fig. 64(b), (d), and (f) the SOC values of the MMShC's phase-A String-Y, phase-B String-Y, and phase-C String-Y submodule batteries are shown, respectively. By observing these figures, one can notice that the SOC values of all the converter's batteries always remain within the pre-defined limits of 40% and 80%. In other words, every time the SOC value of any battery reach either the lower or the upper limits, then a swapping action occurs connecting the string that was connected to the grid terminal (whose batteries were being discharged) to the generator terminal, and connecting the complementary string that was connected to the generator terminal (whose batteries were being charged) to the grid terminal. By observing Fig. 64(a) and (b), where the battery-SOC values of the two complementary strings (phase-A String X and phase-A String Y) are shown, one can notice that while the battery-SOC values of one string are increasing, the battery-SOC values of the complementary string are decreasing, as expected. Nonetheless, the average value of the battery SOCs of both strings are either increasing together or decreasing together, depending on the mismatch between the power injected into the grid and the power produced by the WT. For example, before $t = 4$ s, the power injected into the grid by the converter is greater than the power absorbed from the WT (see Fig. 63(c)). Thus, the the battery-SOC values of both strings decrease in average, i.e., the batteries will be discharged at a higher rate when their corresponding string is connected to the grid terminal than they will be charged when their corresponding string is connected to the generator terminal. Then, as the time passes, the battery-SOC values of both strings will come close to the lower SOC limit as shown in Fig. 64. On the contrary, after $t = 4$ s, the power injected into the grid by the converter becomes less than the power absorbed from the WT (see Fig. 63(c)). Thus, the the battery-SOC values of both strings start to increase in average, i.e., the batteries start to be charged at a higher rate when their corresponding string is connected to the generator terminal than they are discharged when their corresponding string is connected to the grid terminal. In this case, as the time passes, the battery-SOC values of both strings come close to the upper SOC limit as shown in Fig. 64. Obviously, the MMShC's batteries can only be charged/discharged to a limit, which means that the period of time that the converter can keep operating at a given dispatchable condition is limited by the energy of the battery system. If the average SOC values of the batteries of the complementary strings come too close to either the upper or the lower limit, then the operational setpoint of the converter must be changed. This is performed by the last stage of the control algorithm shown in Fig. 62, which is named "Limitation of Swap-Switch Switching Frequency". This control will be explained below through Fig. 65 and Fig. 66. But before that, one last important thing to be observed in Fig. 64 are the zoom sub-figures in the battery SOC curves of each string. These zoomed-in figures show the SOC value of each individual battery pack within the same submodule string. The SOC values of all the battery packs within the same string remain similar

because of the sorting algorithm responsible for the battery-SOC balancing control as depicted in Fig. 62.

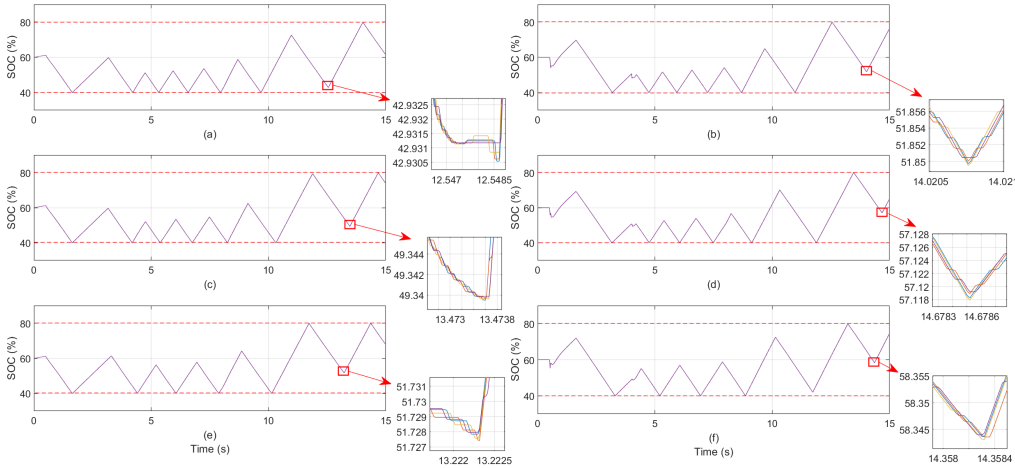

Fig. 64: Simulation results of MMShC's submodule-battery SOC values. (a), (c), and (e) show the SOC values of the converter's phase-A String-X, phase-B String-X, and phase-C String-X submodule batteries, respectively. (b), (d), and (f) show the SOC values of the converter's phase-A String-Y, phase-B String-Y, and phase-C String-Y submodule batteries, respectively.

Two other simulations were performed using the same grid, converter and generator parameters of the previous simulation. The first is related to a situation where the grid power setpoint remains greater than the power produced by the WT for a long time and, then the converter's batteries are discharged to their minimum limit. The results of this simulation are presented in Fig. 65. The second simulation is related to a situation where the grid power setpoint remains less than the power produced by the WT for a long time and, then the converter's batteries are charged to their maximum limit. The results of this simulation are presented in Fig. 66. In Fig. 65(a) and (b), the MMShC's phase-B String-X and phase-B String-Y submodule-battery SOC values are shown, respectively. The reason why the SOC values of the batteries of Strings X and Y of phase B are shown is because they are the first ones to reach the lower limit, leading to the need of change of the grid-side power setpoint. In Fig. 65(c), the grid-side and load-side power values of the MMShC are shown. As previously mentioned, the power injected into the grid by the converter remains considerably higher than the power produced by the WT for a relatively long time and, thus the average values of the String-X and of the String-Y battery SOCs decrease together since the batteries are being discharged at a higher rate than they are being charged. It is interesting to

notice that, the closer to the lower limit the battery-SOC values of the two strings get, the higher the switching frequency of the swap switches becomes. In other words, since the battery-SOC values of both strings are coming close to the lower limit in average, then a faster swapping action starts to be required so that the battery-SOC values of the string being discharged do not exceed the lower limit of 40%. In order to limit the swap-switch switching frequency and to avoid that the converter's batteries are completely discharged to their minimum allowed value, then a control action must be done. The criteria adopted in this thesis is that as soon as the battery-SOC values of the two complementary strings of any converter's phase exceed simultaneously a limit equal to $Lower\ Limit + \Delta_{SOC} = 40 + 2 = 42\%$, then the converter's grid-side power set point must be reduced to a value lower than the power being produced by the generator, since the converter's batteries cannot be discharged any further. In this simulation, this situation happens at approximately $t = 5.8$ s, as shown in Fig. 65. As soon as the grid-side power setpoint is reduced, the battery-SOC values of the two strings start to increase again in average.

In opposition to the simulation results shown in Fig. 65, in Fig. 66, simulation results are shown corresponding to the situation where the MMShC's grid-side power setpoint remains lower than the power produced by the WT for a relatively long time. In this case, the String-X and String-Y submodule-battery SOC values will simultaneously increase in average until the converter's batteries cannot be charged any further. Differently from the previous simulation, in this case the batteries of phase-C Strings X and Y are the ones whose SOC values first exceed the pre-defined upper limit and, thus, they are the ones triggering the power setpoint reduction of the WT. For this reason, in Fig. 66(a) and (b), the MMShC's phase-C String-X and phase-C String-Y submodule-battery SOC values are shown, respectively. In Fig. 66(c), the machine speed is shown and, in Fig. 66(d), the converter's grid-side and load-side power values are shown. Since the power absorbed from the WT remains higher than the power injected into the grid for a relatively long time, then the battery-SOC values of the two complementary strings increase in average and come close to the upper SOC limit. As soon as the battery-SOC values of the two complementary strings exceed simultaneously a limit equal to $Upper\ Limit - \Delta_{SOC} = 80 - 2 = 78\%$, then the generator speed is reduced, so that the power produced by the WT is also reduced, since the converter's batteries cannot be charged any further. As shown in Fig. 66, this situation happens at approximately $t = 4.8$ s in this simulation. The WT driven by the proposed MMShC with integrated ESS is capable to operate in a dispatchable fashion, injecting into the grid a power value different from the instantaneous power being generated, as long as the ESS dimensions are big enough so that the ESS operational limits are not exceeded for a given pre-defined dispatch commitment.

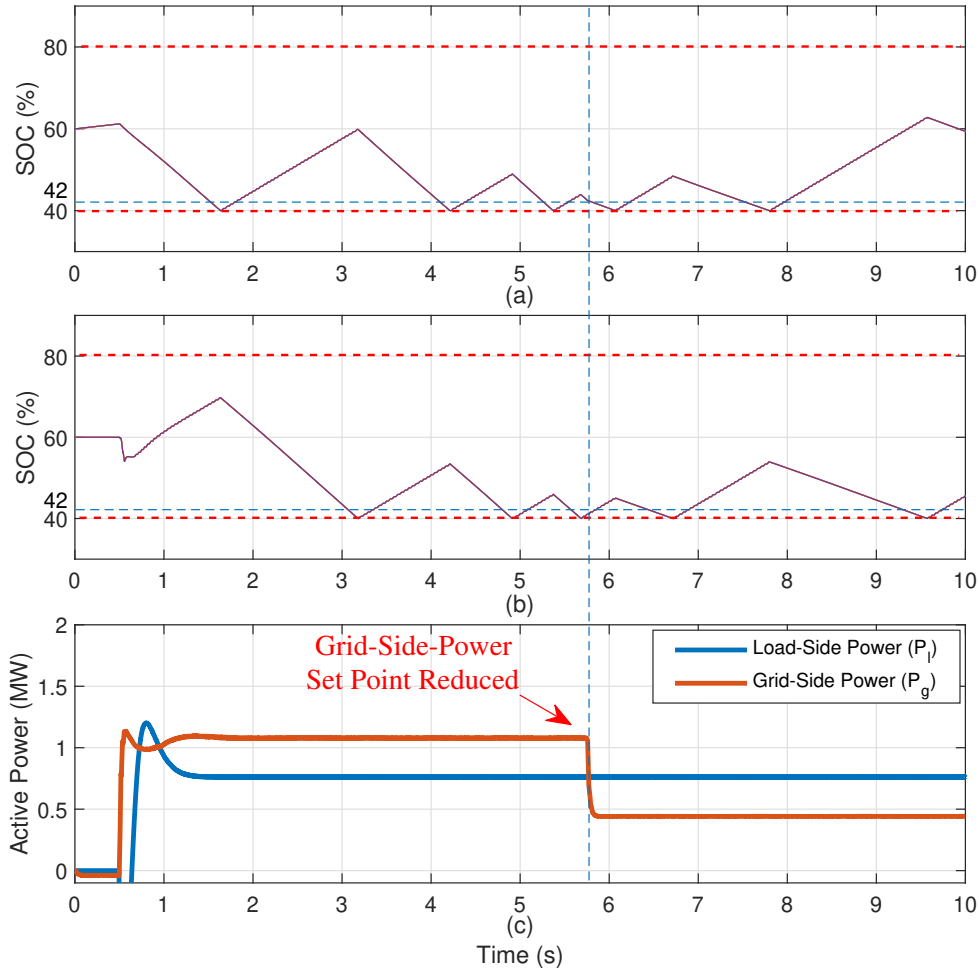

Fig. 65: Simulation results of MMShC operation case where a grid-side setpoint reduction is required. (a) Phase-B String-X submodule-battery SOC values, (b) phase-B String-Y submodule-battery SOC values, and (c) grid-side and load-side power values.

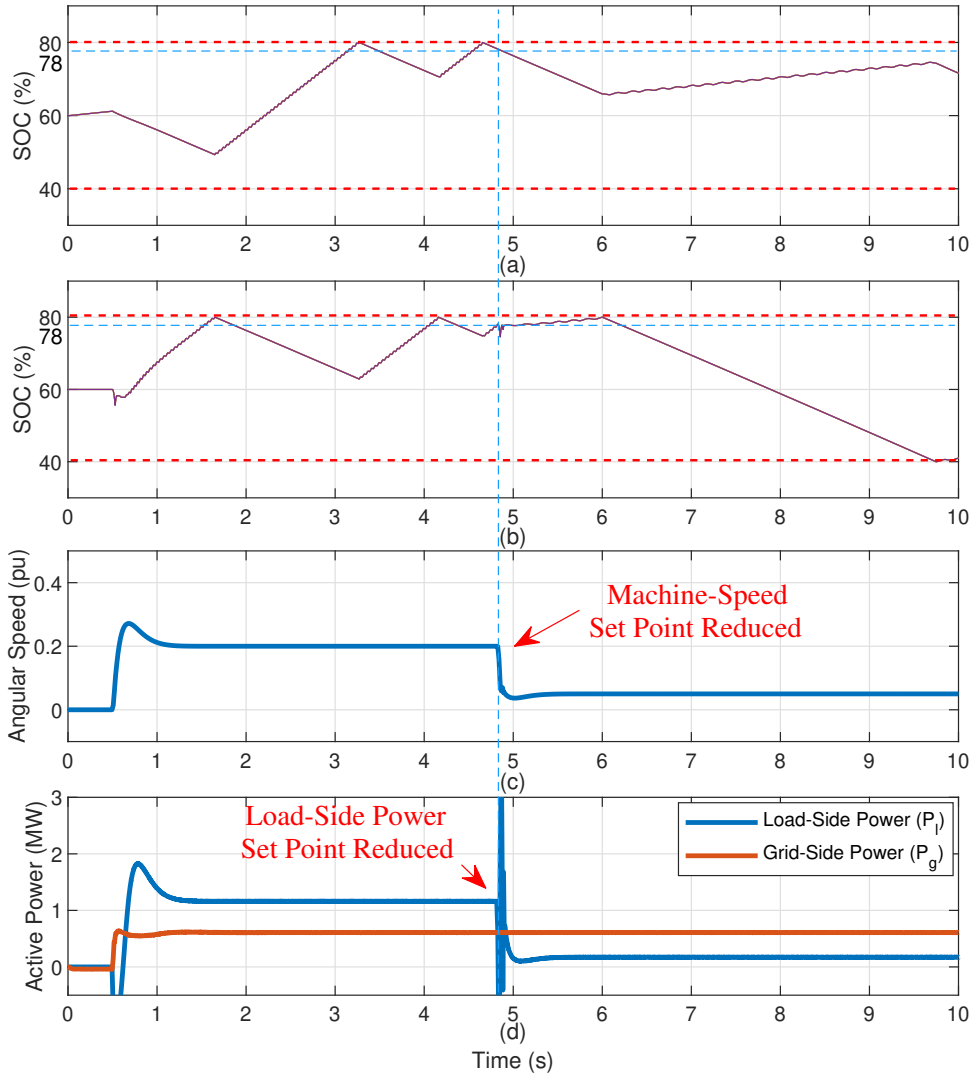

Fig. 66: Simulation results of MMShC operation case where a load-side setpoint reduction is required. (a) Phase-C String-X submodule-battery SOC values, (b) phase-C String-Y submodule-battery SOC values, (c) machine speed, and (d) grid-side and load-side power values.

3.6 Proposed Converter Solution with an Integrated Hybrid Energy Storage System for Optimization of Battery Dimensions

In this section, a hybrid version of the MMShC with integrated ESS is presented. Hybrid means that the converter's strings are built with some of their submodules with integrated batteries and some of their submodules with conventional capacitors integrated. The conventional capacitors are used to transfer to the grid most of the power produced by the WT, similarly to the original MMShC with capacitors only, and the batteries are only used to either absorb the surplus power generated by the WT or to supply to the grid the extra power required to match the pre-defined grid power setpoint. In this case, the battery system dimensions can be optimized in relation to the previous topology with only batteries integrated. Once again, in the topology with batteries only, the battery packs had to be charged/discharged with the full WT power, probably resulting in a solution with low competitiveness potential. In other words, a battery is an expensive ESS with high energy density and with a low lifespan in terms of number of tolerated cycles. Thus, charging/discharging these batteries with the full WT power would probably lead to an expensive solution, with low competitiveness, despite the economic benefits that would come from having an integrated ESS.

3.6.1 Topology and Operation

In this subsection, the topology and operation of the hybrid MMShC are explained in detail. The hybrid MMShC is shown in Fig. 67, and it is very similar to the topology with batteries only, with the difference that each of its submodule strings are built with N FB submodules with conventional capacitors and with M FB submodules with battery packs. In order to explain the converter operation in a didactic manner, three figures are presented below (Fig. 68, Fig. 69 and Fig. 70), which demonstrate a simplified and intuitive version of the converter behavior. The detailed explanation of the hybrid MMShC operation will be presented through flowcharts and through simulation results later in this thesis.

In Fig. 68, The two complementary strings (String X and String Y) of the converter's phase A are illustrated. Let us suppose that, at the considered instant, String X is connected to the grid terminal and it injects into the grid an instantaneous power value of $P_{ga} = 4$ MW, while synthesizing an instantaneous terminal voltage of 4 kV, resulting in an instantaneous current of 1 kA flowing to the grid. Let us also suppose that, at the same considered instant, String Y is connected to the turbine terminal and it absorbs from the generator an instantaneous power value of $P_{la} = 4$ MW, while synthesizing an instantaneous terminal voltage of 4 kV, resulting in an instantaneous current of 1 kA. Finally, let us suppose that the DC value of the submodule-capacitor voltages are regulated to 1 kV.

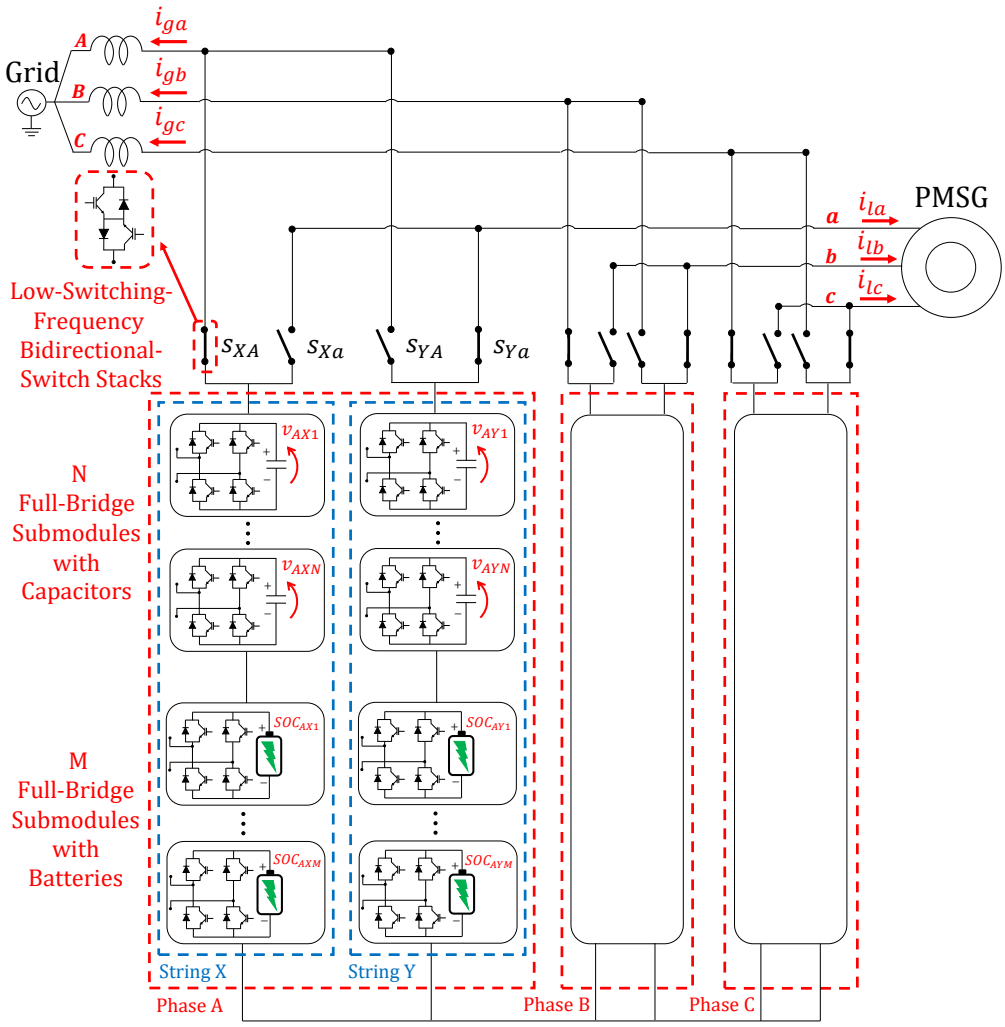

Fig. 67: Topology of the hybrid MMShC whose strings are built with part of their submodules with integrated batteries and part of them with conventional capacitors integrated.

According to the conditions of this example, four FB submodules will be instantaneously inserted at the grid terminal, which means that each of the four capacitors will be discharged with an instantaneous power of 1 MW and the total power discharging these capacitors will be $P_{Xcap} = 4$ MW, which is equal to the power setpoint of the grid. At the same time, four FB submodules will be instantaneously inserted at the

machine terminal, which means that each of the four capacitors will be charged with an instantaneous power of 1 MW and the total power charging these capacitors will be $P_{Ycap} = 4$ MW, which is equal to the total power absorbed from the WT. In this example, the capacitors of String X are being discharged with the same rate as the capacitors of String Y are being charged. In other words, ideally speaking, if the system remained operating in this condition, the average value of the submodule-capacitor voltages would remain constant and regulated with 1 kV, when the swapping actions started to occur, since the capacitors of each string would always be charged/discharged at the same rate when connected to the grid and to the generator terminals.

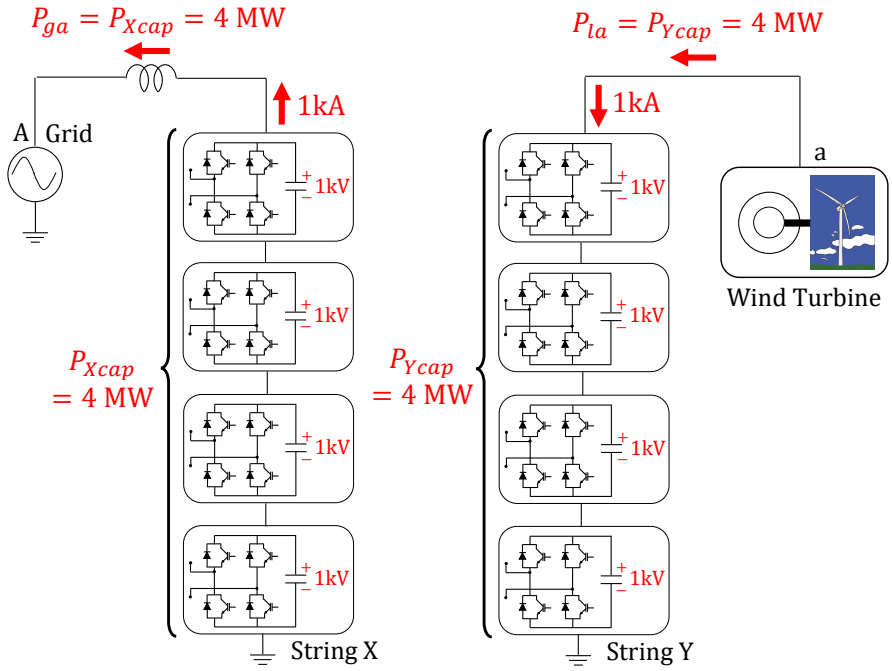

Fig. 68: Explanatory example considering equal instantaneous power at the converter's grid-side and generator-side terminals.

The previous example considered a non-dispatchable operation of the system since the same power generated by the WT was injected into the grid. Let us now consider another example where a dispatchable operation occurs, in which the instantaneous power injected into the grid by the hybrid MMShC is higher than the power instantaneously produced by the WT. This example is illustrated in Fig. 69. Let us suppose that, at the considered instant, String X is connected to the grid terminal and it injects into the grid an instantaneous power value of $P_{ga} = 8$ MW, while synthesizing an instantaneous

terminal voltage of 4 kV, resulting in an instantaneous current of 2 kA flowing to the grid. Let us also suppose that, at the same considered instant, String Y is connected to the turbine terminal and it absorbs from the generator an instantaneous power value of $P_{la} = 4$ MW, while synthesizing an instantaneous terminal voltage of 4 kV, resulting in an instantaneous current of 1 kA. Finally, let us suppose that the battery-pack voltage is also equal to 1 kV, which is the same as the average value of the submodule-capacitor voltage.

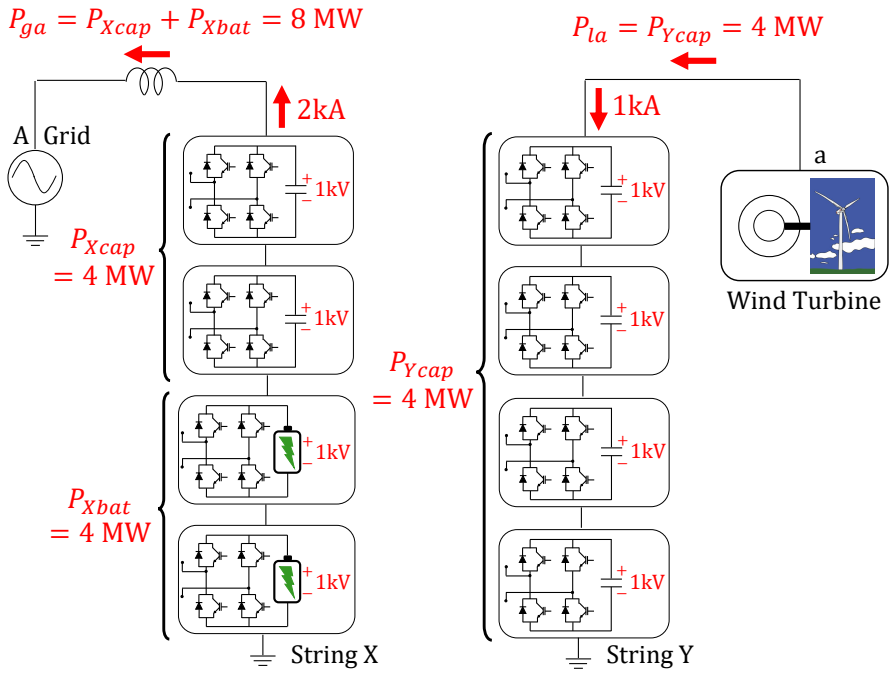

Fig. 69: Explanatory example considering dispatchable operation with higher instantaneous power injected into the grid in relation to instantaneous power produced by the WT.

If two capacitor submodules and two battery submodules from String X are inserted at the grid terminal, then half of the power supplied to the grid would come from the string capacitors and half of it would come from the string batteries. In other words, the power discharging the string capacitors would be equal to $P_{Xcap} = 4$ MW, the power discharging the string batteries would be equal to $P_{Xbat} = 4$ MW, and the total power injected into the grid would be equal to $P_{ga} = P_{Xcap} + P_{Xbat} = 8$ MW. At the same time, four capacitor submodules will be instantaneously inserted at the machine terminal, which means that each of the four capacitors will be charged with an instantaneous power of 1 MW and the total power charging these capacitors will be $P_{Ycap} = 4$ MW,

which is equal to the total power absorbed from the WT. It is interesting to notice that, in this example, the WT was capable to operate in a dispatchable fashion, injecting a higher power value into the grid than the instantaneous power generated by the turbine, but the capacitors of the string connected to the grid terminal were still discharged with the same rate as the capacitors of the string connected to the machine terminal were charged ($P_{Xcap} = P_{Ycap} = 4$ MW). The power generated by the WT was transferred to the grid through the converter's capacitors, and the surplus power injected into the grid was supplied by the converter's batteries. In this operational condition, it would still be possible to keep the MMShC's submodule capacitors regulated with a voltage equal to 1 kV since the capacitors of each string would always be charged/discharged at the same rate when connected to the grid and to the generator terminals.

Finally, let us consider another example where a dispatchable operation occurs, but where the instantaneous power produced by the WT is higher than the instantaneous power injected into the grid by the hybrid MMShC. This example is illustrated in Fig. 70.

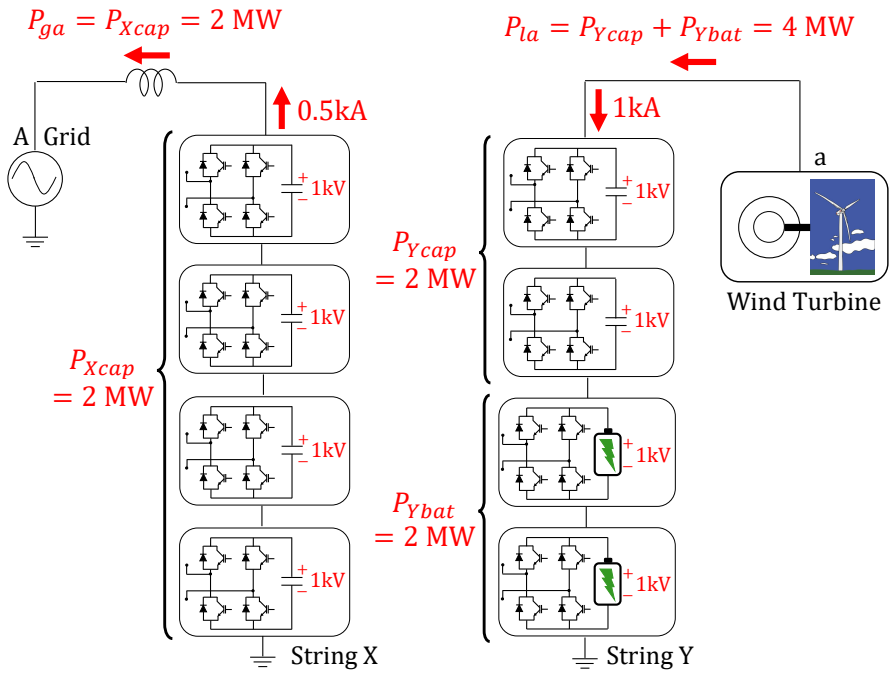

Fig. 70: Explanatory example considering dispatchable operation with higher instantaneous power produced by the WT in relation to instantaneous power injected into the grid.

Let us suppose that, at the considered instant, String X is connected to the grid terminal and it injects into the grid an instantaneous power value of $P_{ga} = 2$ MW, while

synthesizing an instantaneous terminal voltage of 4 kV, resulting in an instantaneous current of 0.5 kA flowing to the grid. Let us also suppose that, at the same considered instant, String Y is connected to the turbine terminal and it absorbs from the generator an instantaneous power value of $P_{la} = 4$ MW, while synthesizing an instantaneous terminal voltage of 4 kV, resulting in an instantaneous current of 1 kA. If two capacitor submodules and two battery submodules from String Y are inserted at the generator's terminal, then half of the power produced by the WT would be absorbed by the string capacitors and half of it would be absorbed by the string batteries. In other words, the power charging the string capacitors would be equal to $P_{Ycap} = 2$ MW, the power charging the string batteries would be equal to $P_{Ybat} = 2$ MW, and the total power absorbed from the WT would be equal to $P_{la} = P_{Ycap} + P_{Ybat} = 4$ MW. At the same time, four capacitor submodules will be instantaneously inserted at the grid terminal, which means that each of the four capacitors will be discharged with an instantaneous power of 0.5 MW and the total power discharging these capacitors will be $P_{Xcap} = 2$ MW, which is equal to the total power injected into the grid. It is interesting to notice that, in this example, the WT was capable to operate in a dispatchable fashion, injecting a lower power value into the grid than the instantaneous power generated by the turbine, but the capacitors of the string connected to the grid terminal were still discharged with the same rate as the capacitors of the string connected to the machine terminal were charged ($P_{Xcap} = P_{Ycap} = 2$ MW). The grid power setpoint was met, and it was transferred from the WT to the grid through the converter's capacitors. The surplus power instantaneously generated by the WT was stored in the MMShC's batteries. Similarly to the previous example, in this operational condition, it would also be possible to keep the converter's submodule capacitors regulated with a voltage equal to 1 kV since the capacitors of each string would always be charged/discharged at the same rate when connected to the grid and to the generator terminals.

The conclusion of the previously presented explanation is that the WT driven by the hybrid MMShC is capable to operate in a dispatchable fashion while the converter's batteries are only charged/discharged with the mismatch between the instantaneous power being generated by the WT and the instantaneous power being injected into the grid. Besides, it was shown that it is possible to keep the converter's submodule-capacitor voltages constant and regulated by controlling the instantaneous number of battery submodules inserted in the converter's strings. The general rule is that, if the instantaneous power to be injected into the grid is higher than the instantaneous power produced by the WT, then only capacitor submodules must be inserted in the strings connected to the generator terminals, and some battery submodules must be inserted in the strings connected to the grid terminals. On the contrary, if the instantaneous power to be injected into the grid is lower than the instantaneous power produced by the WT, then only capacitor submodules must be inserted in the strings connected to the grid terminals, and some battery submodules must be inserted in the strings connected to the generator terminals. A more detailed explanation of this control will be given

through the simulation results and through the flowchart presented below.

3.6.2 Simulation Results to Illustrate Converter Operation and Control

In this subsection, simulation results based on three different simulations are presented. The first simulation explains the operation of the hybrid MMShC in a situation where the WT operates in a dispatchable fashion but with the converter's batteries staying in stand-by mode, and with only the conventional capacitors being used to transfer power between the generator's and the grid's terminals. The second simulation aims at demonstrating and explaining the operation of the hybrid MMShC in a didactic and intuitive fashion. To achieve this objective, some ideal operational conditions are considered in the simulation, which would not occur in a real operation of the solution. A more complete and realistic operational condition of the converter is presented in the third simulation of this subsection. The simulation results were obtained through the software PSCAD/EMTDC. In these simulations, each string of the hybrid MMShC was modeled with $N = 5$ FB submodules with $C = 50$-mF capacitors integrated, and with $M = 4$ submodules with integrated batteries. The battery rated voltage was set to 1 kV and the energy to 65 mAh. The converter was connected to an AC grid with voltage equal to 5 kV and with frequency equal to 50 Hz. A 3-MVA PMSG was connected to the load side of the converter to represent the WT generator. A FOC technique was adopted to regulate the machine speed. The grid side of the converter was controlled in an open-loop fashion by simply varying the phase of the voltage synthesized at the grid-side terminals in order to vary the active power injected into the grid.

As previously explained, the converter's grid-side control was performed in an open-loop fashion by varying the angle of the voltage reference to be synthesized at the converter's grid-side terminal. Throughout the simulation period, this angle was set to different values so that sometimes the power being injected into the grid was higher than the power being absorbed from the generator, sometimes lower, and sometimes equal to the power being absorbed from the generator. In Fig. 71(a), the power injected into the grid (P_g) and the power absorbed from the generator (P_l) by the MMShC are shown. In Fig. 71(b) and (c), the submodule-capacitor voltages of the MMShC's phase-A String X and phase-A String Y are shown, respectively.

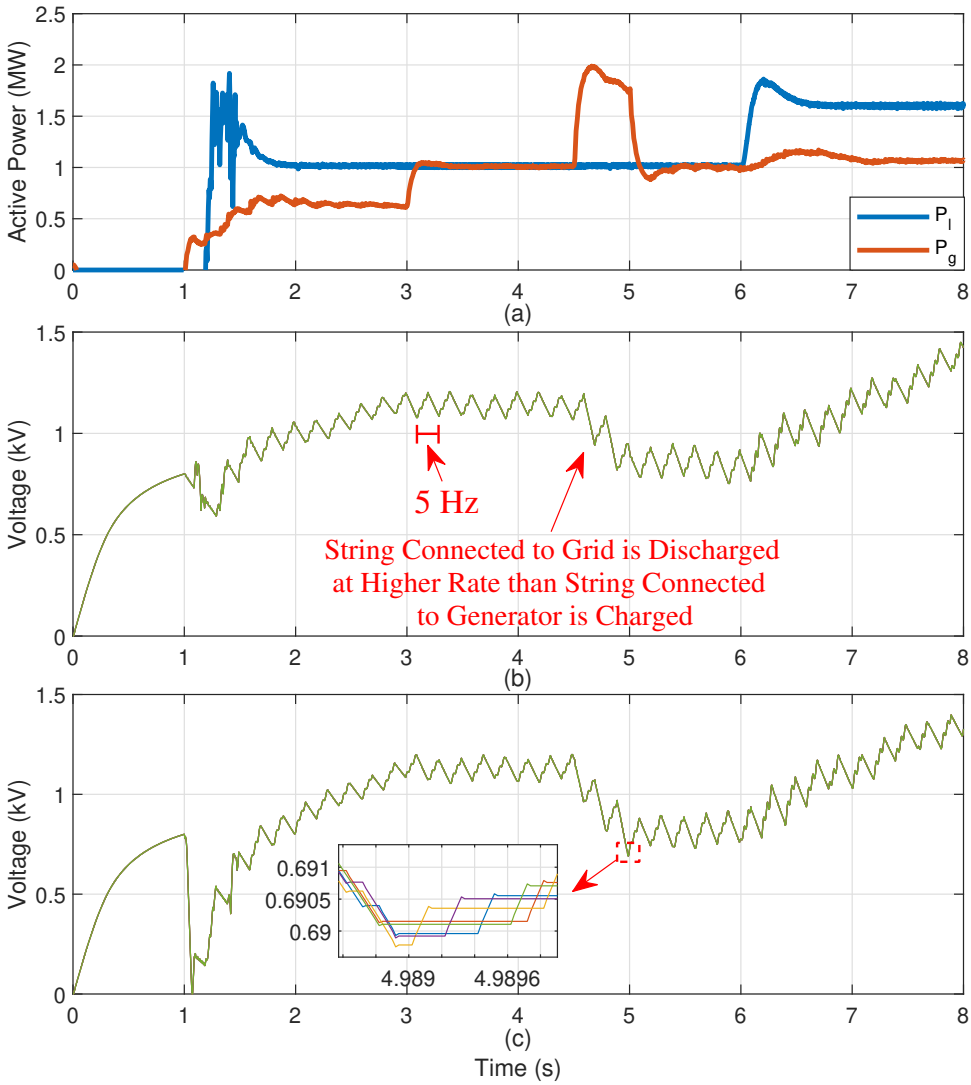

Fig. 71: Simulation results of the hybrid MMShC operation with its batteries in stand-by mode. (a) Grid-side and generator-side power values, (b) MMShC's phase-A String-X submodule-capacitor voltages, and (c) MMShC's phase-A String-Y submodule-capacitor voltages.

At $t = 1$ s, the system is initialized. From $t = 1$ s to $t = 3$ s, the power injected into the grid by the converter is less than the power absorbed from the WT. For this reason, the average value of the submodule-capacitor voltages of both strings increase

(see Fig. 71(b) and (c)) since these capacitors are being charged at a higher rate, when connected to the generator terminals, than they are being discharged, when connected to the grid terminals. Between $t = 3$ s and $t = 4.5$ s, the power injected into the grid is increased so that it becomes equal to the power absorbed from the WT. In this case the average value of the submodule-capacitor voltages of both strings remain constant and regulated with a fixed value since the capacitors are being charged/discharged with the same rate when connected to the generator and to the grid terminals. Between $t = 4.5$ s and $t = 5$ s, the power injected into the grid is further increased so that it becomes higher than the power absorbed from the WT. In this case, the average value of the submodule-capacitor voltages of both strings start to decrease since these capacitors are being discharged at a higher rate, when connected to the grid terminals, than they are being charged, when connected to the generator terminals. Between $t = 5$ s and $t = 6$ s, the power injected into the grid is decreased so that it becomes again equal to the power absorbed from the WT. Then, the average value of the submodule-capacitor voltages of both strings remain constant and regulated with a fixed value. Finally, after $t = 6$ s, the wind speed is increased so that the power generated by the WT becomes higher than the power injected into the grid. Thus, the average value of the submodule-capacitor voltages of both strings start to increase again. As it will be demonstrated in the simulation results of the next two simulations (presented in Fig. 72 and Fig. 73), the WT is capable to operate in a dispatchable fashion (injecting into the grid an instantaneous power different from the instantaneous power being produced by the turbine), while maintaining the submodule-capacitor voltages constant and regulated, if some battery submodules are inserted to absorb/supply the mismatch between the converter's grid-side and generator-side power values. In other words, by properly inserting battery submodules, the converter's capacitors will always be charged with the same power rate, when connected to the generator terminals, that they will be discharged, when connected to the grid terminals, since the surplus power between the two terminals will be absorbed/supplied by the converter's batteries.

An interesting point to be observed in Fig. 71(b) is the 5-Hz swapping ripple that occurs because of the 5-Hz switching frequency of the bidirectional-switch stacks (swap switches). In other words, every $\frac{1}{5\text{Hz}} = 0.2$ s, a full swapping cycle occurs, which means that each submodule string is connected to the opposite terminal and then connected back to its initial terminal (grid and generator terminals). It is important to highlight that this is an extremely low switching frequency for the bidirectional-switch stacks that must be built with a few series-connected semiconductor devices. Even though a relatively large submodule capacitor was adopted (with $C = 50$ mF), a smaller capacitor could be adopted if a slightly higher switching frequency was used, and still a relatively small swapping ripple would be obtained. For instance, if $C = 5$-mF and a 50-Hz swapping frequency were adopted, then the same swapping ripple amplitude would be obtained. This would certainly reduce the overall cost, volume and weight of the solution, and the reliability of the converter would not be very deteriorated since 50 Hz

is still an extremely low switching frequency for a power-electronic device. The trade-off between improved reliability and reduced cost, volume, and weight should be assessed for each individual project. Finally, it is also interesting to observe the zoom that is applied to the voltage signals of Fig. 71(c). In the zoom sub figure, the voltage of each capacitor within the string can be seen. All the capacitors remain with similar voltage values because of the sorting algorithm responsible for the submodule-capacitor voltage balancing.

The results obtained in the second simulation are shown in Fig. 72. The MMShC's strings are built with $N = 5$ FB submodules with integrated capacitors, which means that an 11-level voltage can be synthesized by each string, i.e., the instantaneous number of inserted submodules (Z) can vary between 0 and 5 and these submodules can be inserted with both positive and negative polarities. If the average value of the submodule capacitor voltages is regulated with the same value of the battery packs voltage, then the same instantaneous terminal voltage can be synthesized by the converter with a different combination of inserted capacitor and battery submodules. For instance, let us suppose that to obtain the desired instantaneous grid-terminal voltage, $Z = 4$ submodules must be inserted in the MMShC string. If $N_{cap} = 4$ capacitor submodules and $N_{bat} = 0$ battery submodules were inserted, then the desired voltage would be synthesized at the grid terminals, and only the string capacitors would be discharged to supply power to the grid. As another example, if $N_{cap} = 2$ capacitor submodules and $N_{bat} = 2$ battery submodules were inserted, then the desired voltage would also be synthesized at the grid terminals, but the string capacitors and batteries would share equally the power supplied to the grid considering that they have an equal voltage and that the same current flows through them, which is the string current. Other combinations of capacitor and battery submodules could also be inserted to obtain the same voltage at the converter's terminal. However, depending on the adopted combination, the converter's capacitors and batteries would be discharged at different rates. With this approach, it is possible to maintain equivalent charging/discharging rates for the converter's capacitors, when their strings are connected to the grid and to the generator terminals, in such a way as to maintain the capacitor voltages constant and regulated. In other words, depending on the instantaneous mismatch between the power being injected into the grid and the power being absorbed from the WT, then a different number of battery submodules must be inserted in the string instantaneously connected to the terminal with higher power value to absorb/supply the power mismatch. This operation will be further explained through the simulation results presented in Fig. 72.

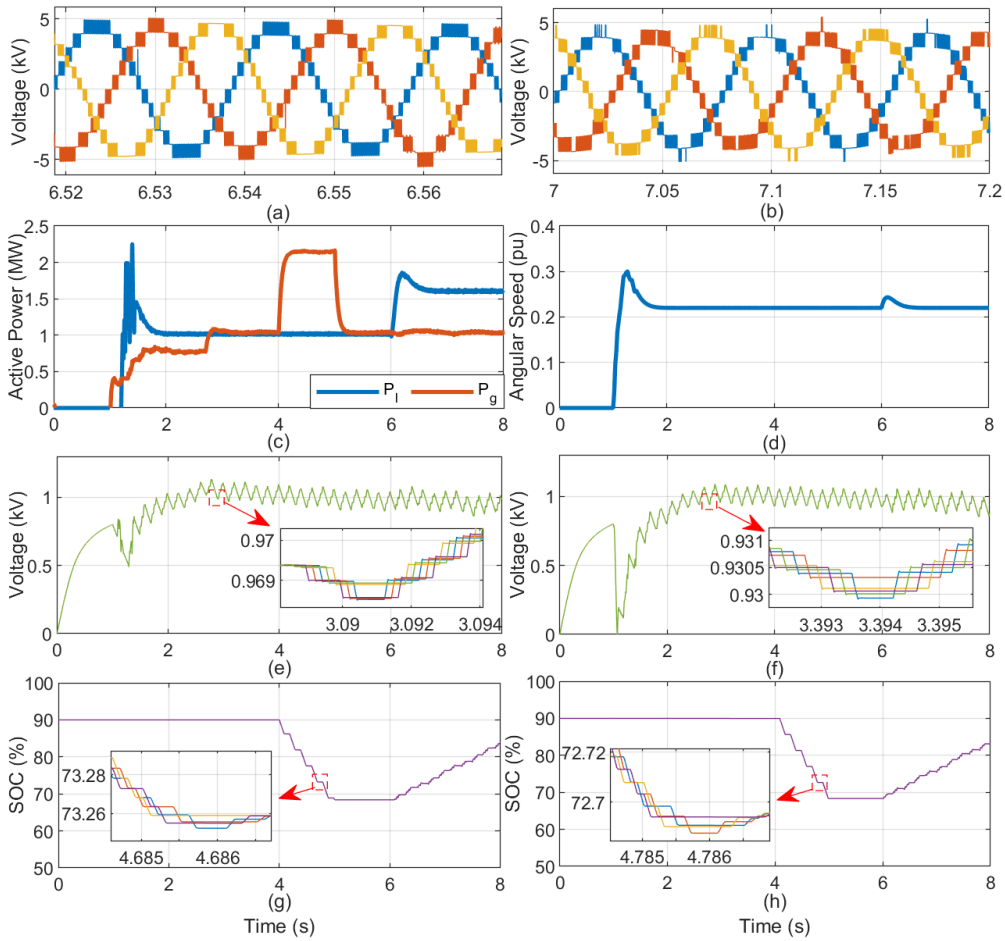

Fig. 72: Simulation results of the hybrid MMShC operation with battery submodules being inserted, and with ideal power mismatch between the converter's grid side and generator side. (a) Voltages synthesized at the grid-side terminals, (b) voltages synthesized at the generator-side terminals, (c) grid-side and generator-side power values, (d) generator's angular speed, (e) MMShC's phase-A String-X submodule-capacitor voltages, (f) MMShC's phase-A String-Y submodule-capacitor voltages, (g) MMShC's phase-A String-X battery-SOC values, and (h) MMShC's phase-A String-Y battery-SOC values.

In Fig. 72(a) and (b), the staircase-shape multilevel voltages synthesized by the hybrid MMShC at its grid-side and generator-side terminals are shown, respectively. These are voltage signals with a relatively high power quality, whose harmonic components can easily be filtered out. In Fig. 72(c), the converter's grid-side and load-side power values are shown. In Fig. 72(d), the generator angular speed is depicted, which is regulated

with a value equal to 0.22 pu throughout the entire simulation. In Fig. 72(e) and (f), the MMShC's phase-A String-X and phase-A String-Y submodule-capacitor voltages are shown, respectively. In Fig. 72(g) and (h), the MMShC's phase-A String-X and phase-A String-Y submodule-battery SOC values are shown, respectively. At $t = 1$ s, the system is initialized and the power injected into the grid by the MMShC is set to a value less than the power generated by the WT. When the system is initialized, all the submodules with batteries are kept by-passed, and only submodules with capacitors are inserted to synthesize the voltages at the grid-side and at the generator-side terminals. Since the power being injected into the grid by the converter is less than the power being absorbed from the generator, then the average value of the submodule-capacitor voltages of both strings increase. The submodule-battery SOC values of both strings, however, remain constant with their initial value equal to 90% since the battery submodules remain by-passed. As soon as the average value of the submodule-capacitor voltages reaches the nominal value equal to 1 kV, then the power being injected into the grid by the converter is increased to match the power being absorbed from the WT in such a way as to maintain the submodule-capacitor voltages regulated with 1 kV, i.e., the converter's capacitors are charged, when connected to the turbine terminals, with the same rate that they are discharged when connected to the grid terminals.

At $t = 4$ s, the power injected into the grid is increased, and it becomes considerably higher than the power produced by the WT. The power mismatch between P_g and P_l in this situation corresponds exactly to the power that would be supplied by the converter's batteries if two battery submodules were inserted in the strings connected to the grid terminals. In other words, in the specific operation condition that occurs between $t = 4$ s and $t = 5$ s, when a given submodule string is connected to the generator terminals, then only capacitor submodules should be inserted to absorb the power produced by the WT, i.e., $N_{cap} = Z$, which means that the instantaneous number of capacitor submodules to be inserted (N_{cap}) should be equal to the instantaneous number of submodules to be inserted (Z) to synthesize the desired instantaneous voltage at the machine's terminals. The instantaneous number of submodules to be inserted (Z) is defined by the modulation. When a given submodule string is connected to the grid terminals, however, the procedure to insert submodules is the following: if $Z \leq 2$, then $N_{cap} = 0$ and $N_{bat} = Z$, and if $Z > 2$, then $N_{cap} = Z - 2$ and $N_{bat} = 2$. This insertion procedure means that, when a given string is connected to the grid terminals, then battery submodules should be inserted with priority, and if the instantaneous number of submodules to be inserted is at least equal to $Z = 2$, then $N_{bat} = 2$ battery submodules should always be inserted, and the rest of submodules to be inserted to complete the instantaneous value of Z are then capacitor submodules. Explaining this operation through words is quite complex and that is why Fig. 68, Fig. 69, and Fig. 70 were presented in this thesis. Essentially, the instantaneous power mismatch between P_g and P_l was intentionally set to a specific value that corresponds to the power supplied by the converter's batteries if two battery submodules are inserted, i.e., considering the battery voltage and the rms value of the

grid-side current, for the specific operation condition, then the power supplied by two batteries will be exactly equal to the mismatch between P_g and P_l. The rest of the power injected into the grid would come from the capacitors, which is exactly equal to the power instantaneously generated by the WT, which is the power charging the capacitors of the string connected to the generator terminal. This way the capacitors of the string connected to the grid terminal are being discharged with the same rate that the capacitors of the string connected to the generator terminal are being charged. For this reason, the average value of the submodule-capacitor voltages remain constant and regulated at the nominal value of 1 kV. By observing Fig. 72(g) and (h), it is possible to notice that the battery-SOC values of the two strings remain constant before $t = 4$ s. From $t = 4$ s, however, the battery-SOC values of both strings start to decrease since the converter's batteries are being inserted at the grid terminals to supply power to the grid. It is interesting to notice in Fig. 72(e) and (f) that the average value of the submodule capacitors remain constant and regulated at 1 kV between $t = 4$ s and $t = 5$ s. In summary, it means that, between $t = 4$ s and $t = 5$ s, the mismatch between P_g and P_l is being supplied to the grid by the converter's batteries, and the converter's capacitors are transferring to the grid only the power generated by the WT, i.e., these capacitors are charged, when connected to the generator terminal, with the same rate that they are discharged, when connected to the grid terminal.

At $t = 5$ s, the power injected into the grid is decreased, and it becomes once again equal to the power being generated by the WT. In this situation, the battery submodules remain by-passed, and only capacitor submodules are used to transfer the power produced by the WT to the grid, i.e., when a given submodule string is connected to either the grid or to the generator terminals, its procedure to insert submodules is always the following: $N_{cap} = Z$ and $N_{bat} = 0$. By observing Fig. 72(g) and (h), it is possible to notice that the battery-SOC values of the two strings remain constant, between $t = 5$ s and $t = 6$ s, since the battery submodules are always by-passed. By observing Fig. 72(e) and (f), it is possible to notice that the average value of the submodule-capacitor voltages remain constant and regulated at 1 kV since these capacitors are being charged at the same rate, when connected to the generator terminals, that they are being discharged, when connected to the grid terminals.

Finally, at $t = 6$ s, the power produced by the WT is increased and it becomes higher than the power injected into the grid. The power mismatch between P_g and P_l in this situation corresponds exactly to the power that would be absorbed by the converter's batteries if one battery submodule was inserted in the strings connected to the generator terminals. In other words, in the specific operation condition that occurs from $t = 6$ s, when a given submdoule string is connected to the grid terminals, then only capacitor submodules should be inserted to inject into the grid the power value according to the pre-defined setpoint, i.e., $N_{cap} = Z$, which means that the instantaneous number of capacitor submodules to be inserted (N_{cap}) should be equal to the instantaneous number of submodules to be inserted (Z) to synthesize the desired in-

stantaneous voltage at the grid terminals. When a given submdoule string is connected to the generator terminals, however, the procedure to insert submodules is the following: if $Z \leq 1$, then $N_{cap} = 0$ and $N_{bat} = Z$, and if $Z > 1$, then $N_{cap} = Z - 1$ and $N_{bat} = 1$. This insertion procedure means that, when a given string is connected to the generator terminals, then battery submodules should be inserted with priority, and if the instantaneous number of submodules to be inserted is at least equal to $Z = 1$, then $N_{bat} = 1$ battery submodule should always be inserted, and the rest of submodules to be inserted to complete the instantaneous value of Z are then capacitor submodules. Essentially, the instantaneous power mismatch between P_g and P_l was intentionally set to a specific value that corresponds to the power absorbed by the converter's batteries if one battery submodule is inserted, i.e., considering the battery voltage and the rms value of the generator-side current, for the specific operation condition, then the power absorbed by one battery will be exactly equal to the mismatch between P_g and P_l. The rest of the power absorbed from the WT would be stored in the capacitors, which is exactly equal to to power instantaneously injected into the grid, which is the power discharging the capacitors of the string connected to the grid terminal. This way the capacitors of the string connected to the grid terminal are being discharged with the same rate that the capacitors of the string connected to the generator terminal are being charged. For this reason, the average value of the submodule-capacitor voltages remain constant and regulated at the nominal value of 1 kV. By observing Fig. 72(g) and (h), it is possible to notice that the battery-SOC values of the two strings start to increase since the converter's batteries are being inserted at the generator terminals to absorb part of the power produced by the WT. It is interesting to notice in Fig. 72(e) and (f) that the average value of the submodule capacitors remain constant and regulated at 1 kV after $t = 6$ s. In summary, it means that the mismatch between P_g and P_l is being stored in the converter's batteries, and the converter's capacitors are transferring to the grid the part of the power generated by the WT that matches the grid power setpoint. In other words, these capacitors are charged, when connected to the generator terminal, with the same rate that they are discharged, when connected to the grid terminal.

It is also interesting to notice that the rate with which the converter's batteries are being charged, after $t = 6$ s, is lower than the rate with which the converter's batteries are being discharged between $t = 4$ s and $t = 5$ s. This is because the power mismatch between $t = 4$ s and $t = 5$ is approximately double the power mismatch after $t = 6$ s and, thus, between $t = 4$ s and $t = 5$, two battery submodules were inserted, when the instantaneous value of Z was greater or equal to 2, while, after $t = 6$ s, only one battery submodule was inserted when the instantaneous value of Z was greater or equal to 1. Obviously, the higher the number of inserted battery submodules, the higher the power absorbed/supplied by the converter's batteries. One last point that is interesting to observe in Fig. 72(e), (f), (g), and (h) are the zoom in the submodule-capacitor voltages and in the submodule-battery SOC values of the two strings. Through the zoom sub figures, it is possible to see each individual voltage of the N capacitors within one string

and each individual SOC value of the M batteries within one string. A sorting algorithm is used to maintain all the capacitors within the same string with similar voltage values, and all the batteries within the same string with similar SOC values.

As previously explained, in the simulation whose results are presented in Fig. 72, the mismatch between P_g and P_l was set intentionally to specific values that corresponded to multiples of the battery power for the considered operation conditions. For example, between $t = 4$ s and $t = 5$ s, the power mismatch between P_g and P_l was exactly equal to the power discharging two batteries, considering the battery voltage and the instantaneous current flowing through the given submodule string. Thus, by using the approach of always inserting two battery submodules to the string connected to the grid, if the instantaneous number of submodules to be inserted was at least equal to two, then the average value of the converter's submodule-capacitor voltages would remain constant. The situation explained through Fig. 72 is a very specific operation condition that would only rarely occur for brief moments. In reality, the mismatch between P_g and P_l will continuously vary, and this mismatch will be equal to a power value between two multiples of the battery power. It means that, even for a fixed power mismatch between P_g and P_l, the number of battery submodules to be inserted will have to vary to maintain the submodule-capacitor voltages regulated within an acceptable range. This operation condition will be explained through Fig. 73 below.

In Fig. 73(a), the MMShC's grid-side and generator-side power values are shown. In Fig. 73(b), the generator's angular speed is shown, which is kept constant throughout the entire simulation period. In Fig. 73(c) and (d), the MMShC's phase-A String-X and phase-A String-Y submodule-capacitor voltages are shown, respectively. In Fig. 73(e) and (f), a zoom of the submodule-capacitor voltages shown in Fig. 73(c) and (d) are shown, respectively. Finally, in Fig. 73(g) and (h), the MMShC's phase-A String-X and phase-A String-Y submodule-battery SOC values are shown, respectively. By observing Fig. 73(a), it is possible to notice that the grid-side power (P_g) is kept less than the machine-side power (P_l) until the average value of the submodule-capacitor voltages of both strings reaches 1 kV. As soon as the capacitor voltages reach 1 kV, then the power being injected into the grid is increased so that it matches the power being absorbed from the WT. Due to the matching grid-side and generator-side power values, the submodule-capacitor voltages remain constant and regulated at 1 kV. At $t = 4$ s, the grid-side power setpoint is increased and it becomes greater than the power being generated by the WT. In this case, the power mismatch between P_g and P_l is obviously greater than the power supplied by the converter's batteries if no battery submodule is inserted, but it is less than the power supplied by the converter's batteries if one battery submodule is inserted. In other words, the instantaneous power mismatch is lower than the power of one battery considering the battery voltage and the instantaneous current flowing through the submodule string (and through the inserted battery). Thus, in order to keep the submodule-capacitor voltage regulated within an acceptable range, the insertion of battery submodules will have to vary between the two previously mentioned

conditions. This operation can be better understood by observing Fig. 73(e) and (f). At $t = 4$ s, the power being injected into the grid becomes greater than the power being produced by the WT and, thus the submodule insertion pattern of the strings connected to the grid terminals becomes the following: if $Z \leq 1$, then $N_{cap} = 0$ and $N_{bat} = Z$, and if $Z > 1$, then $N_{cap} = Z - 1$ and $N_{bat} = 1$. With this insertion pattern, the power supplied to the grid by the converter's batteries is higher than the power mismatch between P_g and P_l. This means that the converter's capacitors will inject into the grid a power value less than the power that they will absorb from the WT. Thus, the average value of the submodule-capacitor voltages of both strings starts to increase as shown in Fig. 73(e) and (f). As soon as the submodule-capacitor voltages exceed the pre-defined upper limit equal to 1.1 kV, then the procedure for inserting submodules changes to: when a given submodule string is connected to the grid terminals, then only capacitor submodules should be inserted, i.e., $N_{cap} = Z$ and $N_{bat} = 0$. With this insertion pattern, the power supplied to the grid by the converter's batteries is null. This means that the converter's capacitors will inject into the grid a power value greater than the power that they will absorb from the WT. Thus, the average value of the submodule-capacitor voltages of both strings starts to decrease as shown in Fig. 73(e) and (f). As soon as the submodule-capacitor voltages exceed the pre-defined lower limit equal to 0.9 kV, then the procedure for inserting submodules goes back to: if $Z \leq 1$, then $N_{cap} = 0$ and $N_{bat} = Z$, and if $Z > 1$, then $N_{cap} = Z - 1$ and $N_{bat} = 1$. Thus, the average value of the submodule-capacitor voltages starts to increase again. With this procedure, the submodule-capacitor voltages remain regulated within the acceptable voltage range of 0.9 kV to 1.1 kV (see Fig. 73(e) and (f)). It can then be concluded that the hybrid MMShC can operate in a dispatchable fashion, injecting into the grid an instantaneous power value different from the power instantaneously generated by the turbine, while its submodule-capacitor voltages are regulated by controlling the number of inserted battery submodules.

By observing Fig. 73(g) and (h), it is possible to notice that the SOC values of the converter's batteries start to decrease at $t = 4$ s since battery submodules start to be inserted to supply the surplus power to the grid. Nonetheless, it is interesting to notice that there are moments that the SOC values are decreasing and moments where they remain constant (steps can be observed in the SOC signals). The moments where the SOC values are decreasing correspond to the situations where the corresponding submodule string is connected to the grid terminals and battery submodules are being inserted, i.e., when the average value of the submodule-capacitor voltages is increasing before these voltages reach the upper limit of 1 kV. The moments where the SOC values remain constant occur in two different situations, i.e., either if the corresponding string is connected to the generator terminals (in which only capacitor submodules are inserted and the battery submodules remain by-passed), or if the corresponding string is connected to the grid terminals, but no battery submodule is being inserted (when the average value of the submodule-capacitor voltages is decreasing before these voltages

reach the lower limit of 0.9 kV).

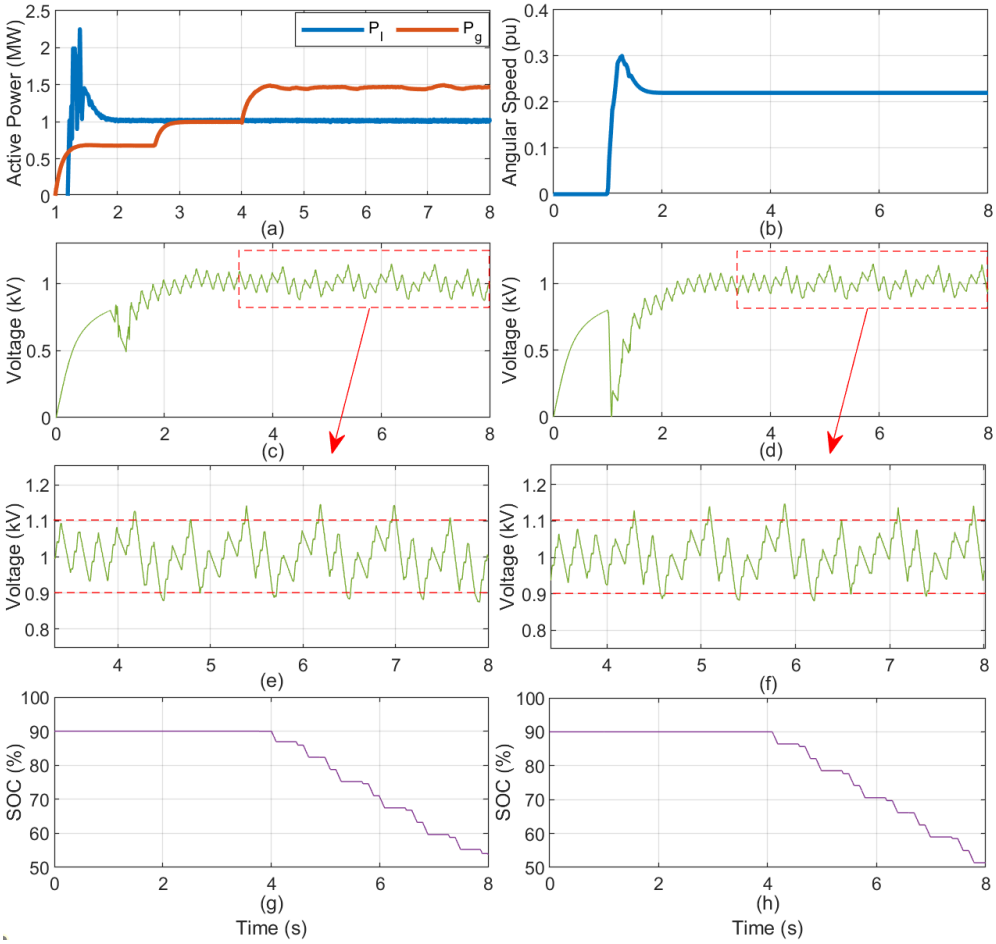

Fig. 73: Simulation results of the hybrid MMShC operation with battery submodules being inserted, and with real power mismatch between the converter's grid side and generator side. (a) Grid-side and generator-side power values, (b) generator's angular speed, (c) MMShC's phase-A String-X submodule-capacitor voltages, (d) MMShC's phase-A String-Y submodule-capacitor voltages, (e) zoom of voltage signals shown in Fig. 73(c), (f) zoom of voltage signals shown in Fig. 73(d), (g) MMShC's phase-A String-X battery-SOC values, and (h) MMShC's phase-A String-Y battery-SOC values.

3.6.3 Internal Control and Modulation

In this subsection, a reduced version of the hybrid MMShC control algorithm is presented through the flowchart shown in Fig. 74. The control algorithm presented

through this flowchart was the one adopted to obtain the specific simulation results shown in Fig. 73, which corresponds to a fixed operation condition of the converter. The full control algorithm is quite complex and hard to explain through a single flowchart. Fig. 74 gives an idea of how the full control would work, and further explanations will be provided in a text format below in this thesis. The control algorithm depicted in Fig. 74 was implemented through a C programming code, and it was adopted for the three phases of the converter, even though the control of phase A is used as an example in Fig. 74. Two of the inputs of the control algorithm are the voltage references to be synthesized at the converter's grid-side and load-side terminals, i.e., v^*_{ga} and v^*_{la}, respectively. These references come from outer control loops. Two other inputs to the control algorithm are the currents measured in the simulation at the MMShC's grid-side and load-side terminals, i.e., i_{ga} and i_{la}, respectively. The control algorithm also receives as inputs the battery SOC values of the M submodules within phase-A String X, and the battery SOC values of the M submodules within phase-A String Y (SOC_{AX1}, SOC_{AX2}, ..., SOC_{AXM}, and SOC_{AY1}, SOC_{AY2}, ..., SOC_{AYM}). Besides, the battery SOC values, the control algorithm also receives as inputs the capacitor voltages of the N submodules within phase-A String X, and the capacitor voltages of the N submodules within phase-A String Y (v_{AX1}, v_{AX2}, ..., v_{AXN}, and v_{AY1}, v_{AY2}, ..., v_{AYN}). Finally, the control algorithm receives as an input a triangular signal (tri), whose amplitude varies between 0 and 1 and whose frequency is equal to 5 Hz. This signal is used for the control of the MMShC's bidirectional-switch stacks.

As shown in Fig. 74, the first stage of the control is the bidirectional-switch-stack control logic that decides the connection of each submodule string depending on the instantaneous value of the signal tri. In other words, if the signal tri is greater than 0.5, then String X is connected to the generator terminal (as it operates in charging mode), and String Y is connected to the grid terminal (as it operates in discharging mode). In this case, the following triggering signals are given to each bidirectional-switch stack: $S_{XA} = 0$, $S_{Xa} = 1$, $S_{YA} = 1$, and $S_{Ya} = 0$, where 1 means ON state and 0 means OFF state. On the contrary, if the signal tri is less than 0.5, then String Y is connected to the generator terminal (as it operates in charging mode), and String X is connected to the grid terminal (as it operates in discharging mode). In this case, the following triggering signals are given to each bidirectional-switch stack: $S_{XA} = 1$, $S_{Xa} = 0$, $S_{YA} = 0$, and $S_{Ya} = 1$. Since the triangular signal has a frequency equal to 5 Hz, then the switching frequency of the bidirectional-switch stacks is also equal to 5 Hz. When $tri > 0.5$, String X is connected to the generator terminal and String Y is connected to the grid terminal. Thus, the voltage to be synthesized across String X becomes equal to the load-side voltage reference ($v^*_{sX} = v^*_{la}$), the voltage to be synthesized across String Y becomes equal to the grid-side voltage reference ($v^*_{sY} = v^*_{ga}$), the String-X current becomes equal to the load-side current ($i_X = i_{la}$), and the String-Y current becomes equal to the grid-side current ($i_Y = i_{ga}$). On the contrary, when $tri < 0.5$, String Y is connected to the generator terminal and String X is connected to the grid terminal.

Thus, the voltage to be synthesized across String Y becomes equal to the load-side voltage reference ($v^*_{sY} = v^*_{la}$), the voltage to be synthesized across String X becomes equal to the grid-side voltage reference ($v^*_{sX} = v^*_{ga}$), the String-Y current becomes equal to the load-side current ($i_Y = i_{la}$), and the String-X current becomes equal to the grid-side current ($i_X = i_{ga}$).

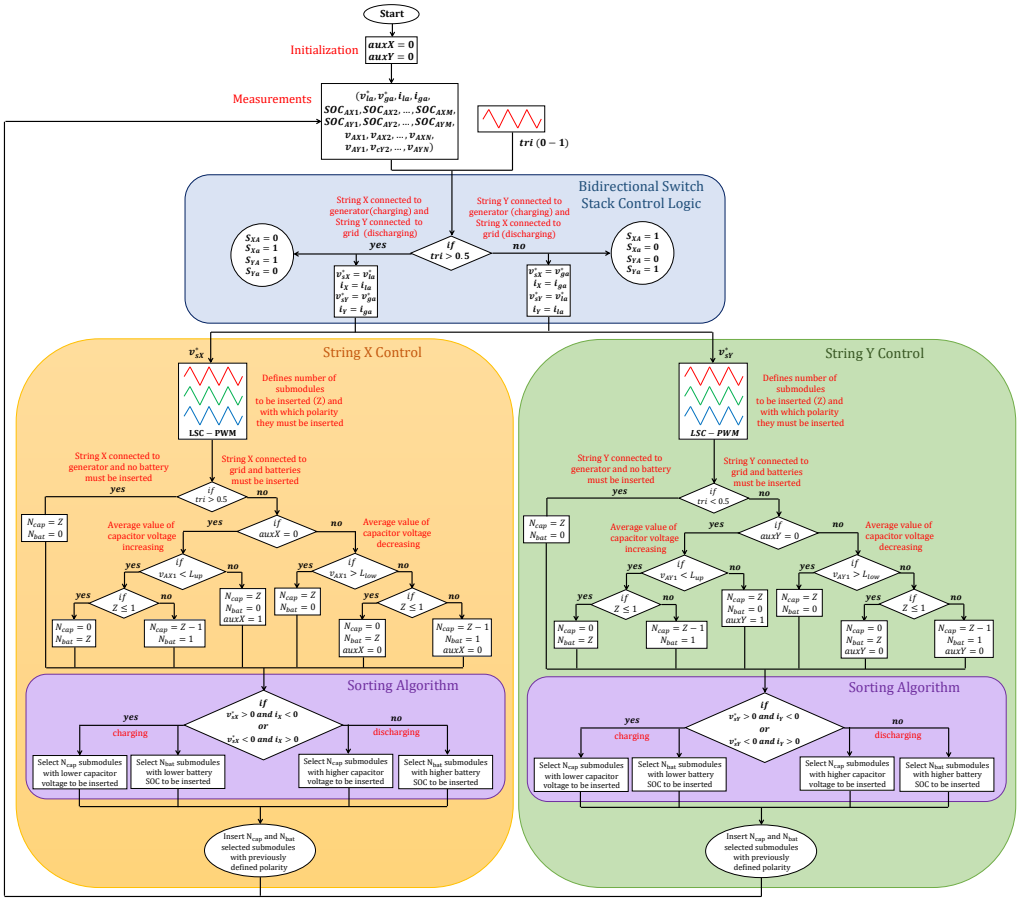

Fig. 74: Flowchart explaining a reduced version of the hybrid-MMShC control, which was used to obtain the simulation results shown in Fig. 73.

After assigning voltage references and currents to the two submodule strings, the next stage of the control is the String X and String Y control. The String X control is used as an explanatory example. The first step of the String X control is the mod-

ulation, based on a LSC-PWM technique, that receives as input the String-X voltage reference (v^*_{sX}), and outputs the instantaneous number of submodules to be inserted (Z) in order to track the received voltage reference. The modulation also defines if the FB submodules should be inserted with positive or with negative polarity to track the instantaneous value of the received reference. As previously mentioned, the flowchart shown in Fig. 74 is a reduced version of the full control, which was used to obtain the simulation results presented in Fig. 73, where a fixed operation point was considered for the hybrid MMShC. In other words, in the mentioned simulation, the hybrid MMShC operated supplying to the grid a fixed power value, which was higher than the fixed power value absorbed from the WT. Thus, in this case, when the strings of the hybrid MMShC were connected to the turbine terminal, then only capacitor submodules had to be inserted, and when the strings were connected to the grid terminals, then some battery submodules had to be inserted to inject the surplus power into the grid, i.e., the mismatch between the instantaneous power generated by the WT and the instantaneous power set point to be injected into the grid. This operation can be understood by observing the String X control illustrated in Fig. 74. Once again, the signal *tri* is the one that defines the connection of the submodule strings to the grid and to the generator terminals, i.e., if *tri* is greater than 0.5, then String X is connected to the generator terminals and only capacitor submodules should be inserted, which means that $N_{cap} = Z$ and $N_{bat} = 0$. On the contrary, if *tri* is less than 0.5, then some batteries submodules should be inserted. In this case, according to the flowchart, the control will test if the variable $auxX$ is equal to zero. Since this variable is initialized with a value equal to zero, then the control will first enter the left-hand side of the *if* statement. Initially, it is supposed that the submodule insertion pattern of String X when connected to the grid terminals is the following: if $Z \leq 1$, then $N_{cap} = 0$ and $N_{bat} = Z$, and if $Z > 1$, then $N_{cap} = Z - 1$ and $N_{bat} = 1$. This situation corresponds to the case where the average value of the submodule-capacitor voltages of String X is increasing since the power injected into the grid by the string's batteries is higher than the power mismatch between the instantaneous power generated by the WT and the power setpoint to be injected into the grid. In other words, the string's capacitors are charged at a higher rate when they are connected to the generator's terminals than they are discharged when they are connected to the grid terminals. Since the submodule-capacitor voltages are increasing in average, then an *if* statement is used to test if the submodule-capacitor voltage of the first submodule of String X (v_{AX1}) is less than the upper voltage limit $L_{up} = 1.1$ kV. While $v_{AX1} < L_{up}$, then the submodule insertion pattern remains equal to: if $Z \leq 1$, then $N_{cap} = 0$ and $N_{bat} = Z$, and if $Z > 1$, then $N_{cap} = Z - 1$ and $N_{bat} = 1$. As soon as v_{AX1} exceeds L_{up}, then the submodule insertion pattern becomes equal to: $N_{cap} = Z$ and $N_{bat} = 0$, and the variable $auxX$ becomes equal to 1. This situation corresponds to the case where the average value of the submodule-capacitor voltages of String X is decreasing since the power injected into the grid by the string's batteries is less than the power mismatch between the instantaneous power generated by the WT and the

power setpoint to be injected into the grid. In other words, the string's capacitors are discharged at a higher rate when they are connected to the grid terminals than they are charged when they are connected to the generator's terminals. Since now $auxX = 1$, then, when String X is connected to the grid terminal, the control algorithm will enter the right-hand side of the *if* statement of Fig. 74. An *if* statement is used to test if the submodule-capacitor voltage of the first submodule of String X (v_{AX1}) is greater than the lower voltage limit $L_{low} = 0.9$ kV. While $v_{AX1} > L_{low}$, then the submodule insertion pattern remains equal to: $N_{cap} = Z$ and $N_{bat} = 0$, which means that the submodule-capacitor voltages of String X continue to decrease in average. As soon as v_{AX1} exceeds L_{low}, then the submodule insertion pattern comes back to: if $Z \leq 1$, then $N_{cap} = 0$ and $N_{bat} = Z$, and if $Z > 1$, then $N_{cap} = Z - 1$ and $N_{bat} = 1$, and the variable $auxX$ comes back to 0. With this insertion pattern, the submodule capacitor voltages start to increase again in average. Now, the control algorithm will enter the left-hand-side of the *if* statement the next time it runs, if $tri < 0.5$, which corresponds to the case where String X is connected to the grid terminal. With this control algorithm, the submodule-capacitor voltages of the hybrid MMShC remain within the pre-defined lower and upper voltage limits ($L_{low} = 0.9$ kV and $L_{up} = 1.1$ kV, respectively), as presented in the simulation results shown in Fig. 73.

Finally, the last stage of the control flowchart is the sorting algorithm responsible for the submodule-capacitor voltage balancing and for the submodule-battery SOC balancing. The previously stage of the control algorithm was responsible to define the instantaneous number of capacitor submodules and of battery submodules to be inserted (N_{cap} and N_{bat}, respectively). The sorting algorithm defines which of the N available capacitor submodules in the string, and which of the M available battery submodules in the string should be inserted. In order to do that, the sorting algorithm checks the polarity of the voltage reference (v^*_{sX}), which is equal to the polarity with which the submodules must be inserted to track the reference, and checks the instantaneous direction of the string current (i_X). Depending on the combination of voltage polarity and current direction, the capacitors and batteries of the inserted submodules will be charged or discharged. If the instantaneous combination results in a charging current, then the N_{cap} submodules with lower capacitor voltage, and the N_{bat} submodules with lower battery SOC are selected to be inserted. On the contrary, if the instantaneous combination results in a discharging current, then the N_{cap} submodules with higher capacitor voltage, and the N_{bat} submodules with higher battery SOC are selected to be inserted. This way, all the N capacitor submodules within the string remain with similar capacitor voltage values, and all the M battery submodules within the string remain with similar battery SOC values, as demonstrated in the simulation results shown in Fig. 72(e), (f), (g), and (h). The output of the control algorithm is the gate signals to the submodule IGBTs, which will result in the insertion of the N_{cap} selected capacitor submodules and of the N_{bat} selected battery submodules.

Once again, the control algorithm described through the flowchart presented in

Fig. 74 is a simplified version of the complete control that would be required in a real application. The control presented in Fig. 74 was the one used to obtain the specific results presented in Fig. 73. The complete control of the hybrid MMShC would require as inputs the power values measured at the grid-side and at the load-side terminals (P_g and P_l, respectively). These two power values would be required to decide whether battery submodules would have to be inserted in the strings connected to the grid terminals or to the generator terminals for the given operation condition, i.e., as previously explained, when the grid power setpoint is greater than the power instantaneously generated by the WT ($P_g > P_l$), then only capacitor submodules should be inserted in the strings that are connected to the generator terminals, but some battery submodules should be inserted in the strings connected to the grid terminals to supply the surplus power to the grid. On the contrary, when the power instantaneously generated by the WT is greater than the grid power setpoint ($P_l > P_g$), then only capacitor submodules should be inserted in the strings that are connected to the grid terminals, but some battery submodules should be inserted in the strings connected to the WT terminals to absorb the surplus power produced by the generator. Moreover, more than one upper and more than one lower voltage limits would be required to decide on the number of battery submodules to be inserted to keep the converter's submodule-capacitor voltages regulated within an acceptable range. An illustrative explanation of the multiple voltage limits is shown in Fig. 75 and in Fig. 76.

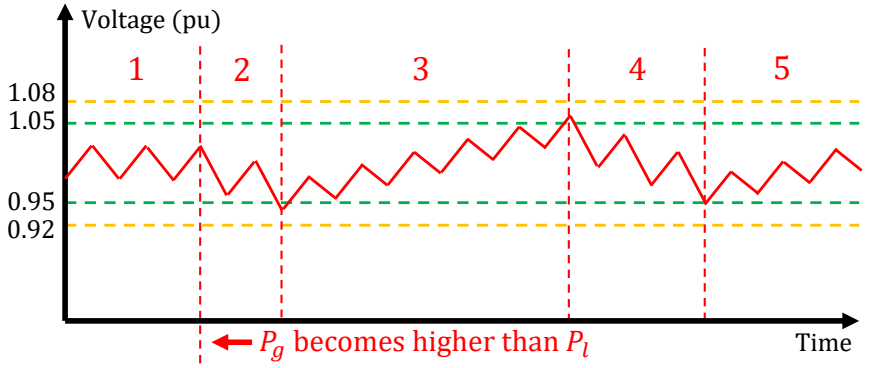

Fig. 75: Explanatory figure showing multiple voltage limits to decide on the number of battery submodules to be inserted to maintain the submodule-capacitor voltage regulated within a pre-defined range.

Let us analyze the example presented in Fig. 75. In this example, it is supposed that, initially (interval 1), the grid power setpoint is equal to the power instantaneously being produced by the WT, which means that the power being inject into grid by the converter is equal to the power absorbed from the WT. In this case, only capacitor submodules are inserted to the strings when they are connected to both the grid and the generator terminals. The average value of the submodule-capacitor voltages remain

constant since these capacitors are being charged and discharged at the same rate when they are connected to the generator and to the grid terminals, respectively. At the beginning of interval 2, the grid power setpoint is increased and it becomes higher than the power produced by the WT ($P_g > P_l$), which is kept fixed with the same previous value. Thus, the average value of the converter's submodule-capacitor voltages starts to decrease since only capacitor submodules are being inserted, and since these capacitors are being discharged at a higher rate when they are connected to the grid terminals than they are being charged when they are connected to the generator terminals. The submodule insertion pattern of the hybrid MMShC during interval 2 is the following: if a given string is connected to either the grid or the generator terminals, then $N_{cap} = Z$ and $N_{bat} = 0$. As soon as the submodule-capacitor voltages exceed the first lower limit equal to $L_{low1} = 0.95$ pu (represented by a dashed green line in Fig. 75), then the submodule insertion pattern changes to: if the submodule string is connected to the grid terminal, then if $Z \leq 1$, then $N_{cap} = 0$ and $N_{bat} = Z$, and if $Z > 1$, then $N_{cap} = Z - 1$ and $N_{bat} = 1$. This insertion pattern means that, if the submodule string is connected to the grid terminal, and the instantaneous number of submodules to be inserted (Z) is at least equal to 1, then one battery submodule will always be inserted. The example presented in Fig. 75 represents a situation where the power supplied by only one battery submodule inserted is greater than the mismatch between P_g and P_l, which means that the power injected into the grid by the submodule capacitors when the string is connected to the grid is less than the power absorbed by these submodule capacitors when the string is connected to the generator terminal. For this reason, the average value of the submodule-capacitor voltages starts to increase as illustrated in the interval 3 of Fig. 75. As soon as the submodule-capacitor voltages exceed the first upper limit equal to $L_{up1} = 1.05$ pu (represented by a dashed green line in Fig. 75), then the submodule insertion pattern comes back to: if a given string is connected to either the grid or the generator terminals, then $N_{cap} = Z$ and $N_{bat} = 0$. Then, the average value of the submodule-capacitor voltages starts to decrease again, which corresponds to the interval 4 of Fig. 75. Finally, interval 5 is the same as interval 3.

Let us now analyze the second example illustrated in Fig. 76. Interval 1 of the second example is identical to interval 1 of the previous example presented in Fig. 75. Similarly to the previous example, at the beginning of interval 2, the power injected into the grid is increased and it becomes higher than the power instantaneously produced by the WT. However, in the second example, the power mismatch between P_g and P_l is higher than in the previous example since the increase in the grid power setpoint (P_g), at the beginning of interval 2, is higher than in the previous case. At the beginning of interval 2, the average value of the submodule-capacitor voltages starts to decrease since ($P_g > P_l$), and since the insertion pattern is still the following: if a given string is connected to either the grid or the generator terminals, then $N_{cap} = Z$ and $N_{bat} = 0$. Similarly to the previous example, as soon as the submodule-capacitor voltages exceed the first lower limit equal to $L_{low1} = 0.95$ pu (represented by a dashed green line in

Fig. 76), then the submodule insertion pattern changes to: if the submodule string is connected to the grid terminal, then if $Z \leq 1$, then $N_{cap} = 0$ and $N_{bat} = Z$, and if $Z > 1$, then $N_{cap} = Z - 1$ and $N_{bat} = 1$. However, differently from the previous example, in this case the average value of the submodule-capacitor voltages continues to decrease, which consists in interval 3 of Fig. 76. Since the grid-side power setpoint was increased more in the second example than in the first one, then the power mismatch between P_g and P_l is higher in the second example, and this mismatch is higher than the power injected into the grid by the converter's batteries if only one battery submodule is being inserted in the strings connected to the grid terminal. In other words, even though one battery submodule is partially providing the power to be injected into the grid, the capacitors of the string when connected to the grid terminal are still being discharged at a higher rate than these capacitors are being charged when the string is connected to the generator terminal. In interval 3 of Fig. 76, the average value of the submodule-capacitor voltages continues to decrease (even though at a slower rate in comparison to interval 2), until these voltages exceed the second lower limit equal to $L_{low2} = 0.92$ pu (represented by a dashed orange line in Fig. 76). As soon as the submodule-capacitor voltages exceed the second lower limit ($L_{low2} = 0.92$ pu), then the submodule insertion pattern becomes equal to: if the submodule string is connected to the grid terminal, then if $Z \leq 2$, then $N_{cap} = 0$ and $N_{bat} = Z$, and if $Z > 2$, then $N_{cap} = Z - 2$ and $N_{bat} = 2$. This insertion pattern means that, if the submodule string is connected to the grid terminal, and the instantaneous number of submodules to be inserted (Z) is at least equal to 2, then two battery submodules will always be inserted. In this case, a bigger percentage of the power being injected into the grid by the string is coming from its batteries, which means that a smaller percentage is coming from its capacitors. In the second example, it is considered that the power injected into the grid by the two batteries is higher than the power mismatch between P_g and P_l, which means that the average value of the submodule-capacitor voltages starts to increase as illustrated in the interval 4 of Fig. 76. In interval 4, two battery submodules can simultaneously be inserted in the submodule string when connected to the grid terminal and, once again, the power supplied by these two batteries is higher than the power mismatch between P_g and P_l. It means that the string capacitors are being discharged at lower rate when connected to the grid terminal than they are being charged when connected to the generator terminal. As soon as the submodule-capacitor voltages exceed the first upper limit equal to $L_{up1} = 1.05$ pu (represented by a dashed green line in Fig. 76), then the submodule insertion pattern comes back to: if the submodule string is connected to the grid terminal, then if $Z \leq 1$, then $N_{cap} = 0$ and $N_{bat} = Z$, and if $Z > 1$, then $N_{cap} = Z - 1$ and $N_{bat} = 1$. Now, a maximum of one battery submodule will be inserted in the string when connected to the grid terminal, which means that the average value of the submodule-capacitor voltages starts to decrease again as illustrated in the interval 5 of Fig. 76. Finally, interval 6 is the same as interval 4, which means that the submodule insertion pattern will remain switching between the two explained conditions

(by inserting either one or two battery submodules when the string is connected to the grid terminal), while the operation condition of the system remains the same (while the values of P_g and P_l don't change).

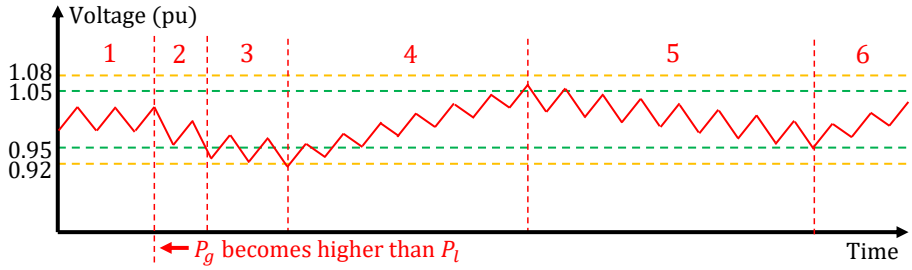

Fig. 76: Explanatory figure showing multiple voltage limits to decide on the number of battery submodules to be inserted to maintain the submodule-capacitor voltage regulated within a pre-defined range.

The two previously presented examples considered cases where a maximum of $N_{bat} = 2$ was required to keep the submodule-capacitor voltages regulated while supplying the surplus power into the grid according to the grid power setpoint. In this case, only two upper and two lower voltage limits were necessary. However, in reality, more limits might be required to perform the control, i.e., to be possible to insert more battery submodules in the converter's strings. Another approach could be to decide the number of battery submodules to be inserted based on an estimation considering the power mismatch between P_g and P_l, and calculating the battery power. In other words, by knowing the battery voltage, the instantaneous string current, and the insertion index of the submodule strings, then it would be possible to calculate the current flowing through the batteries, and it would be possible to calculate the power charging/discharging these batteries. Then, the calculated battery power could be compared with the power mismatch between P_g and P_l to decide how many battery submodules would have to be inserted to supply/absorb the power mismatch between P_g and P_l, without having to rely on the voltage limits explained through Fig. 75 and Fig. 76. This approach should be investigated in future works.

3.7 Operation in Grid-Forming Mode

In this section, different operation modes of the MMShC with an integrated ESS are presented, i.e., in grid-connected mode and in islanded mode. One of the possible applications of the MMShC with an integrated ESS would be to have a wind farm built with some of its WTs driven by a MMShC with an integrated ESS, and some of its WTs driven by a conventional voltage-source converter without an ESS (for example driven by the MMShC with capacitors only). Let us consider the hypothetical example,

illustrated in Fig. 77, where a wind farm is built with two WTs only, i.e., one driven by the MMShC with an integrated ESS, and the other driven by a conventional voltage-source converter with no ESS.

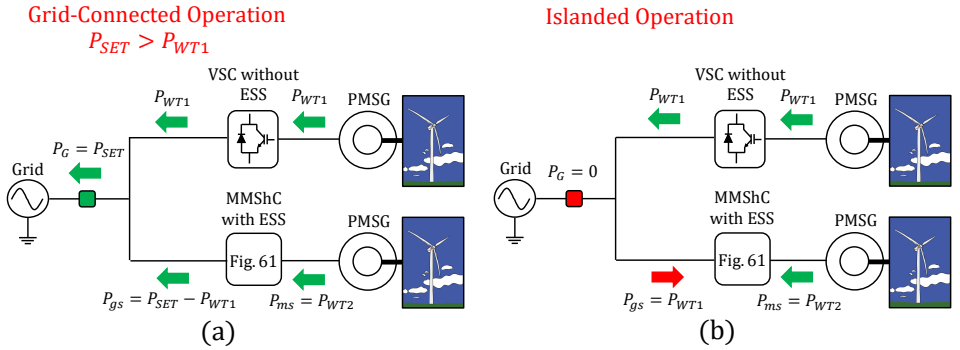

Fig. 77: Different operation modes of the MMShC with integrated batteries. (a) Grid connected and $P_{SET} > P_{WT1}$, and (b) islanded operation.

In the grid-connected mode, the operation illustrated in Fig. 77(a) would occur, i.e., the power to be injected into the grid by the wind farm (P_G) would have to be equal to the set point imposed by the TSO (P_{SET}). Considering that the power produced by the WT without an ESS is equal to P_{WT1}, then the grid-side of the MMShC with an integrated ESS would have to inject into the grid a power value equal to $P_{gs} = P_{SET} - P_{WT1}$ since $P_{SET} > P_{WT1}$ is considered in this case. In other words, the power injected into the grid by the grid-side terminal of the MMShC with an integrated ESS would always be equal to the difference between the grid power setpoint and the instantaneous power generated by the other WT. This way, a dispatchable operation would be obtained, i.e., $P_G = P_{SET}$. It is important to highlight that the power absorbed by the machine-side terminal of the MMShC with an integrated ESS would always be equal to the power generated by its WT ($P_{ms} = P_{WT2}$) despite the value of power injected into the grid by the converter, i.e., the power mismatch between P_{gs} and P_{ms} would be absorbed/supplied by the converter's batteries. In case the system becomes islanded, then the power injected into the grid would obviously become null ($P_G = 0$). In this case, the grid side of the MMShC with an integrated ESS would start absorbing the power produced by the other WT , i.e., $P_{gs} = P_{WT1}$, and its machine side would continue to absorb the power produced by its own WT, i.e., $P_{ms} = P_{WT2}$. It is interesting to notice that, in this case, power would be absorbed by both terminals of the MMShC with an integrated ESS. In a real wind power plant with many WTs, then some of these WTs could be driven by a MMShC with an integrated ESS, and some of them could be driven by a conventional converter with no ESS. In this case, a droop control (or any other load-sharing control technique) would have to be adopted to regulate the amount of power absorbed/supplied by each WT driven by a MMShC

with an integrated ESS.

The first simulation results presented in this subsection correspond to the operation of the MMShC with integrated batteries (see Fig. 61) operating in grid-connected and islanded modes. This simulation was based on the hypothetical wind farm composed of only two WTs, as illustrated in Fig. 77. This hypothetical wind power plant was modeled in the software PSCAD/EMTDC, where the MMShC was designed with $N = 4$ submodules per string, and with batteries with the following rated voltage and rated energy: 1 kV, and 0.125 Ah. The wind power plant was connected to a hypothetical 5-kV, 50-Hz grid. In this simulation, a PMSG was used to model the wind-turbine generator, and the MMShC controlled the machine speed through a FOC algorithm. In this simulation, the PMSG was started with a speed reference equal to 0.2 pu and with a mechanical torque of 0.7 pu imposed to its shaft. At $t = 6.5$ s, the speed reference was increased to 0.3 pu. At 8 s, the mechanical torque was increased to 0.9 pu, which represented a step in the wind speed imposed to the blades of the WT. During the entire simulation, the second WT (the one driven by the voltage-source converter without an ESS) generated a constant power equal to $P_{WT1} = 0.6$ MW. From the beginning of the simulation until $t = 4.8$ s, the wind power plant remained connected to the grid, and operated in the mode illustrated in Fig. 77(a), which means that the MMShC operated in grid-following mode, while injecting into the grid a power value equal to $P_{gs} = P_{SET} - P_{WT1}$. Between $t = 4.8$ s and $t = 6$ s, the wind farm was disconnected from the main grid, which means that the MMShC with an integrated ESS entered the grid-forming mode, as illustrated in Fig. 77(b). Finally, at $t = 6$ s, the system was reconnected to the grid, and it came back to the operation mode illustrated in Fig. 77(a).

The results of the previously presented simulation are shown in Fig. 78 below. In Fig. 78(a), the following power values (described in Fig. 77) are shown: P_G, P_{WT1}, and P_{gs}. In this simulation, the power to be dispatched to the grid according to the predefined setpoint is equal to $P_{SET} = 1.6$ MW. Since $P_{SET} = 1.6$ MW and $P_{WT1} = 0.6$ MW, then the power to be injected into the grid by the grid-side terminal of the MMShC is equal to $P_{gs} = P_{SET} - P_{WT1} = 1$ MW. By observing Fig. 78(a), it is possible to notice that P_{gs} is in fact equal to 1 MW, during the periods where the system is connected to the grid. As previously mentioned, between $t = 4.8$ s and $t = 6$ s, the system becomes islanded, and the MMShC starts to operate in grid-forming mode, and it starts to absorb the power produced by the other WT. In Fig. 78(a), it is possible to observe that, between $t = 4.8$ s and $t = 6$ s, $P_G = 0$ and $|P_{gs}| = |P_{WT1}|$. In Fig. 78, a positive value of P_{gs} means that the grid side of the MMShC is injecting power into the grid, while negative values mean that the grid side of the MMShC is absorbing power, and that is why P_{gs} becomes negative between $t = 4.8$ s and $t = 6$ s. In Fig. 78(b), the voltages synthesized by the MMShC at its grid-side terminals are shown. It is interesting to observe that, at $t = 4.8$ s, the three-phase voltages suffer a phase jump because the converter is changing from grid-following to grid-forming mode. In other words, at this moment, the reference of the voltage to be synthesized at the converter's terminal is

changed because of the change of the adopted control technique. In Fig. 78(c), the voltages synthesized by the MMShC at its machine-side terminals are shown, which are related to the FOC algorithm responsible for regulating the generator speed.

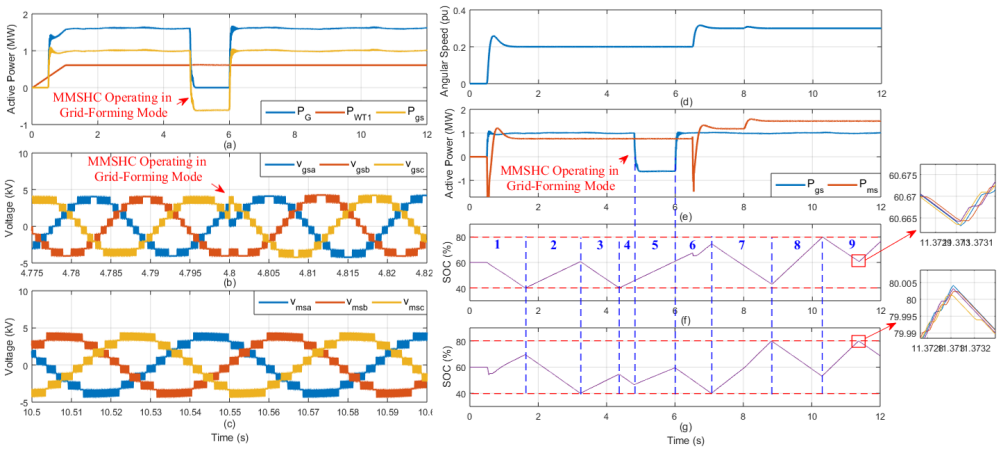

Fig. 78: Simulation results of MMShC with integrated batteries operating in grid-connected and islanded modes. (a) Active power values, (b) voltage synthesized by the MMShC at its grid-side terminals, (c) voltage synthesized by the MMShC at its machine-side terminals, (d) PMSG angular speed, (e) MMShC grid-side and machine-side power values, (f) MMShC phase-A String-X battery SOC values, and (g) MMShC phase-A String-Y battery SOC values.

In Fig. 78(d), the generator speed is shown and it is possible to notice that this speed is properly regulated according to the reference provided to the converter's control. In Fig. 78(e), the MMShC's grid-side and machine-side power values are shown, and it is interesting to notice that they are different from each other throughout the entire simulation period. It means that the system is operating in dispatchable mode and the mismatch between P_{gs} and P_{ms} is either being absorbed or being supplied by the converter's batteries. In Fig. 78(f) and (g), the MMShC's phase-A String-X and phase-A String-Y battery SOC values are shown, respectively. By observing these two figures, it is clear that the two strings operate in a complementary fashion, i.e., while one is connected to the grid terminal, the other is connected to the machine terminal. Since from the beginning of the simulation until $t = 4.8$ s the system is connected to the grid, then the grid-side terminal of the MMShC injects power into the grid, while its machine-side terminal absorbs power from the WT. For this reason, in intervals 1, 2, 3 and 4, while one string is connected to the grid being discharged, its complementary string is connected to the generator being charged. In other words, while the battery SOC values of one string are decreasing, the battery SOC values of its complementary string are increasing. Between $t = 4.8$ s and $t = 6$ s, which corresponds to interval 5, the system is disconnected from the main grid, and both terminals of the MMShC start

to absorb power since the grid-side terminal of the converter is absorbing the power produced by the other WT ($|P_{gs}| = |P_{WT1}|$). Thus, in interval 5, the battery SOC values of both strings simultaneously increase, as shown in Fig. 78(f) and (g). Intervals 6, 7, 8, and 9 correspond to moments where the system is connected to the main grid again. Thus, in these intervals, while one string is connected to the grid being discharged, the other is connected to the generator being charged. In Fig. 78(f) and (g), horizontal dashed red lines are used to represent the SOC limits (equal to 40% and equal to 80%). These limits are used to control the moment in which a swapping action is required to change the connection of the two complementary strings between the grid and the machine terminals. Finally, it is also interesting to observe the zoom sub figures of Fig. 78(f) and (g), where the battery SOC values of each battery within Strings X and Y can be seen. The SOC values of all the batteries within the same string remain similar due to the SOC-balancing algorithm previously explained in this thesis.

In Fig. 79, the simulation results corresponding to the hybrid MMShC operating in grid-connected and in islanded modes are presented. In this simulation, each string of the hybrid MMShC was composed of $N = 5$ FB submodules with 10-mF capacitors integrated, and of $M = 4$ FB submodules with integrated batteries. The batteries of each submodule were designed with the following rated voltage and rated energy: 1 kV, and 0.125 Ah. As previously explained in Section 3.6 of this thesis, the dispatchable operation of the hybrid MMShC requires a complex control. Since the results presented in this subsection were presented in a conference before the dispatchable operation of the hybrid MMShC was proposed, then the hybrid MMShC does not operate in a dispatchable fashion in the simulation results presented in Fig. 79. In other words, in the simulation results presented in Fig. 79, the hybrid MMShC operates as the MMShC with only capacitors when connected to the grid, which means that it injects into the grid an instantaneous power value equal to the power instantaneously produced by the WT, in order to maintain the submodule-capacitor voltages constant and regulated. In the grid-connected mode, the batteries of the hybrid MMShC remain in stand-by mode. When the system becomes islanded, then the battery submodules are enabled, and the capacitor submodules are the ones that enter stand-by mode. The same hypothetical wind farm (illustrated in Fig. 77) is also considered in this simulation. From the beginning of the simulation until $t = 2$ s, the system is initialized. From $t = 2$ s until $t = 4$ s, the hybrid MMShC operates in grid-connected mode. Between $t = 4$ s and $t = 6$ s, the wind power plant is disconnected from the main grid, and the hybrid MMShC enters in grid-forming mode. At $t = 6$ s, the wind farm is reconnected to the main grid and the hybrid MMShC comes back to grid-following mode.

In Fig. 79(a) and (b), the voltages synthesized by the hybrid MMShC at its grid-side and machine-side terminals are shown, respectively. In Fig. 79(c), the power values P_G, P_{WT1}, P_{gs}, and P_{ms} are shown. While the wind power plant is connected to the grid, then the power injected into the grid (P_G) is equal to the sum of the power values produced by the two WTs, i.e., $P_G = P_{WT1} + P_{gs}$, where $P_{gs} = P_{ms} = P_{WT2}$ since

the hybrid MMShC does not operate in a dispatchable fashion in this example. When the wind farm is disconnected from the main grid, then $P_G = 0$, and the grid-side terminal of the hybrid MMShC starts to absorb the power produced by the other WT, i.e., $|P_{gs}| = |P_{WT1}|$. The negative value of P_{gs} means that the grid-side terminal of the hybrid MMShC is absorbing power instead of injecting power into the grid. The machine-side terminal of the hybrid MMShC continues to absorb the power produced by its own WT, i.e., $P_{ms} = P_{WT2}$. In Fig. 79(d), the PMSG speed is shown, which is kept regulated with a value equal to 0.3 pu throughout the entire simulation period. In Fig. 79(e) and (f), the hybrid MMShC's phase-A String-X and phase-A String-Y submodule-capacitor voltages are shown, respectively. In Fig. 79(g) and (h), the hybrid MMShC's phase-A String-X and phase-A String-Y submodule-battery SOC values are shown, respectively. As previously mentioned, while the wind farm is connected to the grid, the batteries of the hybrid MMShC remain in stand-by mode, and their SOC values remain constant, as shown in Fig. 79(g) and (h). The converter's capacitors are the ones transferring the power produced by the WT to the grid. In Fig. 79(e) and (f), the swapping voltage ripple can be observed during the moments in which the system is connected to the main grid. The swapping ripple presents a frequency equal to 10 Hz, which is the switching frequency of the converter's bidirectional-switch stacks (swap switches). Once again, it is important to highlight the fact that 10 Hz is a very low switching frequency for a power-electronic semiconductor device. While the wind power plant is disconnected from the main grid, the submodule-capacitor voltages remain constant (see Fig. 79(e) and (f)) since the submodule capacitors are by-passed as they operate in stand-by mode. The battery-SOC values of both strings (String X and String Y) increase during the period that the wind farm is disconnected from the main grid. This is because both terminals of the hybrid MMShC are absorbing power, i.e., $|P_{gs}| = |P_{WT1}|$ and $P_{ms} = P_{WT2}$. Thus, the batteries of both strings are simultaneously being charged.

The simulation results presented in this section demonstrated some interesting operational possibilities of the MMShC with an integrated ESS, which could allow for interesting configurations of wind power plants. These power plants could operate with an increased flexibility, in both grid-connected and islanded modes, while increasing the revenues of the wind-farm developer. As future works, more complex wind power plants composed of more WTs (some of them driven by the MMShC with an integrated ESS, and some of them with no ESS) should be considered. In this case, a load-sharing technique (as for example a droop control) will be required to decide the share of power to be absorbed/supplied by each WT with an integrated ESS.

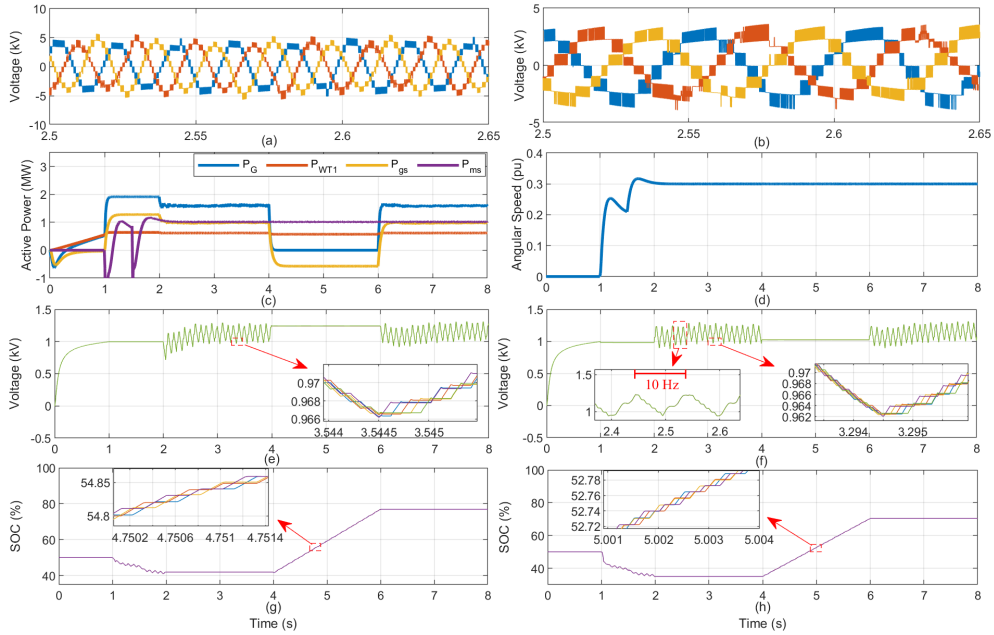

Fig. 79: Simulation results of hybrid MMShC operating in grid-connected and islanded modes. (a) Voltage synthesized by the MMShC at its grid-side terminals, (b) voltage synthesized by the MMShC at its machine-side terminals, (c) active power values, (d) PMSG angular speed, (e) MMShC phase-A String-X submodule-capacitor voltages, (f) MMShC phase-A String-Y submodule-capacitor voltages, (g) MMShC phase-A String-X battery SOC values and (h) MMShC phase-A String-Y battery SOC values.

4 Conclusions

In this thesis, two novel converter topologies with a modular multilevel structure were proposed for high-power medium-voltage electrical machine drive applications. The first topology was named 3x3-MMSC and it was proposed for high-power machine drives that operate at low frequencies. Simulation and experimental results were presented to explain the behavior and advantages of the new converter solution in comparison to the most well-established topologies in the industry, as well as to demonstrate some technical challenges of the new converter topology. As an advantage, the 3x3-MMSC presents a high performance at low-frequency operation as its submodule capacitors experience a low voltage ripple at this frequency range. The 3x3-MMSC also presents a stable and low-ripple operation when connected to an unbalanced grid, which is an advantage in relation to other converters with a modular multilevel structure. Another advantage of the 3x3-MMSC is its simplified control in comparison to other modular multilevel converter topologies due to its simplified structure that leads, for example, to

the absence of undesired circulating currents that must be suppressed by a control technique in the other topologies. Another advantage is the potential compactness of the 3x3-MMSC, with a reduced number of submodules and of capacitors in comparison to other converter topologies suitable for the same applications. However, the converter's lightness and compactness advantage is highly dependent on the configuration of the converter's input filter, which is required to filter out undesired harmonic currents that are injected into the grid. Finding an efficient and compact filter is one of the main challenges of the 3x3-MMSC. Another challenge of the 3x3-MMSC is the control of the reactive power exchanged with the grid by the converter. These are the most important issues that deserve special attention and further investigation in future works.

The second converter solution presented in this thesis was named MMShC, and it was proposed for modern/future high-power medium-voltage WTs. The basic operation and control of the new topology were demonstrated through both simulation and experimental results in this thesis. One of the important advantages of the MMShC is its potentially reduced volume and weight, due to the reduced submodule and capacitor count, in comparison to other converter topologies with a modular multilevel structure that could be suitable for medium-voltage WTs. In this thesis, the integration of batteries into the new MMShC was proposed so that a flexible and dispatchable WT solution was obtained. The solution proposed in this thesis allows for the ESS integration into the same converter that drives the WT, avoiding the need of an extra converter exclusively dedicated to the ESS. Besides, in the proposed solution, the batteries are distributed between the several submodules of the converter, avoiding the need of battery packs with considerably high voltage levels, which is still a challenge in the engineering industry nowadays. As explained in this thesis, the most cost-effective solution should be the presented hybrid MMShC, in which part of the converter's submodules have integrated batteries and part of them have conventional capacitors integrated. These capacitors are the ones responsible for transferring most of the power produced by the WT to the grid, while the converter's batteries only have to deal with the surplus power either produced by the WT or injected into the grid. The complex control of the hybrid MMShC was presented and explained in this thesis. It was also discussed in this thesis the benefits of having an integrated ESS into the WTs, for both the power system operator and for the wind power plant developer.

References

[1] C. Gerster, "Fast high-power/high-voltage switch using series-connected IGBTs with active gate-controlled voltage-balancing," *Proceedings of 1994 IEEE Applied Power Electronics Conference and Exposition - ASPEC'94*, 1994.

[2] J. W. Baek, D.-w. Yoo, and H.-g. Kim, "High-Voltage Switch Using Series-Connected IGBTs With Simple Auxiliary Circuit," *IEEE Transactions on Industry*

Applications, vol. 37, no. 6, pp. 1832–1839, 2001.

[3] F. V. Robinson and V. Hamidi, "Series connecting devices for high-voltage power conversion," *Proceedings of the Universities Power Engineering Conference*, pp. 1134–1139, 2007.

[4] S. Tanabe, S. Kobayashi, and M. Sampei, "Study on overvoltage protection in HVDC LTT valve," *IEEE Transactions on Power Delivery*, vol. 15, no. 2, pp. 545–550, 2000.

[5] B. Jacobson, P. Karlsson, G. Asplund, L. Harnefors, and T. Jonsson, "VSC-HVDC Transmission with Cascaded Two-Level Converters," *CIGRÉ SC B4 Session 2010*, 2010.

[6] K. Sharifabadi, L. Harnefors, H. P. Nee, S. Norrga, and R. Teodorescu, "Design, control and application of modular multilevel converters for HVDC transmission systems," *John Wiley & Sons*, 2016.

[7] M. Basić, P. C. O. Silva, and D. Dujić, "High Power Electronics Innovation Perspectives for Pumped Storage Power Plants," *Hydro 2018*, 2018. [Online]. Available: https://pel.epfl.ch

[8] M. Vasiladiotis, R. Baumann, C. Haderli, and J. Steinke, "IGCT-Based Direct AC/AC Modular Multilevel Converters for Pumped Hydro Storage Plants," *2018 IEEE Energy Conversion Congress and Exposition, ECCE 2018*, pp. 4837–4844, 2018.

[9] P. K. Steimer, O. Senturk, S. Aubert, and S. Linder, "Converter-fed synchronous machine for pumped hydro storage plants," *2014 IEEE Energy Conversion Congress and Exposition, ECCE 2014*, pp. 4561–4567, 2014.

[10] M. Diaz, R. C. Dobson, E. Ibaceta, A. Mora, M. Urrutia, M. Espinoza, F. Rojas, and P. Wheeler, "An overview of applications of the modular multilevel matrix converter," *Energies*, vol. 13, no. 21, pp. 1–37, 2020.

[11] ABB, *PCS 6000 for large wind turbines Medium voltage, full power converters up to 9 MVA*, 2012. [Online]. Available: https://new.abb.com/docs/default-source/ewea-doc/pcs6000wind.pdf?sfvrsn=2

[12] N. Fichaux, J. Beurskens, P. H. Jensen, J. Wilkes, S. Frandsen, J. D. Sorensen, P. Eecen, C. Malamatenios, J. A. Gomez, J. Hemmelmann, G. van Kuik, B. Bulder, F. Rasmussen, B. Janssen, T. Fischer, E. Bossanyi, M. Courtney, J. Giebhardt, R. Barthelmie, O. Holmstrom, D. Iuga, and S. Wokke, "UPWIND - Design Limits and Solutions for Very Large Wind Turbines," The European Wind Energy Association, Technical Report, Brussels, Belgium, 2011.

[13] V. Yaramasu, B. Wu, P. C. Sen, S. Kouro, and M. Narimani, "High-power wind energy conversion systems: State-of-the-art and emerging technologies," *Proceedings of the IEEE*, vol. 103, no. 5, pp. 740–788, 2015.

[14] M. Diaz, R. Cardenas, M. Espinoza, F. Rojas, A. Mora, J. C. Clare, and P. Wheeler, "Control of Wind Energy Conversion Systems Based on the Modular Multilevel Matrix Converter," *IEEE Transactions on Industrial Electronics*, vol. 64, no. 11, pp. 8799–8810, 2017.

[15] M. Diaz, R. Cárdenas, M. Espinoza, A. Mora, and P. Wheeler, "Modelling and control of the modular multilevel matrix converter and its application to wind energy conversion systems," *IECON Proceedings (Industrial Electronics Conference)*, no. 1140337, pp. 5052–5057, 2016.

[16] T. M. Iversen, S. S. Gjerde, and T. Undeland, "Multilevel converters for a 10 MW, 100 kV transformer-less offshore wind generator system," *2013 15th European Conference on Power Electronics and Applications, EPE 2013*, pp. 1–10, 2013.

[17] A. Madariaga, J. L. Martín, I. Zamora, I. Martínez De Alegría, and S. Ceballos, "Technological trends in electric topologies for offshore wind power plants," *Renewable and Sustainable Energy Reviews*, vol. 24, pp. 32–44, 2013. [Online]. Available: http://dx.doi.org/10.1016/j.rser.2013.03.039

[18] Y. Okazaki, M. Hagiwara, and H. Akagi, "A speed-sensorless start-up method of an induction motor driven by a modular multilevel cascade inverter (MMCI-DSCC)," *IEEE Transactions on Industry Applications*, vol. 50, no. 4, pp. 2671–2680, 2014.

[19] A. J. Korn, M. Winkelnkemper, and P. Steimer, "Low output frequency operation of the Modular Multi-Level Converter," *2010 IEEE Energy Conversion Congress and Exposition, ECCE 2010 - Proceedings*, pp. 3993–3997, 2010.

[20] M. Soares and E. H. Watanabe, "MMC Applied to Pumped Hydro Storage using a Differentiable Approximation of a Square Wave as Common-Mode Voltage during Low-Frequency Operation," *2020 IEEE 21st Workshop on Control and Modeling for Power Electronics, COMPEL 2020*, 2020.

[21] A. Antonopoulos, L. Ängquist, S. Norrga, K. Ilves, L. Harnefors, and H. P. Nee, "Modular multilevel converter AC motor drives with constant torque from zero to nominal speed," *IEEE Transactions on Industry Applications*, vol. 50, no. 3, pp. 1982–1993, 2014.

[22] M. Hagiwara, I. Hasegawa, and H. Akagi, "Start-up and low-speed operation of an electric motor driven by a modular multilevel cascade inverter," *IEEE Transactions on Industry Applications*, vol. 49, no. 4, pp. 1556–1565, 2013.

[23] J. Hu, K. Xu, L. Lin, and R. Zeng, "Analysis and enhanced control of hybrid-MMC-based HVDC systems during asymmetrical dc voltage faults," *IEEE Transactions on Power Delivery*, vol. 32, no. 3, pp. 1394–1403, 2017.

[24] G. P. Adam and I. E. Davidson, "Robust and Generic Control of Full-Bridge Modular Multilevel Converter High-Voltage DC Transmission Systems," *IEEE Transactions on Power Delivery*, vol. 30, no. 6, pp. 2468–2476, 2015.

[25] C. Guo, J. Yang, and C. Zhao, "Investigation of small-signal dynamics of modular multilevel converter under unbalanced grid conditions," *IEEE Transactions on Industrial Electronics*, vol. 66, no. 3, pp. 2269–2279, 2019.

[26] Z. Ou, G. Wang, and L. Zhang, "Modular multilevel converter control strategy based on arm current control under unbalanced grid condition," *IEEE Transactions on Power Electronics*, vol. 33, no. 5, pp. 3826–3836, 2018.

[27] B. Bahrani, S. Debnath, and M. Saeedifard, "Circulating Current Suppression of the Modular Multilevel Converter in a Double-Frequency Rotating Reference Frame," *IEEE Transactions on Power Electronics*, vol. 31, no. 1, pp. 783–792, 2016.

[28] R. Darus, J. Pou, G. Konstantinou, S. Ceballos, and V. G. Agelidis, "Controllers for eliminating the ac components in the circulating current of modular multilevel converters," *IET Power Electronics*, vol. 9, no. 1, pp. 1–8, 2016.

[29] L. He, K. Zhang, J. Xiong, and S. Fan, "A repetitive control scheme for harmonic suppression of circulating current in modular multilevel converters," *IEEE Transactions on Power Electronics*, vol. 30, no. 1, pp. 471–481, 2015.

[30] W. Kawamura, K. L. Chen, M. Hagiwara, and H. Akagi, "A Low-Speed, High-Torque Motor Drive Using a Modular Multilevel Cascade Converter Based on Triple-Star Bridge Cells (MMCC-TSBC)," *IEEE Transactions on Industry Applications*, vol. 51, no. 5, pp. 3965–3974, 2015.

[31] S. Du, A. Dekka, B. Wu, and N. Zargari, "Modular Multilevel Converters Analysis, Control and Applications," in *IEEE Press*, 2018.

[32] N. Thitichaiworakorn, M. Hagiwara, and H. Akagi, "A Medium-Voltage Large Wind Turbine Generation System Using an AC/AC Modular Multilevel Cascade Converter," *IEEE Journal of Emerging and Selected Topics in Power Electronics*, vol. 4, no. 2, pp. 534–546, 2016.

[33] M. Muneshima and Y. Nishida, "A multilevel AC-AC conversion system and control method using Y-connected H-bridge circuits and bidirectional switches," *2013 IEEE Energy Conversion Congress and Exposition, ECCE 2013*, pp. 4008–4013, 2013.

[34] M. Glinka and R. Marquardt, "A new AC/AC multilevel converter family," *IEEE Transactions on Industrial Electronics*, vol. 52, no. 3, pp. 662–669, 2005.

[35] P. W. Hammond, "A New Approach to Enhance Power Quality for Medium Voltage AC Drives," *IEEE Transactions on Industry Applications*, vol. 33, no. 1, pp. 202–208, 1997.

[36] R. W. Erickson and O. A. Al-Naseem, "A new family of matrix converters," *IECON Proceedings (Industrial Electronics Conference)*, vol. 2, no. Xcx, pp. 1515–1520, 2001.

[37] B. Liu, Y. Meng, and S. Bai, "A novel high-power AC/AC modular multilevel converter in y configuration and its control strategy," *Asia-Pacific Power and Energy Engineering Conference, APPEEC*, vol. 2016-Decem, pp. 973–977, 2016.

[38] N. Thitichaiworakorn, M. Hagiwara, and H. Akagi, "A single-phase to three-phase direct AC/AC modular multilevel cascade converter based on double-star bridge-cells (MMCC-DSBC)," *1st International Future Energy Electronics Conference, IFEEC 2013*, pp. 476–481, 2013.

[39] B. Fan, K. Wang, P. Wheeler, C. Gu, and Y. Li, "An Optimal Full Frequency Control Strategy for the Modular Multilevel Matrix Converter Based on Predictive Control," *IEEE Transactions on Power Electronics*, vol. 33, no. 8, pp. 6608–6621, 2018.

[40] W. Kawamura, M. Hagiwara, and H. Akagi, "Control and experiment of a modular multilevel cascade converter based on triple-star bridge cells," *IEEE Transactions on Industry Applications*, vol. 50, no. 5, pp. 3536–3548, 2014.

[41] B. Fan, K. Wang, P. Wheeler, C. Gu, and Y. Li, "A Branch Current Reallocation Based Energy Balancing Strategy for the Modular Multilevel Matrix Converter Operating Around Equal Frequency," *IEEE Transactions on Power Electronics*, vol. 33, no. 2, pp. 1105–1117, 2018.

[42] W. Kawamura and H. Akagi, "Control of the modular multilevel cascade converter based on triple-star bridge-cells (MMCC-TSBC) for motor drives," *2012 IEEE Energy Conversion Congress and Exposition, ECCE 2012*, pp. 3506–3513, 2012.

[43] M. Lei, Y. Li, Z. Li, C. Zhao, B. Xia, and P. Wang, "Exploration of a Modular Multilevel Converter for Direct AC-AC Conversion," *Proceedings - 2018 IEEE International Power Electronics and Application Conference and Exposition, PEAC 2018*, pp. 1–6, 2018.

[44] D. Karwatzki and A. Mertens, "Generalized Control Approach for a Class of Modular Multilevel Converter Topologies," *IEEE Transactions on Power Electronics*, vol. 33, no. 4, pp. 2888–2900, 2018.

[45] P. Blaszczyk, "Hex-Y - A New Modular Multilevel Converter Topology for a Direct AC-AC Power Conversion," *2018 20th European Conference on Power Electronics and Applications, EPE 2018 ECCE Europe*, pp. P.1–P.10, 2018.

[46] V. Dargahi, K. A. Corzine, J. H. Enslin, A. K. Sadigh, J. Rodriguez, and F. Blaabjerg, "Modular-Concatenated-Cell (MCC) Multilevel Converter: A Novel Circuit Topology and Innovative Logic-Equations-Based Control Technique," *2018 IEEE Energy Conversion Congress and Exposition, ECCE 2018*, no. Mcc, pp. 2970–2975, 2018.

[47] M. R. Islam, Y. Guo, and J. G. Zhu, "11-kV Series-Connected H-Bridge Multilevel Converter for Direct Grid Connection of Renewable Energy Systems," *Journal of international Conference on Electrical Machines and Systems*, vol. 1, no. 2, pp. 70–78, 2012.

[48] M. S. Diab, A. M. Massoud, S. Ahmed, and B. W. Williams, "A Dual Modular Multilevel Converter with High-Frequency Magnetic Links between Submodules for MV Open-End Stator Winding Machine Drives," *IEEE Transactions on Power Electronics*, vol. 33, no. 6, pp. 5142–5159, 2018.

[49] E. Behrouzian and M. Bongiorno, "Investigation of negative-sequence injection capability of cascaded h-bridge converters in star and delta configuration," *IEEE Transactions on Power Electronics*, vol. 32, no. 2, pp. 1675–1683, 2016.

[50] S. Liu, M. Saeedifard, and X. Wang, "Analysis and control of the modular multilevel matrix converter under unbalanced grid conditions," *IEEE Journal of Emerging and Selected Topics in Power Electronics*, vol. 6, no. 4, pp. 1979–1989, 2018.

[51] S. D'Arco, M. Quraan, P. Tricoli, and L. Piegari, "Low Frequency Operation of Modular Multilevel Converters with Embedded Battery Cells for Traction Drives," *International Symposium on Power Electronics, Electrical Drives, Automation and Motion*, pp. 1375–1382, 2016.

[52] M. Vasiladiotis and A. Rufer, "Analysis and control of modular multilevel converters with integrated battery energy storage," *IEEE Transactions on Power Electronics*, vol. 30, no. 1, pp. 163–175, 2015.

[53] N. Kawakami, S. Ota, H. Kon, S. Konno, H. Akagi, H. Kobayashi, and N. Okada, "Development of a 500-kW modular multilevel cascade converter for battery energy storage systems," *IEEE Transactions on Industry Applications*, vol. 50, no. 6, pp. 3902–3910, 2014.

[54] J. I. Y. Ota, T. Sato, and H. Akagi, "Enhancement of performance, availability, and flexibility of a battery energy storage system based on a modular multilevel

cascaded converter (MMCC-SSBC)," *IEEE Transactions on Power Electronics*, vol. 31, no. 4, pp. 2791–2799, 2016.

[55] C. Zhang, D. Jiang, X. Zhang, J. Chen, C. Ruan, and Y. Liang, "The Study of a Battery Energy Storage System Based on the Hexagonal Modular Multilevel Direct AC/AC Converter (Hexverter)," *IEEE Access*, vol. 6, pp. 43 343–43 355, 2018.

[56] S. K. Chaudhary, A. F. Cupertino, R. Teodorescu, and J. R. Svensson, "Benchmarking of modular multilevel converter topologies for ES-STATCOM realization," *Energies*, vol. 13, no. 13, pp. 1–22, 2020.

[57] B. Novakovic and A. Nasiri, "Modular Multilevel Converter for Wind Energy Storage Applications," *IEEE Transactions on Industrial Electronics*, vol. 64, no. 11, pp. 8867–8876, 2017.

[58] L. Qu and W. Qiao, "Constant power control of DFIG wind turbines with supercapacitor energy storage," *IEEE Transactions on Industry Applications*, vol. 47, no. 1, pp. 359–367, 2011.

[59] L. Miao, J. Wen, H. Xie, C. Yue, and W. J. Lee, "Coordinated Control Strategy of Wind Turbine Generator and Energy Storage Equipment for Frequency Support," *IEEE Transactions on Industry Applications*, vol. 51, no. 4, pp. 2732–2742, 2015.

[60] F. Diaz-Gonzalez, F. D. Bianchi, A. Sumper, and O. Gomis-Bellmunt, "Control of a flywheel energy storage system for power smoothing in wind power plants," *IEEE Transactions on Energy Conversion*, vol. 29, no. 1, pp. 204–214, 2014.

[61] P. Pinson, "Wind energy: Forecasting challenges for its operational management," *Statistical Science*, vol. 28, no. 4, pp. 564–585, 2013.

[62] D. Pagnani, F. Blaabjerg, C. L. Bak, F. M. F. Da Silva, Ł. H. Kocewiak, and J. Hjerrild, "Offshore wind farm black start service integration: Review and outlook of ongoing research," *Energies*, vol. 13, no. 23, 2020.

[63] G. Gontijo, S. Wang, T. Kerekes, and R. Teodorescu, "Performance Analysis of Modular Multilevel Converter and Modular Multilevel Series Converter under Variable-Frequency Operation Regarding Submodule-Capacitor Voltage Ripple," *Energies*, vol. 14, no. 3, p. 776, 2021.

[64] Q. Tu, Z. Xu, Y. Chang, and L. Guan, "Suppressing DC voltage ripples of MMC-HVDC under unbalanced grid conditions," *IEEE Transactions on Power Delivery*, vol. 27, no. 3, pp. 1332–1338, 2012.

[65] N. Holtsmark, "Reactive Power Compensation Using a Matrix Converter," Master's thesis, 2010.

[66] P. W. Wheeler, J. Rodríguez, J. C. Clare, L. Empringham, and A. Weinstein, "Matrix converters: A technology review," *IEEE Transactions on Industrial Electronics*, vol. 49, no. 2, pp. 276–288, 2002.

[67] Z. Malekjamshidi, M. Jafari, J. Zhang, and J. Zhu, "Design and analysis of protection circuits for safe operation of direct matrix converters," *2017 20th International Conference on Electrical Machines and Systems, ICEMS 2017*, pp. 0–3, 2017.

[68] B. Wu, Y. Lang, N. Zargari, and S. Kouro, *Power Conversion and Control Of Wind Energy Systems*. John Wiley & Sons, 2011.

[69] J. I. Ota, Y. Shibano, N. Niimura, and H. Akagi, "A phase-shifted-PWM D-STATCOM using a modular multilevel cascade converter (SSBC) - Part I: Modeling, analysis, and design of current control," *IEEE Transactions on Industry Applications*, vol. 51, no. 1, pp. 279–288, 2015.

[70] H. Akagi, "Classification, Terminology, and Application of the Modular Multilevel Cascade Converter (MMCC)," *IEEE Transactions on Power Electronics*, vol. 26, no. 11, pp. 3119–3130, 2011.

[71] H. Akagi, S. Inoue, and T. Yoshii, "Control and performance of a transformerless cascade PWM STATCOM with star configuration," *IEEE Transactions on Industry Applications*, vol. 43, no. 4, pp. 1041–1049, 2007.

[72] M. M. Merlin and T. C. Green, "Cell capacitor sizing in multilevel converters: Cases of the modular multilevel converter and alternate arm converter," *IET Power Electronics*, vol. 8, no. 3, pp. 350–360, 2015.

ISSN (online): 2446-1636
ISBN (online): 978-87-7573-854-0

AALBORG UNIVERSITY PRESS